

A X-BAND PATCH ANTENNA ARRAY WITH LOW CROSS-POLARIZATION

FOR WEATHER RADAR APPLICATIONS

by Marc Vizcarro i Carretero



(Front picture of the 4x4 sub-array designed and manufactured in this M.Sc. Thesis)

A X-Band Patch Antenna Array with Low Cross Polarization for Weather Radar Applications

THESIS

submitted in partial fulfillment of the
requirements for the degree of

MASTER OF SCIENCE

in

ELECTRICAL ENGINEERING

by

Marc Vizcarro i Carretero

The work presented in this Thesis was performed at:

Antenna and Electromagnetic Modelling Department
Fraunhofer Institute for High Frequency Physics and Radar Techniques FHR

In collaboration with:

Microwave Sensing, Signals and Systems Group
Department of Microelectronics
Faculty of Electrical Engineering, Mathematics and Computer Science
Delft University of Technology

WEATHER RADAR (WRAD)

A X-Band Patch Antenna Array With Low Cross-Polarization
For Weather Radar Applications

Author and Main Supervisors:

Marc Vizcarro i Carretero ^{1,2}	(Fraunhofer FHR, M.Sc. Candidate Antenna Engineer)
Dr. Stefano Turso ¹	(Fraunhofer FHR, M.Sc. Supervisor Project Leader)
Prof. DSc. Alexander Yarovoy ²	(TU Delft, M.Sc. Supervisor Full Professor, MS3 Chair)

Associated Partners:

M.Sc. Carlos Galvís Salzburg ¹	(Fraunhofer FHR, Antenna Engineer)
Dr. Thomas Bertuch ¹	(Fraunhofer FHR, Antenna Department Leader)
Dr. Oleg Krasnov ²	(TU Delft, Associate Professor)

¹Fraunhofer-Institut für Hochfrequenzphysik und Radartechnik, FHR in Wachtberg.

²Delft University of Technology, TU Delft

August 2019.



DELFT UNIVERSITY OF TECHNOLOGY

DEPARTMENT OF ELECTRICAL ENGINEERING

The undersigned hereby certify that they have read and recommend to the Faculty of Electrical Engineering, Mathematics and Computer Science for acceptance a thesis entitled "**A X-Band Patch Antenna Array With Low Cross-Polarization For Weather Radar Applications**" by **Marc Vizcarro i Carretero** in partial fulfillment of the requirements for the degree of **Master of Science**.

Dated: August 30th 2019

Chairman:

Prof. DSc. Alexander Yarovoy

Committee Members:

Prof. Dr-Ing. Peter Knott

Dr. Stefano Turso

Dr. Oleg Krasnov

To the power of randomness and
to the random choices of those who preceded me,

para vosotros Jesús y Manolo.






Abstract

Meaningful dual-polarized radar estimations suitable for radar meteorology require a *cross-polarization discrimination (XPD)* and *isolation (XPI)* in excess of 30 dB to reach a differential reflectivity accuracy lower than 0.1 dB . A planar dual-polarized patch antenna array featuring low cross-polarization is proposed to meet these requirements via a simple implementation of imaged feeding and candidates as a cost-effective electronically steerable array for short-range X-band weather radars.

However, relatively high levels of cross-polarization are to be expected in a patch array and therefore counteracted with specific designs. To this end, a feed rotation technique is implemented via bi-axial imaging of the feeding probes for each logical sub-array of 2 by 2 elements. Improvements in *XPD* respect to a repeated feeding scheme are significant and in excess of 30 dB . Based on successful designs and simulations in CST Microwave Studio and ANSYS HFSS, an X-band array of 4 by 4 patches has been manufactured. Extensive instrumental validation has been largely supporting this specialized feeding concept meeting the theoretical expectations and electromagnetic simulation results.

Acknowledgements

This thesis is nothing but the result of hard work and the mentoring I have received throughout my M.Sc. degree at TU Delft, Fraunhofer FHR, Thales Nederland B.V., or even before, at Indra and UPC. All in all, each organization and its professionals have contributed to my continuous commitment to achieve excellence in Radar Engineering. But this quest of excellence is far from ending and before devising new horizons, I would like to personally acknowledge all the people who have had an impact in my career so far.

  (Delft, the Netherlands)	To <i>Oleg Krasnov</i> for his support and passion in teaching Radar Engineering. But also to <i>Alexander Yarovoy</i> , <i>Andrea Neto</i> , <i>Daniele Cavallo</i> and <i>Núria Llobart</i> , with whom I managed to finally understand the EM phenomena and delve into antenna theory.
 (Wachtberg, Germany)	To <i>Carlos Galvís</i> , <i>Thomas Bertuch</i> with a special mention to <i>Stefano Turso</i> and <i>Peter Knott</i> who gave me the opportunity to join Fraunhofer FHR at the end of the 10 th Radar/SAR summer school.
 (Delft, the Netherlands)	To <i>Ronny Harmanny</i> and <i>Roeland Trommel</i> for mentoring me and promoting me to participate in the EuRAD 2019. Also to <i>Hannah García Doherty</i> along with <i>Lorenzo Cifola</i> for the great moments we spent together.
 (Madrid, Spain)	To <i>Julio Escribano</i> and <i>Ignacio Álvarez</i> for giving me the opportunity to join their team and give my first professional steps within the European Defense industry. And also, to <i>José Andrés Jimenez</i> and <i>José Miguel Pascual</i> for sharing their invaluable vision after my departure.
  (Barcelona, Spain)	To <i>Albert Aguasca</i> , <i>Núria Duffo</i> , <i>Francesc Torres</i> and <i>Carlos López-Martínez</i> (now LIST, Luxembourg) for their academic support and motivation throughout my Bachelor's degree in Barcelona.

Particularly in this thesis, I would like to thank *Dr. Stefano Turso*, M.Sc. *Carlos Galvís* and *Prof. DSc. Alexander Yarovoy* for the invaluable time they spent teaching and indirectly, mentoring me. The only way I have had to pay back their effort and trust so far, is by putting passion in my work, starting by taking care of the tiniest detail up to being a link between leading organizations in European Radar research.

Last but not least, I cannot forget about my parents and friends, who always wished I left home and now complain that I barely go back. Among them, now I also have to include all the new friendships I established in Delft and Bonn. An honorific mention goes to *Andrea Degasperi* for being a great colleague throughout the M.Sc, but also to *Giovanni*, *Matteo* and *Claudio*, as my stay in Bonn would not have been the same without them.

Bonn, June 18th 2019

Table of Contents

Abstract.....	1
Acknowledgements	2
Table of Contents	3
List of Figures	6
List of Tables.....	9
Acronyms	12
Chapter 1 - Introduction	14
1.1 Motivation	14
1.1.1 Why Polarimetric Weather Radar?	15
1.1.2 Why AESA and short-range?	16
1.1.3 Why X-Band Radar?	17
1.2 State-of-the-art and Novelty.....	19
1.3 Objectives	22
1.4 Proposed Approach.....	24
1.5 Outline of the Thesis	26
Chapter 2 - AESA for Weather Radar	27
2.1 Introduction to Phased Array Technology	27
2.1.1 Linear Array Antenna.....	28
2.1.2 Phased Array Design Methodologies	31
2.2 Introduction to Polarimetric Weather Radar	33
2.2.1 PSM Measurement Example	34
2.2.2 Atmospheric Remote Sensing Values of Interest.....	36
2.2.3 Polarization Isolation or Polarization Discrimination?	38
2.3 Suitable Antenna Topologies for low-cost Weather Radar	39
2.4 Challenges in Phased Array Weather Radar	41
2.5 Further Considerations	42
Chapter 3 - Patch Antenna Design.....	43
3.1 Patch Antenna	43
3.2 Radiation Models	44
3.2.1 Physical Interpretation	45
3.2.2 Cavity Model	46

3.3 Feeding Techniques.....	53
3.3.1 Overview and Analysis.....	53
3.3.2 Dual Polarization Techniques for Probe-fed Patch Antennas.....	56
3.3.3 Feeding Probe Isolation Techniques.....	59
3.4 Cross-Polarization Assessment.....	61
3.5 Conclusions on the Dual-Pol Fed-Probe Patch Antenna Analysis.....	69
Chapter 4 - Sub-Array Design.....	71
4.1 Substrate Choice and Unitary Element Design.....	71
4.1.1 Substrate Assessment for the Radiation Stage.....	72
4.1.2 Substrate Assessment for the Feeding Stage.....	73
4.1.3 Proposed Substrate Choice.....	74
4.1.4 Unitary Element Design.....	76
4.2 Baseline 2x2 Sub-Array.....	78
4.2.1 Scanning Asymmetries.....	80
4.2.2 XPD Diagrams for 2x2 Baseline Sub-Array with Ideal Ports.....	81
4.3 Feed Rotation.....	82
4.3.1 Mono-Pol Patch Feed Imaging.....	82
4.3.2 Dual-Pol Patch Feed Rotation.....	83
4.3.3 2x2 Imaged Sub-Array.....	86
4.3.4 4x4 Imaged Sub-Array.....	89
4.3.5 Sidelobe Level Management.....	92
4.4 Conclusions on Feed Rotation.....	93
Chapter 5 - Feeding Network Design.....	94
5.1 Requirements and Constraints.....	94
5.1.1 Space Optimization.....	95
5.2 Passive Splitter Design.....	97
5.2.1 Design Methodology and Requirements.....	98
5.2.2 Proposed T-Junctions and Optimization.....	100
5.3 Integrated Design.....	103
5.3.1 Feeding Network for the 4x4 Baseline Sub-Array.....	103
5.3.2 Feeding Network for the 4x4 Imaged Sub-Array.....	104
5.4 Simulation Results.....	106
5.4.1 Results for the 4x4 Baseline Sub-Array.....	106
5.4.2 Results for 4x4 Imaged Sub-Array.....	109

5.4.3 Comparative Simulation	114
5.5 Prospective Improvements	115
Chapter 6 - Measurements and Validation	116
6.1 Validation Methodology	117
6.2 Set-up Description	117
6.2.1 S-Parameters Measurements	117
6.2.2 Anechoic Chamber Measurements	119
6.3 S-Parameters	123
6.3.1 Scattering Measurements for the 4x4 Baseline Sub-Array	123
6.3.2 Scattering Measurements for the 4x4 Imaged Sub-Array	126
6.4 Beamforming	130
6.5 Further Validations	134
Chapter 7 - Conclusions and Future Work	136
Bibliography	139
APPENDIX – A	A
APPENDIX – B	B
APPENDIX – C	C
APPENDIX – D	D
APPENDIX – E	E
APPENDIX – F	F

List of Figures

Figure 1-1 – Traditional vs Low-cost Weather Radar Concept	14
Figure 1-2 – Low-cost WRAD Art Concept (Electronic Scan in Elevation).....	15
Figure 1-3 – XPD and XPI in Transmission.....	16
Figure 1-4 – Disadvantages of Traditional Weather Radars	17
Figure 1-5 – Tradational Weather Radar and the associated gap to Earth Curvature [9]	18
Figure 1-6 – AESA Scanning Art Concept.....	18
Figure 1-7 – Cylindric Polarimetric Phased Array Radar [23]	20
Figure 1-8 – CASA Phase-Tilt Weather Radar [24]	20
Figure 1-9 – Sub-array Design Approach	22
Figure 2-1 – Generalised Electronically Steering Array Topologies. (a) PESA and (b) AESA with T/R Module concept.	27
Figure 2-2 – Linear Array Antenna, Projection on the YZ Plane with Physical Assumptions	28
Figure 2-3 – Four-linear Array with Broadside Scanning (element spacing comparison)	29
Figure 2-4 – Four-linear Array Scanning	29
Figure 2-5 – Grating Lobe Example	30
Figure 2-6 – Planar Liner Array scanning at Broadside	31
Figure 2-7 – Unit Cell Design	32
Figure 2-8 – Sub-Array Design	32
Figure 2-9 – Ideal PSM Measurement (Alternate-Transmit Alternate-Receive Mode).....	34
Figure 2-10 – Ideal Polarimetric Isolation	34
Figure 2-11 – Finite Polarimetric Isolation	35
Figure 2-12 - Effective Cross Polarimetric Isolation for a Dual-Pol Antenna	38
Figure 2-13 – Sub-Array Design and its benefits for a Low-Cost AESA Weather Radar	39
Figure 2-14 – E-Fields produced by and H and V polarised Electric Current.....	39
Figure 2-15 – Beam Pattern Topologies in Weather Radar	40
Figure 2-16 – Phase Pattern of a 4x4 Patch Antenna Array scanning at Broadside	40
Figure 2-17 – Non-Uniform Beam Filling and Cross-polarization Distribution	41
Figure 2-18 – Proposed Patch based Sub-Array Design for a Low-Cost AESA WRAD.....	42
Figure 3-1 – Advantages of Patch Antenna Technology.....	43
Figure 3-2 – Formulation of the Radiation Mechanism	44
Figure 3-3 – Simplified EM Distributions a Rectangular Patch Antenna (I).....	45
Figure 3-4 – Simplified EM Distributions a Rectangular Patch Antenna (II).....	45
Figure 3-5 – Simplified EM Distributions a Rectangular Patch Antenna (III).....	45
Figure 3-6 – Cavity Model Framework.....	46
Figure 3-7 – Cavity and Geometry Definition.....	47
Figure 3-8 – Cavity and Real E-Field Distributions	49
Figure 3-9 – Field Distribution for <i>TM_{010z}</i>	50
Figure 3-10 – <i>TM_{010z}</i> Equivalent Currents	50
Figure 3-11 – z-directed E-Field for a Fed-probe Patch Antenna	51
Figure 3-12 – Equivalent Slots for Linear Dual-Pol Patch Antenna	51
Figure 3-13 – Cavity Model Polarimetric Performance	52
Figure 3-14 – Initial Dual-pol Probe-fed Patch Antenna	56

Figure 3-15 – Probe-fed Layout Topologies	57
Figure 3-16 – Probe-fed Efficiency Enhancement Techniques.....	57
Figure 3-17 – Initial Unit Cell Concept.....	58
Figure 3-18 – Unit cell sources of isolation and cross-polarization degradation	58
Figure 3-19 – Differential Feeding	59
Figure 3-20 – Via Fence Layout	60
Figure 3-21 – Polarization and Antenna Plane Reference.....	61
Figure 3-22 – Parallel-fed Current Distribution	62
Figure 3-23 – Isolation for a Dual-Pol Probe Fed Patch.....	64
Figure 3-24 – E-Field Distributions and Fringing Fields Decomposition	66
Figure 3-25 – Cavity Model and Dual-pol Probe-fed Patch Antenna Comparison for H-Pol	68
Figure 4-1 – Antenna Multilayer Decomposition.....	71
Figure 4-2 – Measured Radiation Efficiency for a Rectangular Patch Antenna	72
Figure 4-3 – Substrate Effect on Microstrip Lines.....	73
Figure 4-4 – Proposed Symmetric Multi-layer PCB for Dual-pol Probe-fed Patch Antennas	74
Figure 4-5 – Proposed Multilayer Layout	75
Figure 4-6 – Unitary Cell Dimensions.....	76
Figure 4-7 – Unit Cell Extension to Sub-Arrays	77
Figure 4-8 – Array Coupling Effect on Cross-polarization and Element Fencing.....	78
Figure 4-9 – 2x2 Baseline Coupling Mitigation Upgrades.....	78
Figure 4-10 – Intrinsic Element Coupling Asymmetries in Elevation Scanning.....	80
Figure 4-11 – Feed Imaging for Mono-pol Patch Antennas.....	82
Figure 4-12 – 2x2 Baseline and Imaged Sub-arrays.....	86
Figure 4-13 – H-Pol, 2x2 Imaged Sub-array and Phase Patterns	86
Figure 4-14 – H-Pol, 2x2 Imaged Sub-array Theoretically Phase Pattern	86
Figure 4-15 – V-Pol, 4x4 Baseline Sub-Array, E-Plane ($\phi = 90^\circ$).....	89
Figure 4-16 – 4x4 Imaged Sub-Array Proposals	89
Figure 4-17 – Doubling Spacing through Sub-Array Replicas	92
Figure 4-18 – Extended Feed Rotation Scheme.....	93
Figure 5-1 – Feeding Network Sketch for H-Pol Row	97
Figure 5-2 – Feed-net with Excessive Meandering - I	98
Figure 5-3 – Feed-net with Excessive Meandering - II.....	98
Figure 5-4 – Feed-net with Asymmetrical Via Distribution.....	98
Figure 5-5 - Assembled Simulation with Separated T-Junctions	99
Figure 5-6 – Assembled Simulation with Integrated T-Junctions	99
Figure 5-7 – Optimized H-Pol T-Junction, left-hand side	101
Figure 5-8 – H and V Row Feeding Networks Sketch	102
Figure 5-9 – Designed Feeding Network for 4x4 Baseline Sub-Array	103
Figure 5-10 – Designed Feeding Network for 4x4 Imaged Sub-Array	104
Figure 5-11 – Integrated 4x4 Imaged Sub-Array with Feeding Network for 1D Elevation Scanning	105
Figure 5-12 – Manufactured Sub-Arrays with Integrated Feeding Networks.....	114
Figure 5-13 – 4x4 Imaged Sub-Array with Grounded Feeding Network	115
Figure 5-14 – Minimization of cross-talk through an Elevated Ground Plane and Shield.....	115
Figure 6-1 – Microscope Antenna Inspection.....	117
Figure 6-2 – Ad-hoc TRL calibration kit.....	117

Figure 6-3 – S-Parameter Measurement Set-up	118
Figure 6-4 – Simplified Anechoic Chamber of AEM Department (Fraunhofer FHR)	119
Figure 6-5 – Measurement Process for Cross-polarization Assessment	119
Figure 6-6 – Comparison of Original and Time-gated Measurements	120
Figure 6-7 – High Resolution Measurement of XPD Diagram of NARDA – V-Pol.....	121
Figure 6-8 – High Resolution Measurement of XPD Diagram from NARDA – V-Pol (up-down flip)	121
Figure 6-9 – Antenna Positioning using a Spirit Level (Top) and a Plumb Line (Bottom)	122
Figure 6-10 – Mismatched ARC for measured Port 2 (RL > 10 dB)	128
Figure 6-11 – Matched ARC for measured Port 2 (RL > 7 dB)	128
Figure 6-12 – Analytical Beamforming for 4x4 Imaged Sub-Array (H-Pol).....	130
Figure 6-13 – 4x4 Imaged Sub-array with Integrated Feed-net, Full-scan ZDRb Assessment (Simulations vs. Measurements)	133
Figure 6-14 – Microscope Measurement Samples.....	134
Figure 6-15 – Ideal vs Manufactured Microstripline and Etching Effects	135
Figure 7-1 – Concept Feed Rotation applied to a 4x4 Baseline Sub-Array.....	138

List of Tables

Table 1.1 – Notable Weather Radars Prototypes from TU Delft.....	19
Table 1.2 – WRAD Sub-Array Requirements.....	22
Table 1.3 – M.Sc. Thesis Research Goals.....	23
Table 1.4 – Sub-Array Design Roadmap.....	24
Table 2.1 – Atmospheric Remote Sensing Values of Interest.....	36
Table 2.2 – XPI and XPD Definitions.....	38
Table 3.1 - Major Assumptions in Rectangular Cavity Model.....	47
Table 3.2 - Probe Feeding Techniques.....	54
Table 3.3 – Coupled Feeding Techniques.....	54
Table 3.4 – Capacitive Feeding Techniques.....	55
Table 3.5 – Via Fencing Examples (CST MWS Models).....	60
Table 3.6 – Feeding Line Orientations.....	61
Table 3.7 – Horizontally Mono-Polarized Probe-Fed Patch Pattern Comparison (CST MWS FD) .	62
Table 3.8 - Horizontally Mono vs Dual-Pol Probe-Fed Patch Pattern Comparison (CST MWS FD)	63
Table 3.9 – Vertically Dual-Pol Probe-Fed Patch Pattern Comparison (CST MWS FD).....	63
Table 3.10 – Mono vs Dual-Polarized Patches (CST MWS CAD Model).....	65
Table 3.11 – E-Field Carpet Comparison for H-Pol (CST MWS FD).....	65
Table 3.12 – E-Field Phase Contour Comparison for H-Pol (CST MWS FD).....	66
Table 3.13 – Magnitude Surface Currents Comparison for H-Pol (CST MWS FD).....	67
Table 3.14 – Phase Surface Currents Comparison for H-Pol (CST MWS FD).....	68
Table 3.15 – Far-field Magnitude Patterns for a Dual-pol Probe-fed Patch Antenna (CST MWS FD).....	69
Table 3.16 – Far-field Phase Patterns for a Dual-pol Probe-fed Patch Antenna (CST MWS FD)...	70
Table 3.17 – Far-field Phase Patterns for Mono and Dual-Pol Patch Comparison (CST MWS FD)	70
Table 4.1 – Microstripline Synthesis Examples.....	74
Table 4.2 – Updated Dimensions for Unitary Elements.....	76
Table 4.3 – V-Pol, 2x2 Baseline Sub-arrays Broadside Comparison (CST MWS FD).....	79
Table 4.4 – V-Pol, 2x2 Baseline Sub-arrays Scanning Comparison (CST MWS FD).....	79
Table 4.5 – V-Pol, 2x2 Baseline Sub-arrays Scanning Summary (CST MWS FD).....	80
Table 4.6 – UV XPD Diagrams for 2x2 Baseline Sub-Array.....	81
Table 4.7 – H-Pol, Far Field Phase Patterns for Imaged Feeds.....	83
Table 4.8 – H-Pol, Analytical Far Field Symmetries for H-polarised Dual-pol Patch (I).....	84
Table 4.9 – H-Pol, Analytical Far Field Symmetries for H-polarised Dual-pol Patch (II).....	84
Table 4.10 – H-Pol, Far Field Phase Patterns for Imaged H-Polarized Dual-pol Probe-fed Antennas Comparison.....	85
Table 4.11 – 2x2 Imaged Sub-array UV XPD Diagram Comparison at Broadside.....	87
Table 4.12 – UV XPD Diagrams for 2x2 Imaged Sub-Array (Ideal Ports).....	88
Table 4.13 – V-Pol, 4x4 Baseline Sub-array Elevation Scanning Comparison (CST MWS FD).....	89
Table 4.14 – 4x4 Imaged Sub-array UV XPD Diagram Comparison at Broadside.....	90
Table 4.15 – 4x4 Imaged Sub-array with Ideal Ports, Elevation Scan Assessment.....	90

Table 4.16 – 4x4 Imaged Sub-array with Ideal Ports, Post-Processed Polarimetric Scan Assessment.....	91
Table 4.17 – 4x4 Imaged Sub-array, 3D Radiation Patterns.....	92
Table 5.1 – Planar Transmission Lines.....	94
Table 5.2 – Feeding Network Architectures [42].....	95
Table 5.3 – Orthogonal vs Parallel Feeding.....	95
Table 5.4 – 4x4 Imaged Sub-array with Ideal Ports Polarimetric Scanning Comparison.....	96
Table 5.5 – 4x4 Imaged Sub-arrays Scanning Comparison for $\phi = 90^\circ$	96
Table 5.6 – Passive Splitters for Microstripline.....	97
Table 5.7 – Preliminary T-Junctions for H-Pol Feeding Network.....	100
Table 5.8 – S-Parameters for Preliminary H-Pol T-Junction, left-hand side (CST MWS FD).....	100
Table 5.9 – S-Parameters for Optimized H-Pol T-Junction, left-hand side (CST MWS FD).....	101
Table 5.10 – H-Port Specification for 4x4 Imaged Sub-Array.....	104
Table 5.11 – V-Port Specification for 4x4 Imaged Sub-Array.....	104
Table 5.12 – 4x4 Baseline Sub-array with Integrated Feed-net, Post-Processed Polarimetric Scan Assessment.....	106
Table 5.13 – 4x4 Baseline Sub-array with Integrated Feed-net, Full-scan Polarimetric Assessment.....	107
Table 5.14 – 4x4 Baseline Sub-array with Integrated Feed-net (Simulated Reflection Coefficients).....	107
Table 5.15 – 4x4 Baseline Sub-array with Integrated Feed-net (Simulated Co-pol Port Isolations).....	108
Table 5.16 – 4x4 Baseline Sub-array with Integrated Feed-net (Simulated Cross-pol Port Isolations).....	108
Table 5.17 – 4x4 Baseline Sub-array with Integrated Feed-net (Active Cross-polar Port Isolations).....	108
Table 5.18 – 4x4 Imaged Sub-array with Integrated Feed-net, Full-scan Polarimetric Assessment.....	109
Table 5.19 – 4x4 Imaged Sub-array with Integrated Feed-net, ZDR_b	109
Table 5.20 – 4x4 Imaged Sub-array with Integrated Feed-net (Simulated Reflection Coefficients).....	110
Table 5.21 – 4x4 Imaged Sub-array with Integrated Feed-net (Simulated Co-pol Port Isolations).....	110
Table 5.22 – 4x4 Imaged Sub-array with Integrated Feed-net (Simulated Cross-pol Port Isolations).....	111
Table 5.23 – 4x4 Imaged Sub-array with Integrated Feed-net (Active Reflection Coefficients).....	112
Table 5.24 – 4x4 Imaged Sub-array with Integrated Feed-net (Active Cross-polar Port Isolations).....	113
Table 5.25 – 4x4 Imaged Sub-array with Integrated Feed-net (S-Parameters Comparison).....	114
Table 6.1 – Manufacturing and Measurement Highlights.....	116
Table 6.2 – 4x4 Baseline Sub-array with Integrated Feed-net (Measured Reflection Coefficients).....	123
Table 6.3 – 4x4 Baseline Sub-array with Integrated Feed-net (Reflection Coefficients, Simulation vs Measurements).....	124
Table 6.4 – 4x4 Baseline Sub-array with Integrated Feed-net (Measured Co-polar Port Isolations).....	124

Table 6.5 – 4x4 Baseline Sub-array with Integrated Feed-net (Measured Cross-polar Port Isolations)	124
Table 6.6 – 4x4 Baseline Sub-array with Integrated Feed-net (Measured Active Cross-polar Port Isolations)	125
Table 6.7 – 4x4 Imaged Sub-array with Integrated Feed-net (Measured Reflection Coefficients)	126
Table 6.8 – 4x4 Imaged Sub-array with Integrated Feed-net (Reflection Coefficients – Simulation vs Measurements)	126
Table 6.9 – 4x4 Imaged Sub-array with Integrated Feed-net (Measured Co-polar Port Isolations)	127
Table 6.10 – 4x4 Imaged Sub-array with Integrated Feed-net (Measured Cross-polar Port Isolations)	127
Table 6.11 – 4x4 Imaged Sub-array with Integrated Feed-net (Measured Active Reflection Coefficients)	128
Table 6.12 – 4x4 Baseline Sub-array with Integrated Feed-net (Measured Active Cross-pol Port Isolations)	129
Table 6.13 – XPD Results by Rows (4x4 Baseline Sub-Array)	131
Table 6.14 – 4x4 Baseline Sub-array with Integrated Feed-net, Full-scan XPD Assessment (Simulations vs. Measurements)	131
Table 6.15 – 4x4 Baseline Sub-array with Integrated Feed-net, Full-scan IXPD Assessment (Simulations vs. Measurements)	131
Table 6.16 – XPD Results by Rows (4x4 Imaged Sub-Array)	132
Table 6.17 – 4x4 Imaged Sub-array with Integrated Feed-net, Full-scan XPD Assessment (Simulations vs. Measurements)	132
Table 6.18 – 4x4 Imaged Sub-array with Integrated Feed-net, Full-scan IXPD Assessment (Simulations vs. Measurements)	132
Table 6.19 – Microscope Validation and Over-etching	135
Table 6.20 – 4x4 Baseline Sub-array with Integrated Feed-net (Reflection Coefficients, Simulations vs. Measurements)	135

Acronyms

Acronym	Description	Topic
CAD	Computer Aided Design	Electromagnetics
EM	Electromagnetics	
FD	Frequency Domain (Solver)	
FDTD	Finite-Difference Time-Domain (Method)	
FEM	Finite-Element Method	
GF	Green's Function	
MoM	Method of Moments	
PEC	Perfect Electric Conductor	
PMC	Perfect Magnetic Conductor	
PPM	Parallel Plate Mode	
SW	Surface Wave	
TM	Transverse Magnetic	
AF	Array Factor	<i>Phased Arrays</i>
AESA	Active Electronically Scanned Array	
AIC	Active Isolation Coefficient	
ARC	Active Reflective Coefficient	
CPAR	Cylindrical Phased Array	
PESA	Passive Electronically Scanned Array	
PAR	Phased Array Radar	
PCB	Planar Circuit Board	
T/R	Transmit/Receive Module	
SLL	Sidelobe Level	<i>Antenna Theory</i>
Dir	Directivity	
BW	Bandwidth	
Cp	Co-polar	
Xp	Cross-polar	
XPD	Cross-polarization Discrimination	
XPI	Cross-polarization Isolation	
IXPD	Integrated Cross-polarization Discrimination	

COTS	Commercial off-the-shelf	<i>Printed Planar Technology</i>
CALKIT	Calibration Kit	
Feed-net	Feeding Network	
GCPW	Grounded Coplanar Waveguide	
HF	High-frequency	
MMIC	Monolithic Microwave Integrated Circuit	
PCB	Printed Circuit Board	
Prepeg	Pre-impregnated	
ATAR	Alternate Transmit Alternate Receive	<i>Polarimetric Weather Radar</i>
ATSR	Alternate Transmit Simultaneous Receive	
ICPR	Integrated Cross-Polarization Ratio	
PRD	Polarimetric Radar Data	
PSM	Polarimetric Scattering Matrix	
STSR	Simultaneous Receive Simultaneous Transmit	
Z _{DRb}	Differential Reflectivity Vias	
AUT	Standard Gain Antenna	<i>Antenna Measurements</i>
ECU	Engine Control Unit	
RAM	Radar Absorbing Material	
SGA	Antenna Under Test	
VNA	Vector Network Analyzer	
AEM	Antenna and EM Modelling Dept. (Fraunhofer FHR)	<i>EU Institutions</i>
DFG	Deutsche Forschungsgemeinschaft (German)	
	German Research Foundation (English)	
FHR	Fraunhofer-Institut für Hochfrequenzphysik und Radartechnik FHR (German)	
	Fraunhofer Institute for High Frequency Physics and Radar Techniques (English)	
MIUB	Meteorological Institute of University of Bonn	
MS3	Microwave Sensing, Signals and Systems Dept. (TU Delft)	
TU Delft	Delft University of Technology	
ARRC	Advanced Radar Research Center	<i>US Administrations and Projects</i>
FAA	Federal Aviation Administration	
MPAR	Multifunction Phased Array Radar	
NOAA	National Oceanic and Atmospheric Administration	

Chapter 1 - Introduction

This chapter describes the M.Sc. Thesis research **motivation**, **objectives** and **approach** of the research project. The current chapter also reviews the state-of-the-art within phased array technology in the **weather radar** framework. For that, the main objectives are stated and the proposed Thesis approach is derived.

1.1 Motivation

Weather radar is a consolidated field within radar engineering. After more than 50 years of its initial studies, Radar technology is currently used in many weather applications, ranging from tracking movements and trends of thunderstorms, estimation of variability and concentration of precipitation up to further tropospheric studies. Being one of the main radar civilian applications, weather radar has both benefited and contributed to the radar community by importing technology initially restricted to military uses (i.e. phased arrays) or expanding the radar sensing capabilities through polarimetry or even, hydrometeor classification. This dual tendency that has driven weather radar development is starting to converge in the so-called *Multifunction Phased Array Radar* (MPAR) program from the USA.

In Europe, there is already a well-developed long-range radar network and in spite of the ever increasing demand for weather sensing and more accurate forecasts, weather services are in charge of regional authorities. Developments such as the MPAR program are unlikely to happen at a civil stage, where national surveillance necessities of state union members are different. Moreover Europe itself does not suffer from extreme weather phenomena requiring early warning systems (i.e. tornadoes, hurricanes, blizzards...). All in all, in Europe concepts such as micro radar networks [1] or low-cost concepts (see Figure 1-1) are of potential interest.

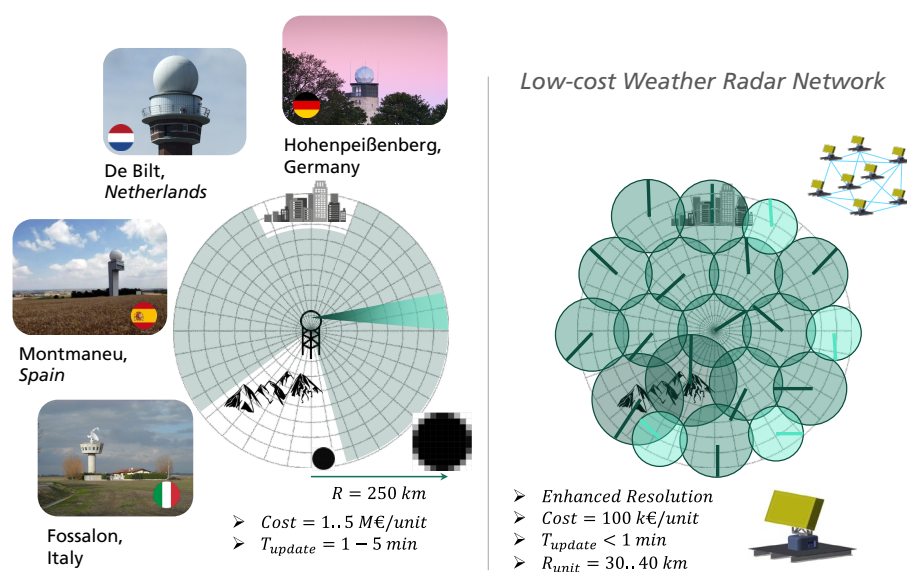


Figure 1-1 – Traditional vs Low-cost Weather Radar Concept

In this context, added to a desire of increased resolution and fast update time, *Fraunhofer FHR* in conjunction with the *Meteorological Institute of University of Bonn* (MIUB) proposed to work on a low-cost weather radar prototype. The initiative resulted in the WRAD pilot project.

This initial project stage has been funded by the *Deutsche Forschungsgemeinschaft* (DFG) and has incorporated the participation of TU Delft and the *Microwave Sensing, Signals and Systems* (MS3) by this initial M.Sc. Thesis.



But before moving on, key questions need to be addressed as the general motivation of work. The main features of the WRAD project will be discussed, focusing mainly on **polarimetry**, **high-resolution** and **low-cost**.

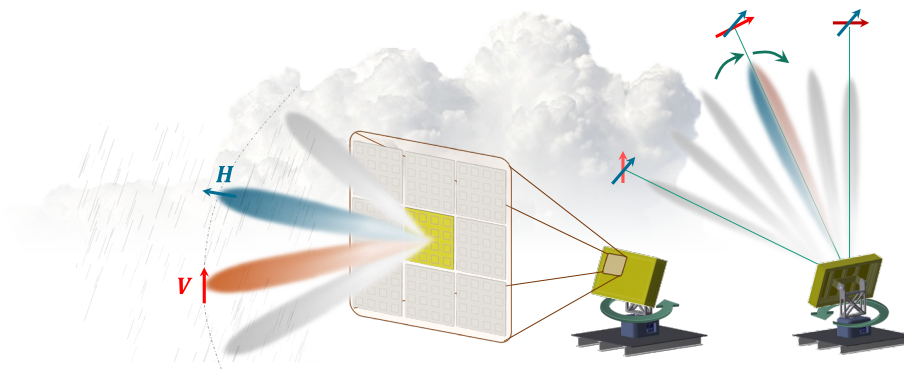


Figure 1-2 – Low-cost WRAD Art Concept (Electronic Scan in Elevation)

1.1.1 Why Polarimetric Weather Radar?

Using traditional weather radar two main parameters can be retrieved: the amount of energy scattered from a target to the radar (*intensity and amount of precipitations*) and the relative radial target velocity to the radar (*air motion and cloud circulation*). Although *radar reflectivity* and *Doppler* sensing measurements are the pillars of weather quantification and forecasting, **polarimetry** brings an incremental improvement in terms of accuracy, resolution, estimation and target classification [2].

Endowing a weather radar with polarimetric features requires the ability to transmit in two orthogonal polarizations, for instance, *linear vertical* and *linear horizontal* as shown in Figure 1-2. For weather sensing capabilities, **polarimetric purity** is a constraint and as it will be seen in this thesis, such requirement will drive the antenna sub-system design. The capacity to transmit and receive ideally in one single polarization is in fact limited by the *antenna radiation mechanism* and the *isolation* between the orthogonal channels as well as the receiver channel isolation.

For this issue, two main figures of merit are defined, the *cross-polarization discrimination* (*XPD*) and the *cross-polarization isolation* (*XPI*). Their definition follows:

- *XPD*: ratio between the co-polar component over the orthogonal cross-polar component at a given direction, over a sector or beamwidth angle.
- *XPI*: ratio of power coupled between two orthogonally polarized ports of a dual-pol antenna.

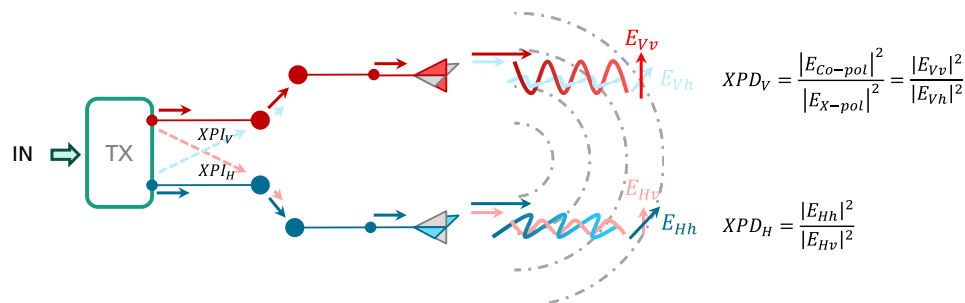


Figure 1-3 – XPD and XPI in Transmission

1.1.2 Why AESA and short-range?

In order to obtain **high-resolution** weather measurements, a short-range weather radar is preferred. The desire of increased resolution is dual, first on a significant time of update reduction and second on improving the volumetric resolution by decreasing the range. To understand why an *Active Electronically Scanned Array* (AESA) can provide such features, traditional weather radars must be reviewed, quantizing somehow their performance while setting up a term of comparison.

Traditional weather radar consists of a high gain antenna steered mechanically in elevation and azimuth. Based on the polarimetric and gain requirements, a dual-pol horn antenna is used to feed a reflector dish, yielding a so-called pencil beam pattern ($G \approx 30.45 \text{ dB}$). Especially for L and S-band, the resulting structure is substantially large and heavy. Steering it mechanically with high accuracy is thus expensive and requires the usage of a settling delay (to limit the system vibrations). Moreover, to achieve long-range the structure needs to be sited on an elevated position, increasing even more the installation costs. All in all, in spite of the disadvantages depicted in Figure 1-4, this legacy concept is time-tested and is widely accepted within the scientific community [3].

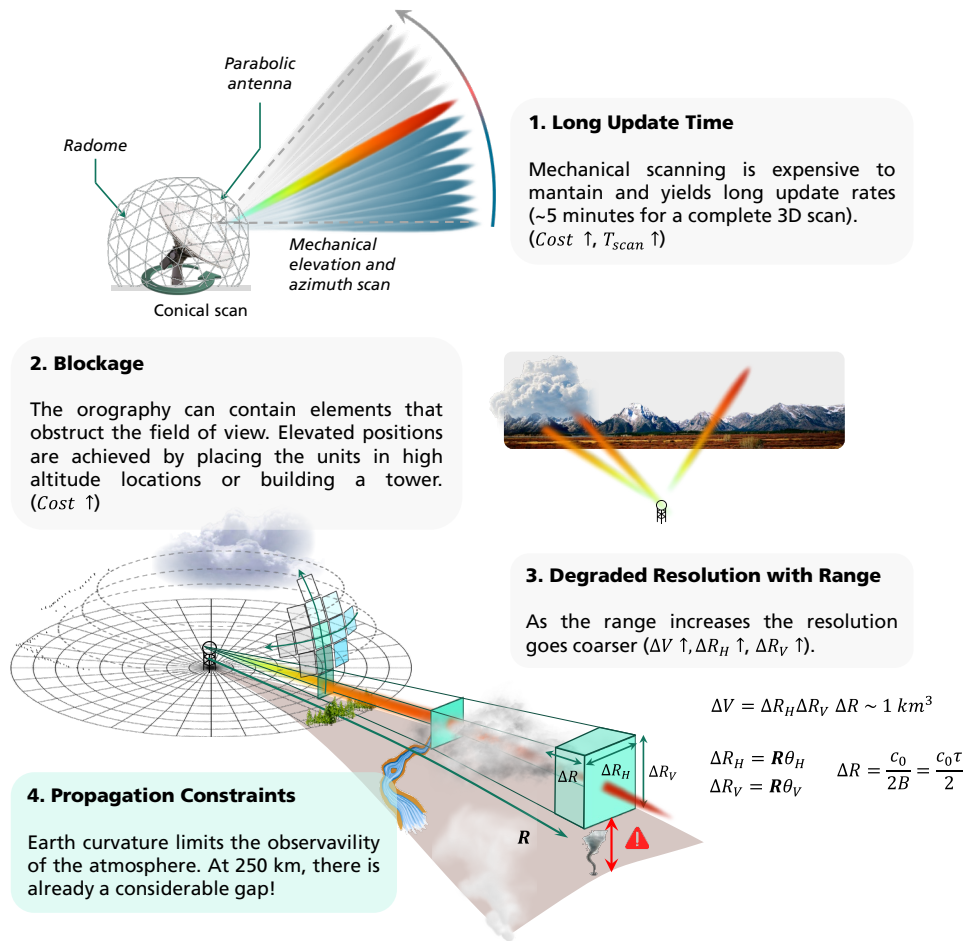


Figure 1-4 – Disadvantages of Traditional Weather Radars

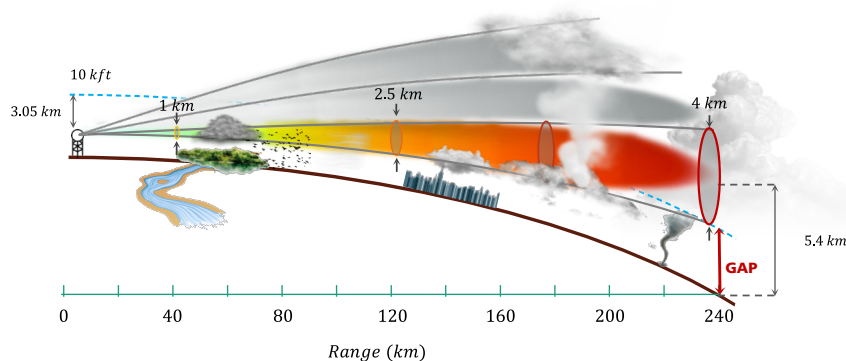
In this context, the introduction of AESA technology within Weather Radar represents a drastic reduction of the update time thanks to the *electronic beam agility*. This would allow to increase the time resolution, while being able to allocate more resources on a specific target or including other functionalities within the same radar, *Multifunction Phased Array Radar* (MPAR). While this is the ultimate research goal of the state-of-the-art weather AESA radars [4, 5], in our project, the AESA capability is restricted only to elevation. In this way the proposed WRAD [6] would still benefit from a potential time resolution improvement ($T_{update} \sim 1 \text{ min}$), while still benefiting from the mechanical installation and maintenance cost reduction.

1.1.3 Why X-Band Radar?

As seen in Figure 1-4, reducing the *range* ($R_{max} \downarrow$) would allow increasing the *volumetric resolution* ($\Delta V \downarrow$). To improve the overall resolution even more, the concept of *map composition* could be exploited [7]. To implement a dense *weather radar network* lots of units would be required, which ideally should be **low-cost**, unmanned and remotely controlled. A suitable frequency allocation for this use case could be X-band, which would allow high system integration minimizing the weight and cost.

On the contrary, X-band radars suffer from high atmospheric attenuation, limiting their effective range. Beyond 30-40 km, complicate mathematical models aided by several assumptions are required to compensate for the attenuation [8]. But still, within that range, meteors such as rain would fall into the Mie Scattering region [2]. In L, C and S Bands for instance, rain would be in the Fraunhofer region, where it is easier to take into account the atmospheric attenuation, allowing to achieve long-range weather sensing.

The range reduction brought by the X-band sensing constraints would not affect the proposed short-range AESA radar. In fact short-range would also allow to minimize the effect of Earth curvature and ensure coverage of the lower part of the troposphere [6]. In long-range radars, earth curvature generates a gap at distant ranges in spite of the electromagnetic beam bending for standard atmospheric propagation as shown in Figure 1-4 and Figure 1-5.



Based on original drawing from "WakeNet-Europe 2013",
by Mr. McLaughlin (UMASS) and Mr. Drake (Raytheon)

Figure 1-5 – Traditional Weather Radar and the associated gap to Earth Curvature [9]

In addition to the rain sensing interest, based on the MIUB research activities, X-band would be also suitable to perform vertical profiling measurements. By sensing the refraction index of the troposphere, studies could investigate and reconstruct the tropospheric microphysics. For this reason, the AESA WRAD shall be able to steer the beam pointing from the horizon up to the zenith, as depicted in Figure 1-6.

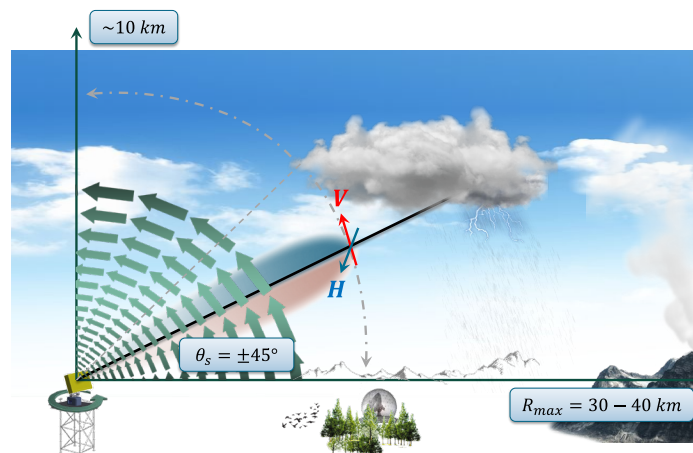


Figure 1-6 – AESA Scanning Art Concept

1.2 State-of-the-art and Novelty

In order to understand the current state-of-the-art within Weather Radar a clear link to traditional polarimetric systems and AESA technology developments has to be established. For this reason, the research advancements of three different institutions will be reviewed to provide context for this research framework. Starting from TU Delft, traditional polarimetric weather radar will be discussed focusing in two operating systems, PARSAX and IDRA. Thereafter, advances in the USA through AESA technology will be shown, allowing the integration of weather radar with other radar system functionalities.

Last but not least, Fraunhofer FHR research in MMIC T/R module technology will set the engineering landscape upon which the AESA WRAD project starts. Based on the current European needs for weather radar, the main requirements of the system are discussed.

TU Delft, polarimetric and X-band Radars

Delft University of Technology is currently one of the main European institutions devoted to Weather sensing research through radar technology. Through the MS3 and the Geoscience & Remote Sensing departments, TU Delft focuses on *Atmospheric Remote Sensing* (ARS) and high resolution precipitation estimation through a wide variety of polarimetric and Doppler systems (see some examples in Table 1.1).



a) PARSAX (S-Band)



b) TARA (S-Band)



c) IDRA (X-Band)

Table 1.1 – Notable Weather Radars Prototypes from TU Delft

The research at TU Delft has been backed up by traditional weather radar systems (dual-pol reflector antenna), focusing on the development of high resolution weather radar [10], signal processing and information extraction algorithms. Research activities such as the development of dual-orthogonal waveforms [11] or a multi-sensor information system for situational awareness [12] are examples of the current state-of-the-art advancements in the field.

The effective usage of traditional weather radars from TU Delft shows the apparent non-necessity for AESA. However, the involved high-costs in installation and maintenance added to the low update time of dual-pol reflector antenna motivate the introduction of low-cost AESA weather radars in the system (see Figure 1-2). AESA systems would provide polarimetric performance while including beam agility capabilities, allowing to increase the spatial and time resolution of the systems.

USA, advances in weather radar, NEXRAD and MPAR programs

To support of the previous considerations, in the United States there are already well documented high resolution dual-polarized and Doppler AESA radars used for weather applications [9, 13]. As a result of the common need of radar technology from both the *National Oceanic and Atmospheric Administration* (NOAA) and the *Federal Aviation Administration* (FAA), new multifunctional radars are being investigated using AESA technology. These radars are to be integrated in the MPAR and SENSR programs [4]. The main goals of the MPAR program are [14]:

- *Affordability*
 - Need to decrease production costs to update existing networks.
- *Multifunctionality*
 - Surveillance and weather functionalities.
- *Dual-polarization* [15] [16]
 - Weather requirement, yet to be seen if it can benefit aircraft characterization.
 - Simultaneous or alternating modes available.

While MPAR, dual polarization and AESA features make technology still highly expensive, there have been major breakthroughs in the industry in the past few years (2010 onwards) [17]. The decrease of manufacturing costs of AESA [18] makes it now affordable for civil purposes such as weather radars [6]. In the long run and even with a frequency shift, state-of-the-art telecommunication fields such as 5G will eventually benefit from the current advances in radar engineering at a global scale [17, 19].

In the meantime, as a successful output of the on-going research, the current North American weather radar network is being upgraded with cost-effective dual-polarization AESA technology.

The novel planar array topologies are offering optimal cross-polarization performance [20] [21] [22] for narrowband applications S-Band (2.7 – 2.9 GHz, US meteorological band), achieving values for *XPI* and *XPD* in excess of 40 dB.



Figure 1-8 – CASA Phase-Tilt Weather Radar [24]

Of high interest for this project is the *phase-tilt weather radar* proposed and reviewed in [9, 25], where a similar scheme to our AESA weather radar is proposed for 1D scanning in azimuth. This prototype also aims at providing a low-cost and short-range solution at X-band, achieving a polarimetric performance of at least 20 dB in *XPD* over the $\pm 45^\circ$ azimuth scan range.

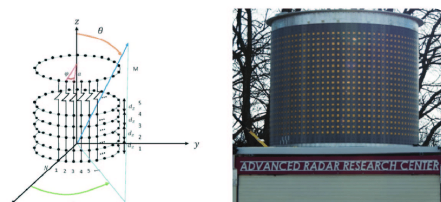


Figure 1-7 – Cylindric Polarimetric Phased Array Radar [23]

Fraunhofer FHR, advances in T/R modules, a game-changing technology

In contrast with the North American precedents, in Europe there is no such a high demand of high-tech short-range weather radars. Although national defense programs are starting to converge with initiatives such as the *European Defense Agency and European Defense Industrial Development Program*, allied European nations still consider national security as a private endeavor. These two facts in terms of European weather and surveillance radar needs have jeopardized the appearance of American programs such as NEXRAD, MPAR or SENSr.

In this context, Fraunhofer FHR takes initiative to foster European weather radar progression by providing a low-cost dual-pol AESA radar system using state-of-the-art AESA advancements. Building an initial micro radar prototype could set the direction towards an upgraded European weather radar network. The demonstrator shall use a new generation of Transmitter-Receiver Module (TRM) providing affordable AESA capabilities compared to traditional phase-shifters and attenuators on-chip (usually around 500 to 1000 € per antenna element). Based on Anokiwave's state-of-the-art COTS MMIC TR modules and Fraunhofer FHR solid expertise on the topic [26], investigation on low-cost weather micro-radar is undergoing [6, 7]. The fact that no airspace surveillance functions are required simplifies the AESA design and the main consequences are:

- *No need of wideband operation*
 - Only 10 MHz are needed for a successful weather operation.
 - Planar structure decrease of complexity (no need for a multilayer stacked patches [27])
- *No need of 3D scanning*
 - Volumetric AESA capability is not required and the azimuth scan can be performed mechanical.

Fraunhofer FHR WRAD AESA, a novel low-cost approach

Based on the depicted research framework, the novelty of this project relies on the low-cost approach. Such novelty starts in this Thesis through the initial development of a suitable polarimetric sub-array for X-band weather radar applications. The expected cross-pol performance reduction over traditional weather radar is the implementation challenge so to achieve fast volumetric scanning within a low-cost constraint.

1.3 Objectives

The objective of this M.Sc. Thesis is to design and characterize a **sub-array tile** suitable for weather radar applications using AESA technology. Due to time constraints the Thesis will only deal with the initial design iteration. Further developments will aim at including new design features.

Meanwhile the final antenna sub-system (integrated with Front-end) will be finally conceived and ready to be implemented using a modular sub-array approach (see Figure 1-9).

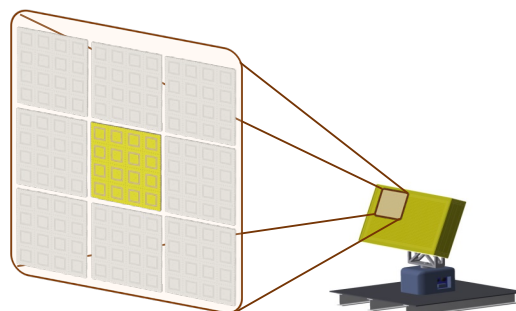


Figure 1-9 – Sub-array Design Approach

For this reason, the list of requirements concerning the work of this M.Sc. Thesis are summarized in Table 1.2. In there, not all the desired weather radar AESA features of WRAD project are included. The exclusion of other relevant requirements was done to relax the Thesis workload and also to retain have some system design freedom to conceive other system concepts. Major guidelines for phased array Weather Radar systems can be found in [16] and will be properly related to this MSc Thesis in Chapter 2.

<i>ID</i>	<i>Requirement Description</i>
WRAD_SA_1	The AESA shall be implemented with planar antenna technology.
WRAD_SA_2	The AESA shall be modular . Since each T/R module can feed up to 4 ports, 4x4 subarrays configuration shall be exploited.
WRAD_SA_3	The AESA shall be low-cost .
WRAD_SA_4	The AESA shall be dual-polarized (linear horizontal and vertical), with similar radiation performance for each polarization.
WRAD_SA_5	The AESA shall operate at X-Band ($f_0 = 9.4 \text{ GHz}$) with a bandwidth of at least 10 MHz (narrowband)
WRAD_SA_6	The AESA shall scan in elevation only, providing a scan range of $\pm 45^\circ$.
WRAD_SA_7	The AESA shall have an element spacing of 15 mm ($\sim \lambda/2$).
WRAD_SA_8	The AESA shall provide 30 dB in excess for <i>XPI</i> and <i>XPD</i> throughout the scan range.
WRAD_SA_9	The AESA shall have integrated feeding networks within the planar structure.
WRAD_SA_10	The AESA shall be interfaced through SMP connectors.

Table 1.2 – WRAD Sub-Array Requirements

Key requirements such as *gain*, *Sidelobe Level* (SLL) or even panel size will be subject of a second iteration and are therefore outside the scope of this work. Targeting these requirements at a sub-array level is not possible, based on the small size of the discussed sub-arrays.

In this work the majority of the focus will be focused on polarimetric optimization, designing of a prototype and instrumental validation of the manufactured sample. Using this approach, the research goals expected from this M.Sc. Thesis will be limited to:

<i>ID</i>	<i>Goal Description</i>
MSC_RG_1	To analyze and provide physical insight on the cross-polarization generation for the chosen planar structure and its extended versions.
MSC_RG_2	To provide cross-polarization suppression techniques.
MSC_RG_3	To conceive, design, implement and validate the proposed prototype.

Table 1.3 – M.Sc. Thesis Research Goals

1.4 Proposed Approach

To fulfill the specified sub-system requirements (Table 1.2) and the research goals (Table 1.3) this work is mainly divided in three conceptual sections: **analysis**, **synthesis** and **validation**. Along these key pillars of the project, the *antenna development process* is reviewed, integrating all of these ideas within the following table:

Academic Approach	Antenna Development	Associated Tasks	Timeline
Analysis	System Conception	Literature Review	Nov 2018
		Review Antenna Models	
Synthesis	Antenna Design	Feeding Topology Choice	Jan – April 2019
		Unit Cell Choice	
		Multi-layer Design	
		Cross-polarization Assessment	
		Cross-polarization Suppression	
	Implementation / Manufacturing	Feed Network Design and Integration	<i>Mid-term, (Delft, NL)</i>
		Connector Selection and Optimization	
		Validation with CST MWS and HFSS	
		Manufacturer Standard Compliance	
		TRL Cal Kit	
Validation	Measurements	Tolerance Analysis	May –June 2019
		Request and Bidding Process	
		Antenna Connectorization	<i>IRS 2019 (Ulm, DE)</i>
		Visual / Microscope Inspection	
		S-Parameter Characterization	
Anechoic Chamber Measurements	July - Aug 2019		
Analytical Beamforming			
		Cross-polarization Validation	

Table 1.4 – Sub-Array Design Roadmap

In this project the next phase would involve a second iteration (synthesis + validation) followed by an *integration* and *system calibration* stage. However, due to the 9 months time limit of the Thesis, the project was adapted to the expected academic outputs of the M.Sc. program from TU Delft.

To provide scientific insight, this report will provide an extensive discussion on cross-polarization generation, thus, setting the foundations required to understand how to achieve high cross-polarization suppression and isolation at **low-cost**. In this context, starting from the cavity model and reviewing the fundamentals of patch antennas, multiple cross-polarization sources are identified, targeted and suppressed, providing an in-depth analysis that can benefit any polarimetric design using planar technology.

1.5 Outline of the Thesis

Based on the initial M.Sc. Thesis introduction and its framework within TU Delft and Fraunhofer FHR, the Thesis structure is organized as follows:

Chapter 2 introduces the AESA technology applied to weather radar, delving into the current proposals and expected challenges from the antenna sub-system point of view. Based on an initial literature review, the AESA sub-system is conceived and the major Thesis guidelines are derived, among them, the required polarimetric requirements for weather radar.

Chapter 3 clarifies the radiation mechanisms of patch antennas. Reviewing the *cavity model*, the radiated cross-polarization component can be targeted while extending the simplified model to a real design. Further design choices such as *feeding techniques* or *dual-polarization* upgrades are supported by theoretical reasoning combined with initial simulations at a unitary cell level.

Chapter 4 targets the AESA concept design with *high cross-polarization suppression* and *isolation* by using a sub-array concept. An initial discussion on the most suitable *Computer Electromagnetics* (CEM) solver follows a detailed design approach concerning substrate choice and the dual-pol probe-fed patch element definition. A *feed rotation* technique supported by exhaustive simulation comparisons provides the desired polarimetric performance throughout the desired scan range.

Chapter 5 integrates a *feeding network*, starting from an ideal approach extending it to advanced designs based on microstripline technology. The polarimetric degradation introduced by the feeding network is evaluated and suppressed by optimization of the network and minimization of meandering and line discontinuities. A cross-validation using CST MWS and ANSYS HFSS validates the design at a simulation level.

Chapter 6 validates the manufactured prototype through *S-Parameters* and *anechoic chamber measurements*. Arising frequency shifts are justified by microscopic inspections, where manufacturing tolerances in patch over-etching and substrate permittivity are observed. Post-design simulations taking into account the manufacturing concerns provide the required insight for future design development.

Chapter 7 summarizes the antenna development cycle. Based on the polarimetric design validation, the guidelines for a second iteration are set. Manufacturing concerns and future goals are discussed, providing the future steps of the AESA panel design.

Aside from the proposed main Chapters, a total of six appendices are included. Appendix A provides an additional derivation for phased arrays, while Appendix B provides major guidelines to designing a dual-pol fed-probe patch antenna. Appendix C, D, E and F contain the main results of the designed sub-arrays at a simulation level (CST MWS) and after the measurement runs.

Chapter 2 - AESA for Weather Radar

This chapter introduces the reader to **AESA technology** applied to **weather radar**, delving into the current proposals and expected challenges from the antenna sub-system point of view. Based on an initial literature review, the AESA sub-system is conceived and major Thesis guidelines are derived, among them, the required polarimetric requirements for weather radar.

2.1 Introduction to Phased Array Technology

Phased arrays are reconfigurable antennas that can change their radiation properties, mainly by changing the phase (φ_i) and amplitude (a_i) that feed the array elements. By exploiting the constructive and destructive combination of the radiated far-fields, phased arrays can be used to synthesize high gain, static or dynamic beam steering or pattern beamforming, among others.

In this Thesis phased array technology will be used to actively steer the beam while ensuring that specific requirements in terms of **bandwidth**, **cross-polarization discrimination** and **cross-polarization isolation** are achieved within the entire scan range ($\theta_s = \pm 45^\circ$). The beam steering capacity leads to the introduction of the so-called *Active Electronically Scanned Arrays* (AESA) in which elements are connected to active *Transmit/Receive Modules* (T/R). These kind of phased arrays differ from *Passive Electronically Scanned Arrays* (PESA) as they do not use individual amplifiers for every element. The differentiation of the terms *Active* and *Passive*, comes from the fact that T/R modules are active elements and they operate as independent transmitters and receivers units that are controlled by a central unit (i.e. microprocessor, chipset). Conceptualization of PESA and AESA topologies is shown in Figure 2-1.

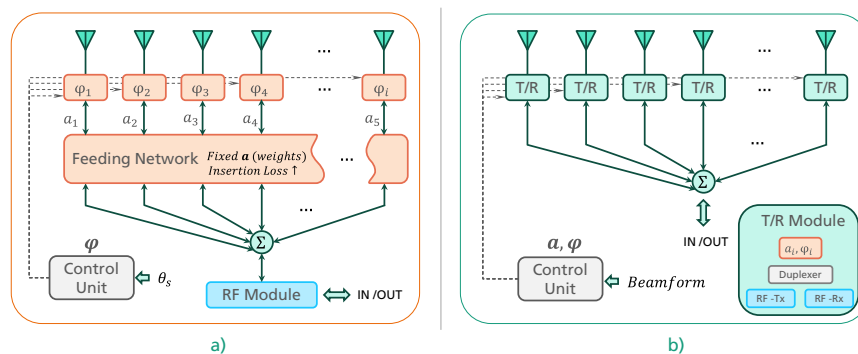


Figure 2-1 – Generalised Electronically Steering Array Topologies. (a) PESA and (b) AESA with T/R Module concept.

The decrease in cost of T/R modules makes it possible to bring AESA technology for civilian applications [17, 19], such as in our case, weather radar [6]. The improved resource management and beam agility that PESA and AESA provide comes at a cost though, namely, a generalized degradation of the radiation performance. From the impedance bandwidth reduction ($BW \downarrow$) up to the polarimetric degradation ($XPD \downarrow$), this project will focus on understanding the relevant electromagnetic phenomena to achieve the required specifications for the proposed weather radar.

2.1.1 Linear Array Antenna

A visual approach to introduce phased arrays commonly consists on drawing a linear antenna array and defining the phase differences to analyze a given wavefront (see Figure 2-2). Alternatively to this explanation, an additional analytical derivation is provided in Appendix A.

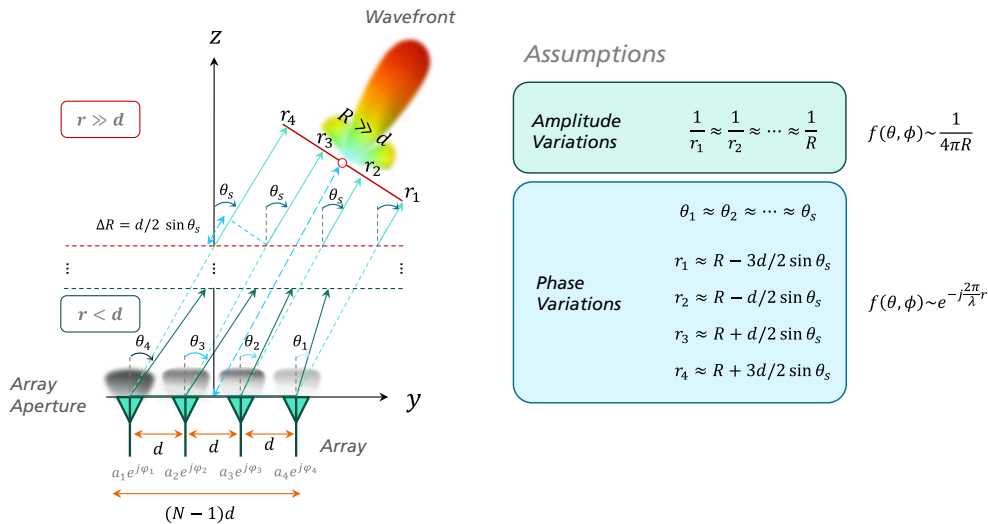


Figure 2-2 – Linear Array Antenna, Projection on the YZ Plane with Physical Assumptions

In the far-field region and assuming that $R \gg (N - 1)d$, it can be shown that the resulting field combination is the product of the unitary element field ($\vec{E}_u(r, \theta, \phi)$) and the so-called Array Factor ($AF(\theta, \phi)$). For a $N = 4$ linear array as displayed in Figure 2-2, the total radiated field can be found as for Eq. 2.1, where amplitudes and phase shifts of each element are also taken into account.

$$\vec{E}_{array}(r, \theta, \phi) = a_1 \vec{E}_u(r, \theta, \phi) e^{j\varphi_1} e^{-jk_y d_1} + \dots + a_4 \vec{E}_u(r, \theta, \phi) e^{j\varphi_4} e^{-jk_y d_4} \quad \begin{matrix} k_x = k \sin \theta \cos \phi \\ k_y = k \sin \theta \sin \phi \\ k_z = k \cos \theta \end{matrix} \quad \text{Eq. 2.1}$$

Rearranging the terms, the $\vec{E}_u(r, \theta, \phi)$ can be factorized in Eq. 2.2.

$$\vec{E}_{array}(r, \theta, \phi) = \vec{E}_u(r, \theta, \phi) \times AF(\theta, \phi) \quad \text{Eq. 2.2}$$

$$AF(\theta, \phi) = \sum_{i=1}^N a_i e^{-j(k_y d_i - \varphi_i)} = \sum_{i=1}^N a_i e^{-j(k_y (\frac{N+1}{2} - i) d - \varphi_i)} \quad \text{Eq. 2.3}$$

Assuming a uniform distribution ($a_i = 1$) and a progressive phase-shift ($\varphi_i = (\frac{N+1}{2} - i) \beta_y$) an analytical expression for the $AF(\psi)$ can be found.

$$AF(\psi) = \frac{\sin(\frac{N}{2} \psi)}{\sin(\frac{1}{2} \psi)} \quad \text{Eq. 2.4}$$

Where

$$\psi = d k_y + \beta_y = kd \sin \theta \sin \phi + \beta_y \tag{Eq. 2.5}$$

While $AF(\psi)$ is a 2π periodic function, $AF(\theta, \phi)$ is bounded by the so-called *visual range* (VR). The fact that $\theta \in [0, \pi]$ and $\phi \in [0, 2\pi]$ are finite variables will limit $AF(\psi)$. To understand this effect, a linear array of idealized patch antennas can be taken into account. In the example of Figure 2-3 a four element linear array where β_y is left constant. Two different element spacings are compared, leading to different visual ranges, beamwidths, and thus different directivities ($Dir_1 < Dir_2$).

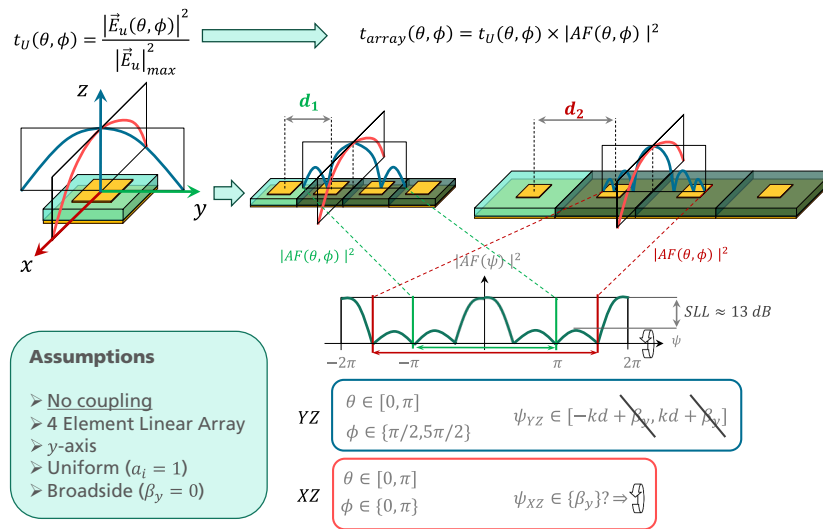


Figure 2-3 – Four-linear Array with Broadside Scanning (element spacing comparison)

Following this formulation, pattern reconfiguration (beamforming) can be achieved by tuning the weights (a_i) and the progressive phase-shift (β). While a_i provide sidelobe control capabilities, β allows *beam steering*.

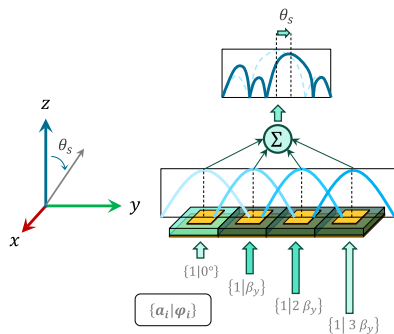


Figure 2-4 – Four-linear Array Scanning

For instance, Figure 2-4 shows a 1D scanning situation. The desired scanning angle (θ_s) is related to the β_y as in Eq. 2.6, where a beam is to be steered in the ZY plane ($\phi = 90^\circ$).

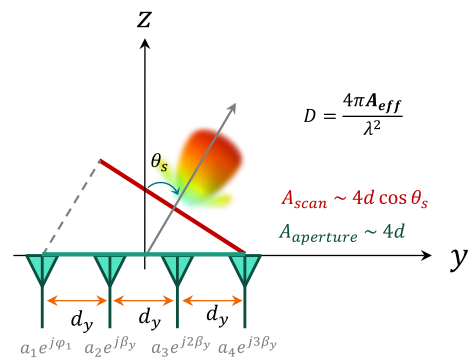
Note: In this Thesis due to the small size of the proposed sub-array, no sidelobe optimization will be considered. On the other hand, only 1D scanning in elevation is required, which simplifies the phased array design.

The analytical expression relating θ_s and β_y is derived in Eq. 2.6.

$$AF_{max} @ \psi = 0 \Rightarrow 0 = kd_y \sin \theta_{max} \sin \phi + \beta_y \xrightarrow{+ZY, \phi=90^\circ} \beta_y = -kd_y \sin \theta_{max} \tag{Eq. 2.6}$$

Steering the beam has an impact on the directivity, which will decrease as the variation of the scanning angle translated into a reduction of the scanning array aperture.

The scan loss can be seen as the result of area reduction due to the aperture projection. For this reason, for the exemplified array, directivity will decay with a factor of $\cos \theta_s$, but in reality, if taking into account the unit element pattern, a $\cos^\alpha \theta_s$ is a better approximation (where α is a scalar factor).



However, both d and β can cause undesired periodic lobes to fall onto the visual range. Appearance of grating lobes will dramatically decrease the power density in the intended direction as shown in Figure 2-5.

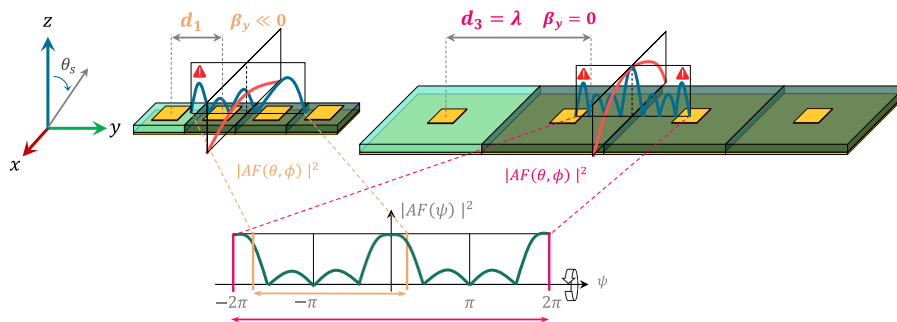


Figure 2-5 – Grating Lobe Example

For an AESA design with a specific θ_{max} , grating lobes can be avoided by finding the maximum element spacing (d_{max}) or using alternate lattice distributions for planar arrays. Since the distribution is required to be linear, the d_{max} condition was derived. Considering a grating lobe the first periodic lobe ($\psi = \pm 2\pi$) in the $AF(\psi)$, Eq. 2.7 was found using Eq. 2.5 and Eq. 2.6

$$d_{y,max}^{scan} = \frac{\pm 2\pi}{k \sin \theta_{GR} \sin \phi_{GR} - k \sin \theta_{max}} \tag{Eq. 2.7}$$

Note: the grating lobe condition will be found when a grating lobe starts appearing at $\theta_{GR} = 90^\circ$. If scanning in the right hemisphere of the ZY plane the associated grating lobe conditions $\psi_{GR} = 2\pi$ and $\phi_{GR} = 270^\circ$.

Assuming a scan in the right hemisphere within the ZY plane, Eq. 2.8 follows

$$d_{y,max}^{scan} = \frac{2\pi}{k + k \sin \theta_{max}} = \frac{\lambda}{1 + \sin \theta_{max}} \tag{Eq. 2.8}$$

For $\theta_s = 45^\circ$, the maximum spacing would be $\lambda/1.71$, while for a $\theta_s = 90^\circ$, $d_{y,max}^{scan} = \lambda/2$. However, to gain resilience against potential appearing of grating lobes given the small size of the sub-array here investigated (namely, increased phase shifting requirements to achieve the maximum nominal scanning angle of 45°) a conservative element spacing of $\lambda/2$ has been selected.

In that sense, to increase the gain, adjacent rows of elements allow concentrating the radiation in the scanned dimension (see Figure 2-6).

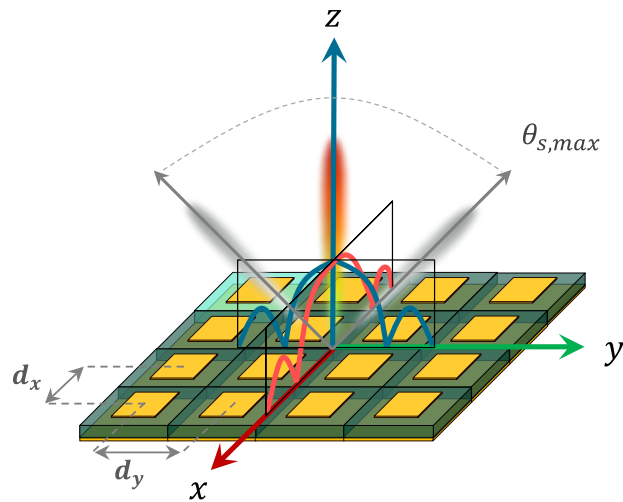


Figure 2-6 – Planar Liner Array scanning at Broadside

2.1.2 Phased Array Design Methodologies

Though the previous explanation does bring physical insight, it assumes that there is no coupling among the array elements. The assumption comes from the fact that the radiated fields of the unitary element will be the same from element to element, hence, allowing to use Eq. 2.2 and the AF idealization. In an antenna design stage this assumption cannot be used, since coupling will degrade the radiation pattern of the array and will have a major impact on the elements matching at the feeding port (input impedance).

Modern design methodologies to conceive AESA systems are supported by commercial CEM software. Although initial analytical design is computationally efficient [28, 29], full-wave solvers are ultimately used to validate the design [30] due to the versatility and accuracy they provide. However, large EM structures require relevant computational resources and iterative design based on parameter tuning is not always advisable. Despite nowadays available processing power (further enhanced by use of GPUs for acceleration of CEM computation) there are still traditional design approaches to be considered, namely: **Unit Cell design** and **Sub-Array design**.

For large phased arrays, an initial hybrid approach based on periodic boundary conditions (*Floquet analysis*) allows designing of the unitary element using a full-wave solver in a sub-optimal way. This approach, known as **Unit Cell design** (Figure 2-7), assumes that elements in the central region of an electrically large array have similar performance (similar input impedance Z_{in}) as that of an element in an infinite array [31]. While the performance of the unitary cell can be optimized for the desired scan range, a second design iteration needs to consider the finite size of the array to validate the array. For structures greater than 8×8 elements, this unitary cell optimization will yield an accurate enough estimate.

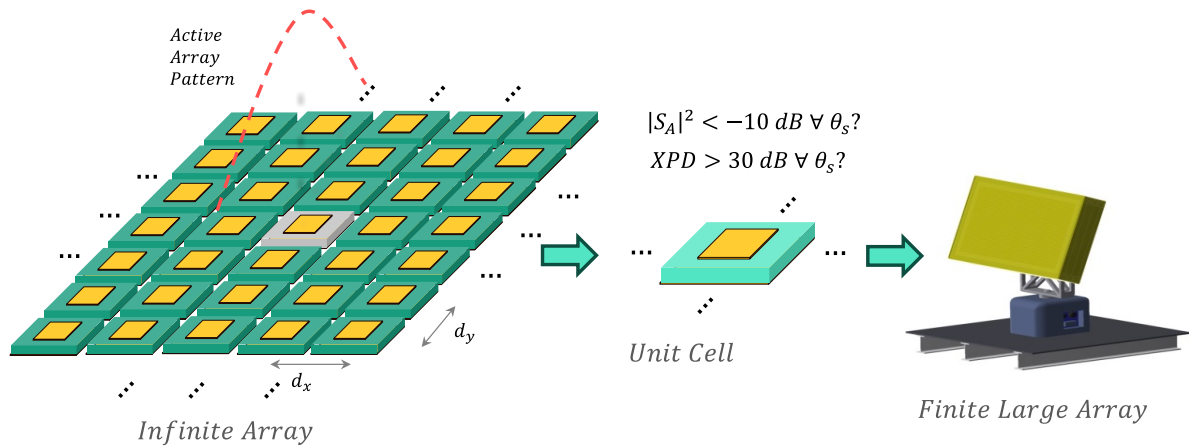


Figure 2-7 – Unit Cell Design

Alternatively, in practice, based on cost concerns mainly derived from active front-ends and its associated circuitry, large arrays are normally assembled based on integrated sub-arrays [32, 33]. For 1D scanners elements integrated within a sub-array might share the same T/R module, yielding a significant cost reduction [34]. From an EM point of view, **Sub-Array design** (see Figure 2-7) can also be used when the array is asymmetric and no periodic conditions apply at a unit cell level [35]. Consequently, in a second design iteration, the sub-array can be periodically replicated to develop the final desired structure as shown in Figure 2-8.

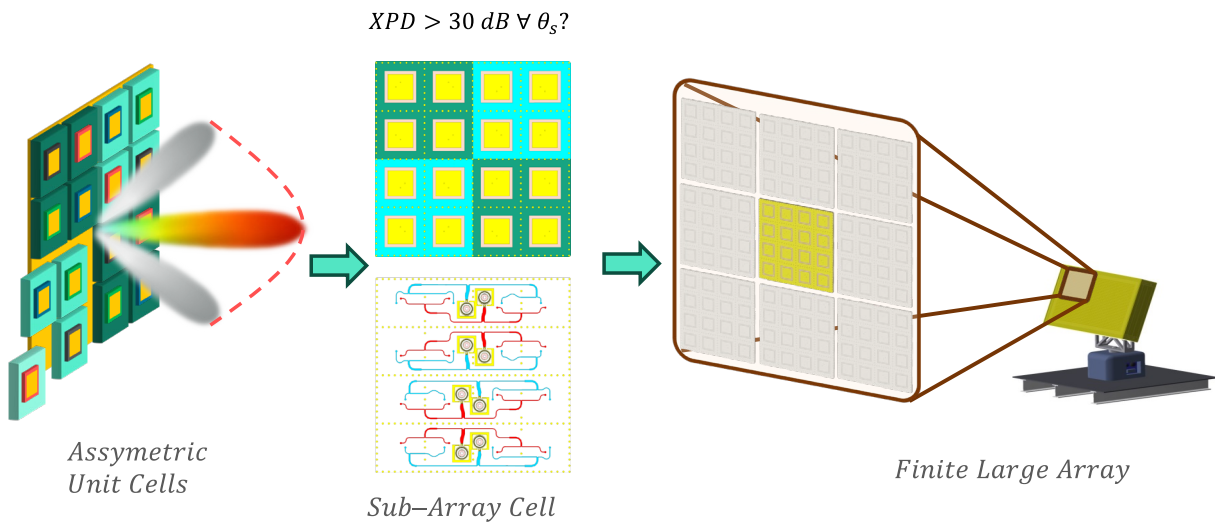


Figure 2-8 – Sub-Array Design

From the research point of view of this work, the sub-array methodology is preferred. Based on the *XPD* requirement, a feed rotation technique is applied to suppress major cross-polarization components [35]. This technique exploits the asymmetry of the rotated feeds while using out-of-phase excitation to suppress major cross-polarization components. The introduction of such asymmetry added to the fact that the proposed AESA controller can control up to four branches supports the suitability of this sub-array design choice.

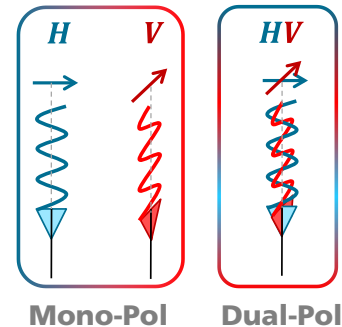
2.2 Introduction to Polarimetric Weather Radar

In order to understand the key requirements that will drive the polarimetric AESA design, a brief review on polarimetric weather radar is preferred to justify the need of cross-polarization purity. Additionally, the main values of interest of *atmospheric remote sensing* will be also related to those figures of merit concerning the polarimetric antenna array performance.

An initial step to review polarimetric weather radar is to introduce the polarimetric radar equation with an ideal dual-pol antenna (Eq. 2.6). Note that the same equation applies to fully polarimetric systems such as the ones in Table 1.1 which use two orthogonally polarized antennas.

$$\mathbf{V}_{Rx} = \mathbf{s}_{Target} \mathbf{V}_{Tx}$$

Eq. 2.9



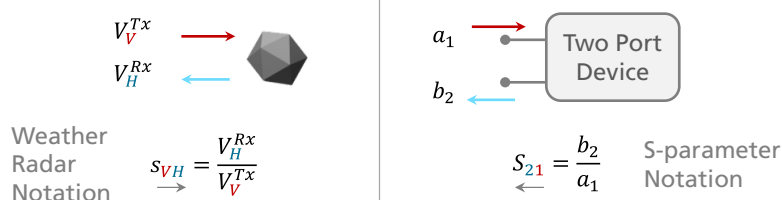
Where E_{Rx} , E_{Tx} are the *received* and *transmitted complex voltages* in the input ports of dual-pol antenna and \mathbf{s}_{Target} is target *polarization scattering matrix* (PSM)¹. Propagation effects and unit conversion factors have been ignored to simplify conceptually the expression. In case a linearly polarized basis for horizontal and vertical decomposition (H, V) is used, Eq. 2.9 can be rewritten as

$$\begin{pmatrix} V_V^{Rx} \\ V_H^{Rx} \end{pmatrix} = \begin{pmatrix} s_{VV}^T & s_{HV}^T \\ s_{VH}^T & s_{HH}^T \end{pmatrix} \begin{pmatrix} V_V^{Tx} \\ V_H^{Tx} \end{pmatrix}$$

Eq. 2.10

To determine the PSM matrix a total of four measurements are required as depicted in Figure 2-9 referring to *Alternate-Transmit Alternate-Receive* (ATAR) mode. Other transceiver modes such as *Alternate-Transmit Simultaneous-Receive* (ATSR) or *Simultaneous-Transmit Simultaneous-Receive* (STSR) require two and one measurement steps.

¹ Note that non-capital 's' it is used in the PSM definition. This is done to differentiate the notation from the usual scattering matrix notation (such as the S-Parameters).



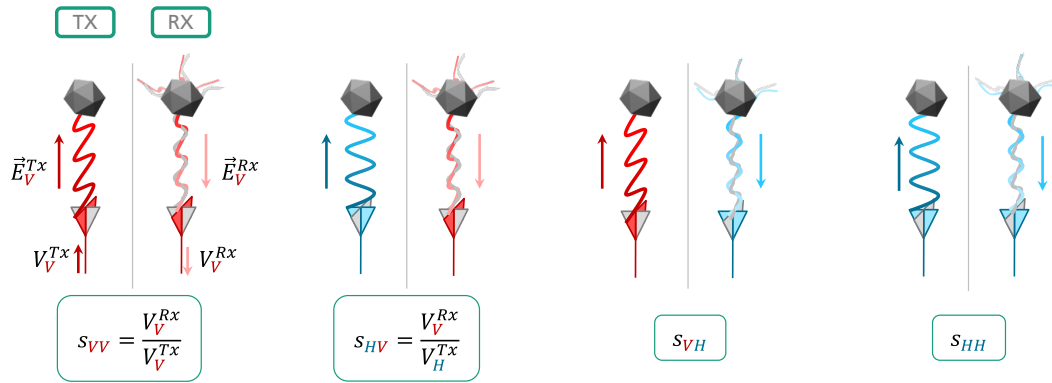


Figure 2-9 – Ideal PSM Measurement (Alternate-Transmit Alternate-Receive Mode)

In Eq. 2.10 major assumptions have been made, mainly, considering an ideal dual-pol antenna. In other words, an antenna with an infinite narrow beam and with perfect polarimetric purity. Considering only for now a finite polarimetric isolation, Eq. 2.10 can be expanded into

$$\begin{pmatrix} V_V^{Rx} \\ V_H^{Rx} \end{pmatrix} = \mathbf{R} \begin{pmatrix} s_{VV}^T & s_{HV}^T \\ s_{VH}^T & s_{HH}^T \end{pmatrix} \mathbf{T} \begin{pmatrix} V_V^{Tx} \\ V_H^{Tx} \end{pmatrix} \tag{Eq. 2.11}$$

Where \mathbf{T} and \mathbf{R} are the *effective polarimetric radiation patterns* for the transmitting and receiving antenna. Within a simplified dual-pol antenna model, it will be assumed that $\mathbf{R}(\theta, \phi) = \mathbf{T}(\theta, \phi) = \mathbf{T}$, yielding

$$\begin{pmatrix} V_V^{Rx} \\ V_H^{Rx} \end{pmatrix} = \begin{pmatrix} T_{VV} & T_{VH} \\ T_{HV} & T_{HH} \end{pmatrix} \begin{pmatrix} s_{VV}^T & s_{HV}^T \\ s_{VH}^T & s_{HH}^T \end{pmatrix} \begin{pmatrix} T_{VV} & T_{VH} \\ T_{HV} & T_{HH} \end{pmatrix} \begin{pmatrix} V_V^{Tx} \\ V_H^{Tx} \end{pmatrix} \tag{Eq. 2.12}$$

The fact that the antenna can also radiate in the orthogonal polarization has a major impact in the PSM measurement accuracy. The impact of this non-ideality is dual fold, as it also means that the antenna will sense both backscattered polarizations, thereby, contaminating the PSM measurements.

2.2.1 PSM Measurement Example

To quantize the impact of the antenna polarimetric non-idealities, the following example extracted from [36] is presented. The target under test, will be an ideal metallic sphere with a given radar cross section (RCS) σ . From EM theory the associated PSM is shown in Eq. 2.13.

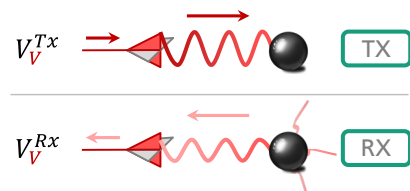


Figure 2-10 – Ideal Polarimetric Isolation

$$S_{sphere} = \sqrt{\sigma} \begin{pmatrix} 1 & 0 \\ 0 & 1 \end{pmatrix} \tag{Eq. 2.13}$$

To retrieve the PSM, the four measurements showed in Figure 2-9 are to be carried out. If only vertical polarization is transmitted, combining Eq. 2.12 and Eq. 2.13 leads to Eq. 2.14.

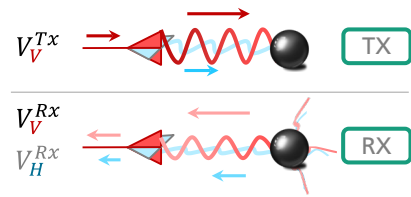


Figure 2-11 – Finite Polarimetric Isolation

$$\left. \begin{pmatrix} V_V^{Rx} \\ V_H^{Rx} \end{pmatrix} \right|_{V_H^{Tx}=0} = \begin{pmatrix} V_{VV} \\ V_{VH} \end{pmatrix} = \sqrt{\sigma} \begin{pmatrix} T_{VV}^2 + T_{HV}T_{VH} \\ T_{VH}T_{VV} + T_{HH}T_{VH} \end{pmatrix} V_V^{Tx} \quad \text{Eq. 2.14}$$

Thus the measured parameters from the PSM can be computed through the voltage ratios

Vertical Tx	Horizontal Tx
$s_{VV}^{meas} = \frac{V_V^{Rx}}{V_V^{Tx}} = \sqrt{\sigma}(T_{VV}^2 + T_{HV}T_{VH})$ Eq. 2.15	$s_{HH}^{meas} = \frac{V_V^{Rx}}{V_V^{Tx}} = \sqrt{\sigma}(T_{HH}^2 + T_{VH}T_{HV})$ Eq. 2.16
$s_{VH}^{meas} = \frac{V_H^{Rx}}{V_V^{Tx}} = \sqrt{\sigma}(T_{VH}T_{VV} + T_{HH}T_{VH})$ Eq. 2.17	$s_{HV}^{meas} = \frac{V_H^{Rx}}{V_V^{Tx}} = \sqrt{\sigma}(T_{HV}T_{HH} + T_{VV}T_{HV})$ Eq. 2.18

$$\mathbf{s}_{sphere}^{meas} = \sqrt{\sigma} \begin{pmatrix} T_{VV}^2 + T_{HV}T_{VH} & T_{HV}T_{HH} + T_{VV}T_{HV} \\ T_{VH}T_{VV} + T_{HH}T_{VH} & T_{HH}^2 + T_{VH}T_{HV} \end{pmatrix} \quad \text{Eq. 2.19}$$

Assuming that the dual-polarization antenna has (1) finite polarization isolation ($T_{HV} = T_{VH} = 0.1 \xrightarrow{20 \log_{10}} 20 \text{ dB}$) and that (2) the radar is properly calibrated ($T_{HH} = T_{VV} = 1$), the measured PSM in Eq. 2.19 can be rewritten into

$$\mathbf{s}_{sphere}^{meas} = \sqrt{\sigma} \begin{pmatrix} 1 + 0.01 & 0.2 \\ 0.2 & 1 + 0.01 \end{pmatrix} \quad \text{Eq. 2.20}$$

In the following section the main parameters relevant to weather monitoring are presented, establishing a proper link with the polarimetric requirements.

2.2.2 Atmospheric Remote Sensing Values of Interest

In *Atmospheric Radar Sensing* the measured parameters from the PSM are combined to obtain the so-called *Polarimetric Radar Data* (PRD), so that further weather products can be built. Through the data, hydrometeor classification is possible, being able to generate for example cloud and rain maps that support daily forecasts. The main parameters used for atmospheric remote sensing characterization and its associated values with clouds and precipitation are shown in Table 2.1 [11].

	Formula	Clouds and Precipitation
Radar Reflectivity	$Z_{HH} = s_{HH} ^2$	$-50 \text{ dBZ} \leq Z_{HH} \leq 50 \text{ dBZ}$
Differential Reflectivity	$Z_{DR} = s_{HH} ^2 / s_{VV} ^2$	$-3 \text{ dB} \leq Z_{HH} \leq 5 \text{ dB}$
Linear Depolarization Ratio	$L_{DR} = s_{HV} ^2 / s_{HH} ^2$	$L_{DR} \leq -12 \text{ dB}$
Specific Differential Phase	$K_{dp} \sim \arg(s_{HH}^* s_{VV})$	-
Correlation Coefficient	$\rho = \frac{\langle s_{HH}^* s_{VV} \rangle}{\sqrt{\langle s_{HH} ^2 \rangle \langle s_{VV} ^2 \rangle}}$	-
	$Z_{DRb}(\text{dB}) = (Z_{DR}^{meas} - Z_{DR})(\text{dBZ})$	
Bias	$L_{DRb}(\text{dB}) = (L_{DR}^{meas} - L_{DR})$	-
	...	

Table 2.1 – Atmospheric Remote Sensing Values of Interest

If going back to the example from [36] (reedited in subsection 2.2.1), the measurement of the sphere Z_{DR}^{meas} would be 0 dB , but the L_{DR}^{meas} would be -14 dB , a value considerably greater than the expected value for a sphere ($L_{DR}^{sphere} \rightarrow -\infty \text{ dB}$). If using the same antenna for rain measurements, the measured PSM would lead to different meteorological interpretations.

Rain has a $L_{DR} < -28 \text{ dB}$ [16], if allowing a 1 dB bias, that is to say a $L_{DR}^{meas} = -27 \text{ dB}$, a maximum bound for the total system polarimetric isolation would be 35 dB . Though there is no scientific minimal agreement on acceptable bias values for L_{DRb} , current research AESA weather radar systems are aiming at isolations over 30 dB [16].

On the other hand, when taking as a reference Z_{DR} , a more stringent bias requirement is claimed in [16, 20], where the maximum error between Z_{DR} and Z_{DR}^{meas} is required to be less than 0.1 dB . In [5] expressions to compute the Z_{DRb} (bias) are provided for the ATSR mode (also applicable to ATAR). In Eq. 2.21 reciprocity is assumed considering that no active elements such as T/R modules are included in the phased array.

$$Z_{DRb} \triangleq \frac{\oint_S |T_{HH}R_{HH} + T_{HV}R_{HV}|^2 d\Omega}{\oint_S |T_{VH}R_{VH} + T_{VV}R_{VV}|^2 d\Omega} \xrightarrow{R=T \text{ (Reciprocity)}} \frac{\oint_S |T_{HH}^2 + T_{HV}^2|^2 d\Omega}{\oint_S |T_{VH}^2 + T_{VV}^2|^2 d\Omega} \quad \text{Eq. 2.21}$$

From the *effective polarimetric radiation patterns* (\mathbf{T}), two terms can be distinguished, the *polarimetric pattern* (F) and *gain mismatch and isolations* from the antenna front-end (\hat{T}) [13]. In a phased array where no T/R modules / feeding network are used, or where their gain mismatch and HV port cross-talk have been calibrated, it is argued that only the pattern has a major impact on the Z_{DRb} [16], simplifying equation Eq. 2.21 into

$$i. i. f. \mathbf{T} = \mathbf{F} \Rightarrow Z_{DRb} = \frac{\oint_S |F_{HH}^2 + F_{HV}^2|^2 d\Omega}{\oint_S |F_{VH}^2 + F_{VV}^2|^2 d\Omega} \quad \text{Eq. 2.22}$$

Under the conditions that there has not been any angle-dependent calibration and that sidelobes are negligible, a further simplified expression is derived [20].

$$Z_{DRb} \cong \frac{|F_{HH}^2 + F_{HV}^2|}{|F_{VV}^2 + F_{VH}^2|} < 0.1 \text{ dB} \quad \text{Eq. 2.23}$$

A similar metric can be found for the L_{DR} . In this case it is not the bias, but it is the *Integrated Cross-Polarization Ratio* (ICPR), which indicates the cross-talk between the H and V polarizations [13] and thus, the minimum L_{DR}^{meas} that can be obtained. The ICPR for a ATSR mode follows

$$ICPR_V \triangleq \frac{\oint_S |F_{VV}F_{HV} + F_{VH}F_{HH}|^2 d\Omega}{\oint_S |F_{VV}^2 + F_{VH}^2|^2 d\Omega} < -30 \text{ dB} \quad \text{Eq. 2.24}$$

$$ICPR_H \triangleq \frac{\oint_S |F_{HH}F_{VH} + F_{HV}F_{VV}|^2 d\Omega}{\oint_S |F_{HH}^2 + F_{HV}^2|^2 d\Omega} < -30 \text{ dB} \quad \text{Eq. 2.25}$$

Note that for a parabolic reflector antenna the pattern matrix (\mathbf{F}) remains the same independently from the pointing direction ($\mathbf{F}_{parabolic}(\theta, \phi)$). In a phased array, the pattern will change with the scanning angle ($\mathbf{F}_{phased-array}(\theta, \phi, \theta_s, \phi_s)$), including possible polarimetric degradations that can drastically tighten the bias requirements.

2.2.3 Polarization Isolation or Polarization Discrimination?

While in a weather radar framework the relevance performance metric is the *effective polarimetric isolation*, from an antenna validation point of view, two concepts are to be distinguished. The undesired cross-polarization components can be either generated by the antenna, or by leakage at the antenna ports radiation as shown in Figure 2-12.

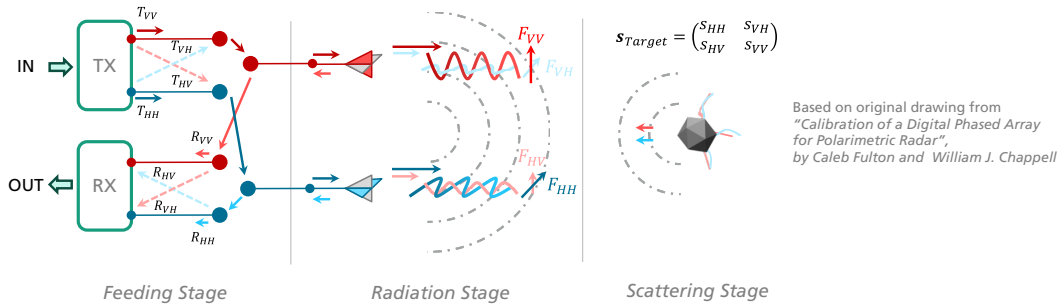


Figure 2-12 - Effective Cross Polarimetric Isolation for a Dual-Pol Antenna

From the finite isolation at the ports and the undesired cross-polarization of the antennas, two different figures of merit are identified, namely the *Cross-Polarization Isolation*² (*XPI*) and the *Cross-Polarization Discrimination* (*XPD*).

Vertical Tx	Horizontal Tx
$XPI_H \triangleq \frac{1}{ S_{HV} ^2} = \left \frac{a_V}{b_H} \right ^2$ <p style="text-align: right;">Eq. 2.26</p>	$XPI_V \triangleq \frac{1}{ S_{VH} ^2} = \left \frac{a_H}{b_V} \right ^2$ <p style="text-align: right;">Eq. 2.27</p>
$XPD_V(\theta, \phi) \triangleq \frac{ F_{VV}(\theta, \phi) ^2}{ F_{VH}(\theta, \phi) ^2} = \frac{ E_{Vv}(\theta, \phi) ^2}{ E_{Vh}(\theta, \phi) ^2}$ <p style="text-align: right;">Eq. 2.28</p>	$XPD_H(\theta, \phi) \triangleq \frac{ F_{HH}(\theta, \phi) ^2}{ F_{HV}(\theta, \phi) ^2} = \frac{ E_{Hh}(\theta, \phi) ^2}{ E_{Hv}(\theta, \phi) ^2}$ <p style="text-align: right;">Eq. 2.29</p>

Table 2.2 – XPI and XPD Definitions

XPI and *XPD* are undoubtedly related to each other, but finding a direct analytical relationship is a complex task. From a phased array point of view, the total radiated field from unit elements can be combined in such way that the cross-polarization component can be suppressed in specific planes (i.e. using feed rotation [35]). Specific beam calibration [16] can also provide on-axis cross-polar suppression. These techniques will lead to much higher *XPD* at the co-polar peak beam than the orthogonal port to port isolation (*XPI*).

On the other hand, as discussed in the previous section, polarimetric radiation patterns and their imbalances play a key role to limit to Z_{DRb} to 0.1 dB and *ICPR* to -30 dB (assuming a ATSR mode, but also valid for ATST). For this reason and following the recommendations from [37], the weather radar requirements can be translated into on-axis *XPD*, the co- and cross-polar E-Field ratio at the peak of the beam. But, the weather radar mode (STSR or ATSR) and the antenna topology (parabolic, planar...) will set the required value [5, 20, 37]. The modes will lead to different meteorological requirements as the antenna topology impacts the pattern integrals from Eq. 2.22 and Eq. 2.25.

² Note the usage of capital 'S', referring to the port H and V and using the S-Parameters notation.

2.3 Suitable Antenna Topologies for low-cost Weather Radar

The proposed weather radar is expected to be AESA, polarimetric and low-cost, three requirements that conflict with each other. AESA and low-cost features can be achieved through an hybrid sub-array topology [6] (see Figure 2-13). Following the previous discussion, excellent polarimetric performance has to complement the previous requirements.

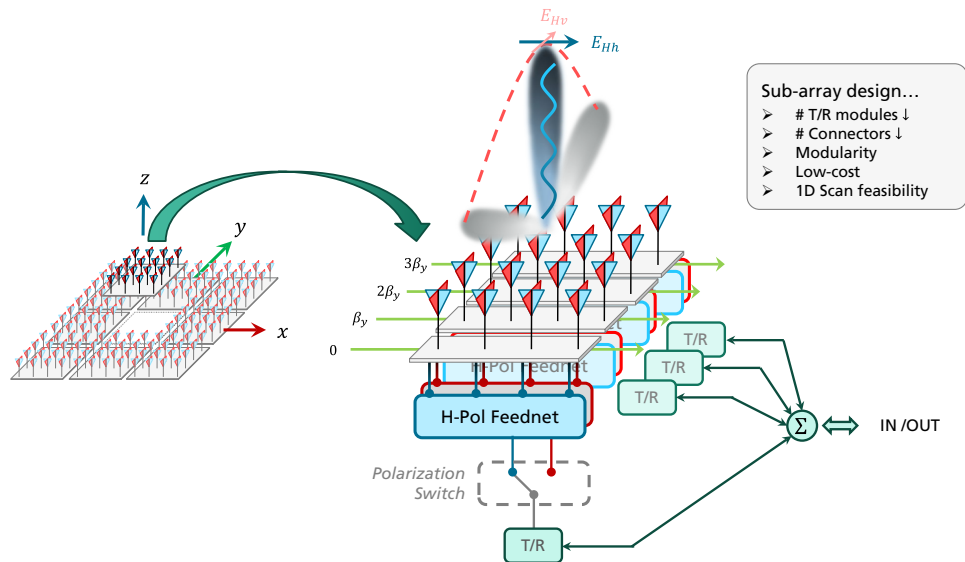


Figure 2-13 – Sub-Array Design and its benefits for a Low-Cost AESA Weather Radar

Minimizing the polarimetric degradation associated to electronic beam steering requires that an excellent dual-pol radiator is to be used. In this context, from the antenna design point of view, two EM phenomenas are required to be addressed to achieve sufficient polarimetric radiation performance, these are:

- The inter-element coupling and potential propagation of undesired EM modes that will add-up to cross-polarization.
- Secondly the fact that off the main planes the E-Field is no longer orthogonal. This is why, a *Cylindrical Phased Array* (CPAR) and combined electric and magnetic dipoles have been proposed [23, 37].

For a dual-pol antenna, whose radiation is generated by dipole-like radiation, the E-Fields in the diagonal planes will produce maximum cross-polarization due to the projection on the polarimetric basis, as depicted in Figure 2-14.

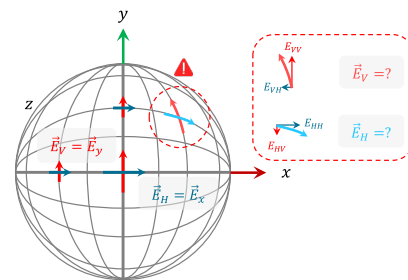


Figure 2-14 – E-Fields produced by H and V polarised Electric Current

Nonetheless, for a single axis scan application the field orthogonality off the main planes is not relevant. If the scanning direction falls into one of the main antenna planes the cross-polar requirement can be easily achieved using simple dual-pol patch antennas. Supported by PCB technology, a phased array of patches is affordable, making it ideal for low-cost, low-profile and

modular applications where high radiation efficiency is not a requirement. The array should be however optimized to compensate for the coupling effects and achieve low cross-pol radiation within the scanning range.

The usage of patch antennas is also beneficial from the antenna perspective. Traditional *parabolic antennas* have co-polar and deep null cross-polar beam with coaxial phase pattern.

In contrast patch antennas and its associated phased array topologies, have a co-polar and null co-polar beams surrounded by four cross-polar main lobes with alternating phase around the main peak lobe (see Figure 2-15 and Figure 2-16) [38].

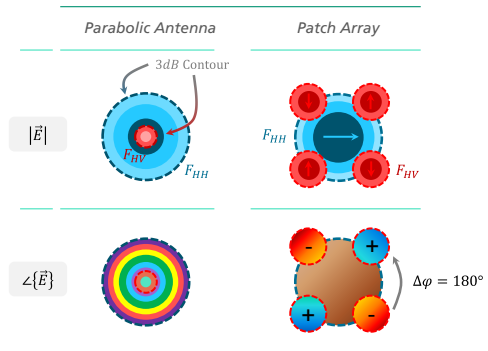


Figure 2-15 – Beam Pattern Topologies in Weather Radar

The implications arisen from the cross-polar pattern and its phase distribution along the beam is caused by the fact that Z_{DRb} as shown in Eq. 2.22 depends on the integrals of the pattern functions (F). While F_{HH} and F_{VV} are real functions, F_{HV} and F_{VH} are complex, with a phase relative to co-polar patterns (γ_{HV} and γ_{VH}) [2, 38]. The patterns³ are not normalized and contain the gain as shown in

$$F_{HH} \triangleq \sqrt{g_{HH}} f_{HH} \quad \text{Eq. 2.30}$$

$$F_{HV} \triangleq \sqrt{g_{HV}} f_{HV} e^{j\gamma_{HV}} \quad \text{Eq. 2.31}$$

In [38], Zrnica and Zhang argue and show the different on-axis *XPD* requirements for different types of co and cross-polar lobes. Constraining the requirement to a ATSR mode, systems with coaxial phase patterns should reach at least 45 dB of *XPD* for a point evaluation.

For patch antenna array, suggested *XPD* values at the boresight of any scanned beam should be at least 30 dB [16, 37, 38], so that in both case, $Z_{DRb} < 0.1$ dB can be achieved.

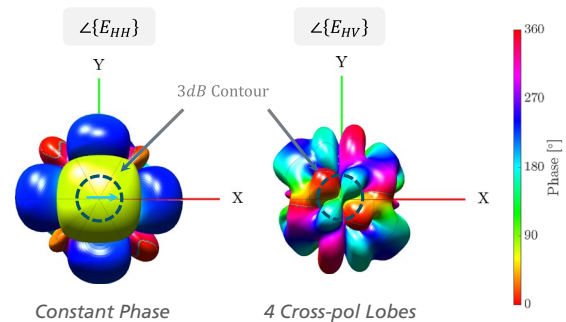


Figure 2-16 – Phase Pattern of a 4x4 Patch Antenna Array scanning at Broadside

Following these recommendations, the proposed antenna design is based on patch antenna technology. Thus, the antenna subsystem shall have a *XPD* at the peak of the co-pol beam of at least 30 dB. Yet, as it will be seen in the next section, based on the *non-uniform beam filling* effect for cloud monitoring, the *XPD* requirement will comprise the whole beam aperture down to the -6 dB level, yielding, a more robust performance metric, the *Integral Cross-Polarization Discrimination (IXPD)*.

³

$$f_{HH} = \frac{|E_{Hh}|}{|E_{max}|} \quad g_{HH} = \eta \frac{4\pi}{\Omega_{eq,HH}} = \eta \frac{4\pi}{\iint f_{HV}^2 d\Omega} \quad \gamma_{HV} = \angle\{E_{Hv}\} - \angle\{E_{Hh}\}$$

2.4 Challenges in Phased Array Weather Radar

One of the main challenges in polarimetric PAR systems is the depolarization of the radiated field when scanning off-broadside and off the principal planes. The polarimetric degradation and the associated geometrical corrections to be applied have been shown not to be relevant for the proposed elevation scan. Limiting to a 1D scan provides a cost-reduction and the possibility to achieve suitable polarimetric performance in the radiation stage with a decrease of antenna complexity.

The advantage provided by this architectural choice allows to address significant such as improved coverage of the lower troposphere through a short-range network of units, or even, non-uniform beam filling (see Figure 2-17).

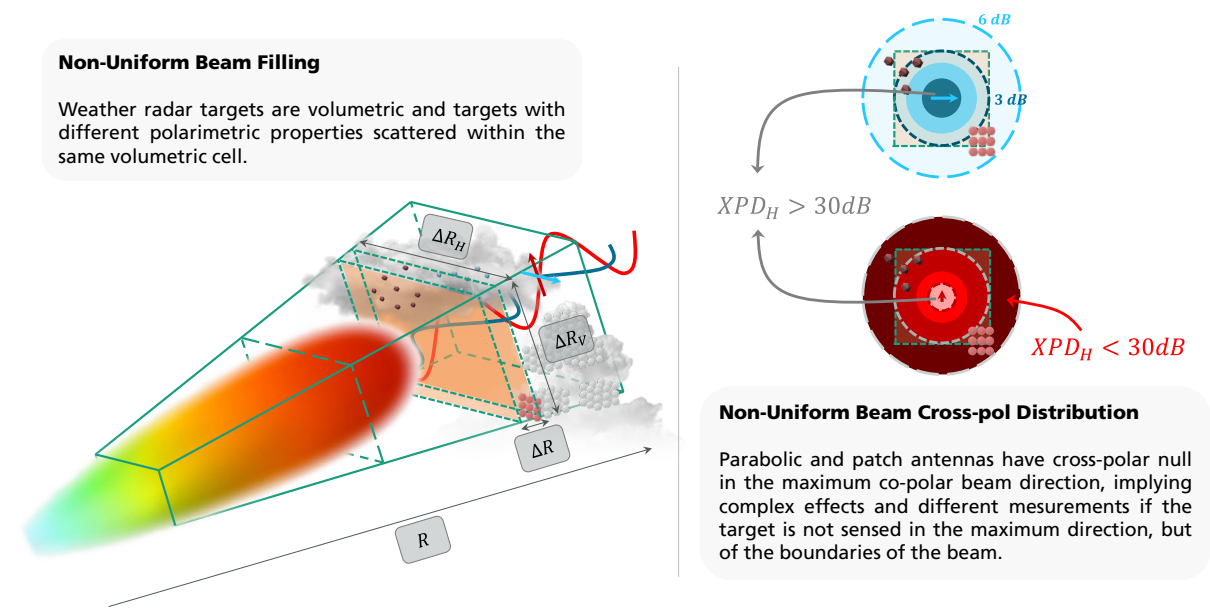


Figure 2-17 – Non-Uniform Beam Filling and Cross-polarization Distribution

Due to the reduced polarimetric degradation of the proposed AESA antenna, we propose to further constrain a bit more the XPD requirement for current PAR based on patch antennas. The discussion on the previous section concluded with a $XPD > 30\text{ dB}$ at the peak of the co-polar beam. We propose to extend the requirement to the beam pattern, up to the 6 dB beamwidth, to acknowledge the still on-going discussions of non-uniform beam filling.

For this reason a polarimetric assessment metric is presented, the *Integral Cross-Polarization Discrimination (IXPD)*, which depends on the beam aperture. The reference aperture will be initially set to the -6 dB level. The definitions of $IXPD$ follows

Vertical Tx		Horizontal Tx
$IXPD_V^{6dB} \triangleq \frac{\oint E_{Vv}(\theta, \phi) d\Omega_{6dB}}{\oint E_{Vh}(\theta, \phi) d\Omega_{6dB}}$	Eq. 2.32	$IXPD_H^{6dB} \triangleq \frac{\oint E_{Hh}(\theta, \phi) d\Omega_{6dB}}{\oint E_{Hv}(\theta, \phi) d\Omega_{6dB}}$

2.5 Further Considerations

In this chapter a brief introduction on phased array technology and weather radars has been outlined. The convergence of both topics has led to the formulation of polarimetric requirements for intended application. While *effective polarimetric isolation* between H and V ports does play a key role, in sub-sections 2.2.2 and 2.2.3 the co-polar and cross-polar pattern of phased arrays have been recognized to have a major impact on the Z_{DRb} and L_{DRb} . Major assumptions on the usage of T/R modules and homogeneous beam filling have been made. More specifically, patch antenna arrays for ATSR or ATAR modes have been shown to require XPD values at the peak of the co-polar axis in excess of 30 dB to achieve a Z_{DRb} of less than 0.1 dB

For AESA operations XPD severely degrades if the beam is steered. However, based on the low-cost requirement of our system, electronic scanning is limited to be monodimensional in elevation. The advantages of this scan constraint are the potential cost-reduction of the aperture and the less severe polarimetric degradation due to scanning vertically along the antenna principal plane. A concept of the antenna sub-system architectural choices is shown in....

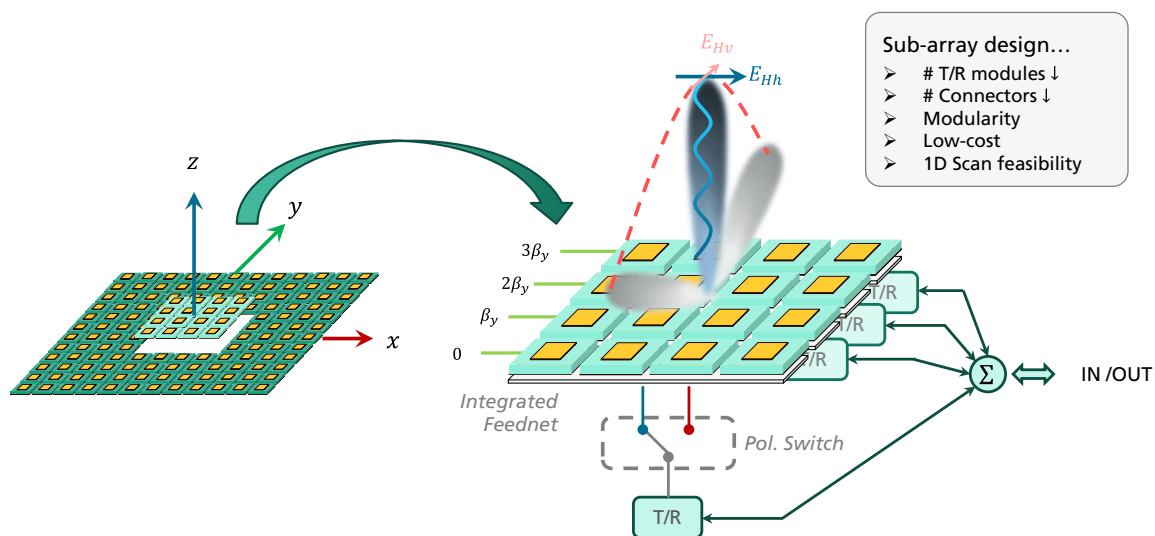


Figure 2-18 – Proposed Patch based Sub-Array Design for a Low-Cost AESA WRAD

Finally, a new polarimetric figure of merit will be used to assess the polarimetric performance within the 6 dB contour beam, the $IXPD^{6dB}$. For this, the Ludwig 3 definition [39] will be used.

Chapter 3 - Patch Antenna Design

This chapter is dedicated to reviewing the radiation mechanism of planar antennas, namely, **dual polarized patch antenna**. Physical understanding of the EM radiation phenomena is required to optimize polarimetric performance as well to mitigate coupling. For that, the main figures of merit are presented in order to evaluate the available design options.

Moreover, aspects such as **patch shape**, **feeding techniques** and **cross-polarization suppression techniques** will be discussed in this chapter, providing an initial background to justify the following design decisions.

3.1 Patch Antenna

The so-called **microstrip** or **patch antenna** is a well-known radiator based on PCB technology. Its spread usage for either civil or military applications relies on the *lower-cost*, *less-weight* and *planar profile* requirements of modern communication systems. In this context, it is no exception that in the AESA weather radar conception [6], planar antennas were already considered as a viable option. Patch antennas also provide great flexibility in terms of *shape*, *multi-layer layout* and *feeding techniques*, hence, allowing some freedom to optimize the cross-polarization performance while fulfilling the weather radar requirements (namely low-cost, narrowband and cross-polarization purity). Other notable features range from system istackability with other subsystems, scalability and modularity at the array level.

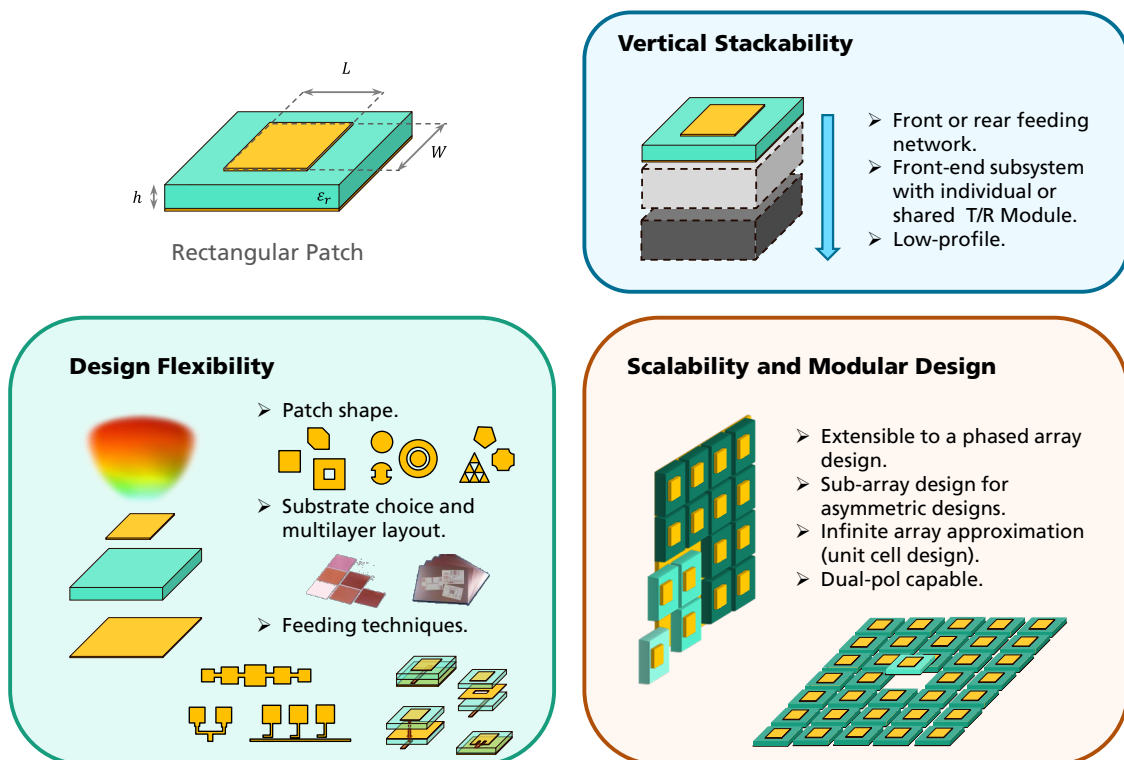


Figure 3-1 – Advantages of Patch Antenna Technology

At the design stage of the Antenna sub-system here presented, an initial literature review has been carried on to the usage of linearly polarized patch antennas for weather radars in spite of their known *inefficiency* and relatively *low cross-polarization* performance. This is why, in order to gain insight and to understand the cross-polarization suppression techniques to be discussed, an initial review on the associated radiation phenomena is presented. Supported by two different approaches (physical and cavity models), the EM radiation phenomena is revisited. In the analysis, specific emphasis is put on the cross-polarization generation in order tackle its appearance at a phased array level, namely using the feed-rotation technique among other design additions (see Chapter 4).

Starting from a **theoretical overview** (section 3.2), practical details on **feeding techniques** and **substrate choices** are also provided in sections 3.3 and 4.1 respectively. Based on the system design choices, major **design guidelines** for a dual-pol probe-fed patch antenna are listed in Appendix B.

3.2 Radiation Models

Three major radiation models have been used to understand and design patch antennas. The first two, the **(I) cavity** and **(II) transmission-line** models rely on a purely analytical approach that is limited by the model simplicity. As the complexity increases, modelization is no longer viable leading to a **(III) full-wave analysis** based on a CAD model and using industrial simulation software such as CST MWS or HFSS to enable extended design capabilities. Within an industrial context, due to time concerns and design easiness the full-wave analysis is preferred. However, theoretical models set a knowledge-base that allows deeper understanding of the patch antenna design process and the foundation of cross-polar components generation.

Before delving into the theoretical complexity or the computational abstraction of CEM software, let us raise a fundamental question: why does a patch antenna radiate? The patch radiation mechanism is relatively simple to understand and based on the current distributions appearing on an excited patch (see Figure 3-2).

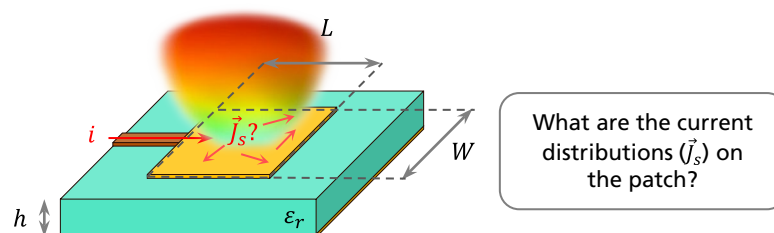


Figure 3-2 – Formulation of the Radiation Mechanism

3.2.1 Physical Interpretation

A simple, but intuitive initial approach is to treat the patch as a mere open-circuited transmission line. The discontinuity at the end of the patch defines the current (i) and voltage (v) distribution.

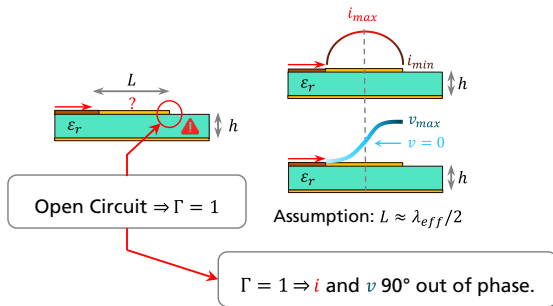


Figure 3-3 – Simplified EM Distributions a Rectangular Patch Antenna (I)

It is important to remark the impact of the i and v distributions on the input impedance (Z_{in}). First, because in the center of the patch the ratio v/i is zero and $Z_{in} \approx 0$ and on the edges $Z_{in} \uparrow\uparrow$.

Second, because of matching purposes. When desiring to match the patch antenna ($Z_{in} = Z_{REF}$) to a given characteristic impedance (Z_0), it will be required to connect the feeding line to a non-edge point of the patch antenna.

From a physical perspective, the distributions shown in Figure 3-3 can be associated to the field distribution established between the patch and the ground plane.

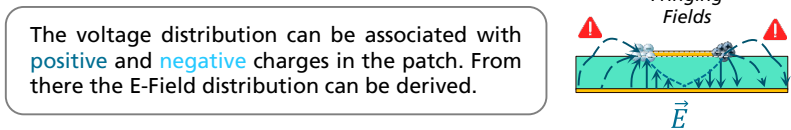


Figure 3-4 – Simplified EM Distributions a Rectangular Patch Antenna (II)

Using Figure 3-3 and Figure 3-4 the current and field distributions can be decomposed to understand which components have an active role in the radiation mechanism. As explained in Figure 3-5, the appearance of fringing fields allows the EM radiation mechanism to take place [40], which act as equivalent current sources (see subsection 3.2.2).

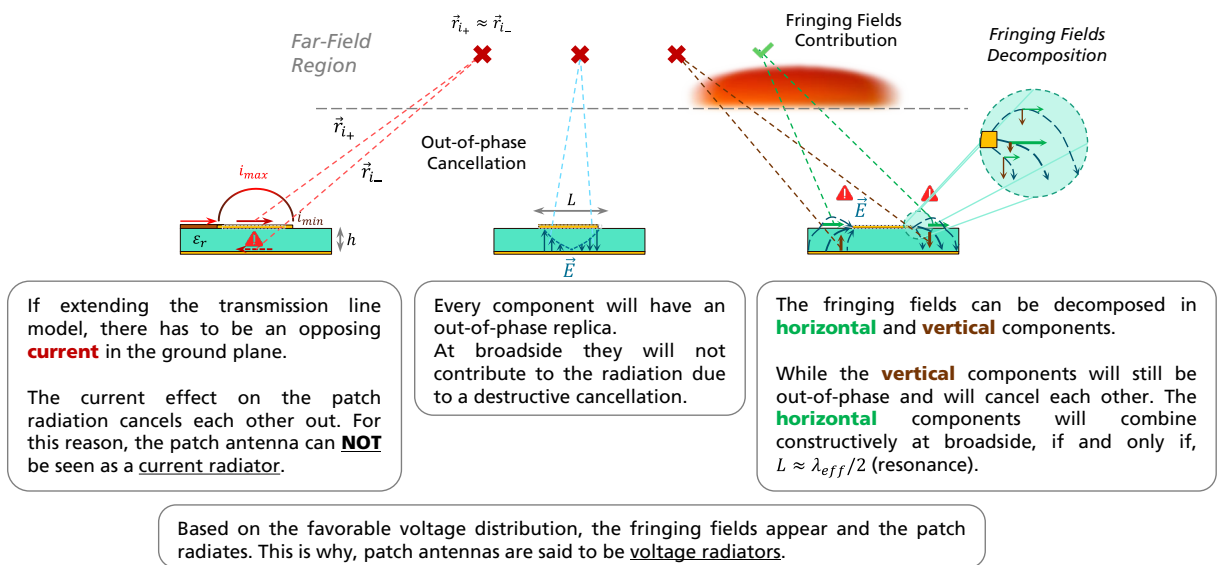


Figure 3-5 – Simplified EM Distributions a Rectangular Patch Antenna (III)

Although this explanation simplifies the radiation mechanism and the importance of the fringing fields, does not justify the appearance of the cross-polarization terms of a rectangular patch antenna. For this reason, the **cavity model** is reviewed in what follows, while the transmission-line and full-wave analysis will not be further discussed.

3.2.2 Cavity Model

After defining and understanding the simplified radiation mechanism of a rectangular patch antenna, a deeper insight of its theoretical performance when ideally fed is needed. The introduced time-varying field in the patch and its effect can be studied from an analytical point of view. By treating the patch antenna as a cavity formed by *Perfect Electric Conductors* (PEC) and *Perfect Magnetic Conductors* (PMC), the field distribution can be derived and thus, the associated Far-Fields.

Thanks to this cavity representation, the boundary conditions are simplified. Imposing them in the Maxwell equations will yield a discrete number of solutions, or in other words, allowed field distributions within the cavity, the so-called **modes**. For a mode to propagate in the cavity, a resonance at a specific frequency is required, thus, implying a somewhat narrowband performance.

The conceptual steps involved in the cavity model are summarized in Figure 3-6. In this context, the introduction of this representation does not respond to the need to theoretically derive the Far-Fields of a patch antenna. Instead, the cavity model will be used to understand the cross-polarization generation mechanism inherent to the radiation from a rectangular patch antenna.

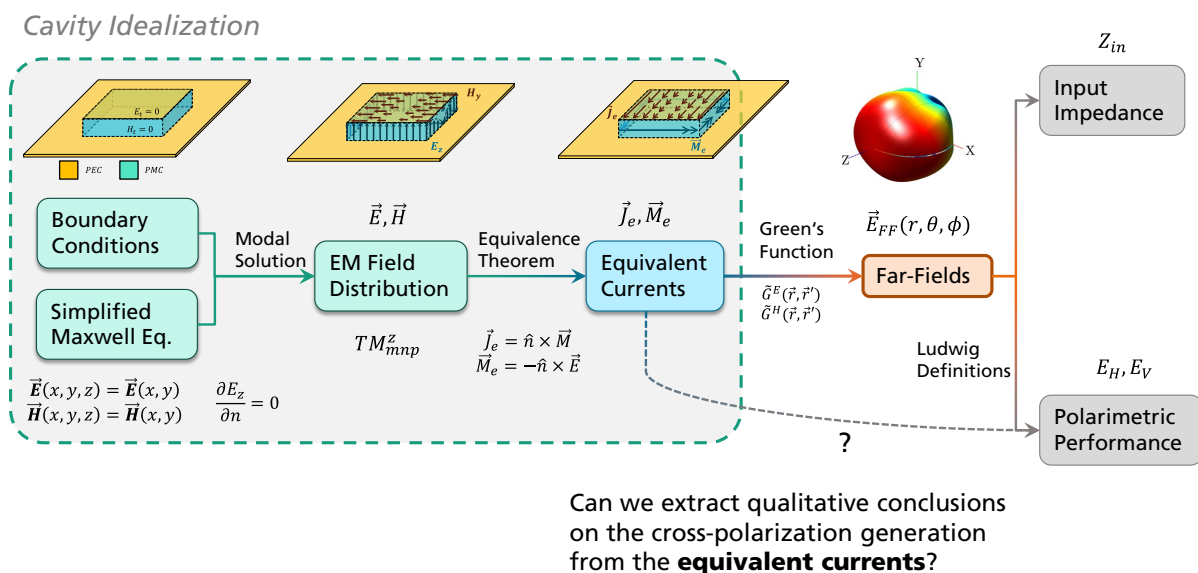


Figure 3-6 – Cavity Model Framework

Defining the Cavity

To define the cavity the radiation mechanism will be simplified. The main initial assumption is that the substrate thickness (h) is much smaller than λ . Consequently, three major assumptions follow, with implications in how the fields in the cavity are contained and the associated boundary conditions.

The three major assumptions [41] and consequences are summarized in Table 3.1 and displayed in Figure 3-7:

	Assumption	Consequence
(1)	<p>The fields within the cavity do not vary with z. Since $h \ll \lambda$, the field variations along the height are considered to be negligible.</p> <p>Note I: the fields can still have a z-directed component.</p> <p>Note II: this assumption generates model inaccuracies, especially for thick substrates. [42]</p>	$\vec{E}(x, y, z) = \vec{E}(x, y)$ $\vec{H}(x, y, z) = \vec{H}(x, y)$ <p>(Simplified fields for the Maxwell Equations)</p>
(2)	<p>Since $h \ll \lambda$, the ratio $h/W \ll 1$ and the current flow from the patch to the ground plane and viceversa is negligible. [43]</p> <p>This causes the tangential H-Field on the cavity edges to be null.</p>	<p>(Cavity sidewalls can be treated as PMC)</p>
(3)	<p>The tangential E-Field on the cavity faces is null, due to the conductor nature of the material. The faces of the cavity can be dealt as a PEC.</p> <p>The tangential H-Field on the cavity sidewalls is null, thus including 4 PMC walls in the cavity.</p>	$\begin{cases} \vec{E} \cdot \hat{z} = 0, & \vec{H} \times \hat{z} = 0 & z = 0 \text{ and } h \\ \vec{H} \cdot \hat{z} = 0, & \vec{E} \times \hat{z} = 0 & \text{on PMC walls} \end{cases}$ <p>(Boundary conditions)</p>

Table 3.1 - Major Assumptions in Rectangular Cavity Model

The power of the cavity model relies on the analytical treatment and the physical insight it provides with accurate enough results. By doing this, the proposed conceptual scheme in Figure 3-6 is used to derive the equivalent currents and understand the appearance of **co-polar** and **cross-polar** components.

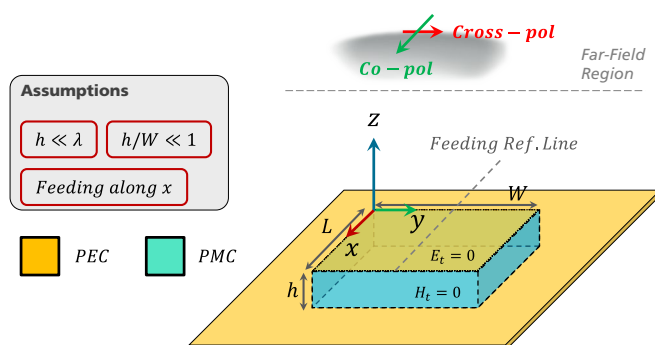


Figure 3-7 – Cavity and Geometry Definition

Cavity Modal Solution

Applying the consequences from assumptions 1 and 3 to the Maxwell Equations, the modal field solutions can be computed [42, 41, 44]. The resulting modal solutions are discrete and they are specified by the indexes m , n and p . Such indexes refer to the number of half cycles of the E-Field in the z , x and y directions⁴.

For a given mode mnp (TM_{mnp}^z), the associated resonant frequencies [43] are:

$$(f_r)_{mnp} = \frac{1}{2\pi\sqrt{\mu\epsilon}} \sqrt{\left(\frac{m\pi}{h}\right)^2 + \left(\frac{n\pi}{L}\right)^2 + \left(\frac{p\pi}{W}\right)^2} \quad (f_r)_{010} = \frac{1}{2\sqrt{\mu\epsilon}L} = \frac{c_0}{2L\sqrt{\epsilon_r}} \quad \text{Eq. 3.1}$$

For rectangular patch antennas with $h \ll L$ and $h \ll W$, if $L > W$ the first resonant mode will be the TM_{010}^z [43], usually followed by the TM_{020}^z or the TM_{001}^z . In the TM_{010}^z mode, the resonance will take place when the distance between the radiating cavity laterals is $\lambda_g/2$, as stated in Eq. 3.2. In that situation the co-polar radiated fields will add in-phase and the imaginary input impedance will be null.

$$L = \frac{c_0}{2(f_r)_{010}\sqrt{\epsilon_r}} = \frac{\lambda_0}{2\sqrt{\epsilon_r}} = \frac{\lambda_g}{2} \quad \text{Eq. 3.2}$$

In this work, only the TM_{010}^z mode will be discussed as it provides the best polarimetric performance. Moreover, the proposed antenna to be designed (a dual-pol fed-probe patch antenna) is symmetric ($W = L$), which would lead to the resonance of the TM_{010}^z and the TM_{001}^z at the same frequency. However, for actual implementations the feeding will play a major role in the excitation of the fundamental mode (TM_{010}^z).

Omitting the modal field solution, the analytic **electric field**⁵ distribution associated to the TM_{010}^z is described in Eq. 3.3 and 3.4.

$$E_x = E_y = 0 \quad \text{Eq. 3.3} \quad E_z = -E_0 \cos\left(\frac{\pi x}{L}\right) \quad \text{Eq. 3.4}$$

The **magnetic field** component is given in Eq. 3.5 and 3.6

$$H_y = -H_0 \sin\left(\frac{\pi y}{L}\right) \quad \text{Eq. 3.5} \quad H_x = H_z = 0 \quad \text{Eq. 3.6}$$

⁴ The reference system used has been changed compared to that one described in the literature [41, 60]. Usually the normal vector to the patch is x -directed, while the z and y -directed laterals have a respective length of W and L . Such change is suitable so that the coordinate system matches with the Ludwig definitions and the defined reference system to measure co- and cross-polarization. For this reason, in this report, the TM is referenced as TM_{mnp}^z ($mnp \sim zxy$) instead of TM_{mnp}^x ($mnp \sim xyz$).

⁵ Where the values E_0 and H_0 are treated as constants to simplify the notation. More details on their dependence to the wavenumbers and the mnp index modes can be found in [22, 29].

In the cavity model, based on assumption (2) from Table 3.1, *fringing fields* have been ignored. However, such fields are the actual responsible for the radiation mechanism as shown in Figure 3-8 as they act as the equivalent radiation sources of the cavity model.

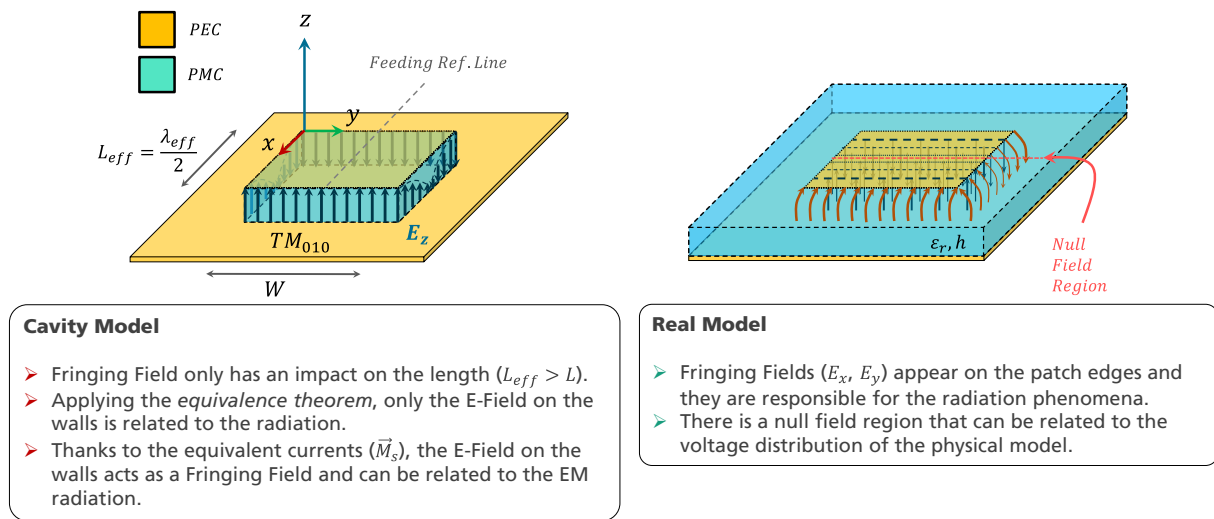


Figure 3-8 – Cavity and Real E-Field Distributions

In the cavity model, the influence of the *fringing fields* can be taken into account by extending the length of the patch and updating the resonant frequency of the modes. This effect is described in Eq. 3.8 and 3.9, where the *effective dielectric constant* (ϵ_{reff}) is required to compute the *length increment* (ΔL). Eq. 3.9 shows the updated *resonant frequency* (f_r') taking into account the fringing fields

$$\epsilon_{reff} = \frac{\epsilon_r + 1}{2} - \frac{\epsilon_r - 1}{2} \left[1 + 12 \frac{h}{W} \right]^{-1/2} \quad i. i. f. h \ll W \quad \text{Eq. 3.7}$$

$$\frac{\Delta L}{h} = 0.412 \frac{(\epsilon_{reff} + 0.3) \left(\frac{W}{h} + 0.264 \right)}{(\epsilon_{reff} - 0.258) \left(\frac{W}{h} + 0.8 \right)} \quad L_{eff} = L + 2\Delta L \quad \text{Eq. 3.8}$$

$$(f_r')_{010} = \frac{c_0}{2(L + 2\Delta L)\sqrt{\epsilon_{reff}}} \quad \text{Eq. 3.9}$$

The next step of the cavity model, is to treat the associated modal fields as equivalent current sources, so that, using the Green's Function, the Far-Fields can be derived.

Equivalent Currents

Through the Equivalence Theorem, the TM_{010}^z fields of a rectangular patch can be seen as six magnetic dipoles: two **co-polar** dipoles adding in-phase at broadside and four **cross-polar** dipoles cancelling each other at broadside. Particularly for the M_{010}^z , the resulting modal field distribution results in the appearance of two metallic slots associated to the radiating cavity walls (see Figure 3-9).

The *Equivalence Theorem*, also known as the *Huygens' Principle* (Eq. 3.10 and 3.11), allows to represent the patch antenna by a composition of equivalent sources

$$\vec{J}_e = \hat{n} \times \vec{H} \quad \text{Eq. 3.10}$$

$$\vec{M}_e = -\hat{n} \times \vec{E} \quad \text{Eq. 3.11}$$

where \hat{n} is the normal vector with respect to the surface of application or aperture. Figure 3-9 shows the field distributions for the TM_{010}^z and the normals to the surfaces of interest.

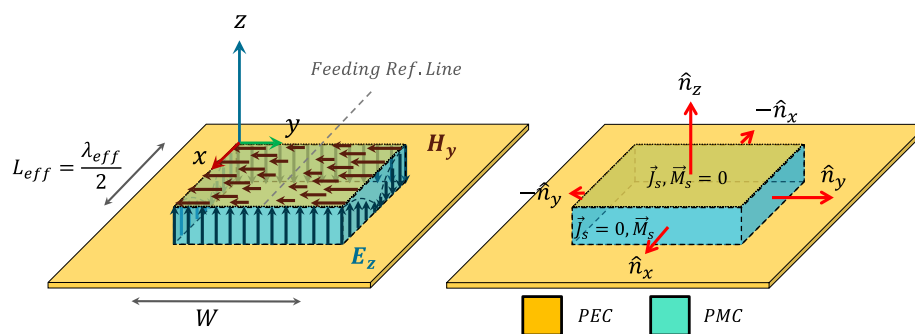


Figure 3-9 – Field Distribution for TM_{010}^z

By applying the Equivalence Theorem the *equivalent currents* are found, as it is shown in Figure 3-10 and equations 3.12 and 3.13.

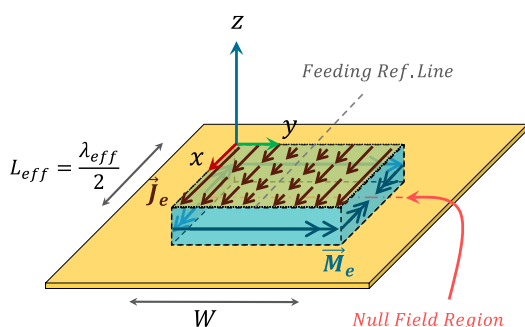


Figure 3-10 – TM_{010}^z Equivalent Currents

$$\vec{M}_s = H_0 \begin{cases} \hat{y}, & x = 0 \\ \hat{y}, & x = L_{eff} \\ -\cos \frac{\pi x}{L} \hat{x}, & y = 0 \\ \cos \frac{\pi x}{L} \hat{x}, & y = W \end{cases} \quad \text{Eq. 3.12}$$

$$\vec{J}_e = E_0 \sin \left(\frac{\pi x}{L} \right) \hat{x} \quad \text{Eq. 3.13}$$

In reality, underneath the patch there are fields, but the equivalent principle and the cavity model simplify the current distribution by assuming PEC and PMC walls. Despite the model simplifications, it is important to remark that in reality, along the feeding line which is orthogonal to the resonant dipoles (y -direction), there is a null field region.

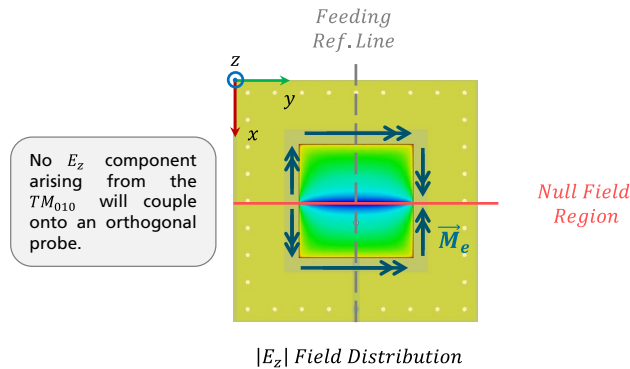


Figure 3-11 – z-directed E-Field for a Fed-probe Patch Antenna

This matches with the null voltage distribution at the patch center seen in the simplified physical model ($Z_{in}^{center} = 0$) and moreover shows the possibility to add a second probe orthogonally placed to achieve **dual-linear polarization** shown in Figure 3-12.

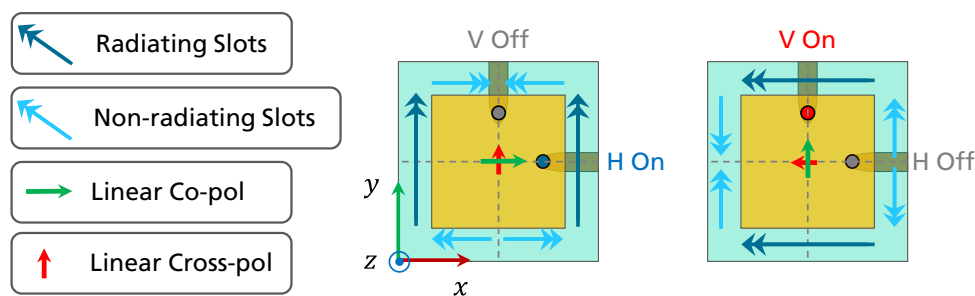


Figure 3-12 – Equivalent Slots for Linear Dual-Pol Patch Antenna

After the *equivalent currents* are derived, the *Green's function* can be applied to obtain the Far-Fields. A traditional approach to simplify the problem relies on the usage of the *image theorem* [43] to remove the *electric currents* (\vec{J}_e). This workflow has been omitted due to the difficulty to construct the Green's Function taking into account the actual feeding probes and vias, but also, because the equivalent currents distributions are unknown. In reality, the currents will have a z -variation and the feeding probes will also have an impact on such distribution, mainly due to the asymmetries introduced by the feeding inset, probe or aperture.

Due to the aforementioned reasons, full-wave solvers such as CST MWS or ANSYS HFSS were used. Comparison between the cavity model and simulated *simple-pol* and *dual-polarized fed-probe* patch antennae are provided in sub-section 3.4.

Polarimetric Performance of a Single-Pol Patch Antenna

Based on the equivalent currents distributions using the cavity model, it is possible to predict the polarimetric performance of a rectangular microstrip antenna. The direction of the equivalent currents provides information on how the radiated fields will be related to their co-polar and cross-polar linear polarization components. Understanding how such components will be combined with each other at broadside and off-broadside already gives some physical insight on how the antenna performs, an insight that a full-wave solver will not provide.

Assuming that the cavity is fed along the x-axis, Figure 3-13 separates the equivalent currents by the two polarizations that comprise the radiated fields.

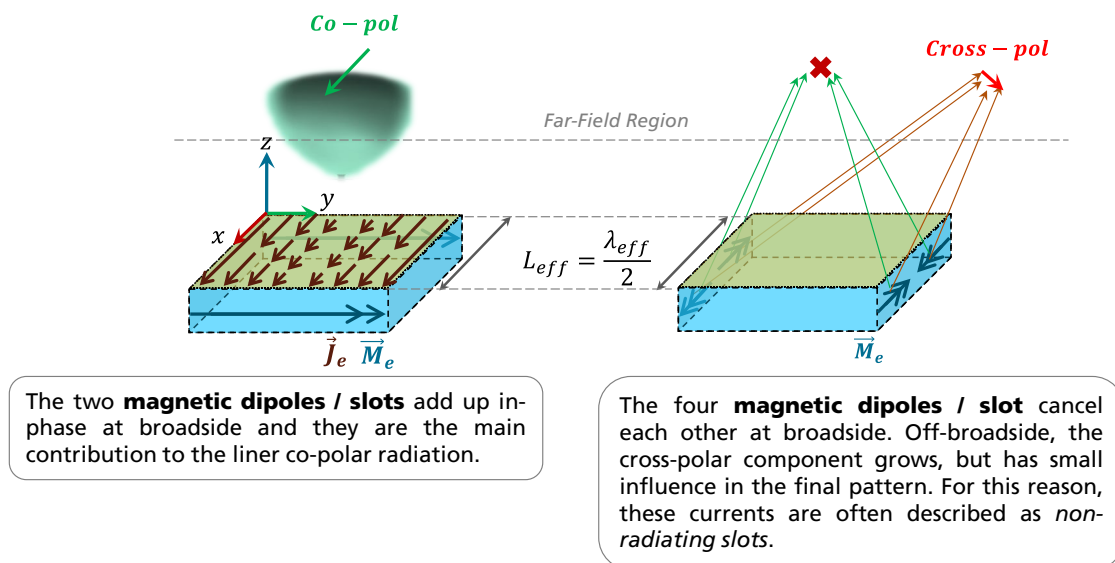


Figure 3-13 – Cavity Model Polarimetric Performance

Cavity Model Conclusions

Through the *cavity model* it has been shown that the rectangular microstrip antenna radiating under the TM_{010}^z conditions has great polarimetric performance at broadside (is ideally purely linearly co-polarized). Off-broadside, the *non-radiating slots* have an impact on the cross-polar components. These two ideas will help understanding the polarimetric degradation that planar phased arrays undergo when scanning off-broadside. Nonetheless, as it will be seen in Chapter 4, the *feed rotation technique* will partially be able to suppress the cross-polarization terms arising from the TM_{010}^z among other contributors such as inter-element coupling.

From a practical point of view, the cavity model lacks the versatility to integrate more advanced elements such as feeding effects or even stacked patches. The limitation not only comes from the incapability to model the field distributions, but also from the complexity involved in the Green's function definition in the presence of vias, additional ground planes or integrated antenna structures. For this reason, at a final design level, a full-wave approach has been preferred.

3.3 Feeding Techniques

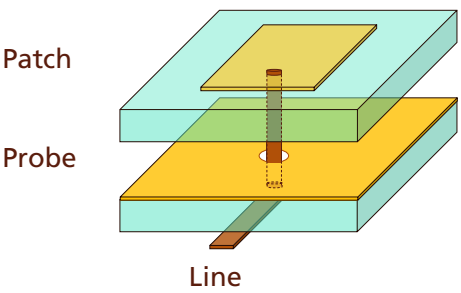
Patch antennas provide a large degree of freedom in terms of design. Among all the possible design choices, one of the most important considerations is the **feeding technique**. The way the radiating element is excited plays a key role not only in coupling between adjacent elements but also in the choice of the feeding network architecture [45]. In our application, there is a third aspect to be taken into account, the cross-polarization purity and isolation between orthogonal channels. Since there will be two channels (namely H and V), a combination of different feeding techniques is possible, but undesired as it will lead to a non-symmetric performance.

In order to choose the feeding technique providing the best trade-off between *polarimetric performance* and *cost*, an initial overview of the available techniques is provided.

3.3.1 Overview and Analysis

The presented feeding techniques represent a small selection of the most common options. There is still research ongoing on the topic and it is not here intended to provide innovation from the unit cell feeding point-of-view. This is why, based on the reported performance, some (but not all) patch feeding techniques follow.

Three major feeding techniques can be derived, mainly based on whether the patch is *directly connected* (1), *coupled* (2) or *capacitively* (3) fed by a probe [46].

Probe Feeding (with microstrip line or coaxial connection)	
 <p>The diagram illustrates the probe feeding technique. It shows a three-layer structure. The top layer is a light blue substrate with a yellow patch. A vertical probe passes through a hole in the ground layer (middle layer, light green) and is connected to a microstrip line on the bottom layer (yellow). Labels 'Patch', 'Probe', and 'Line' are placed next to their respective components.</p>	<ul style="list-style-type: none"> ▲ Dual-pol possible. ▲ Differential feeding possible ($XPI \uparrow$). ▲ Easy to manufacture and simple matching. ▲ Possibility to integrate a rear feeding network.
	<ul style="list-style-type: none"> ▼ Narrowband ($BW \downarrow$), due to copper clearance in the ground layer. ▼ Probe coupling within the substrates due to <i>Surface Waves (SW)</i> or <i>Parallel Plate Mode (PPM)</i> propagation⁶. ▼ Multilayer design (cost\uparrow).

⁶ PPM propagation only if probes go through two or more layers.

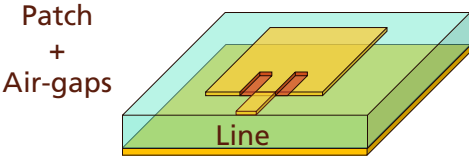
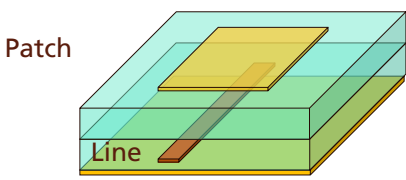
Inset Probe	
 <p>Patch + Air-gaps</p> <p>Line</p>	<ul style="list-style-type: none"> ▲ Easy to manufacture and simple matching. ▲ Possibility to integrate an upper feeding network. <hr/> <ul style="list-style-type: none"> ▼ Narrowband ($BW \downarrow$). ▼ Dual-pol is possible but suffers from high cross polarization (air-gaps distort the patch shape)⁷. ($XPD \downarrow$) ▼ Upper feeding network can decrease polarimetric performance. ($XPD \downarrow, XPI \downarrow$)

Table 3.2 - Probe Feeding Techniques

Proximity Coupled	
 <p>Patch</p> <p>Line</p>	<ul style="list-style-type: none"> ▲ No surface waves losses. ($\eta_{eff} \uparrow$) ▲ Low interferences with circuitry. ($XPI \uparrow$) ▲ Widest bandwidth. ($BW \uparrow$) <hr/> <ul style="list-style-type: none"> ▼ Highly complex dual-pol design. ▼ Complex feeding network scheme using stripline technology. ▼ Difficult fabrication. ($cost \uparrow$) ▼ Poor coupling performance ($\eta_{eff} \downarrow$)

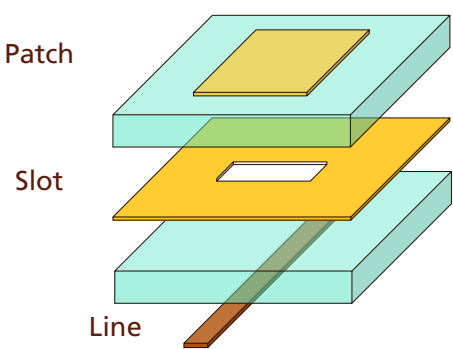
Aperture Coupled	
 <p>Patch</p> <p>Slot</p> <p>Line</p>	<ul style="list-style-type: none"> ▲ Easier dual-pol design. ▲ No surface waves losses. ($\eta_{eff} \uparrow$) ▲ Coupling is increased with respect to the suspended stripline. ($\eta_{eff} \uparrow$) ▲ Possibility to integrate a rear feeding network. ▲ Tunability of the aperture to optimize cross-polarization performance. ▲ Independent design of feeding line, slot and radiator. [47] ▲ Relative wide bandwidth. ($BW \uparrow$) <hr/> <ul style="list-style-type: none"> ▼ Poor front to back radiation performance (spurious radiation from the front-end can affect the antenna performance). ($\eta_{eff} \downarrow, XPI \downarrow$) ▼ Difficult fabrication. ($cost \uparrow$) ▼ Multilayer design. ($cost \uparrow$)

Table 3.3 – Coupled Feeding Techniques

⁷ Possibility to keep the symmetry by adding a third and fourth port (differential feeding, see section 3.3.2).

Following the previous options, hybrid techniques can be used to excite the patch antenna capacitively. For this, a probe is placed close enough to the radiating element without establishing any physical connection.

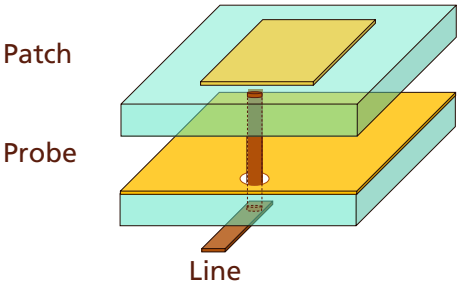
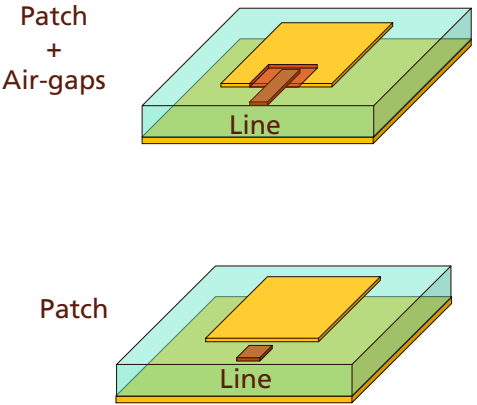
Capacitive Probe [28]	
	<ul style="list-style-type: none"> ▲ Dual-pol possible. ▲ Differential feeding possible. ($XPI \uparrow$) ▲ Possibility to integrate a rear feeding network. <hr/> <ul style="list-style-type: none"> ▼ Narrowband ($BW \downarrow$), due to copper clearance in the ground layer and capacitance with patch. ▼ Probe coupling within the substrates (SW and /or PPM).⁸ ▼ Multilayer design. ($cost \uparrow$) ▼ Complex design in terms of optimization (pad shape, distance to the patch...)
Capacitive Inset Probe (with Air Gaps) and Proximity Coupled (no Air Gaps)	
	<ul style="list-style-type: none"> ▲ Possibility to integrate an upper feeding network. ▲ Easiness to apply tapering by changing the capacitive inset. <hr/> <ul style="list-style-type: none"> ▼ High cross polarization [45]. ($XPD \downarrow$) ▼ Possibility to keep the symmetry by adding a third and fourth port (differential feeding, see section 3.3.2). ▼ Upper feeding network can decrease polarimetric performance. ($XPD \downarrow$, $XPI \downarrow$) ▼ Difficult matching (high input impedance).

Table 3.4 – Capacitive Feeding Techniques

Based on the polarimetric performance requirement **probe feeding** was chosen. Capacitive probe feeding was discarded due to the increase in complexity and the non-disclosed reports of designs achieving 30 dB in XPD . However in the following iterations to come, capacitive feeding should be considered as it allows separating the probes while increasing the isolation and providing more space for the associated rear feed network. This might allow the usage of the techniques discussed in the following section.

⁸ In case of a dual-pol design, the usage of capacitive probes allow to separate more the probes, reducing the coupling taking place within the substrates (isolation \uparrow).

3.3.2 Dual Polarization Techniques for Probe-fed Patch Antennas

Upgrading probe-fed patch antennas to operate in two polarizations is relatively simple. Adding another probe in the orthogonal cross-section has a small impact on the central frequency and no major design modifications are required. An initial sketch of this technique with different art-concept views is depicted in Figure 3-14.

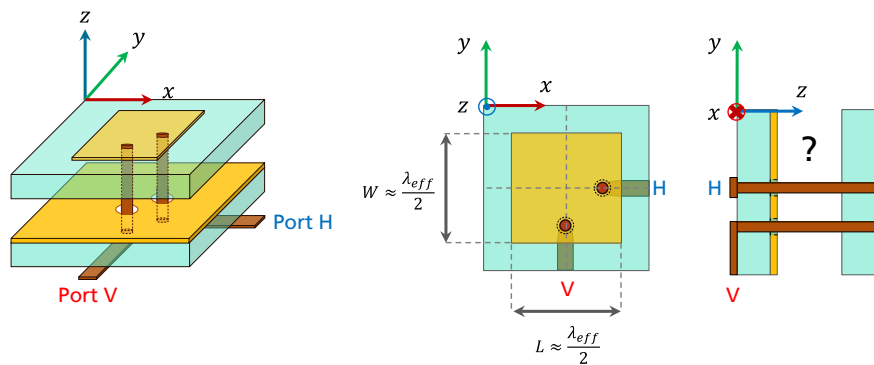


Figure 3-14 – Initial Dual-pol Probe-fed Patch Antenna

One of the main drawbacks of using probes is the excitation of PPM within the substrates [45]. This EM phenomenon arises in case the probe crosses a substrate confined between two ground planes, with remarkable impact for thick substrates. The transfer of energy to this kind of modes can be seen as a **loss** and also as a source of **coupling** between two adjacent probes.

Ideally, in Figure 3-14 there is no possibility of PPM excitation since there is only one ground. Having a shared ground between the patch antenna (*radiation stage*) and the feeding network (*feeding stage*) is not advisable, for the following reasons:

1. *Radiation* and *feeding stages* are coupled since they have a common ground. Currents excited in the ground can have an influence in both stages.
2. **Manufacturing concerns.**
 - In order to glue together High-Frequency (HF) substrates like the Rogers RO4350B, there is the possibility to use as an interface layer (called 'prepeg'), like for example the Rogers RO4400 Bondply.
 - Using HF prepegs allows to achieve higher performance and to keep a low-profile antenna, at the expense of a light cost increase.
3. **Asymmetric design**
 - Having an asymmetric layer structure makes the PCB prone to delamination in the long run. For weather radars this is highly critical as the system is expected to operate outdoors, suffering constant thermal gradients throughout the year and also from the day/night cycle.
 - To mitigate the impact of thermal expansion and compression, symmetric designs are preferred.

The alternative to a HF prepreg is to use a FR-4 core layer that acts as a prepreg at a reduced cost, allowing decoupling of both the radiation and feeding stage and making the layout symmetric, at the expense, however, of PPM propagation (see Figure 3-18). The comparison of both approaches is depicted in Figure 3-15.

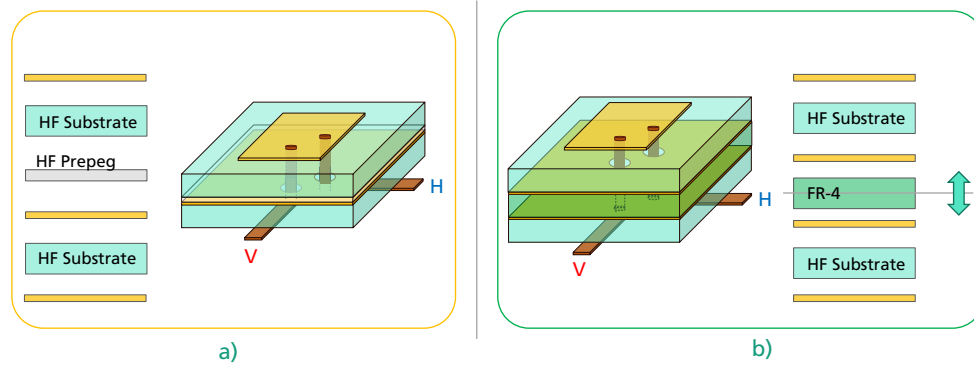


Figure 3-15 – Probe-fed Layout Topologies

The fact that the layout b) (from Figure 3-15) has been chosen, implies the appearance of PPM which will propagate as cylindrical waves within the substrate [48]. Part of this energy will be coupled into the orthogonal probe, decreasing the cross-polarization performance and the probe isolation, two significant figures of merit associated with the radiation and feeding stages of the proposed antenna.

Nonetheless, PPM excitation can be strongly attenuated using mode-suppressing vias [45]. In PCB terminology this is known as a *RF through via*. By placing through RF vias, not only it is possible to attenuate the PPM excitation, but also to suppress the appearance of Surface Waves (SW) at a later stage when placing the unit cell into a phased array [49] [30]. Overall, RF via fence allows to enhance the efficiency of the proposed unit cell.

As a rule of thumb to achieve both PPM attenuation and SW suppression, vias should have minimal fence spacing of $\lambda_g/4$, being $\lambda_g = \lambda_0/\sqrt{\epsilon_r}$. Concept art pictures involving these techniques are shown in Figure 3-16.

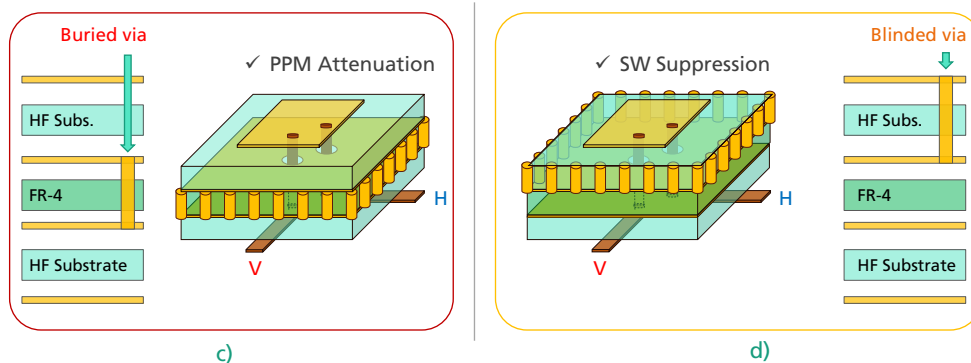


Figure 3-16 – Probe-fed Efficiency Enhancement Techniques

However, there are manufacturing concerns in terms of **feasibility** and **cost**. Buried RF vias in layout c) are expensive and discouraged for most PCB manufacturers. Blinded vias in Figure 3-16 d) are possible, with a slight increment of cost with respect to through RF vias.

On the other hand, the usage of through RF vias would be suitable at the expense of limiting the space of the rear feeding network. When constraints imposed by the feeding network require to remove some of the through vias, it is advisable to replace such vias by blinded ones to avoid asymmetries at the antenna stage and the consequent increase of cross-polarization. This is why a combination of blinded and through RF vias was selected as shown in Figure 3-17.

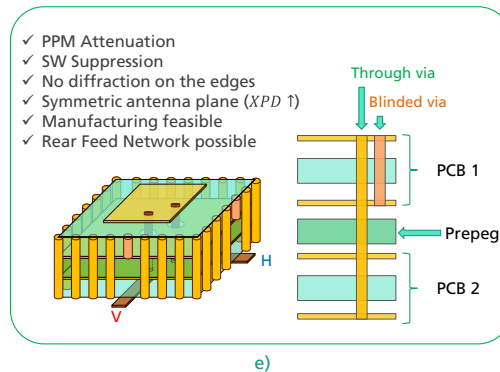


Figure 3-17 – Initial Unit Cell Concept

Despite the enhancement achieved using a combined distribution of blinded and through vias, the dual-pol probe-fed patch antenna achieves reasonable polarimetric performance in terms of radiation ($XPD_{Broadside} \approx 30 \text{ dB}$), but fails to perfectly isolate the orthogonal channels ($XPI = 1/|S_{HV}|^2 = 1/|S_{VH}|^2 \approx 20 \text{ dB} < 30 \text{ dB}$). This is mainly caused by the coupling between two ports taking place at (1) the radiation stage and the coupling arisen from (2) the cross-talk of microstrip feeding lines and (3) the residual PPM propagation. The excited cylindrical waves are partially attenuated by the vias, but they still couple onto the adjacent probe due to the lack of isolation. Sources (1) and (2) are depicted in Figure 3-18, while microstrip cross-talk will be later on discussed.

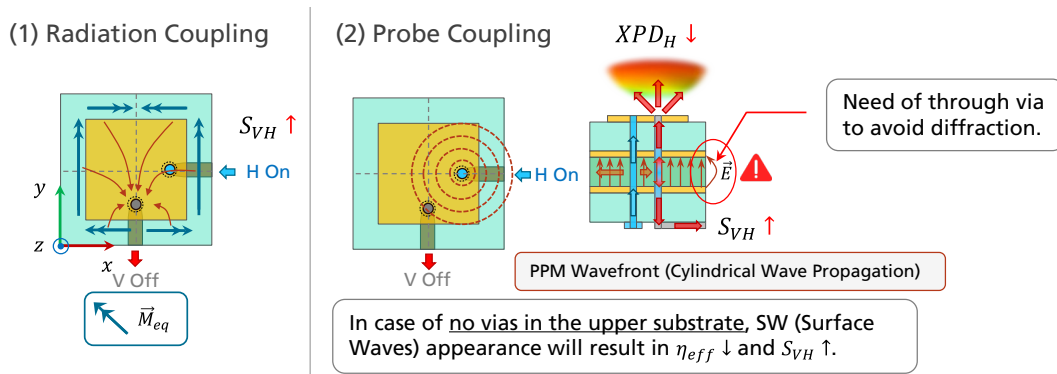


Figure 3-18 – Unit cell sources of isolation and cross-polarization degradation

3.3.3 Feeding Probe Isolation Techniques

Despite the relative low isolation that dual fed-probe patches provide, there are still a set of techniques to tackle the issue. In this section three main solutions are presented, none of these applied to the proposed design, but they are to be considered for future iterations. A brief review of each technique is provided here.

Combination of Feeding Techniques

The usage of the same technique within the feeding stage will lead to increased coupling but symmetric performance. Instead, using different techniques could be a way to achieve higher isolation values. An example is the combined usage of different aperture coupling schemes in [22] [50].

Combining aperture coupled with a feeding probe could be a potential candidate, but based on system requirements, aperture coupling has been avoided due to the poor back radiation performance ($FTBR \approx 15..20 \text{ dB}$) [13] [5] and its possible interaction ($XPI \downarrow$) with the feeding network and the front-end circuitry to be placed behind the antenna.

Differential Feeding

On the other hand, when using a probe-fed technique for both polarimetric channels, isolation can be enhanced by considering a differential feed approach [42] as shown in Figure 3-19. By making all channels differential, probe coupling gets cancelled achieving up to 40 dB isolation [20].

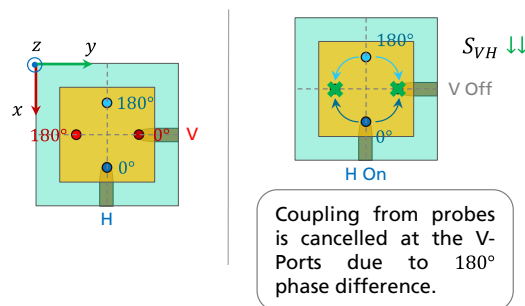


Figure 3-19 – Differential Feeding

In the proposed antenna design, differential feeding has been considered, but later on discarded due to a shortage of board surface at X-band. The difficulty to synthesize the 180° phase shift for both channels made it unfeasible. Alternatively, applying differential feeding to one port only added asymmetry at the antenna stage, with drastic impact on the polarimetric performance ($XPD \downarrow$).

Via Fencing

If total freedom to play with vias and their height is granted; a possibility could be isolate the feeding probes [51]. Case study examples are shown in Table 3.5, stating an improvement of 2.3 dB in terms of *XPD* and 5 dB in isolation.

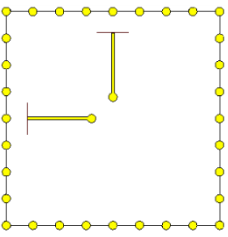
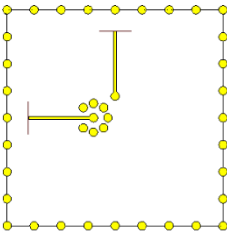
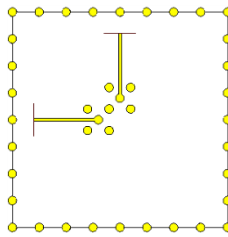
		
a) No via fence	b) Circular via fence	c) Symmetric via fence

Table 3.5 – Via Fencing Examples (CST MWS Models)

This approach relies on the usage of blinded vias, which are usually feasible if they only penetrate completely in one or more layers. As soon as customization in the via insertion depth is required, manufacturing and cost issues arise.

Blinded vias usually require a wider hole and suffer from greater tolerances due to the complexity of copper filling. Additionally, if the vias do not penetrate completely in one layer, the tip of the drill bit will also add another source of uncertainty.

Ultimately, the increase in cost and design complexity discouraged actual implementation of via fencing.

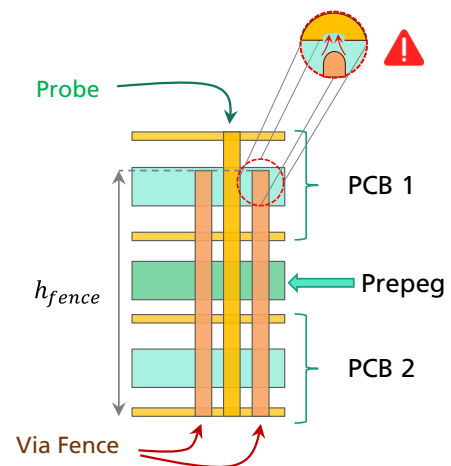


Figure 3-20 – Via Fence Layout

3.4 Cross-Polarization Assessment

As discussed, feeding probes for dual polarization patch antennas have to deal with the propagation of PPM. This has an effect on the XPD and the isolation ($|S_{HV}|^2, |S_{VH}|^2$), critical parameters in the design of low-cross polarization antennas. However, cross-polarization suppression techniques can be provided at a sub-array level as it will be seen in Chapter 4.

Yet, to get deeper insight on the radiated cross-polarization component, the fields, currents distribution and far-fields have been analyzed for a single- and dual-pol fed-probe patch antenna. From it to major questions could be answered, understanding the cross-polarization EM phenomena and ways to mitigate it. Using EM simulations supported by CST MWS, aspects such as the **feeding line orientation** or the effect of an **additional probe** on the patch are also reviewed. The study was made using the reference system shown in Figure 3-21.

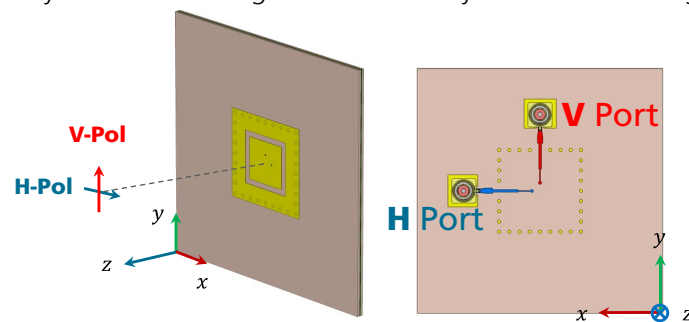


Figure 3-21 – Polarization and Antenna Plane Reference

Mono Fed-Probe Patch Antenna⁹

Omitting for now the design stage of a patch antenna (see section 4.1 and Appendix B), a single-pol fed-probe patch antenna has been simulated and compared to the cavity model expectations. In the study major conclusions regarding the probe feeding line orientation were drawn. A total of three cases were investigated as depicted in Table 3.6, where the line orthogonality is defined with respect to the radiating slots:

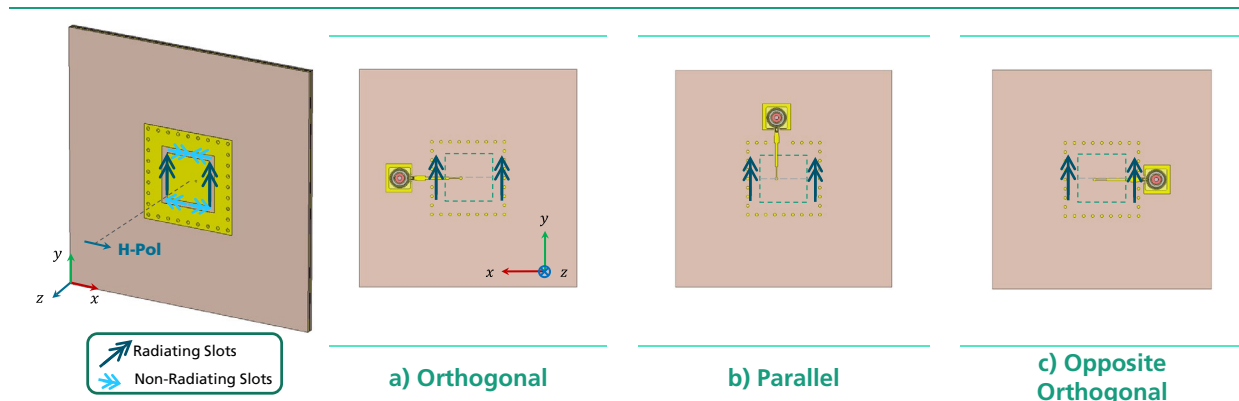


Table 3.6 – Feeding Line Orientations

⁹ The metallization around the patch was used to reduce mutual coupling at the array level. For a simple cell it has no effect on the S-Parameters nor on the polarimetric performance.

When comparing the polarization performance for the three cases, the radiation pattern has been found to be practically the same, but an effect has been noted on the cross-polarization performance. Using Ludwig III definition, the co- and cross-polarization components are plotted for the E, D and H-Plane in Table 3.7. For all cases, major polarimetric degradation can be observed in the D-plane, but also in the E and H-Plane when looking off-broadside angles.

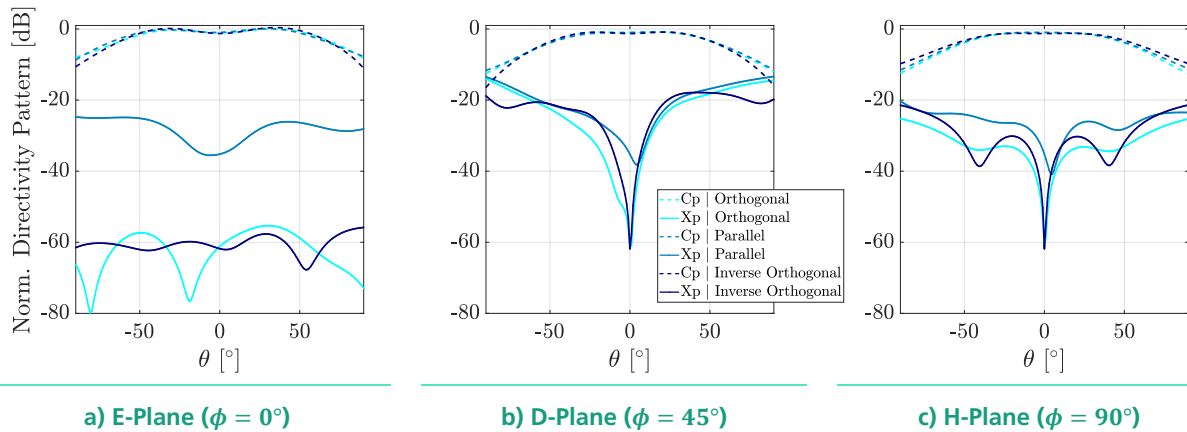
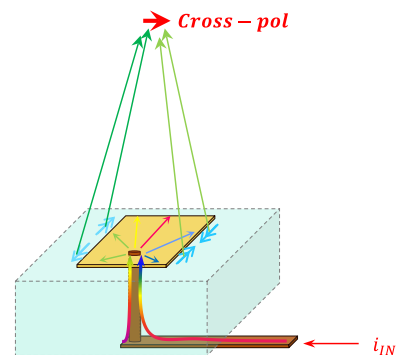


Table 3.7 – Horizontally Mono-Polarized Probe-Fed Patch Pattern Comparison (CST MWS FD)

While the *orthogonally-fed* patch antennas reach the same polarimetric performance at broadside ($XPD_{Broad} \approx 60 \text{ dB}$), the *parallel-fed* case differs ($XPD_{Broad} \approx 35 \text{ dB}$). To understand this polarimetric degradation, we can resort to visualizing the current distribution along the probe and later on, to the *cavity model*.

Specifically, Figure 3-22 shows the polarimetric degradation when the cross-polarization dipoles are fed with different phases, as a result of the asymmetric feeding, as pointed out also by [52].

Based on these initial simulations, *parallel line feeding* should be avoided to maximize antenna symmetry and polarimetric performance.



Due to different phases, at broadside, the 4 magnetic dipoles do not cancel each other and cross-polarization increases.

Figure 3-22 – Parallel-fed Current Distribution

Dual-pol Fed-probe Patch Antenna

As discussed in 3.3.2, introducing a second probe in the parallel cross-section to the radiating slots allows adding the dual-polarization feature (see Figure 3-12). The probes as depicted in Figure 3-18 will cross-talk degrading the polarimetric performance of the antenna in terms of XPI but also in terms of reradiation of the coupled energy into the undesired polarimetric component ($XPD \downarrow$). As a case study, a dual-pol patch antenna with the H-port energized was compared to the previous single-polarized horizontally antenna with an orthogonal feeding line (Table 3.6 - a).

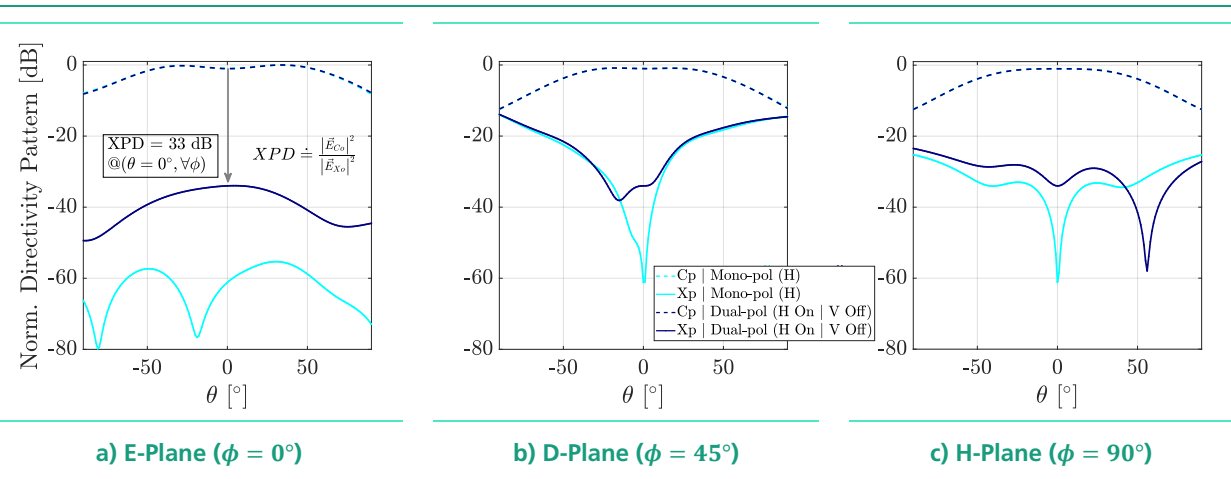


Table 3.8 - Horizontally Mono vs Dual-Pol Probe-Fed Patch Pattern Comparison (CST MWS FD)

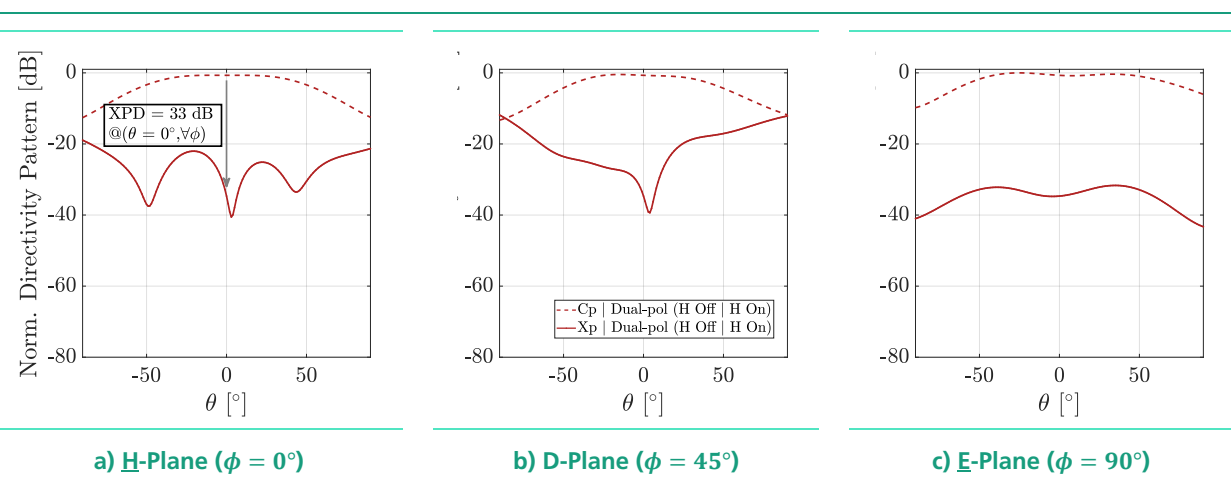


Table 3.9 – Vertically Dual-Pol Probe-Fed Patch Pattern Comparison (CST MWS FD)

Based on the results in Table 3.8, the effect of adding a secondary probe to generate an orthogonal polarization degrades the *XPD* performance by circa 30 dB (being about 60 dB the *XPD* for the single probe case and the 33 dB for the dual-pol configuration). It can be noted this value in *XPD* for the dual-pol set-up coincides with *XPI* value reported in Figure 3-23. However, this will not hold true for the actual sub-array with integrated feeding network.

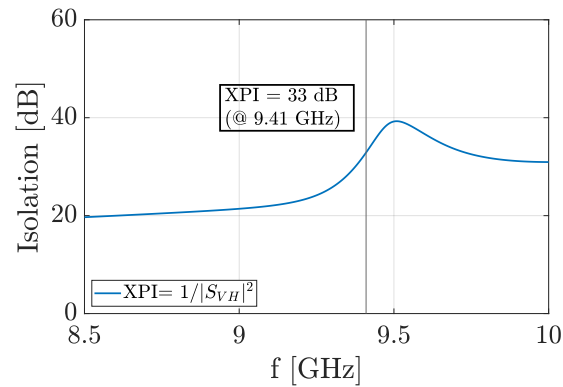


Figure 3-23 – Isolation for a Dual-Pol Probe Fed Patch

If no vias are used to attenuate PPM and suppress SW, both the cross-polarization isolation and discrimination (*XPD* and *XPI*) are degraded due to the increased coupling between probes within the substrate.

Simulated Current Distributions

To better understand the sources of polarimetric degradation, CST MWS provides the *fields* (\vec{E} and \vec{H}) and *surface currents* (\vec{J}_s) distributions. Visualizing the fields on a cutting plane, the simulated single- and dual-pol patches can be compared (see Table 3.10). From there, physical insight can be extracted to explain the appearance of additional cross-polarized terms.

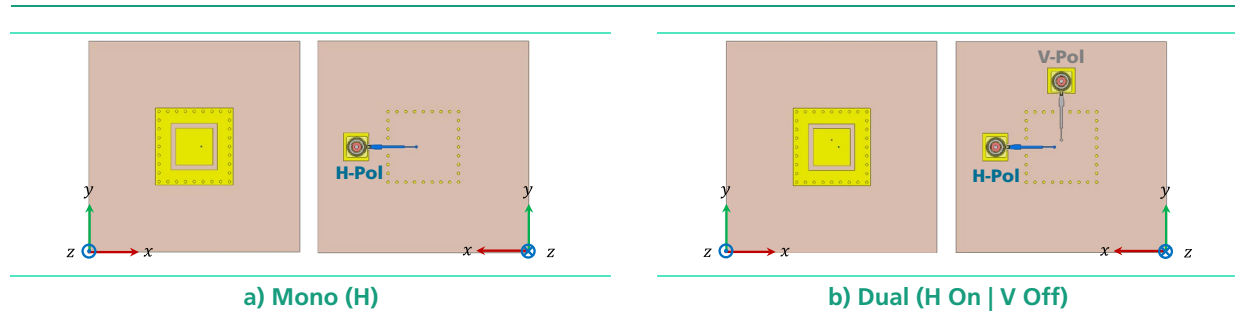


Table 3.10 – Mono vs Dual-Polarized Patches (CST MWS CAD Model)

The distributions of the fringing E-field components are depicted in Table 3.11. From there no major conclusions can be extracted regarding the cross-polarization degradation.

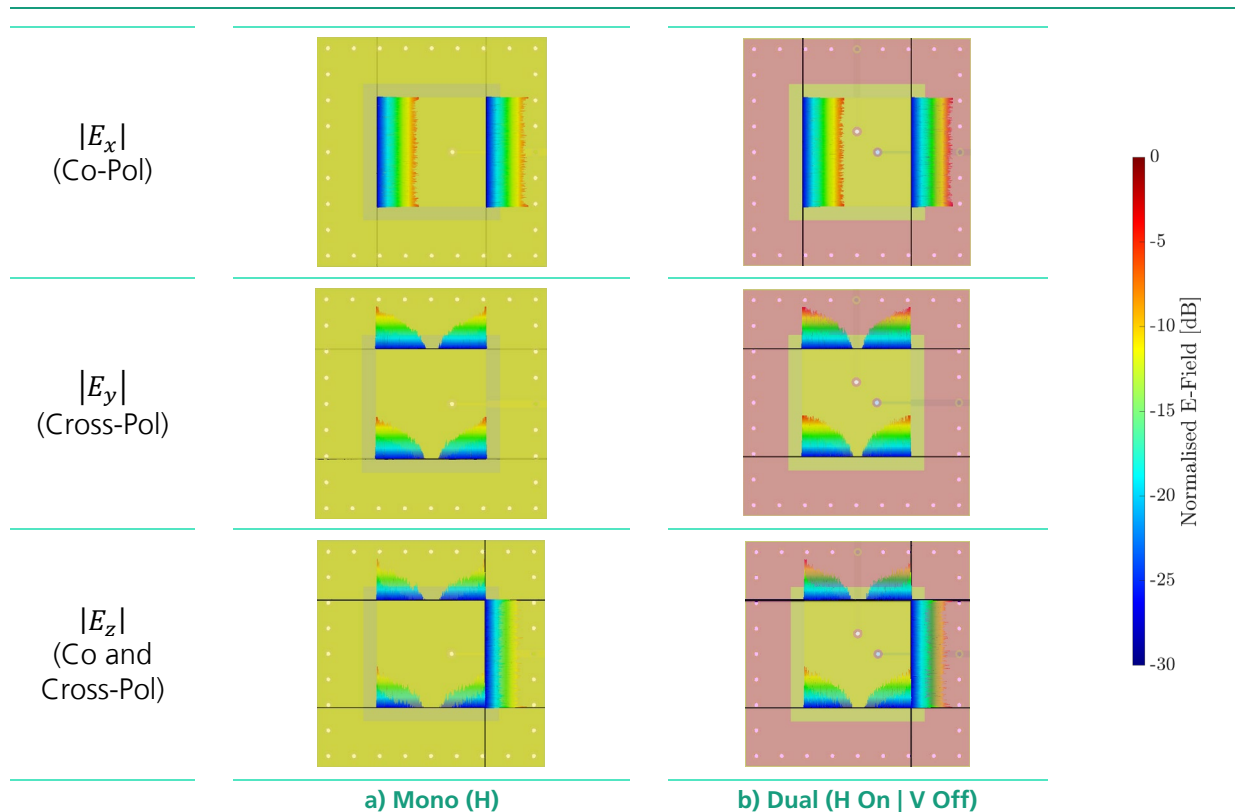


Table 3.11 – E-Field Carpet Comparison for H-Pol (CST MWS FD)

In Table 3.11 the carpet visualization from CST MWS has been used. By setting cutting planes around the patch laterals, the amplitude field distribution of the fields within the planes is orthogonally represented. Due to limitations of the software it was not possible to change orientation of the distributions, as they were always shown in the right and vertical orientations

orthogonal to the defined planes. Nonetheless, the carpet representation combined with the phase distribution in Table 3.12 matches the traditional representation of the fringing fields [43, 53, 54] shown in Figure 3-24.4

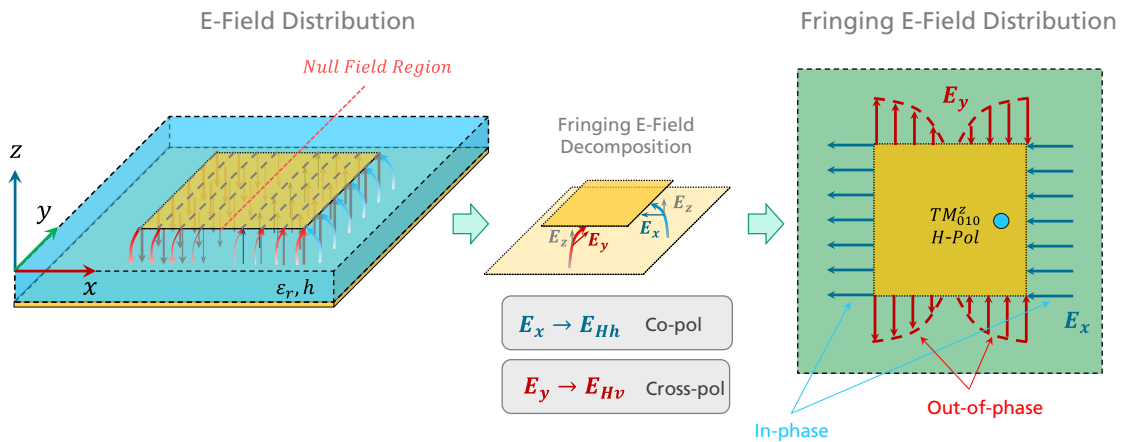


Figure 3-24 – E-Field Distributions and Fringing Fields Decomposition

To gain more physical insight, the phase of the fields using a contour plane is depicted in Table 3.12. To read the phase representation properly, it is required to look at the phase between the patch and the upper ground. Within conducting surfaces, the tangent E-Field is ideally null and therefore, in the phase results, a blurred phase distribution appears.

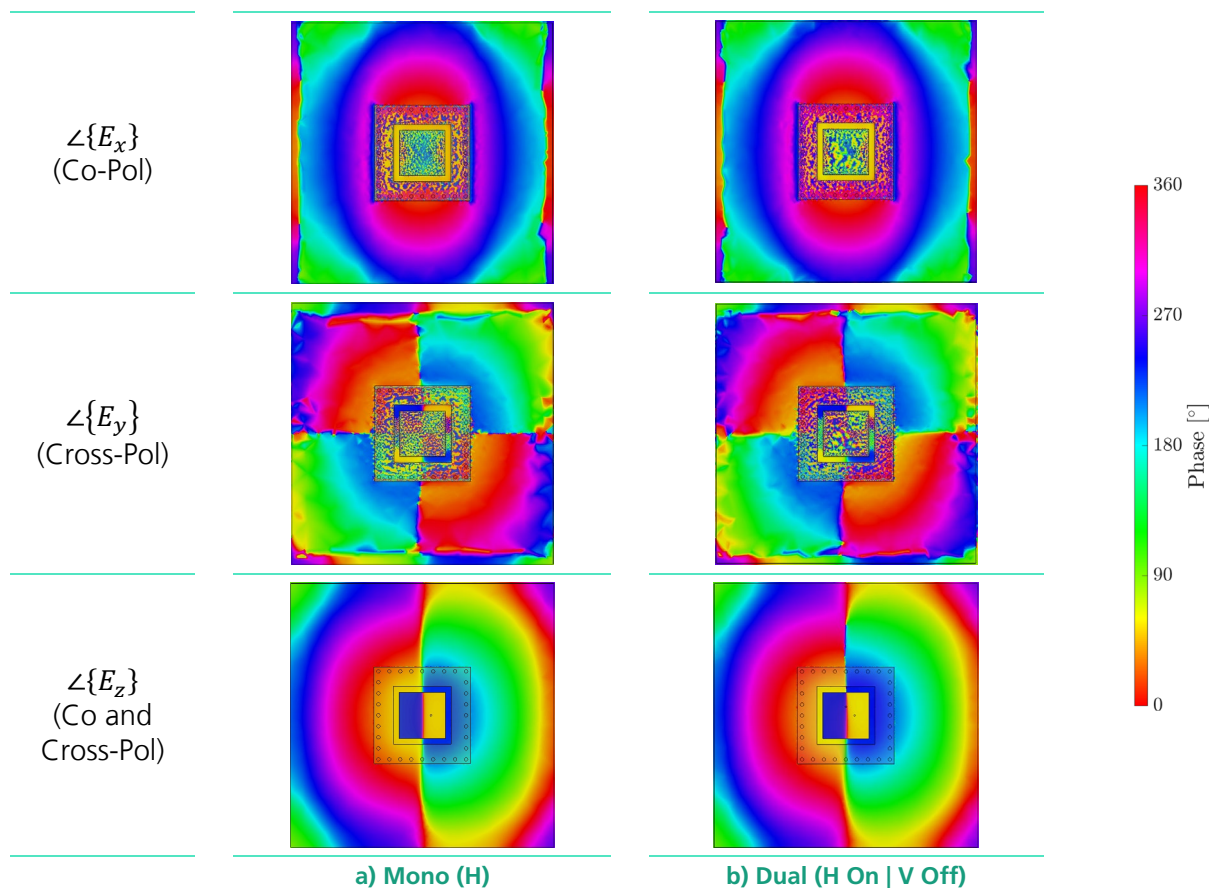


Table 3.12 – E-Field Phase Contour Comparison for H-Pol (CST MWS FD)

For E_x and E_y (the real physical sources of radiation) it can be seen that E_x is in-phase, while E_y , the cross-pol associated field, has four quadrants being about the two symmetry axes out-of-phase. For the E_z phase¹⁰, the same effect can be appreciated by applying the equivalent theorem as done in the cavity model (see Figure 3-9 and Figure 3-10).

Overall, the results from Table 3.11 and Table 3.12 show the influence of the fringing fields (E_x and E_y) as explained in subsection 3.2.1 through the physical interpretation. Instead, in the cavity model the E-Field is only assumed to be z-directed, which later on allow to apply the equivalence theorem and get the far-fields through a simplified model. Overall, the cavity model also matches with the E_z distribution and a secondary probe, does not seem to have an effect on the symmetry. From the E-Field magnitude and phase distribution, no major conclusions on polarimetric degradation can be extracted. For that, the surface currents on the patch shall be investigated, where patch asymmetry will actually have an impact on the \vec{J}_s .

As for the surface current distribution in Table 3.13, the y -directed component differs for the mono- and dual-polarized configurations. For the dual-polarized patch, $|J_y|$ appears to lose symmetry in magnitude thus, increasing the radiated cross-polarization component due to imperfect cancellation of the cross-polarized terms of the radiated far-fields at broadside.

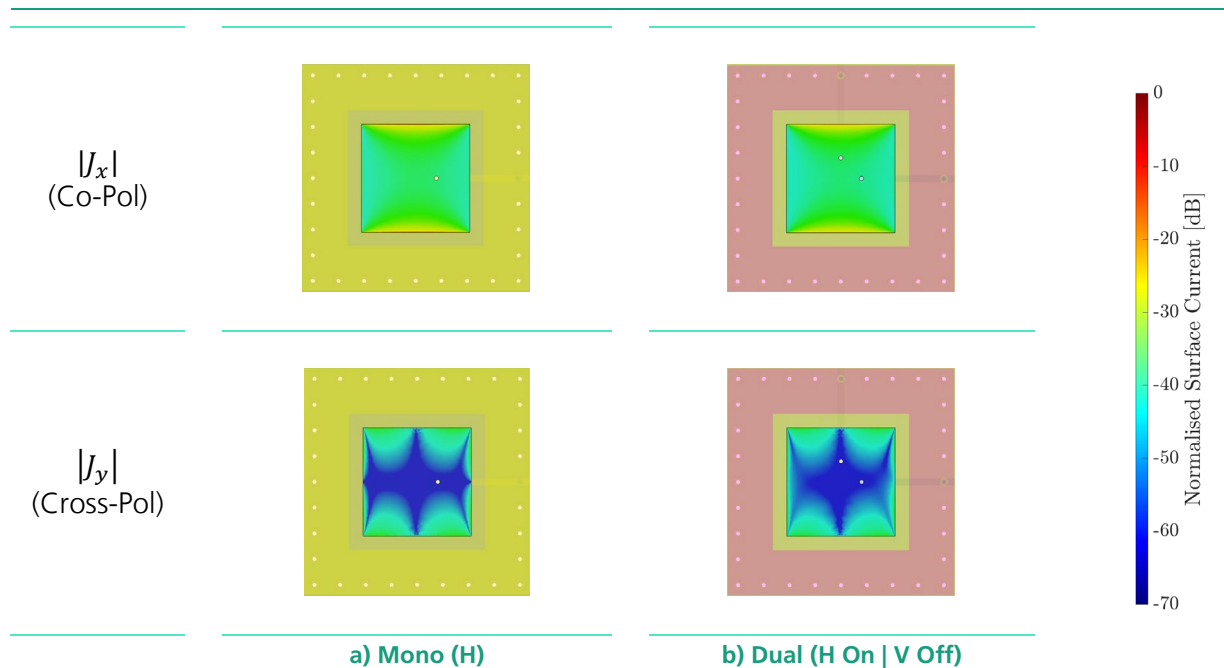


Table 3.13 – Magnitude Surface Currents Comparison for H-Pol (CST MWS FD)

As done for the E-Field, the phase performance in Table 3.14 is also analyzed to understand how the components combine at broadside and off-broadside. Again, in b) the lack of symmetry in $|J_y|$ justifies the polarimetric degradation.

¹⁰ The phase values are irrelevant as the port reference is set at the connector (see Table 3.10). The information relies on the 180° phase-shifts and the region where they take place.

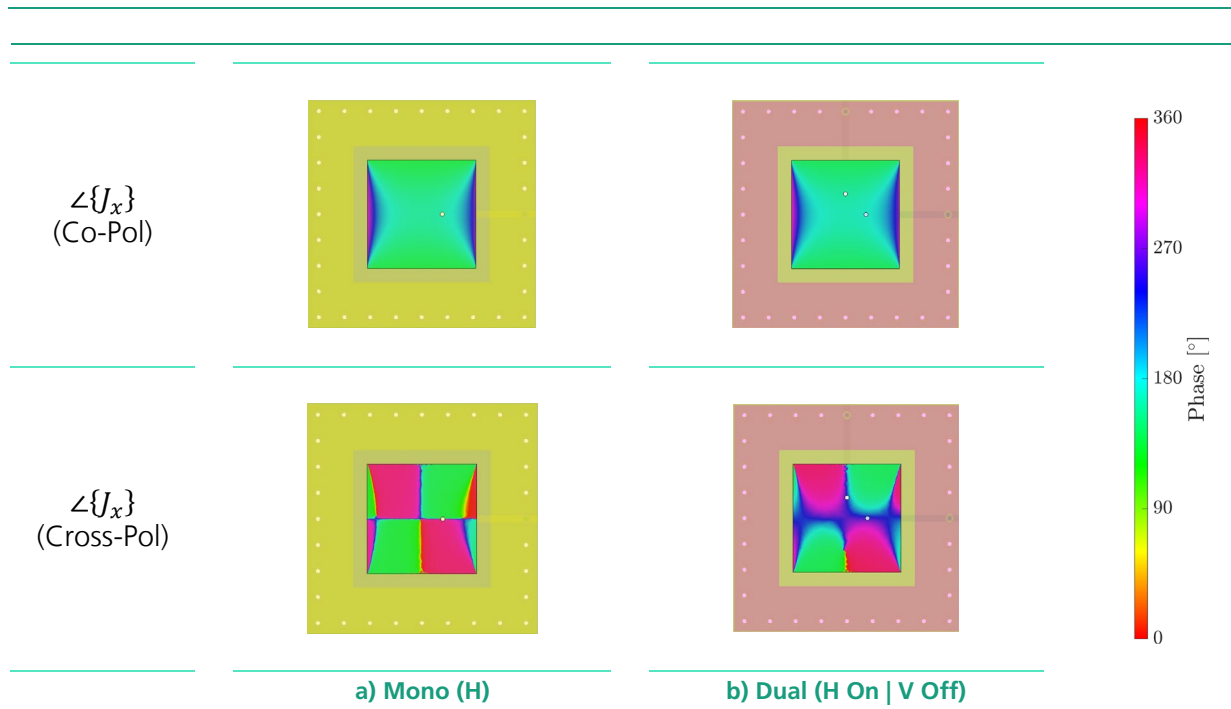
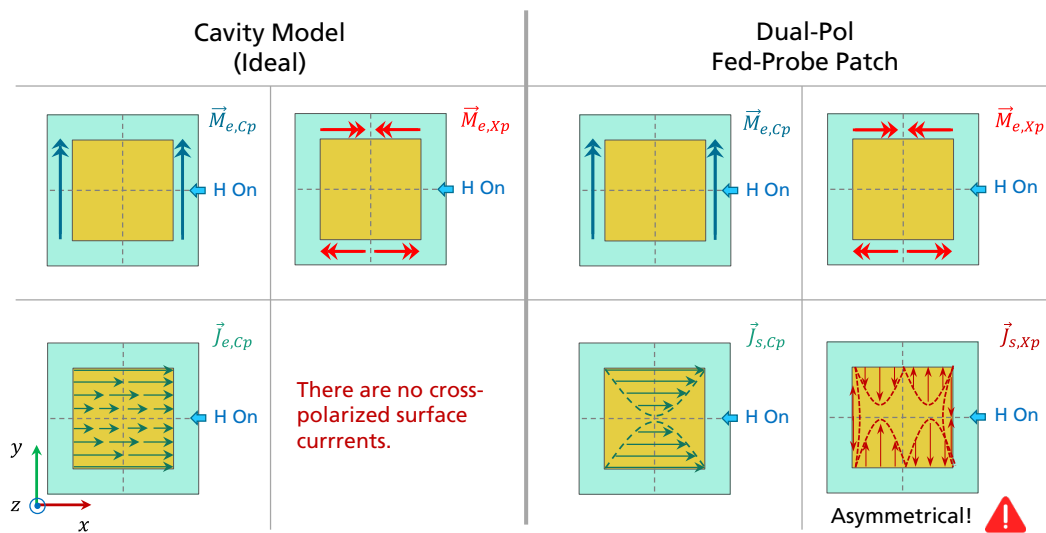


Table 3.14 – Phase Surface Currents Comparison for H-Pol (CST MWS FD)

In Table 3.13 and Table 3.14, it can be clearly seen that for the y -directed currents, the probes do have an impact on current distributions. In the mono-pol patch the asymmetry is minimal, but it in dual-pol one it is remarkable. This explains why at broadside there is an XPD degradation from 60 dB to 33 dB . Off-broadside, cross-polarization still takes place in the E and H planes, but being remarkable on the diagonal planes.



At broadside and in the main planes there is no cross-pol component ($XPD \rightarrow \infty$).

A second probe in the orthogonal cross-section allows to provide dual-pol features.

But it has a dramatic impact on the surface currents distributions, specially on the $\vec{J}_{s,xp}$, which will generate a residual cross-pol component at broadside and in the main planes!

Figure 3-25 – Cavity Model and Dual-pol Probe-fed Patch Antenna Comparison for H-Pol

Note that both in the E-Field and the \vec{J}_s there are four regions with mirrored phase for the cross-polarized components. This will generate the appearance of four lobes with diagonally mirrored phases in the cross-polarization pattern (see Table 3.17). This explains the physical cross-pol cancellation at broadside and in the principal planes, which for a dual-pol patch antenna is no longer ideal due to asymmetries in the \vec{J}_s .

3.5 Conclusions on the Dual-Pol Fed-Probe Patch Antenna Analysis

By reviewing the cavity model and including a feeding probe technique two polarimetric sources have been detected. The first one arises from the intrinsic cavity field distribution of the TM_{010}^z (1), where non-radiating slots cancel ideally at broadside (see Figure 3-13). With the introduction of a probe, asymmetry (2) is added to the patch antenna achieving still a finite **cross-polarization** cancellation at broadside $XPD_{mono} \approx 60 \text{ dB}$.

The antenna asymmetry effect (2) is increased even more when a second probe is added in the orthogonal cross-section. This added to the effect of probe coupling (3) and PPM propagation (4) are the sources of the \vec{J}_s distribution asymmetry. In a dual-pol probe-fed patch antenna the polarimetric performance is reduced significantly $XPD_{dual} \approx 33 \text{ dB}$ at broadside. In the D-Plane major polarimetric degradation can be observed when retrieving the simulated antenna patterns shown in Table 3.15. In there, asymmetries in the cross-polarization lobes can also be observed.

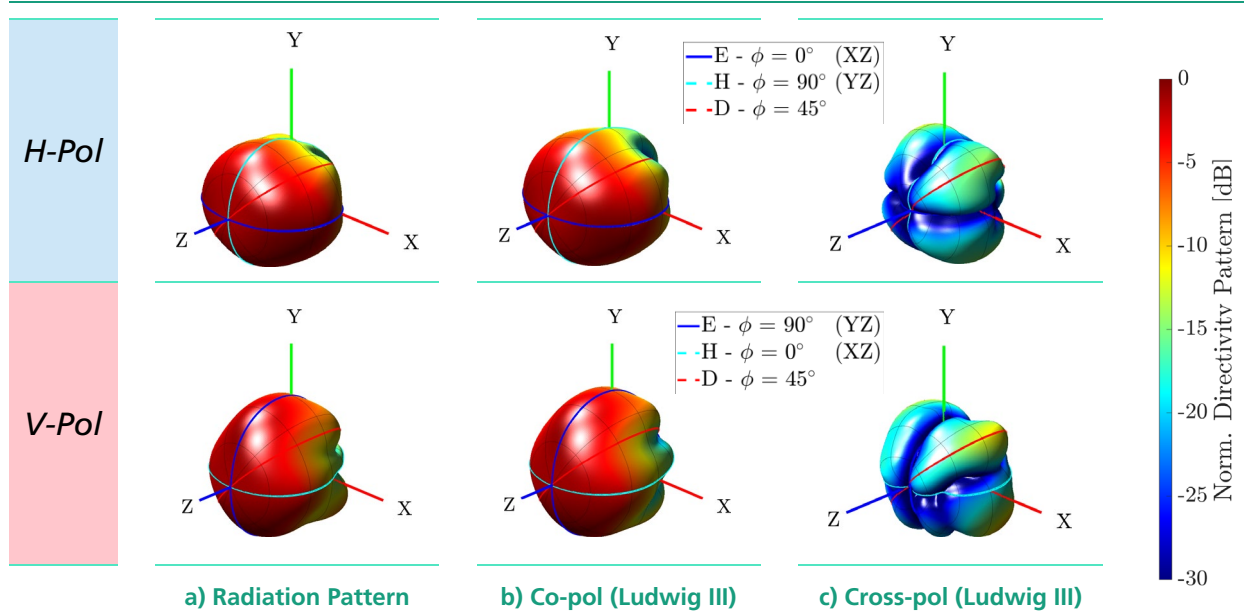


Table 3.15 – Far-field Magnitude Patterns for a Dual-pol Probe-fed Patch Antenna (CST MWS FD)

As for the radiated phase distribution, for the co-polarized component, the phase remains constant within the beam. Instead, for the cross-polarization four lobes out-of-phase with respect to the main planes appear. An effect predicted already due to the E-Field and \vec{J}_s cross-polar phase distributions.

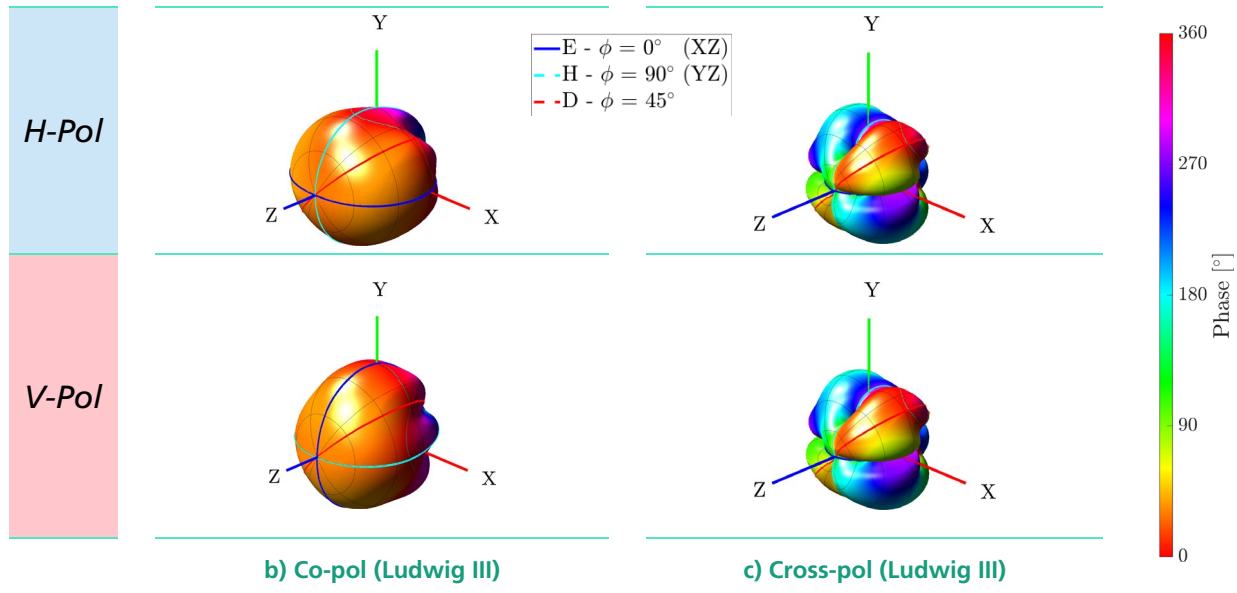


Table 3.16 – Far-field Phase Patterns for a Dual-pol Probe-fed Patch Antenna (CST MWS FD)

The polarimetric degradation is even more noticeable when comparing the cross-polarization patterns of a mono a dual polarized probe antenna. The fact that in Table 3.17 a) there is no full cancellation in the plane ZY is caused by the lateral asymmetries of \vec{J}_s (see table Table 3.13 and Table 3.14)

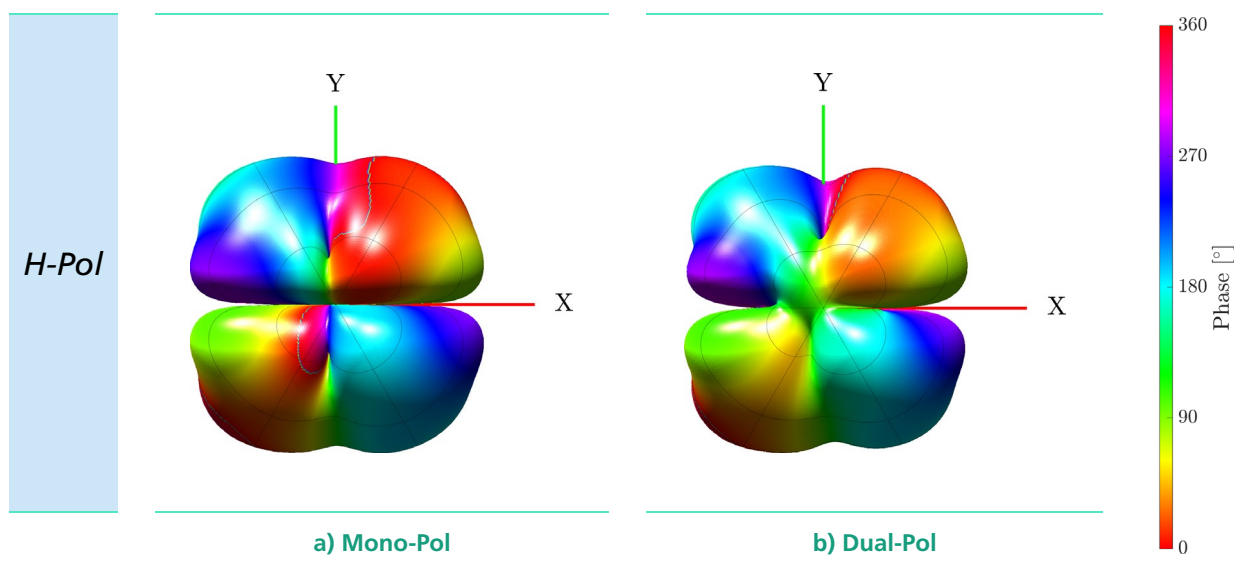


Table 3.17 – Far-field Phase Patterns for Mono and Dual-Pol Patch Comparison (CST MWS FD)

Chapter 4 - Sub-Array Design

This chapter is devoted to the conception and design of a dual-polarized patch-based AESA with **low-cross polarization** within an elevation scan range of $\pm 45^\circ$. Starting by the substrate choice, a system analysis is proposed by decoupling the antenna system requirements from the radiation and feeding standpoint

Based on an initial dual-pol probe-fed patch design, the unitary element is expanded to multiple sub-array topologies where a **feed rotation technique** provides suppression of the main cross-polar components and fulfills the **low-cost** requirement.

4.1 Substrate Choice and Unitary Element Design

Patch antennas assemblies benefit from current and low-cost PCB manufacturing. In this sense, choosing the right substrates of a multilayered design is one of the main steps for an effective planar antenna design. In this section, an overview of the most suitable substrates will be provided. Deriving the desired performance and taking into account major system requirements such as cost, a multi-layer structure is proposed. Due to the dual nature of antenna and integrated feeding network, the substrate assessment is logically divided into radiation and feeding stages (see Figure 4-1).

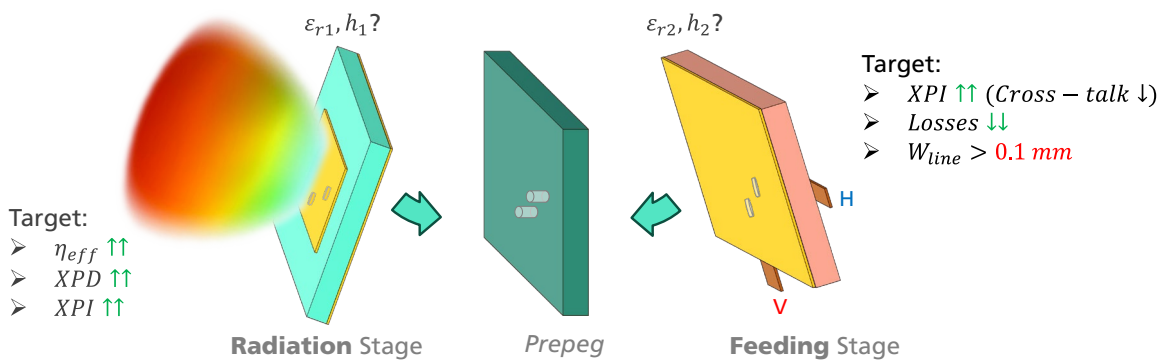


Figure 4-1 – Antenna Multilayer Decomposition

The main parameters driving the substrate choice are the *electric permittivity* (ϵ_r) and the available standard *substrate thicknesses* (h). There are secondary parameters that have an impact on the substrate performance, such as the *loss factor* (δ_{tan}), the metallization *conductivity* (σ_c) or the *thermal expansion coefficient* of expansion. High polarimetric performance and tighter tolerances increase the substrate cost.

4.1.1 Substrate Assessment for the Radiation Stage

As an initial guideline, low ϵ_r (\downarrow) substrates with printed circuitry will radiate more, whereas high ϵ_r (\uparrow) substrates will keep the field lines constrained within the circuit structure. As a consequence radiation of the printed lines is minimized [43] at the expense of increasing the *characteristic impedance* ($\uparrow Z_0$) or the *input impedance* ($\uparrow Z_{in}$) and consequently reducing the *line width* ($w \downarrow$).

In a patch antenna, low ϵ_r (\downarrow) is desired in order to maximize the *bandwidth* ($BW \uparrow$) and radiation efficiency ($\eta_{rad} \uparrow$), consequently increasing the *patch size* ($L \uparrow$). The increase of L extends the fringing fields, which enhance the radiation and justifies the efficiency increase ($\eta_{rad} \uparrow$). In [55], increasing ϵ_r (\uparrow) was reported to increase the E-H pattern asymmetry, thus increasing the *cross-polarization discrimination* ($XPD \downarrow$). Nonetheless, from an array perspective, the increase in the patch size ($L \uparrow$) results in an increase of coupling between elements ($XPI \downarrow$, $XPD \downarrow$), whose spacing (d_x, d_y) is a fixed parameter defined from center to center of patches.

On the other hand, a greater h (\uparrow) is mainly related to an increase of bandwidth ($BW \uparrow$) but also to a decrease of η_{eff} (\downarrow) due to the appearance of surface waves. If vias are used to suppress SW, increasing h (\uparrow) also extends the fringing fields having a minimal impact on the η_{eff} . Moreover thin substrates ($h \downarrow$) will perform as those with ϵ_r (\uparrow) with the associated consequences, (L , $XPD \downarrow$), with a remarkable increase of the conductor losses ($\alpha_{cond} \uparrow$) and η_{eff} (\downarrow). The relationship between h , ϵ_r and η_{eff} is summarized in Figure 4-2.

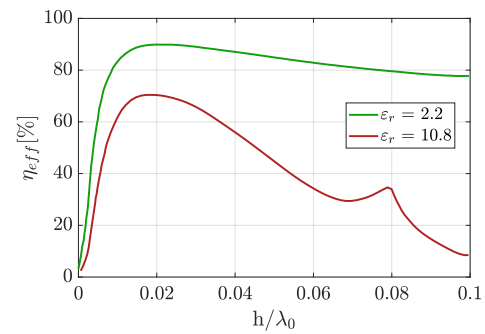


Figure 4-2 – Measured Radiation Efficiency for a Rectangular Patch Antenna

In the cavity of the patch antenna, the main losses [41] will be caused by the *dielectric loss* (P_d , δ), the *conductor loss* (P_c , σ) and surface waves if excited by the feeding technique. Together with *radiated power* (P_{rad}), their definitions are:

$$P_d = \frac{\omega \epsilon_r \delta_{tan}}{2} \iiint_V |E_z|^2 dv \quad \text{Eq. 4.1}$$

$$P_c = R_s \iint_S |\vec{H}|^2 ds \quad R_s = \sqrt{\frac{\omega \mu_0}{2\sigma}} \quad \text{Eq. 4.2}$$

$$P_{rad} = \frac{1}{4\eta_0} \int_0^{2\pi} \int_0^\pi |\vec{E}|^2 r^2 \sin \theta d\theta d\phi \quad \text{Eq. 4.3}$$

Final Substrate Recommendation (Radiation Stage)

Overall, a desired substrate for the radiating stage should have a ϵ_r of 2..3 with h/λ_0 not exceeding 0.08 [53]. To minimize losses, δ should tend to zero and σ_c should be as high as possible. Additionally via element fences shall be used to suppress surface waves. Using the previous recommendations, a η_{rad} around 75 to 85% should be achieved. As for the bandwidth, based on the narrowband performance of probe-fed patch antennas, lower ϵ_r and greater h would be preferred to compensate for the bandwidth loss due to the capacitive effect in-between the probe and ground hole.

4.1.2 Substrate Assessment for the Feeding Stage

Due to the low-cost constraints, the feeding network was to be synthesized with microstrip transmission lines to avoid the usage of buried bias and additional layers (see more in Figure 4-5). This choice constrained the substrate for the feeding stage to the one minimizing the radiation losses. This primary objective arose from the need to isolate orthogonal feeding networks, or in other words, to suppress the cross-talk and maximize the *XPI*.

Substrate Considerations to Minimize Radiation

As indicated in the previous section, to suppress radiation, a substrate with high ϵ_r is desired. This increases the concentration of energy within the substrate [56], strongly bounding the fields of the planar transmission line to the ground, thereby reducing *radiation losses* ($\alpha_{rad} \downarrow$) and cross-talk to adjacent structures (see Figure 4-3).

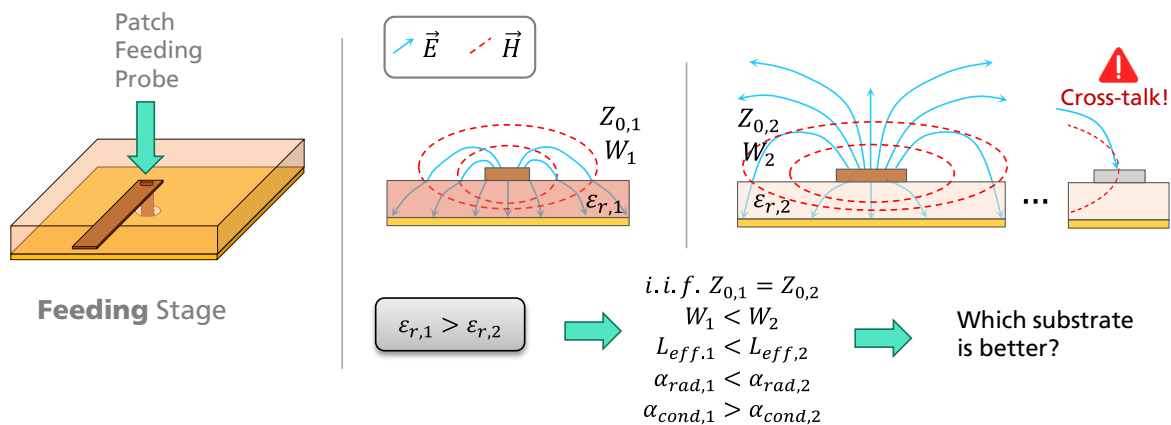


Figure 4-3 – Substrate Effect on Microstrip Lines

On the other hand, synthesizing the same *characteristic impedance* (Z_0) decreases the *line width* (w) as well as the *effective wavelength* (λ_{eff}). The minimization of w is critical for values smaller than 0.1 mm for manufacturing concerns.

Fixed Parameters		Required w to synthesize a $Z_0 = 100\Omega$
$\epsilon_r = 2.2$	$h = 0.256 \text{ mm}$	$\sim 0.223 \text{ mm}$
$\epsilon_r = 2.2$	$h = 0.508 \text{ mm}$	$\sim 0.455 \text{ mm}$
$\epsilon_r = 10.8$	$h = 0.256 \text{ mm}$	$\sim 0.029 \text{ mm} < 0.1 \text{ mm}$
$\epsilon_r = 10.8$	$h = 0.508 \text{ mm}$	$\sim 0.058 \text{ mm} < 0.1 \text{ mm}$

Table 4.1 – Microstripline Synthesis Examples

Other Considerations

As for the substrate height (h), thinner substrates ($h \downarrow$) are used to reduce the *radiation losses* ($\alpha_{rad} \downarrow$) [57]. As seen in Table 4.1, to synthesize the same Z_0 , if $h(\uparrow)$, then $w(\uparrow)$ increases. For very wide lines $w(\uparrow)$, $\alpha_{rad}(\uparrow)$ is dominant, while for extremely thin ones $w(\downarrow)$, *conductivity losses* ($\alpha_c \uparrow$) is remarkable if $\sigma(\downarrow)$. However, as it will be seen in Chapter 5 convoluted meandering and discontinuities within the microstrip feed network are to be avoided to minimize α_{rad} .

Final Substrate Recommendation (Radiation Stage)

Since the patch antenna was chosen to be matched at 100Ω , in order to be able to synthesize Z_0 while minimizing radiation an ϵ_r of 4.6 is addressable. The substrate height should be as thin as possible ($h \downarrow$), bearing in mind the manufacturing constraint of $w > 0.1\text{mm}$, if and only if, the conductivity of the metallization is high enough ($\sigma_c \uparrow$, $\alpha_c \downarrow$). Moreover, *dielectric losses* (α_d) can be reduced by selecting a high performing substrate with low *loss factor* ($\delta \downarrow$).

4.1.3 Proposed Substrate Choice

Despite all the previous concerns, from a system design perspective, the multilayer design has been chosen desired to be symmetrical to minimize *delamination* arising from different thermal expansion coefficients. This severely constrained the substrate choice, limiting the choice to the same substrate and height for both the *radiation* and *feeding stages*.

In sub-section 3.3.2 two possible topologies for probe-fed patches have been already presented (see Figure 3-15), arguing that an FR-4 core layer (prepeg) would be suitable for a low-cost application. Such multi-layer topology is revisited in Figure 4-4.

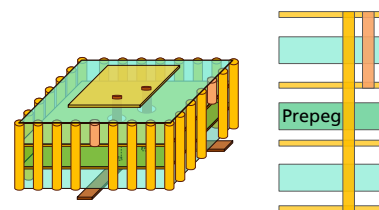


Figure 4-4 – Proposed Symmetric Multi-layer PCB for Dual-pol Probe-fed Patch Antennas

In this context, the substrate Rogers 4350B ($\epsilon_r = 3.66$) with a thickness of $h = 0.508 \text{ mm}$ was found to provide the best trade-off for the electromagnetic requirements of both stages. The low tolerances and the low loss performance comes at reasonable cost. This substrate is being often used in other fields such as automotive radars and other high-tech printed circuit applications.

For the prepreg separating the patch antenna from the feeding network, a FR4 core comprised of two layers of 0.80 mm has been selected. The low cost and minor relevance on the antenna radiation performance were the main reasons for this choice. Moreover, the high losses of this prepreg, effectively attenuate the PPM radiation arising from the probe feeding.

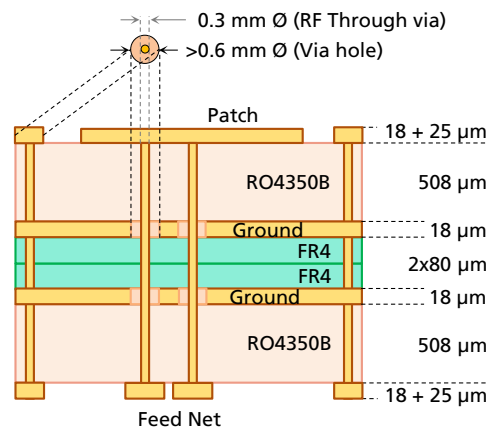
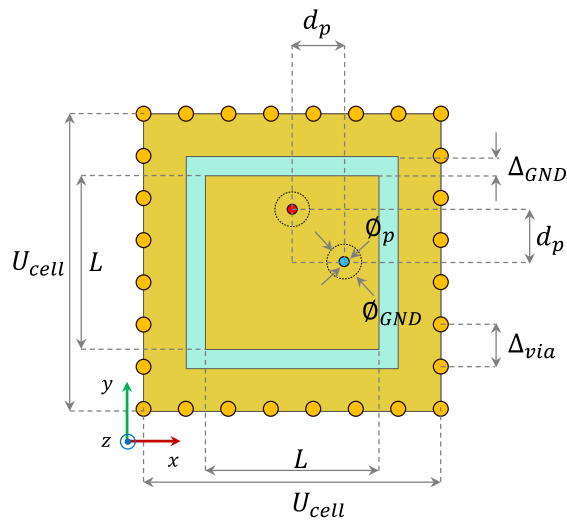


Figure 4-5 – Proposed Multilayer Layout

Having chosen the multi-layer structure and its substrates, a dual-pol probe-fed patch antenna has been designed with a Z_{REF} of 100Ω . The feeding line has a width of 0.205 mm to synthesize a characteristic impedance Z_0 equal to the *reference impedance* (Z_{REF}). The proposed topology is depicted in Figure 4-5.

4.1.4 Unitary Element Design

The design guidelines for the unitary dual-pol probe-fed patch antenna can be found in [Appendix B](#), where a brief discussion on the most suitable EM solvers for low cross-polarization is also provided. The resulting patch, simulated using the *Frequency Domain* (FD) solver from CST MWS has the following dimensions:



U_{cell}	$15 \text{ mm} \approx \lambda_0/2$
L	7.8 mm
d_p	1.5 mm
ϕ_p	0.3 mm
ϕ_{GND}	0.7 mm
Δ_{GND}	1 mm
Δ_{via}	1.875 mm

Figure 4-6 – Unitary Cell Dimensions

The same patch has been simulated to compare the cavity model and support the cross-polarization assessment presented in sub-section 3.4, where 33 dB have been measured for the *XPD* and *XPI*. The unitary element has then been extended to a 2x2 and a 4x4 sub-array. Small tuning on the dimensions have been performed independently of feed rotation. The optimized updated dimensions to achieve matching at 9.41 GHz follow:

	Unitary – 1x1	Unitary – 2x2	Unitary – 4x4	Unitary – ∞
L	7.89 mm	7.91 mm	7.9 mm	7.93 mm
d_p	1.5 mm	1.5 mm	1.4 mm	1.4 mm
ϕ_{GND}	0.7 mm	0.95 mm	0.95 mm	0.95 mm

Table 4.2 – Updated Dimensions for Unitary Elements

For sub-arrays larger than 8x8, the unitary element can be assessed based on simulations with periodic boundary conditions, decreasing the required computational resources. Feed rotation techniques can be then applied for finite structures, since matching is not likely to be affected by this alteration of periodicity.

Nonetheless, in this work the maximum sub-array size has been constrained to a 4x4 sub-array due to the surface board constraint of the row feeding networks (see Figure 5-9). This initial sub-array has been used to validate cross-polarization suppression techniques and support future decisions in the WRAD project.

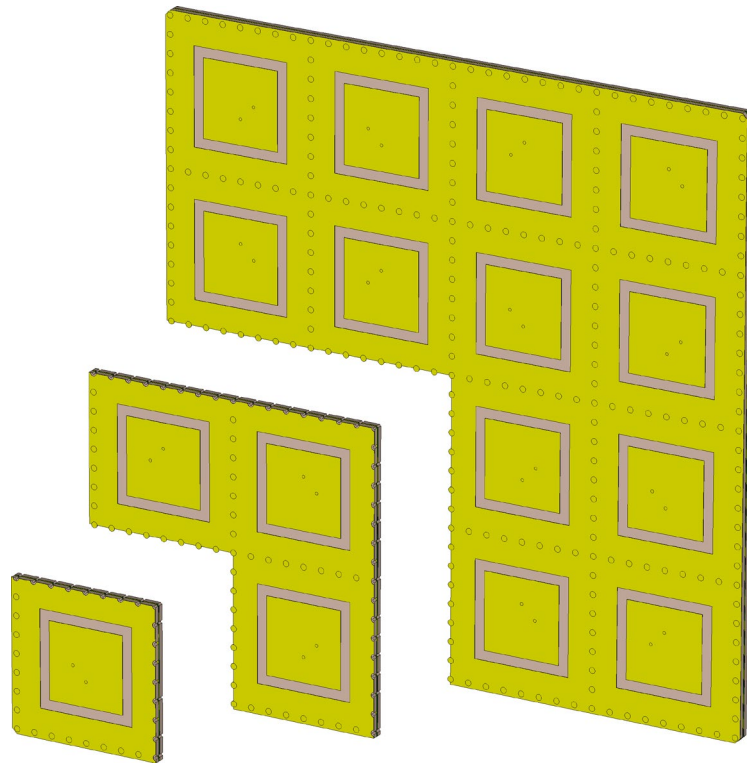


Figure 4-7 – Unit Cell Extension to Sub-Arrays

4.2 Baseline 2x2 Sub-Array

Based on the results of unitary element ($XPD \sim 30 \dots 35 \text{ dB}$) when extending the antenna element into an array structure, the polarimetric performance can reach critical values, thus compromising the XPD requirement for weather radar applications. Polarimetric degradation is expected due to the **coupling** effect among array elements, which will become even more remarkable when scanning. Similarly to the unit cell, Figure 4-8 shows the influence of coupling on the antenna plane and within the substrate.

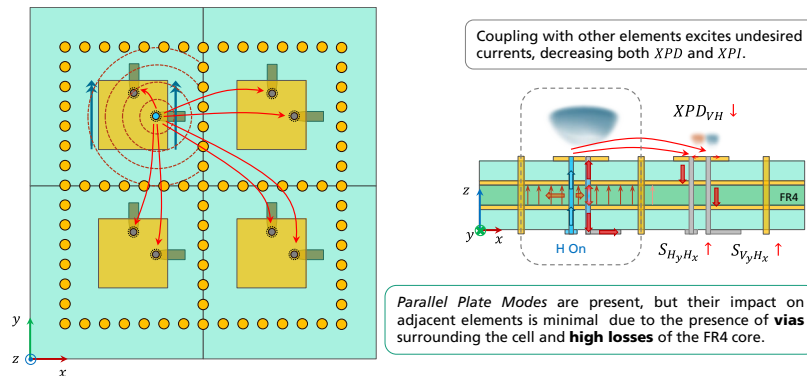


Figure 4-8 – Array Coupling Effect on Cross-polarization and Element Fencing

To mitigate the effect of coupling on the antenna plane, *elevated walls* surrounding the elements [58] could be used. However this technique is suitable for arrays designed to be vertically stacked and would impede integrating a rear feeding network behind the multi-layer antenna. In this context, an alternate solution consists of incorporating an upper ground plane as seen in Figure 4-9.

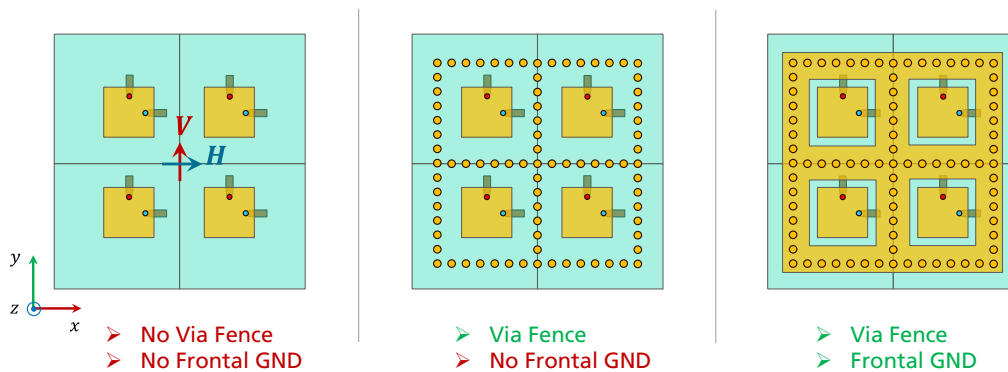
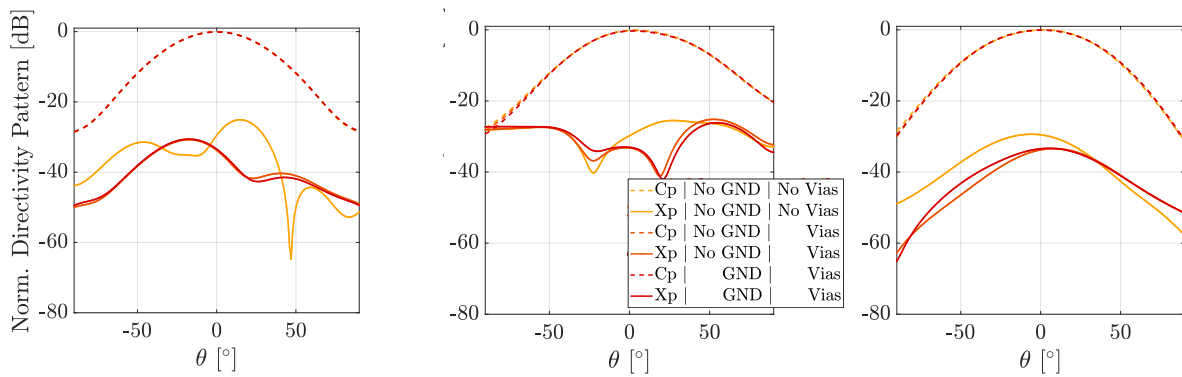


Figure 4-9 – 2x2 Baseline Coupling Mitigation Upgrades

The next step is to quantify the coupling mitigation by analyzing the polarimetric performance of the baseline 2x2 sub-array. In Table 4.3 the main pattern cuts are shown for a broadside scan using the V-pol, showing the co-pol (V) and cross-pol (H) components according to the Ludwig III definition.



a) H-Plane ($\phi = 0^\circ$)

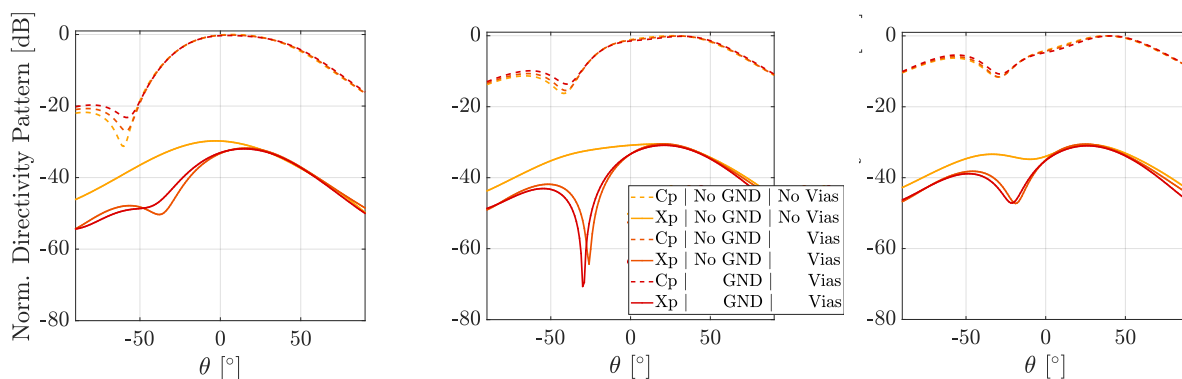
b) D-Plane ($\phi = 45^\circ$)

c) E-Plane ($\phi = 90^\circ$)

Table 4.3 – V-Pol, 2x2 Baseline Sub-arrays Broadside Comparison (CST MWS FD)

Adding a via element fence, does provide a 4 dB improvement in cross-pol (-29.5 to -33.5 dB), while the frontal ground does not provide any polarimetric enhancement. Nonetheless the ground addition allowed minimizing the frequency shift in the S-parameters due to a significant reduction of inter-element coupling. Thus, reducing the effort in tuning the patch size and the probe position.

The same cases depicted Figure 4-9 where analyzed under scanning situations, where port excitations were set to a nominal scan of $\theta_{ns} = 15^\circ, 30^\circ$ and 45° in contrast with the real scanning angle (θ_{rs}). The progressive phase-shift from row to row (starting from upper rows) was computed using Eq. 2.6, leading to $\beta_y \approx -44^\circ, -84^\circ$ and -120° respectively. In Table 4.4, the E-Plane for V-Pol ($\phi = 90^\circ$) cut is depicted, since it contains the steered beam in elevation¹¹.



a) $\theta_{sn} = 15^\circ \mid \theta_{sr} \approx 5.7^\circ$

b) $\theta_{sn} = 30^\circ \mid \theta_{sr} \approx 27.32^\circ$

c) $\theta_{sn} = 30^\circ \mid \theta_{sr} \approx 38.40^\circ$

Table 4.4 – V-Pol, 2x2 Baseline Sub-arrays Scanning Comparison (CST MWS FD)

¹¹ As discussed in section 2.6, the reference system is not suitable to obtain the main pattern cuts under scanning conditions. The H-Plane for the V-Pol patch sub-array does not have a fixed θ and ϕ and its extraction requires interpolating pattern values due to the angular resolution of the simulations (set to $\Delta\theta = \Delta\phi = 1^\circ$). The proposed alternative in this thesis is the usage of the 2D UV pattern, where the polarimetric performance of the entire beam can be easily analyzed.

Two main effects can be observed in the plots of Table 4.4, the difference between actual and nominal scanning angles, and the cross-polarimetric degradation.

The scanning angle mismatch is related to the small size of the array, as the pattern will be largely contributed by the unit element and not by the array factor. On the other hand, the polarimetric degradation is inherent for off-broadside directions in patch antennas. A summary of both effects follows for the three analyzed cases follows

		No Via Fence				Via Fence			
		0°	15°	30°	45°	0°	15°	30°	45°
Nom. Scanning (θ_{sn})	[°]	0°	15°	30°	45°	0°	15°	30°	45°
Real Scanning (θ_{sr})	[°]	0°	7°	27°	38°	0°	5°	30°	39°
$XPD^V(\theta_{sr}, \phi = 90^\circ)$	[dB]	29.12	30	30.9	31.3	33.5	32.2	31	31.6

Table 4.5 – V-Pol, 2x2 Baseline Sub-arrays Scanning Summary (CST MWS FD)

As seen in Table 4.5, the simulated polarimetric performance¹² with ideal ports is already critical for a 2x2 sub-array. For this reason, a feed rotation technique was introduced to reduce the cross-polarization and reach XPD levels in excess of 40 dB in the $\pm 45^\circ$ elevation scanning range. This has been done to improve the expected polarimetric performance for an actual array with a rear feeding network.

4.2.1 Scanning Asymmetries

A part from the desired XPD , the array should also provide similar radiation performance in both channels when scanning in elevation. This desired requirement be hardly achieved due to the asymmetric nature of the array. In fact, for each polarization, the antenna elements will be coupled in a different way as depicted in Figure 4-10, where idealized magnetic dipoles will couple differently by the H and V polarizations.

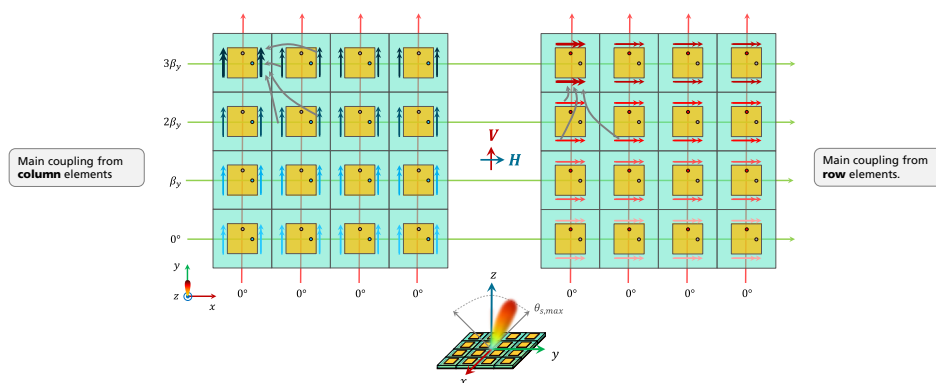


Figure 4-10 – Intrinsic Element Coupling Asymmetries in Elevation Scanning

The orthogonality of the H and V equivalent magnetic dipoles minimizes the polarization leakage between polarizations, allowing to reach XPD and of XPI values over 35 dB. However, for isolations of co-polarized adjacent elements within an elevation scan will be different, leading to different active S-parameters, patterns and thus, generating a polarimetric imbalance.

¹² Values for isolation between H and V ports are not provided since no feeding network was included.

4.2.2 XPD Diagrams for 2x2 Baseline Sub-Array with Ideal Ports

In order to assess such antenna performance (i.e. *polarimetric imbalance*), the usage of the UV pattern is proposed. Despite the visual simplification that 1D pattern cuts provide, it is also relevant to analyze the entire 3D pattern. Moreover, for a weather application, where targets are volumetric, it is also pertinent to assess the polarimetric performance within the main beam. Overall, the UV pattern, a 2D projection of the spherical pattern, was found to be a great tool to assess the ongoing antenna designs.

For instance, in Table 4.6 the UV XPD diagrams for an ideal 2x2 baseline sub-array are shown. Combined information of the radiation pattern is also provided through the -3 dB and -6 dB beamwidths contour lines. To enhance the polarimetric visualization, contour lines containing XPD values over 30 and 40 dB were included in black and white respectively.

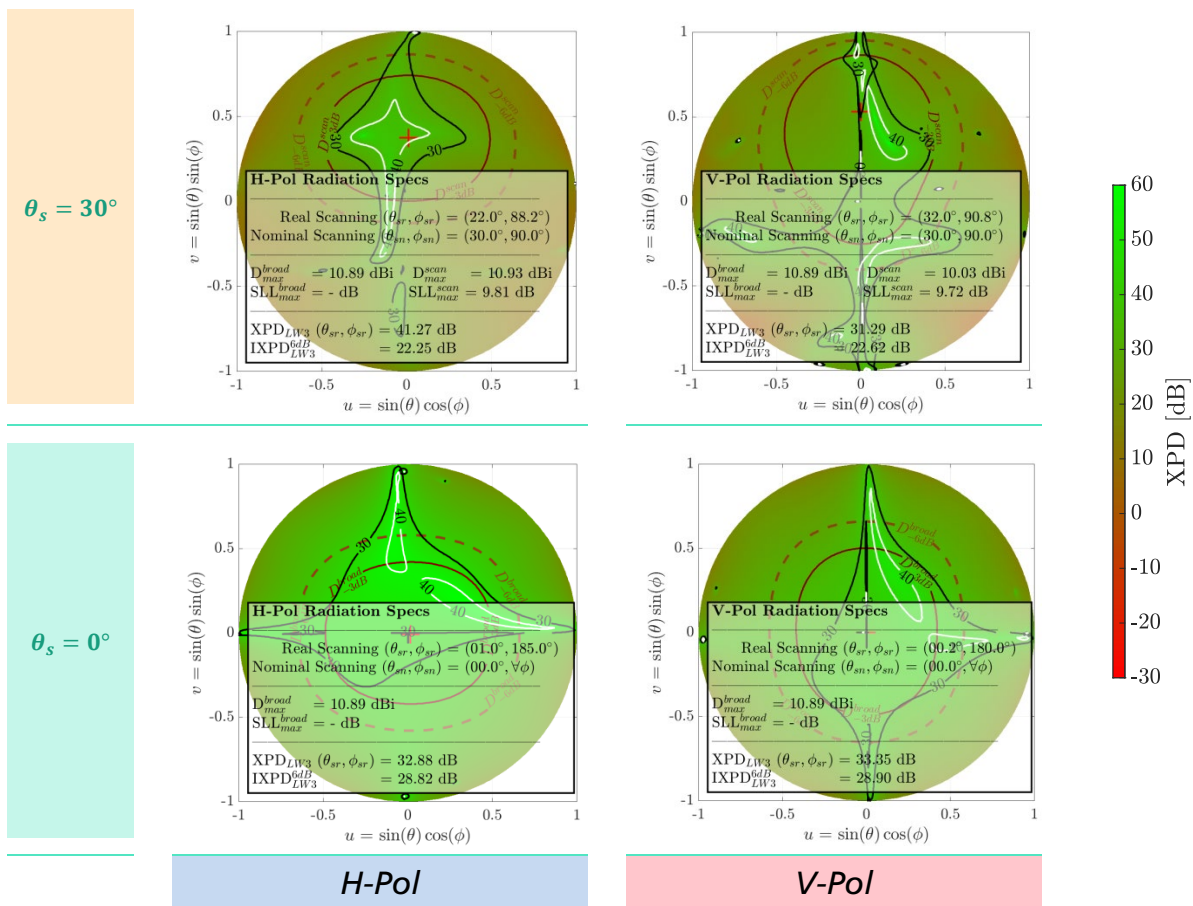


Table 4.6 – UV XPD Diagrams for 2x2 Baseline Sub-Array

Through the UV XPD pattern it can already be noted that the scanning performance in elevation is not the same for each polarization. While for broadside the H and V patterns are simply its rotated version for the Ludwig III definition, for other scanning elevation angles this will not be true, due to the scanning asymmetries augmented by different coupling mechanisms of the dual-pol probe-fed patch antenna.

4.3 Feed Rotation

Exploiting the patch antenna design versatility, the probe can also be mirrored and positioned towards the opposite edge. Given a 180° phase compensation for the mirrored feeds, the feed rotation technique mitigates the effects of patch asymmetries at an array radiation level. Available imaged combinations are extensively discussed by [35] and [59], where it is also argued that as a trade-off, stronger sidelobes are to be expected.

To understand this technique without using the formulation of *odd* and *even field decomposition* (as done in [35]), it is proposed to constrain the analysis to the currents and fields distributions on the patch, paying special attention to the phase distribution. In this way, the patch asymmetries can be clearly linked to the cross-polarization generation and therefore harness the benefits of the anti-symmetry that feed rotation provides.

4.3.1 Mono-Pol Patch Feed Imaging

An initial step to understand the implications of feed imaging is by showing the \vec{E}_{FF} components in the main planes (E, H and D). Additionally, supported by the cavity model discussed in section 3.2, the \vec{M}_{eq} can also be shown. The imaging effect can be graphically described as follows

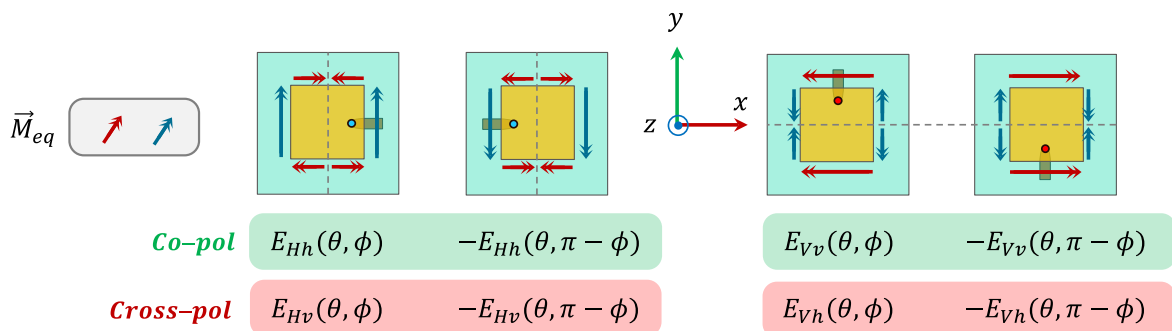


Figure 4-11 – Feed Imaging for Mono-pol Patch Antennas

For mono-pol patch antennas the imaging effect on the radiated fields is obvious as there is only one source of cross-polarization, the TM_{010}^z mode, and the orthogonally distributed currents (see Table 3.11 and Table 3.13). Overall, the great asymmetry in magnitude and phase of the fields and currents generate a cancellation in the E-Plane (at and off-broadside) and the H-Plane (only at broadside). In contrast, in the D-Plane the increase of cross-polarization levels follows the geometric combination (no longer destructive).

4.3.2 Dual-Pol Patch Feed Rotation

For a dual-pol probe-fed antenna, the previous simplified analysis is no longer valid. The addition of an orthogonal probe, brings new cross-polarization sources and more asymmetries to the patch. At an array level, combining the imaged structures without phase compensation will cancel the co-polar component. For this reason, a 180° phase shift on the imaged feeds is required to achieve the intended effect (cross-polar component cancellation).

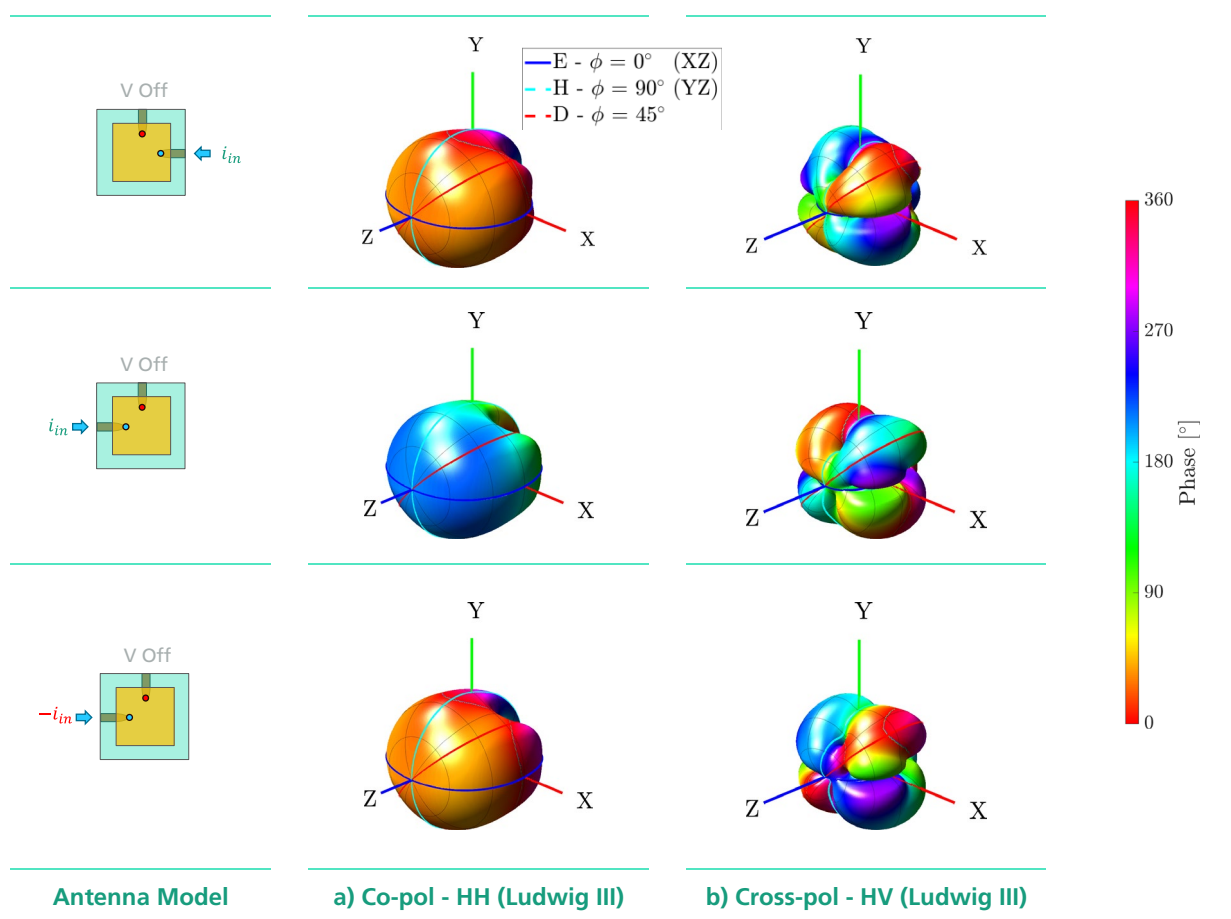


Table 4.7 – H-Pol, Far Field Phase Patterns for Imaged Feeds

Taking as a reference the H-polarized dual-pol patch antenna with the H-feed on the right and the V-feed on the top, *Woelders and Granholm* in [35] provide the following assumption for H and V polarized fields:

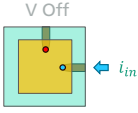
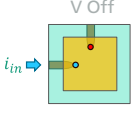
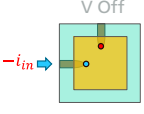
	Input Phase-Shift		
Non-Imaged (H-Pol)	$\varphi_0 = 0^\circ$		$\vec{E}_H(\theta, \phi) = \begin{Bmatrix} E_{H-cp}(\theta, \phi) \\ E_{H-xp}(\theta, \phi) \end{Bmatrix} \triangleq$ $= \begin{Bmatrix} E_{Hh}(\theta, \phi) \\ E_{Hv}(\theta, \phi) \end{Bmatrix}$
H-Imaged (H-Pol)	$\varphi_0 = 0^\circ$		$\vec{E}_{H,2}(\theta, \phi) = -\vec{E}_H(\theta, \pi - \phi) =$ $= \begin{Bmatrix} -E_{Hh}(\theta, \pi - \phi) \\ -E_{Hv}(\theta, \pi - \phi) \end{Bmatrix}$
H-Imaged (H-Pol)	$\varphi_0 = 180^\circ$		$\vec{E}_{H,3}(\theta, \phi) = \vec{E}_H(\theta, \pi - \phi) =$ $= \begin{Bmatrix} E_{Hh}(\theta, \pi - \phi) \\ E_{Hv}(\theta, \pi - \phi) \end{Bmatrix}$

Table 4.8 – H-Pol, Analytical Far Field Symmetries for H-polarised Dual-pol Patch (I)

Comparing the real model (Table 4.7) with the theoretical approach from Table 4.8, it can be observed that it holds for the co-pol component, but it does not for the cross-pol. At broadside ($\theta = 0, \forall \phi$) the phase for the non-imaged and H-imaged feeding with opposite input phase excitation is different (119.87° against 242.5°). However, the phase in the four cross-polar lobes agrees with the field symmetries proposed by the *cavity model* (see sections 3.2 and 3.4).

If the V feed is also imaged, a similar analytical approach follows

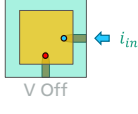
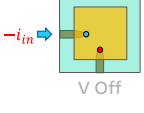
V-Imaged (H-Pol)	$\varphi_0 = 0^\circ$		$\vec{E}_{H,4}(\theta, \phi) = \vec{E}_H(\theta, \pi/2 - \phi) =$ $= \begin{Bmatrix} E_{Hh}(\theta, \pi/2 - \phi) \\ E_{Hv}(\theta, \pi/2 - \phi) \end{Bmatrix}$
H-Imaged V-Imaged (H-Pol)	$\varphi_0 = 180^\circ$		$\vec{E}_{H,5}(\theta, \phi) = \vec{E}_H(\theta, 3\pi/4 - \phi) =$ $= \begin{Bmatrix} E_{Hh}(\theta, 3\pi/4 - \phi) \\ E_{Hv}(\theta, 3\pi/2 - \phi) \end{Bmatrix}$

Table 4.9 – H-Pol, Analytical Far Field Symmetries for H-polarised Dual-pol Patch (II)

As done before, the cavity model can be compared with the real simulated fields, more specifically, using a dual-pol probe-fed patch. Based on the results from sub-section 3.4, the same conclusions are reached, the co-polar components agree with the theoretical model, but the cross-polar ones differ. At broadside, due to the appearance of a **residual cross-polar component** arising from asymmetries in the surface current distribution on the patch metallization, the polarimetric performance of probe-fed patch antennas is degraded, especially if a second probe is added, increasing even more the asymmetry of the cross-polarized \vec{J}_s .

Supported, by the *phase distribution of \vec{J}_s cross-polar* components and the resulting *cross-polar phase patterns*, Table 4.10 shows the impact of feed rotation and off-phase excitation. The phase distributions allow foreseeing a suppression of the residual cross-polarization term at broadside when combining the four rotated cases in an array.

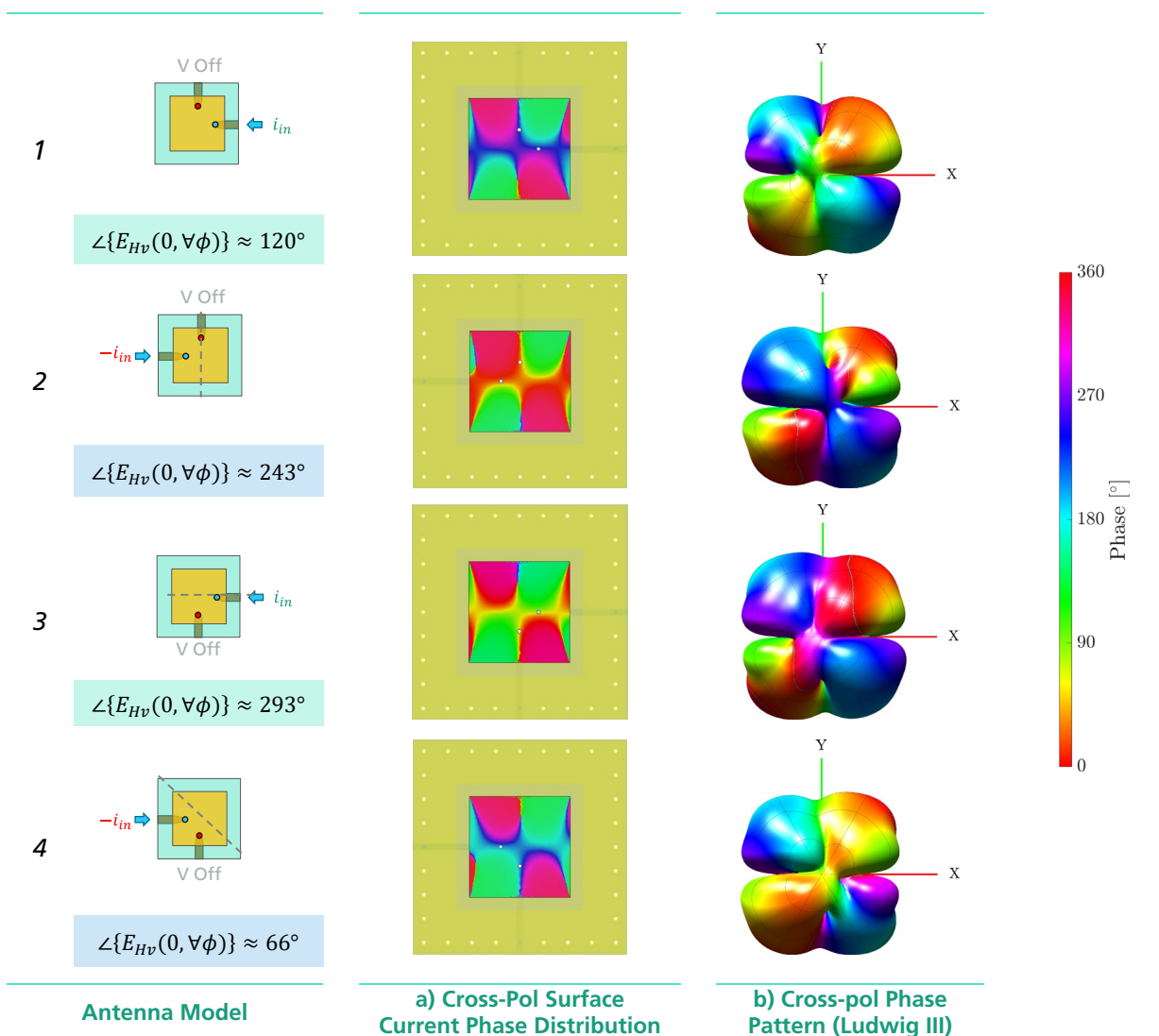


Table 4.10 – H-Pol, Far Field Phase Patterns for Imaged H-Polarized Dual-pol Probe-fed Antennas Comparison

The phase value at broadside of the cross-polarized E-field is also provided to justify later on the suppression mechanism, when extending the rotated antennas into sub-arrays.

4.3.3 2x2 Imaged Sub-Array

Combining rotated patch antennas and compensating the rotations with opposite-phase excitations allows a significant reduction of the cross-polarization for specific main planes [35, 54]. Meanwhile co-polarized fields are combined constructively, having no major impact in the radiation pattern. The suppression of residual cross-polarization terms (mainly due to asymmetries of cross-polarized \vec{J}_s) allows achieving great polarimetric performance and its application was found to be suitable to meet the weather radar requirements.

To analyze the performance of a feed rotated array, an original feed rotated arrangement from [35] was selected. Such topology is argued to provide cross-polarization suppression in the main planes, with the same performance for the H and V polarizations.

This is why, in order to ensure balanced polarimetric performance between H and V ports, the 2x2 array in Figure 4-12 is proposed.

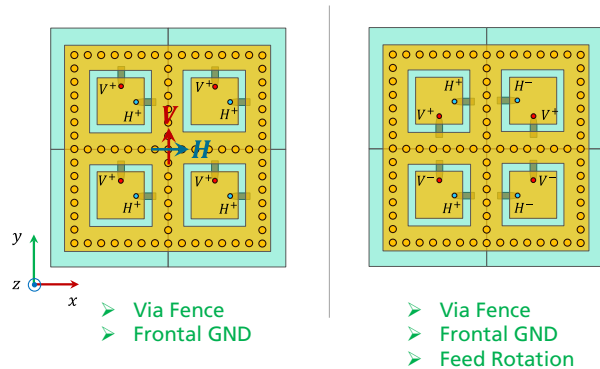


Figure 4-12 – 2x2 Baseline and Imaged Sub-arrays

To understand and provide the physical insight behind the cross-pol suppression, the cross-pol phase surface current distributions and phase patterns obtained in Table 4.10 are arranged as in Figure 4-13. Odd diagonal symmetries can be devised, already visualizing a cross-polar suppression between adjacent elements.

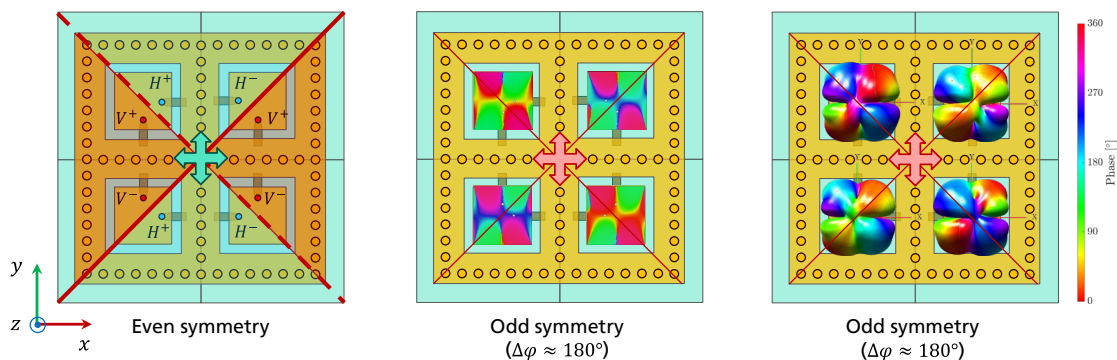


Figure 4-13 – H-Pol, 2x2 Imaged Sub-array and Phase Patterns

It is the diagonal anti-symmetry of the phases which allows suppression of the cross-polarization at the array level. For the proposed distribution, the cross-pol cancellation occurs at broadside and in the E and H plane cuts. Combining geometrically the patterns in Figure 4-13 according to phased array theory, Figure 4-14 is obtained, where at broadside, more than 60 dB of XPD are obtained, together with four main cross-polar lobes with odd symmetry with respect to the bisectors.

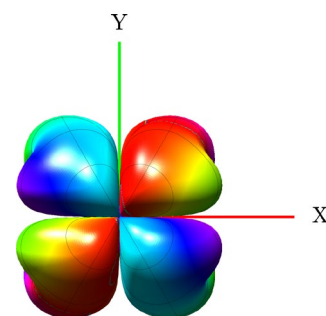


Figure 4-14 – H-Pol, 2x2 Imaged Sub-array Theoretically Phase Pattern

When comparing the analytically combined array pattern with the actual EM simulation, where coupling is considered, it can be observed that the cross-pol suppression is extended off-broadside, so to achieve XPD over 30 dB within the half power beamwidth.

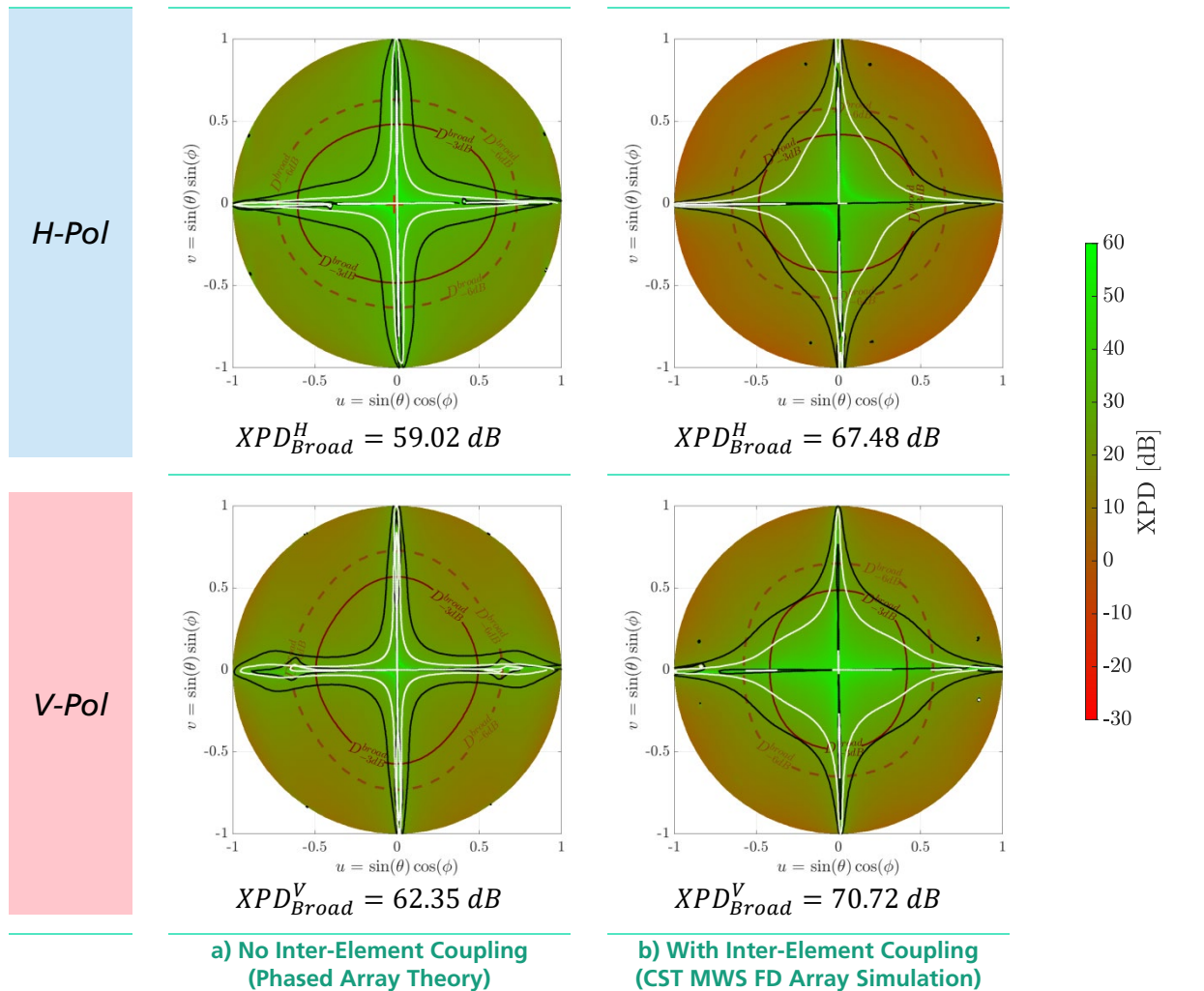


Table 4.11 – 2x2 Imaged Sub-array UV XPD Diagram Comparison at Broadside

The finite cross-pol suppression is caused by the fact that as depicted in Table 4.10, the phase at broadside is not exactly 180° between the bisectors. Nonetheless, as shown in Table 4.11, a 30.40 dB improvement is obtained with respect to the 2x2 baseline sub-array ($XPD_{Broad}^H \cong XPD_{Broad}^V \cong 32.9\text{ dB}$). Additionally, when taking into account the inter-element coupling, the proposed feed rotation technique appears to also mitigate the coupling effect and provide even better performance.

Nonetheless, the downside of the feed rotation technique is a slight additional increase of radiation imbalance between the H and V polarizations. At broadside, the patterns will no longer be a simple rotated version of one another, since there is no symmetry with respect to the main axis (XY) as shown in Figure 4-13. The fact that there is symmetry only at a bisector level (see Figure 4-13) will introduce notable polarimetric imbalances within the elevation scan. But still, as shown in Table 4.12, the XPD will be well off the required 30 dB , demonstrating its feasibility of the technique up to $\pm 45^\circ$ elevation scan.

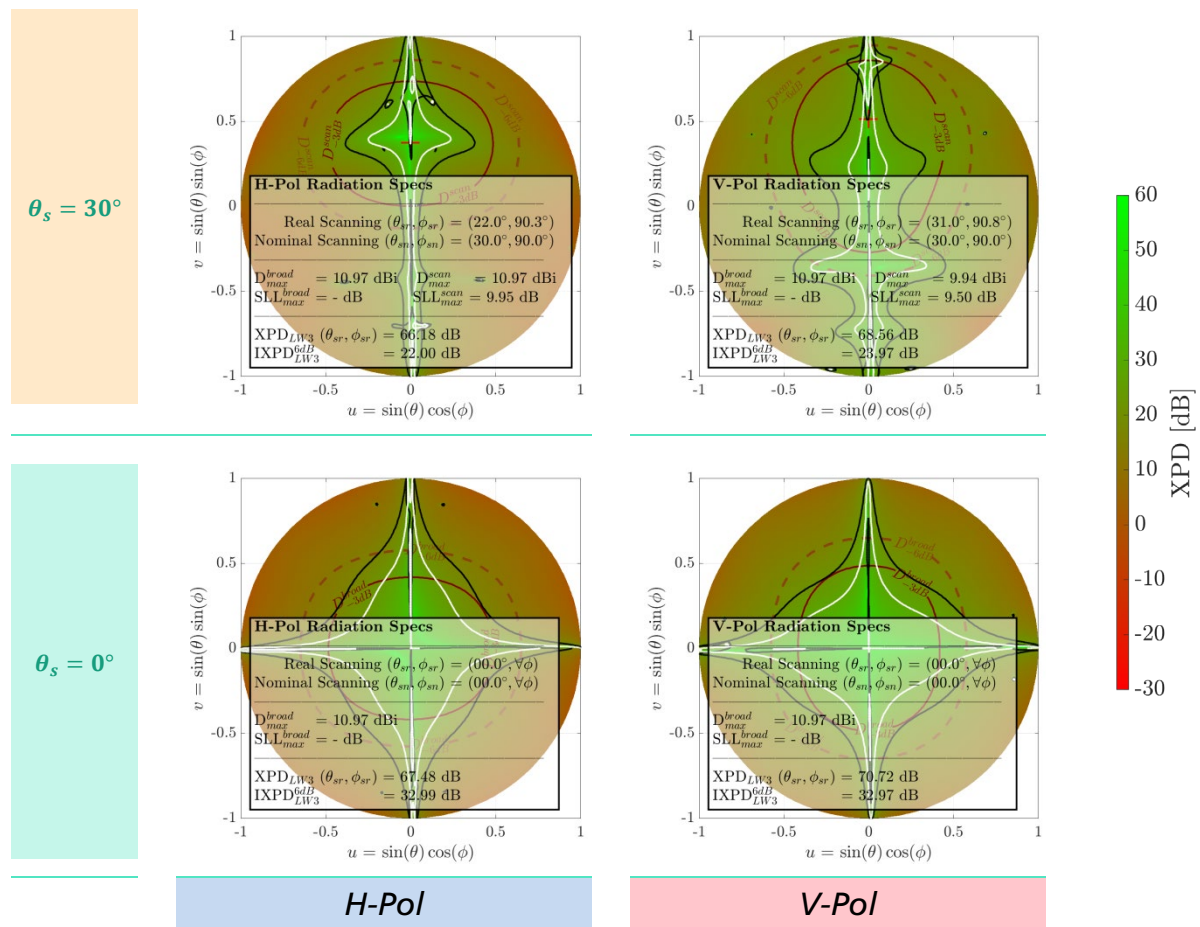


Table 4.12 – UV XPD Diagrams for 2x2 Imaged Sub-Array (Ideal Ports)

Overall, the proposed **feed rotation technique** has been demonstrated to be a powerful technique to improve the cross-polarization purity. Although polarimetric degradation is still present when canning in elevation, the cross-polarization suppression mechanism still takes place, allowing to achieve XPD values over 60 dB at the peak of the co-polar beam.

4.3.4 4x4 Imaged Sub-Array

Following the feed rotation technique analysis, a 4x4 scaled version has been investigated. The 4x4 Baseline sub-array has been taken as a benchmark, where no element imaging is applied; in there, as shown in Figure 4-16, polarimetric degradation is more severe and the XPD over 30 dB requirement is no longer achieved when scanning in elevation (see Figure 4-15 and Table 4.13).

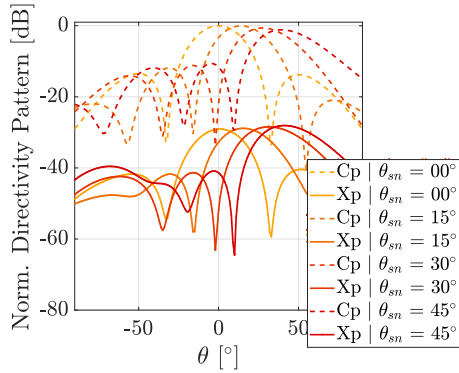


Figure 4-15 – V-Pol, 4x4 Baseline Sub-Array, E-Plane ($\phi = 90^\circ$)

Nominal Scanning (θ_{sn})	Real Scanning (θ_{sr})	XPD^V ($\theta_{sr}, \phi = 90^\circ$)
00°	00°	29.09 dB
15°	14°	28.86 dB
30°	27°	28.02 dB
45°	39°	26.98 dB

Table 4.13 – V-Pol, 4x4 Baseline Sub-array Elevation Scanning Comparison (CST MWS FD)

Based on the successful investigations on the feed rotation technique [35] at a 2x2 level, the same idea has been extended to a 4x4 sub-array. Two suitable topologies have been reviewed: (1) a simple upgraded structure comprised of four 2x2 imaged sub-arrays and (2) an extension of the feed rotation philosophy to the 4x4 structure.

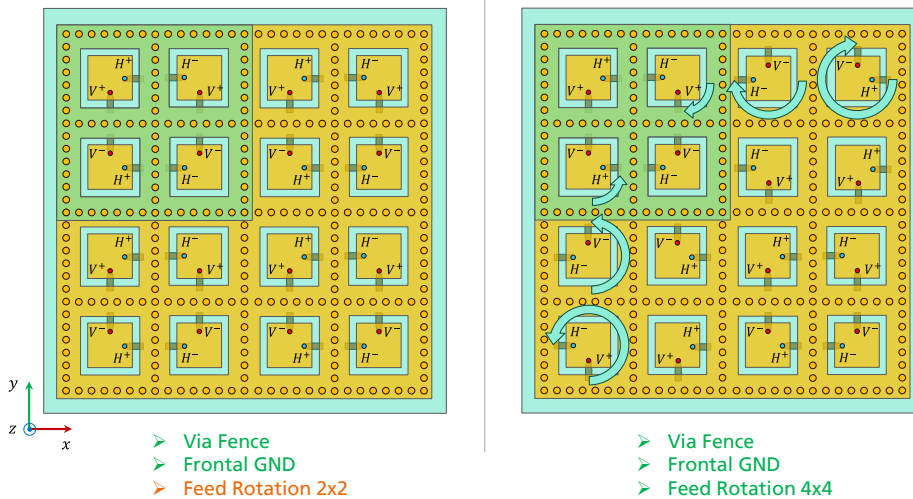


Figure 4-16 – 4x4 Imaged Sub-Array Proposals

Via EM full-wave simulations it has been verified that the first proposal introduces major polarimetric imbalances between the H and V channels (see Table 4.14). This is mainly caused by the faulty odd diagonal symmetry of the replicated 2x2 phase patterns. At broadside, there is a 50 dB imbalance on XPD , leading to critical performance for the H-pol case (see Table 4.14 case a) for H and V-Pol).

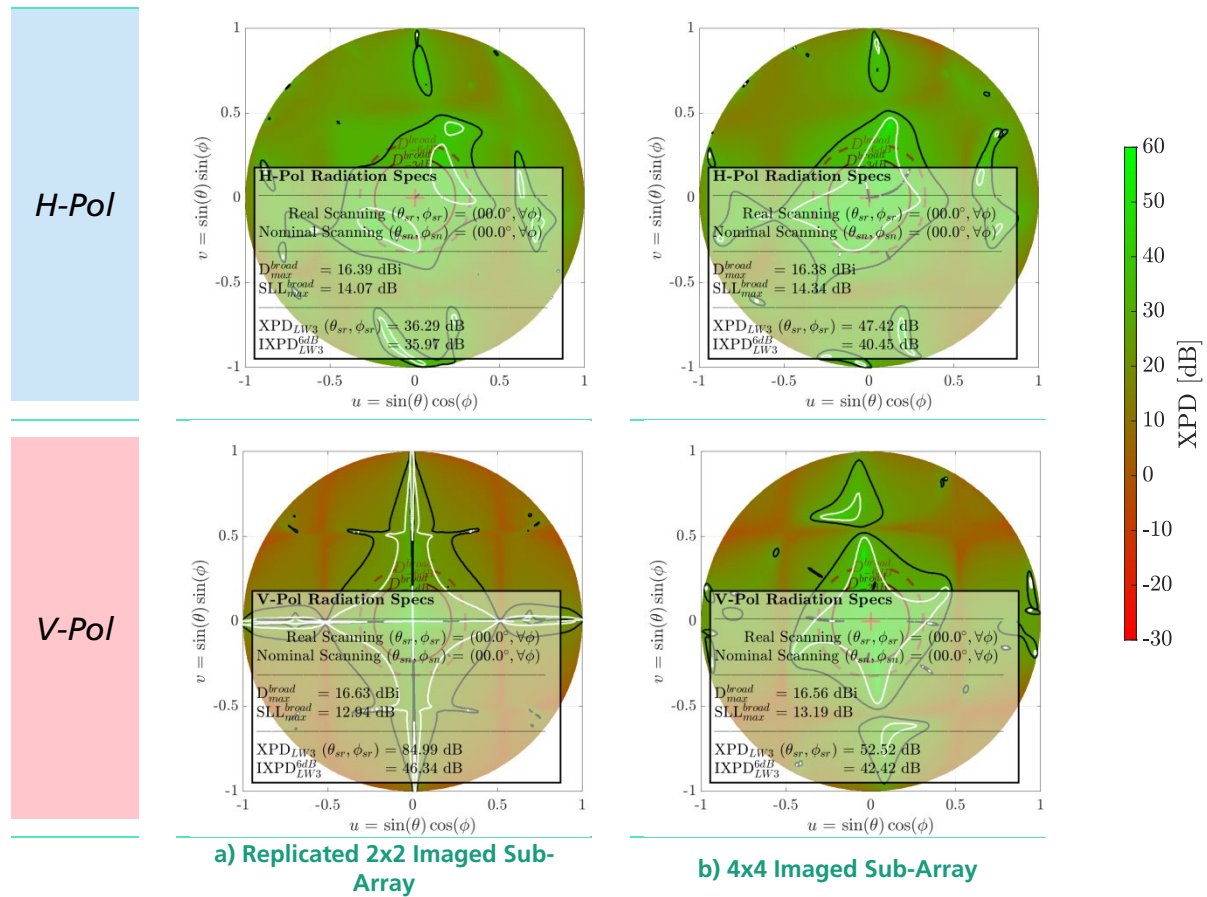


Table 4.14 – 4x4 Imaged Sub-array UV XPD Diagram Comparison at Broadside

On the other hand, the 4x4 imaged sub-array provides improved polarimetric performance, as *XPD* values over 40 *dB* have been calculated for the entire elevation scan range. The main figures of merit are gathered in the following table:

	Nominal Scanning (θ_{sn}, ϕ_{sn})	Real Scanning (θ_{sr}, ϕ_{sr})	<i>XPD</i> @(θ_{sr}, ϕ_{sr})	<i>SLL</i> _{max}	<i>Dir</i>
H-Pol	(00°, $\forall\phi$)	(00.0°, $\forall\phi$)	47.42 <i>dB</i>	14.3 <i>dB</i>	16.4 <i>dBi</i>
	(15°, 90°)	(14.0°, 89.7°)	50.01 <i>dB</i>	13.8 <i>dB</i>	16.3 <i>dBi</i>
	(30°, 90°)	(28.0°, 90.3°)	44.26 <i>dB</i>	12.8 <i>dB</i>	15.9 <i>dBi</i>
	(45°, 90°)	(40.7°, 90.3°)	40.95 <i>dB</i>	11.9 <i>dB</i>	15.4 <i>dBi</i>
V-Pol	(00°, $\forall\phi$)	(00.0°, $\forall\phi$)	52.52 <i>dB</i>	13.2 <i>dB</i>	16.6 <i>dBi</i>
	(15°, 90°)	(14.0°, 90.8°)	53.59 <i>dB</i>	12.3 <i>dB</i>	16.5 <i>dBi</i>
	(30°, 90°)	(27.7°, 89.7°)	47.00 <i>dB</i>	12.8 <i>dB</i>	15.9 <i>dBi</i>
	(45°, 90°)	(40.0°, 90.3°)	47.08 <i>dB</i>	09.7 <i>dB</i>	15.4 <i>dBi</i>

Table 4.15 – 4x4 Imaged Sub-array with Ideal Ports, Elevation Scan Assessment

Moreover, in a post-processing analysis the fields have been integrated to obtain an advanced polarimetric assessment for weather radar applications. The metrics used in Table 4.16 are introduced in sub-sections 2.2.3 and 2.2.3.

	Nominal Scanning (θ_{sn}, ϕ_{sn})	XPD @(θ_{sr}, ϕ_{sr})	$IXPD^{6dB}$	$ICPR$	Z_{DRb}
H-Pol	($00^\circ, \forall\phi$)	47.42 dB	40.45 dB	-34.63 dB	-0.23 dB
	($15^\circ, 90^\circ$)	50.01 dB	33.20 dB	-28.13 dB	-0.23 dB
	($30^\circ, 90^\circ$)	44.26 dB	27.57 dB	-22.74 dB	-0.22 dB
	($45^\circ, 90^\circ$)	40.95 dB	23.10 dB	-18.89 dB	0.05 dB
V-Pol	($00^\circ, \forall\phi$)	52.52 dB	42.42 dB	-34.39 dB	-0.23 dB
	($15^\circ, 90^\circ$)	53.59 dB	35.63 dB	-27.90 dB	-0.23 dB
	($30^\circ, 90^\circ$)	47.00 dB	30.17 dB	-22.52 dB	-0.22 dB
	($45^\circ, 90^\circ$)	47.08 dB	25.99 dB	-18.84 dB	0.05 dB

Table 4.16 – 4x4 Imaged Sub-array with Ideal Ports, Post-Processed Polarimetric Scan Assessment

Recalling the polarimetric weather requirements ($Z_{DRb} < 0.1$ dB and $ICPR < -30$ dB) it can be seen in Table 4.16 their degradation over the scanning range. Of crucial importance is the Z_{DRb} requirement for rain measurements and its fulfillment validates the antenna design for the WRAD project. The $ICPR$ requirement has not been fulfilled mainly due to the H and V scanning pattern asymmetries, but also due to the relative high SLL that cannot be managed in a small 4x4 sub-array. Additionally, since the $ICPR$ is related to L_{DR} and it does not play a key factor of rain estimation, in the present stage of this work, the $ICPR$ requirement will be discarded.

On the other hand, the $IXPD^{6dB}$ degradation appears to be a more realistic metric than simple XPD measured at the peak of the co-polar beam. It is also a great indicator on the ratio of power radiated in the co and cross-pol within the 6 dB beamwidth, which is relevant for both antenna and weather radar requirements.

4.3.5 Sidelobe Level Management

Results from Table 4.15 show the appearance of high *sidelobe levels (SLL)*. The initial reasoning provided in 2.1.1 introduced the pattern reconfigurability of phased arrays through the element excitation (a_{ij}) and the progressive phase shifts (β_y). While β_y is set for each sub-array row to steer the beam in elevation as shown in Table 4.17, the element excitation weights are uniform. As known, a uniform element distribution yields around 13 dB for the array *SLL* independently from the number of elements. In order to reduce the level of secondary lobes, other non-uniform weight distributions need to be used.

For the 4x4 sub-array, due to the low number array elements, no major sidelobe control could be performed, but, using an extended feed rotation technique prevented the appearance of new sidelobes [35, 59]. The usage of replicated 2x2 sub-arrays, is not only undesired for the polarimetric imbalances shown in Table 4.14, but also because of the sub-array spacing increase. Replicating identical sub-arrays can be seen as doubling d_x and d_y , which can eventually lead to the inclusion of grating lobes in the visual range of the *AF*.

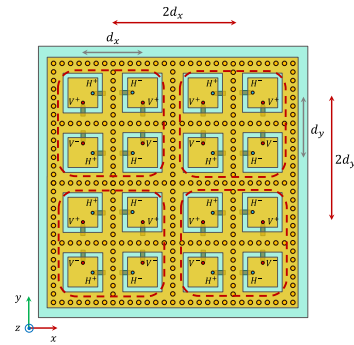


Figure 4-17 – Doubling Spacing through Sub-Array Replicas

For this reason, it is important to understand that the benefits of a continuous feed rotation technique are dual, the **cross-polarization suppression** and **suppression of new sidelobes**.

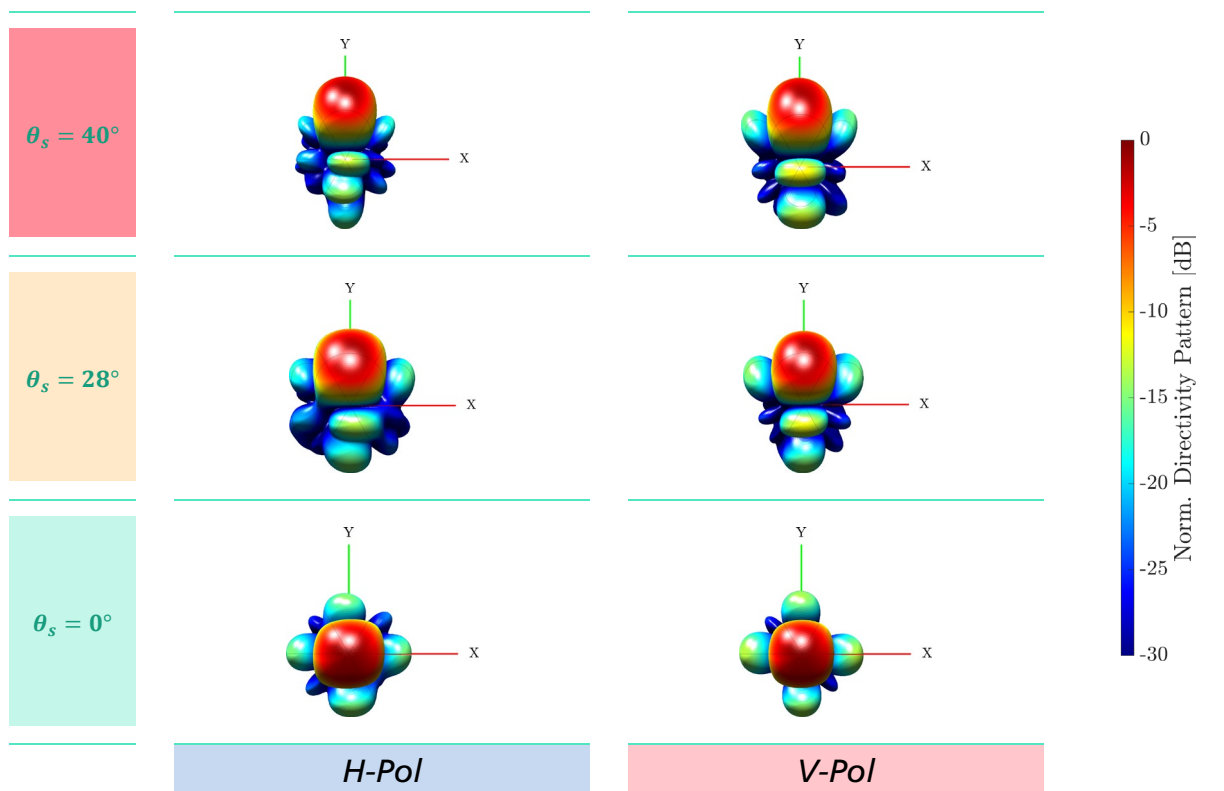


Table 4.17 – 4x4 Imaged Sub-array, 3D Radiation Patterns

4.4 Conclusions on Feed Rotation

The *feed rotation technique* initially proposed by *Woelders* and *Granholm* [35, 59] has been assessed and validated for mono dimensional scanning applications. The cross-polarization suppression mechanism relies on combining the cross-polarization phase patterns of the elements. Imaging the patterns and compensating the phase-shift via opposite excitation, allows generation of phase symmetries to improve the polarimetric performance within a specific radiation plane with symmetric performance for H and V polarizations

In our case, based on the polarimetric requirements, the proposed feed rotation yielded quasi-symmetric performance for both polarizations (linear H and V). The simplicity and effectiveness of this technique appears ideal for **low-cost** weather radar applications. Moreover, feed rotation supports the **modularity** concept, enabling extensible sub-array designs. Based on the initial 4x4 tile, the initial element rotation can be iterated on a larger sub-array as shown in Figure 4-18.

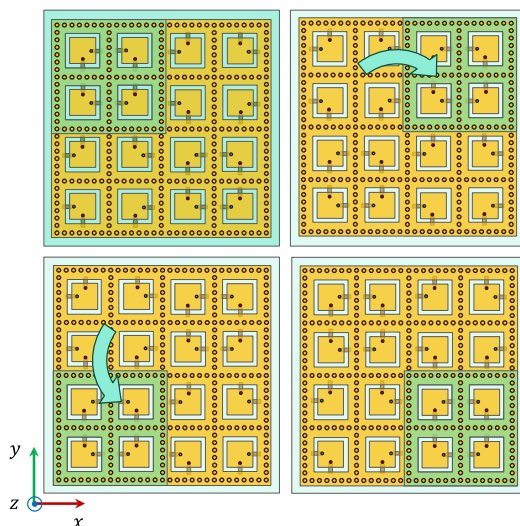


Figure 4-18 – Extended Feed Rotation Scheme

After feasible simulation results, a feeding network has been added to the 4x4 sub-array. Limited to elevation scanning only, progressive phases are required per each row, offering a potential cost reduction on the number of T/R modules to be used. Such integrated concept requires a judicious design process, where polarimetric requirements still drive the main design decisions for the presented feeding network described in Chapter 5.

However, due to the uniform excitation, high *SLL* are to be expected. Of course, feed rotation can yield great polarimetric performance and be combined with *SLL* management techniques [35].

In this sense, following this study, *SLL* optimization can be implemented at a panel level. Providing such optimization for a 4x4 sub-array is not possible, mainly due to the small size of the array.

Chapter 5 - Feeding Network Design

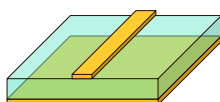
This chapter focuses on the design methodology of the integrated microstrip feeding network. The AESA antenna layout on the top layer severely constrains the allowed space and design options of the network. While mono dimensional elevation scanning allows grouping of elements by row, the dual-pol requirement implies two independent feeding networks. The limited board surface added to the need for **cross-talk suppression** required judicious analysis that led to the design guidelines reviewed throughout this chapter.

After reviewing polarimetry related considerations, an integrated antenna with feeding network interface with a $50\ \Omega$ connector is presented. Through the process, specific emphasis is placed on the methodology and the polarimetric implications of the architectural choices, which will possibly benefit future polarimetric antenna designs.

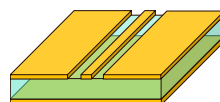
5.1 Requirements and Constraints

The ultimate goal of a feeding network is to reduce the number of T/R modules and connectors for electronics. As shown in Chapter 2 and Chapter 4, such AESA feature requires feeding the array rows with a *progressive phase shift* (β_y). For this reason, feeding networks to group the row elements have been used.

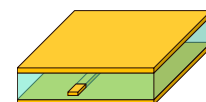
Moreover, current PCB technology allows integrating the feeding network at the back of the PCB, thereby, decoupling radiation and feeding stages while minimizing the front-end cost. For this reason, a selection of planar PCB transmission line options is proposed.



a) Microstripline



b) Grounded Co-planar Waveguide (CPW)



c) Stripline

Table 5.1 – Planar Transmission Lines

Additionally, different feeding network strategies are depicted in Table 5.2.

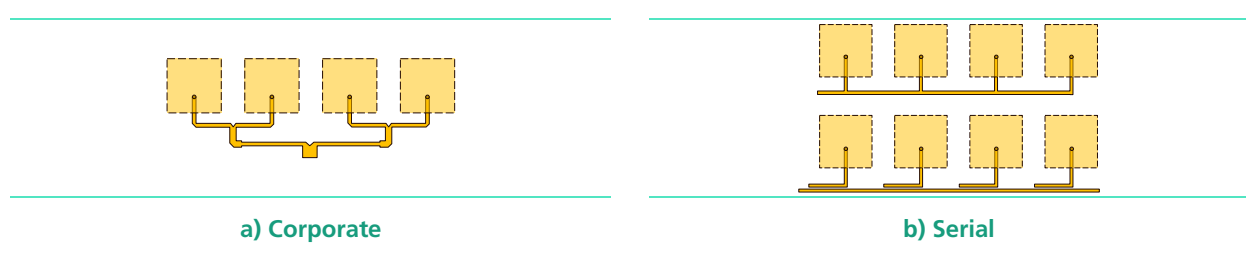


Table 5.2 – Feeding Network Architectures [42]

Based on the **polarimetric** and **low-cost** antenna sub-system requirements, a simple unshielded microstripline corporate feeding network has been found to provide the best trade-off between performance and cost. The cross-talk between the H and V feed networks has been minimized by avoiding meandering and line discontinuities, which are known to contribute to radiation losses [56, 60]. On the other hand, *Grounded Coplanar Waveguide* (GCPW) and stripline topologies would suppress the undesired cross-talk at a notable cost increase due to the need of vias, or even due to the addition of extra layers for the stripline case [57].

5.1.1 Space Optimization

Due to the architectural design choice of having the same substrate for both radiation and feeding stages so to limit PCB delamination, high integration in the feeding network is necessary. For this reason, initial studies have shown that based on the chosen substrate (RO4350B, $\epsilon_r = 3.66$) a maximum of four elements per row could be fed, while leaving enough space to place the two separate feeding networks.

At this stage it has also been proposed to investigate once again the effect of the feeding line orientation on the polarimetric performance. Although in sub-section 3.4 it has been shown that the feeding line should be orthogonal to the radiating edges to increase antenna symmetry and minimize cross-pol, when using the feed rotation technique, parallel feeding has been observed to improve the polarimetric performance.

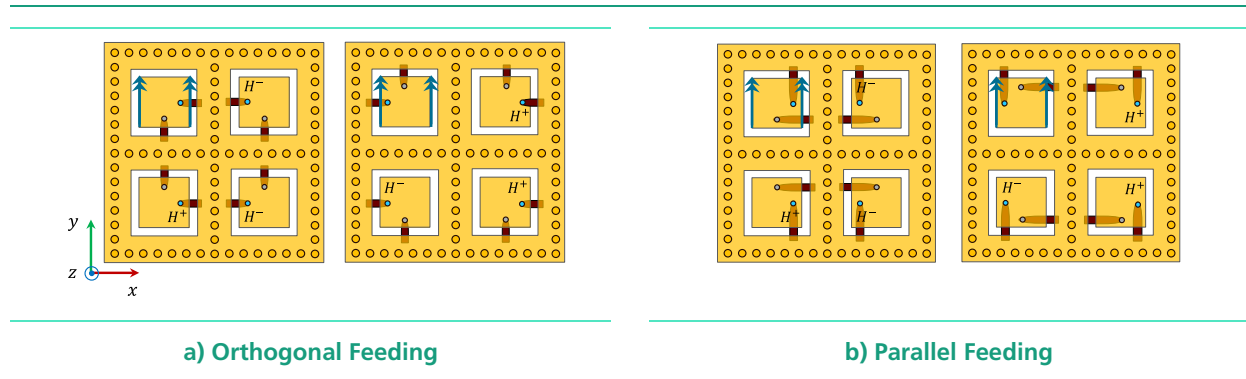


Table 5.3 – Orthogonal vs Parallel Feeding

The improvement of topology b) in Table 5.3 is of dual nature. First, an increase for XPD values at boresight has been measured at a simulation level while maintaining the $IXPD^{6dB}$ levels. Second, it allows to connect the 2x2 sub-arrays avoiding crossings between the H and V feeding networks. Polarimetric comparisons between both layouts are shown in Table 5.4 and Table 5.5.

Nominal Scanning (θ_{sn}, ϕ_{sn})	Orthogonal				Parallel			
	H-Pol		V-Pol		H-Pol		V-Pol	
	XPD_{peak} [dB]	$IXPD^{6dB}$ [dB]	XPD_{peak} [dB]	$IXPD^{6dB}$ [dB]	XPD_{peak} [dB]	$IXPD^{6dB}$ [dB]	XPD_{peak} [dB]	$IXPD^{6dB}$ [dB]
($00^\circ, \forall\phi$)	47.42	40.45	52.52	42.42	48.49	39.16	63.46	40.68
($15^\circ, 90^\circ$)	50.01	33.20	53.59	35.63	62.96	33.14	55.62	35.35
($30^\circ, 90^\circ$)	44.26	27.57	47.00	30.17	47.05	27.61	48.17	30.39
($45^\circ, 90^\circ$)	40.95	23.10	47.08	25.99	42.86	23.16	47.28	26.22

Table 5.4 – 4x4 Imaged Sub-array with Ideal Ports Polarimetric Scanning Comparison

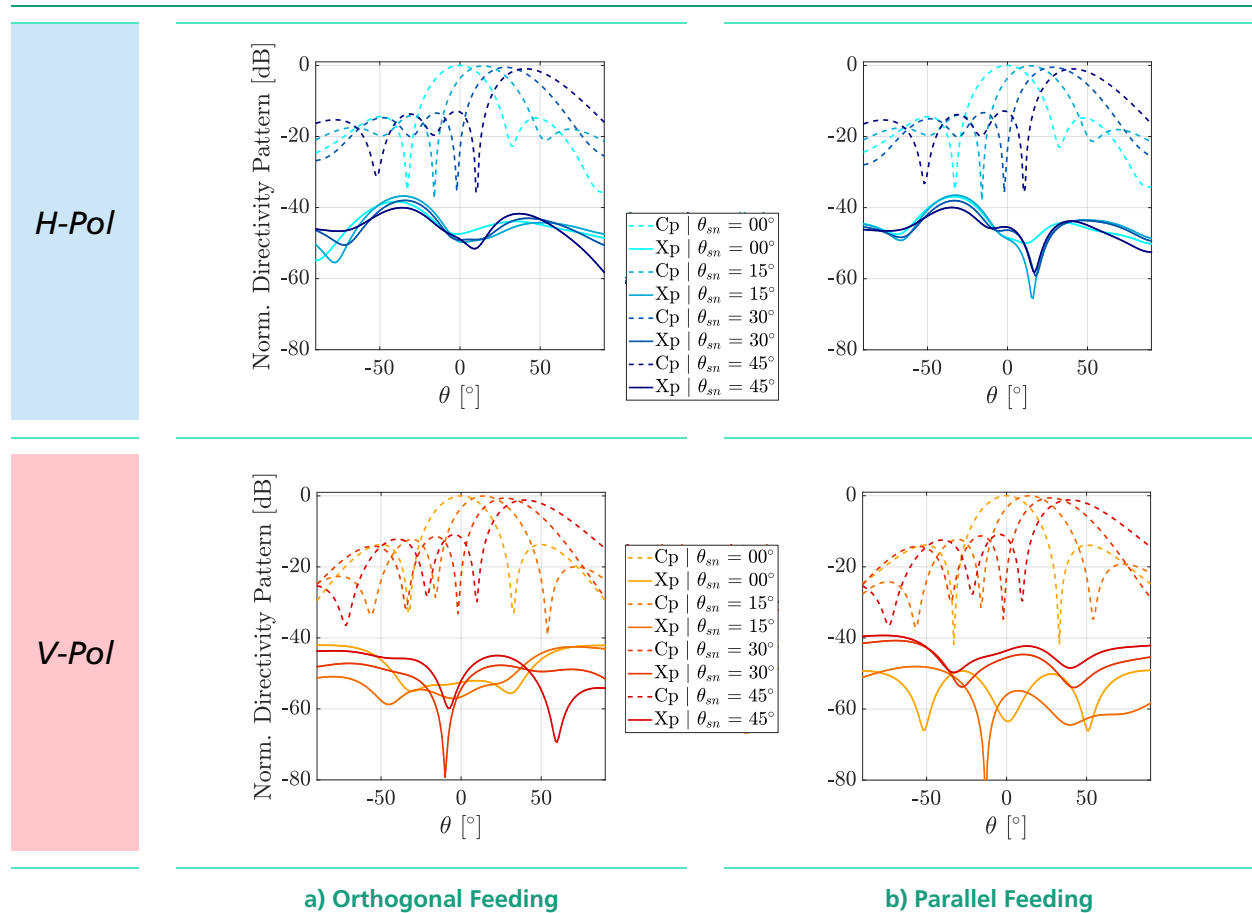


Table 5.5 – 4x4 Imaged Sub-arrays Scanning Comparison for $\phi = 90^\circ$

Nonetheless, for both feeding topologies, it can be clearly seen that, when grouping elements by complete row, symmetry can no longer be targeted. Such imperfection will be shown to increase the pattern asymmetries between the orthogonal polarizations.

5.2 Passive Splitter Design

In order to build a corporate feeding network based on microstrip lines, passive splitters have been used. Initial simulations with ideal feed-nets using the CST MWS Circuits & Systems module have been showing similar performances between the T-Junction and the Wilkinson divider.

	<ul style="list-style-type: none"> ▲ No need of external components. ▲ Compact and versatile. ▼ P2 and P3 are not decoupled. If one of them is not matched, part of the reflection propagate to the other ports. 		<ul style="list-style-type: none"> ▼ Need to solder a SMD resistor. ▼ Increased board surface requirements. ▲ P2 and P3 decoupled.
$S = \frac{1}{2} \begin{pmatrix} 0 & -j\sqrt{2} & -j\sqrt{2} \\ -j\sqrt{2} & 1 & -1 \\ -j\sqrt{2} & -1 & 1 \end{pmatrix}$		$S = \frac{1}{2} \begin{pmatrix} 0 & -j\sqrt{2} & -j\sqrt{2} \\ -j\sqrt{2} & 0 & 0 \\ -j\sqrt{2} & 0 & 0 \end{pmatrix}$	
a) T-Junction		b) Wilkinson Divider	

Table 5.6 – Passive Splitters for Microstripline

The CST MWS FD simulation was only performed from port to port, meaning that no active performance was taken into account when designing the feeding networks. Still, the active S-Parameters of the model using a total of 32 ports (16 ports for each polarization) were computed to validate the matching condition at $f_0 = 9.41 \text{ GHz}$ and the chosen $Z_{REF} = 100\Omega$. In this context, for an active simulation where all the co-polarized ports are excited, a Wilkinson divider would be preferred, as it would provide perfect isolation thanks to the resistor. In this sense, the arising reflections from a port whose active Z_{in} did not match Z_{REF} would be dissipated in the Wilkinson divider resistor.

Nonetheless, due to lack of PCB surface, the Wilkinson divider has been discarded, decreasing the feeding network complexity and cost (no SMD components required). The feed rotation technique substantially increases complexity as 180° phase-shifts were required to be achieved within the network. For illustration purposes, an sketch of the top row network of the H-Pol follows:

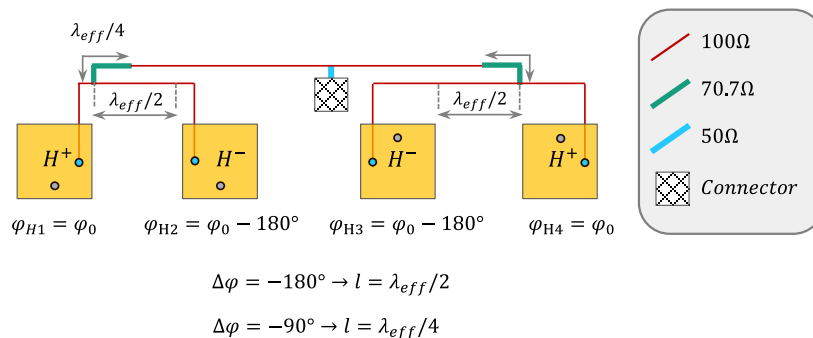


Figure 5-1 – Feeding Network Sketch for H-Pol Row

5.2.1 Design Methodology and Requirements

Preliminary integrated simulations failed to reach 30 dB of XPD due to the high cross-talk between feeding networks. Attempts such as the ones depicted in Figure 5-2 and Figure 5-3, provided an insufficient polarimetric performance already for 2x2 imaged sub-arrays. For these networks the bending condition of $R > 3w_{line}$ [61] was not respected, increasing radiation losses that led to increased feed-net cross-talk. This ultimately yielded unsuitable results ($XPD_{Broad} < 30$ dB).

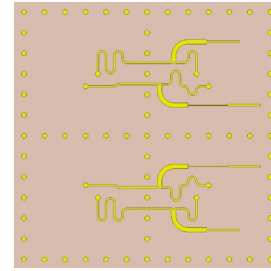


Figure 5-2 – Feed-net with Excessive Meandering - I

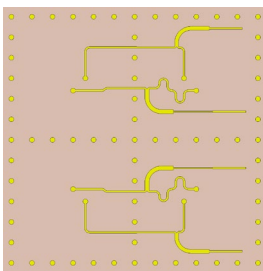


Figure 5-3 – Feed-net with Excessive Meandering - II

The excessive meandering led to increased cross-talk between the orthogonal feeding networks. Based on the space constraints imposed by the *through vias*, alternative arrangements were proposed to avoid line bending (see Figure 5-4).

In this way, meandering was minimized while ensuring a distance between lines and *via clads* of at least twice the line width ($d_{via,line} \geq 2w_{line}$) to ensure stability of the characteristic impedance of the line.

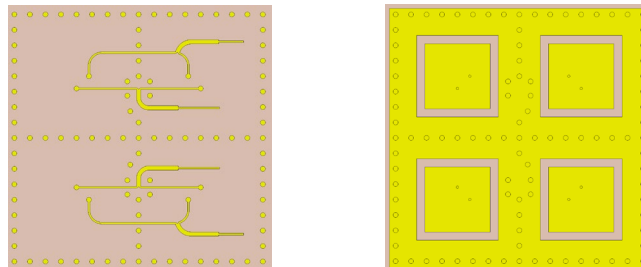


Figure 5-4 – Feed-net with Asymmetrical Via Distribution

Asymmetries in the antenna plane due to rearrangement of *through vias* also proved to be critical for the polarimetric performance. Basically, any sort of asymmetry in the antenna plane will most likely turn into a cross-polarization increase. For this reason, if a via has to be removed to arrange the feeding network lines, a *blinded via* is set to replace it in the antenna plane.

Tracing Cross-talk Sources in the Feeding Network

Owing to the initial attempted designs, assembly simulations were performed to show the effect of cross-talks between the orthogonal feeding networks. In this way, the polarimetric feeding networks performance has been assessed and the real source of cross-polarization was traced.

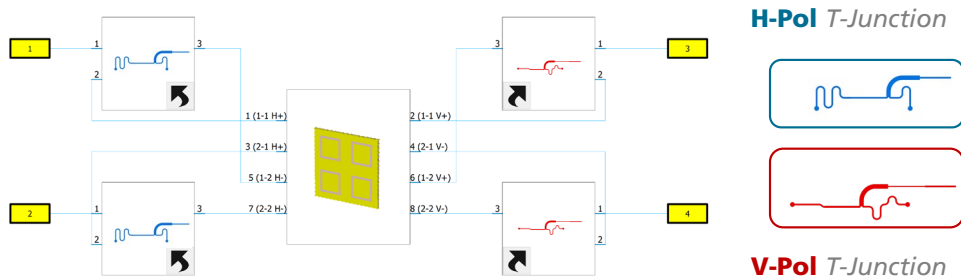


Figure 5-5 - Assembled Simulation with Separated T-Junctions

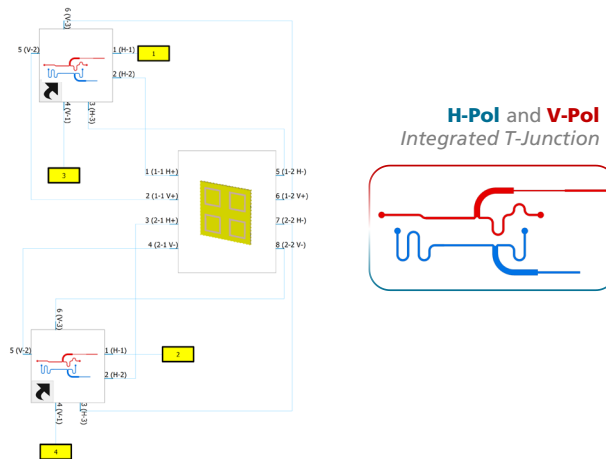


Figure 5-6 – Assembled Simulation with Integrated T-Junctions

While Figure 5-5 yielded a good polarimetric performance, Figure 5-6 already failed to provide the required polarimetric performance. The cross-talk of the integrated T-Junctions was found to be the reason behind the severe degradation.

This iterative process has allowed to conceive the final network design, later on integrated within the 4x4 imaged sub-array. As a result, meandering minimization and antenna plane symmetry have been foremost prioritized at the design stage, yielding the proposed T-Junctions arrangements shown in the following sections.

5.2.2 Proposed T-Junctions and Optimization

Based on the initial sketch of Figure 5-1, two different splitters have been designed and simulated using CST MWS (FD¹³ solver). Due to space constraints, some residual meandering has been required to include the 180° phase-shift and avoid placing the T-splitter junction in a bending line.

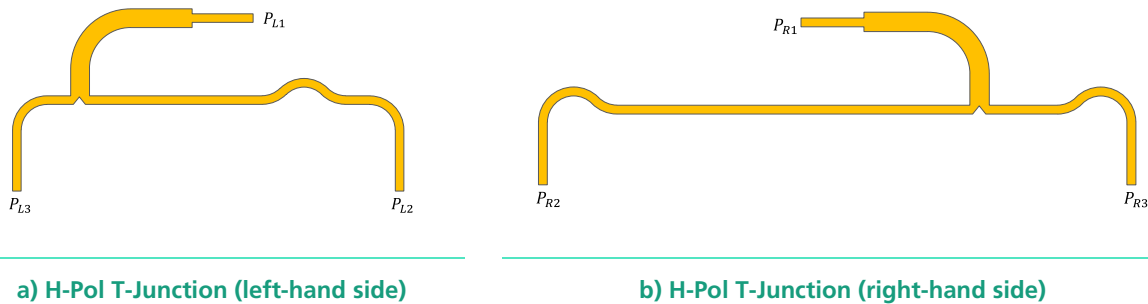


Table 5.7 – Preliminary T-Junctions for H-Pol Feeding Network

Chamfering the T-Junction allowed to remove parasitic reactances [44] and it improved the transmission coefficient by 0.1 dB at the expense of including line discontinuities that increase feed-net radiation. The design of the bends have been following the recommendations of [62, 61], where the $R > 3w_{line}$ rule is stated to provide controlled impedance and radiation minimization. Alternatively a chamfered corners could also have been used, but bends were preferred to minimize radiation.

Overall, the first design iteration in Table 5.7 has showed feeding imbalances between ports P_{R2} - P_{R3} and P_{L2} - P_{L3} . Despite managing to obtain the intended phase shift between ports by tuning the T-junction position, the transmission parameters S_{31}^L and S_{21}^L had an imbalance around 0.5dB ($|S_{31}^L| > |S_{21}^L|$ and $|S_{21}^R| < |S_{31}^R|$), possibly leading to undesired tapering.

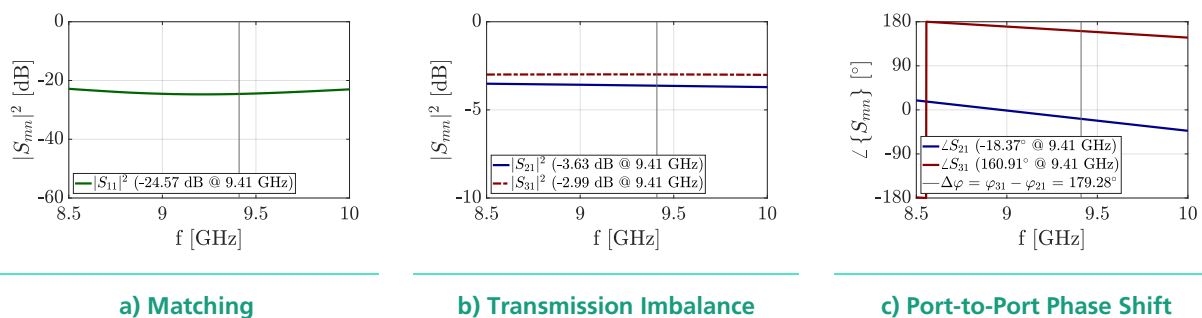


Table 5.8 – S-Parameters for Preliminary H-Pol T-Junction, left-hand side (CST MWS FD)

¹³ The local mesh of the lines has been tuned so that at least two mesh cells fit within the width the narrowest line.

To account for these imbalances, $\lambda_{eff}/4$ transformers have been used. Making the lines wider decreases the impedance and increases the current flow. On the other hand, the transformer connected to the T-junction also has to be tuned to control the matching seen at port P1. A sketch of this design strategy is shown in Figure 5-7, while the updated S-Parameters with minimized imbalance are shown in Table 5.9.

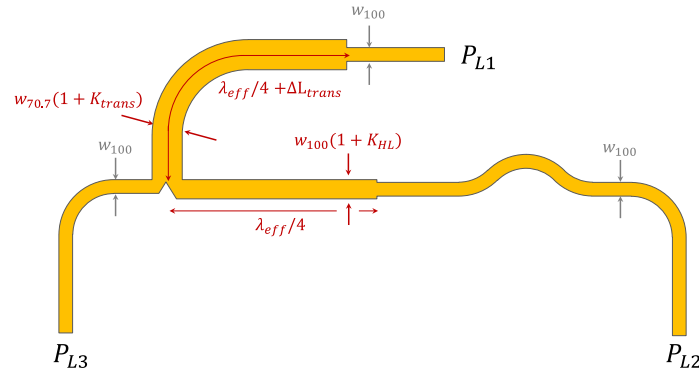


Figure 5-7 – Optimized H-Pol T-Junction, left-hand side

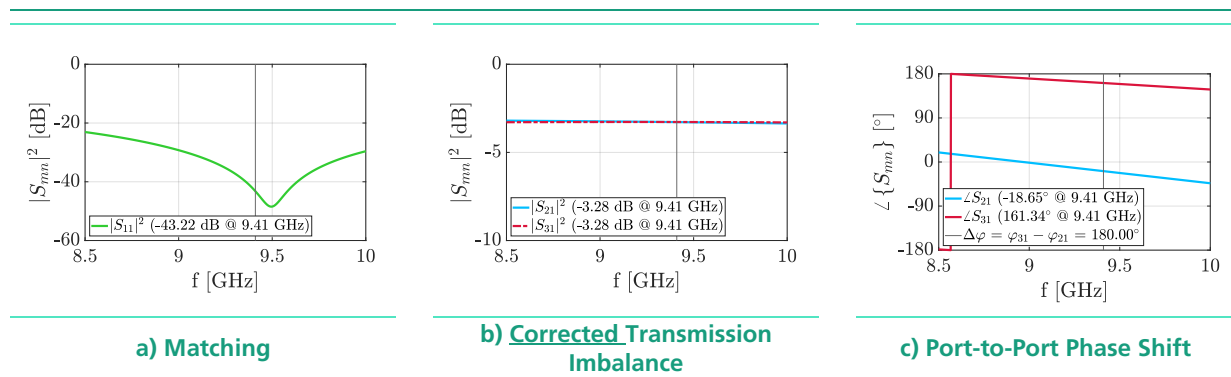


Table 5.9 – S-Parameters for Optimized H-Pol T-Junction, left-hand side (CST MWS FD)

Following this approach the imbalances between ports have been removed to provide uniform tapering of the four ports of each row. To exemplify, based on initial widths of $w_{100} = 0.205 \text{ mm}$ and $w_{70.7} = 0.505 \text{ mm}$ correction factors K_{HL} of 0.25 and K_{trans} of -0.05 have been applied. Moreover, the length of the transformer after the T-Junction also had to be optimized to maximize matching at port 1 ($|S_{11}^L|^2 < -30 \text{ dB}$). Last but not least, a standard bending radius has been set for each linewidth: $R_{100} = 0.75 > 3w_{100}$ and $R_{trans} = 1.5 > 3w_{trans}$.

A total of three different T-Junctions have been designed to interconnect the horizontal (two designs) and vertical (one design) feeding networks.

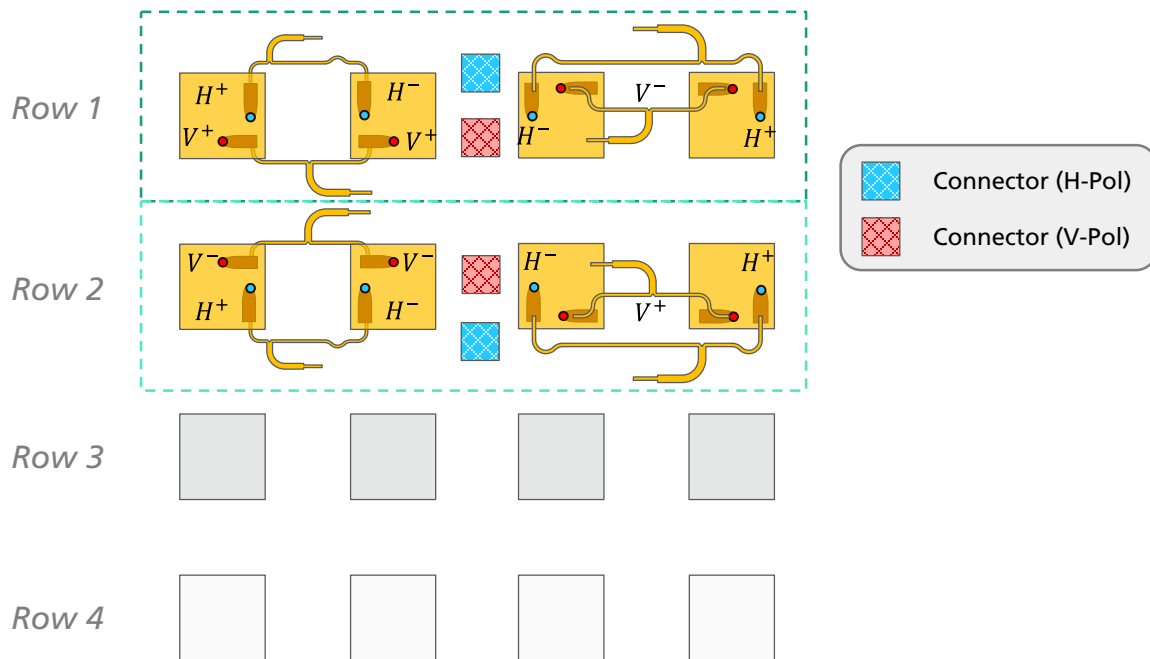


Figure 5-8 – H and V Row Feeding Networks Sketch

The feeding network has been interfaced with a 50Ω SMP connector, whose optimization is not reported in the Thesis. However, it is important to remark that a specific footprint with blinded vias and line transitions has been designed specifically for the Rogers 4350B substrate with a standard height of 0.508 mm .

5.3 Integrated Design

Following a similar optimization process for the T-Junction design, feeding networks for the 4x4 *baseline* and *imaged* sub-arrays have been integrated in the initial CAD models.

5.3.1 Feeding Network for the 4x4 Baseline Sub-Array

Omitting the design and connector optimization of the proposed feeding network, in Figure 5-9 an integrated design for the 4x4 baseline sub-array is presented. Complementary to the design of the imaged case (see Figure 5-11), the 4x4 baseline sub-array has been still investigated to provide further comparisons between the ideal port simulations and also to analyze the benefits of the feed rotation technique.

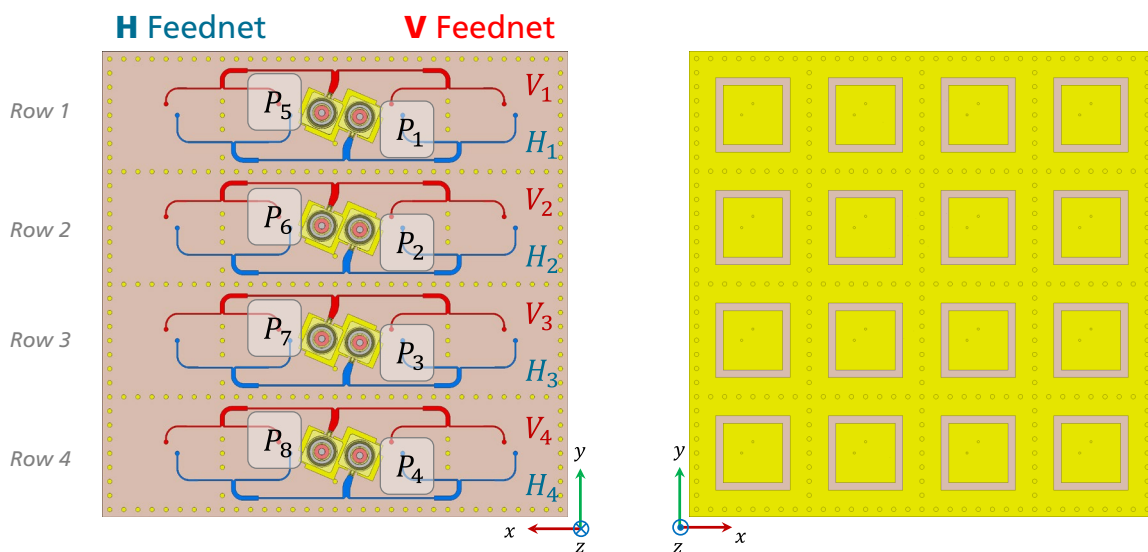


Figure 5-9 – Designed Feeding Network for 4x4 Baseline Sub-Array

5.3.2 Feeding Network for the 4x4 Imaged Sub-Array

To maintain symmetry, the same feeding networks have been used for rows 3 and 4. To provide the required excitations, a phase-shift of 180° is provided at the input signal (see Figure 5-10, Table 5.10 and Table 5.11).

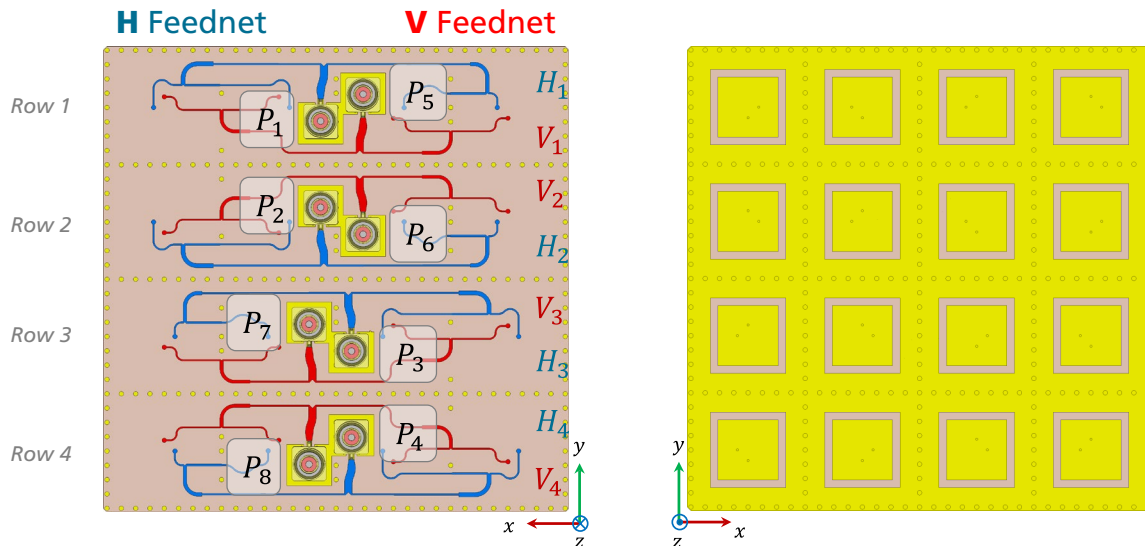


Figure 5-10 – Designed Feeding Network for 4x4 Imaged Sub-Array

The required excitations, given the considerations for a symmetric usage of feeding networks, are shown in Table 5.10 and Table 5.11.

Port	1	2	3	4
H-Port	H_1	H_2	H_3	H_4
Phase Excitation	0°	β_y	$2\beta_y + 180^\circ$	$3\beta_y + 180$

Table 5.10 – H-Port Specification for 4x4 Imaged Sub-Array

Port	5	6	7	8
V-Port	V_1	V_2	V_3	V_4
Phase Excitation	0°	$\beta_y + 180^\circ$	$2\beta_y$	$3\beta_y + 180$

Table 5.11 – V-Port Specification for 4x4 Imaged Sub-Array

Where β_y is the progressive phase-shift, whose expression is derived in Eq. 2.6 and hereby it is reported for convenience:

$$\beta_y = -\frac{2\pi}{\lambda_0} d_y \sin \theta_{max} \xrightarrow{d_y = \lambda_0/2} \beta_y = -\pi \sin \theta_{max} \text{ [rad]} \quad \text{Eq. 5.1}$$

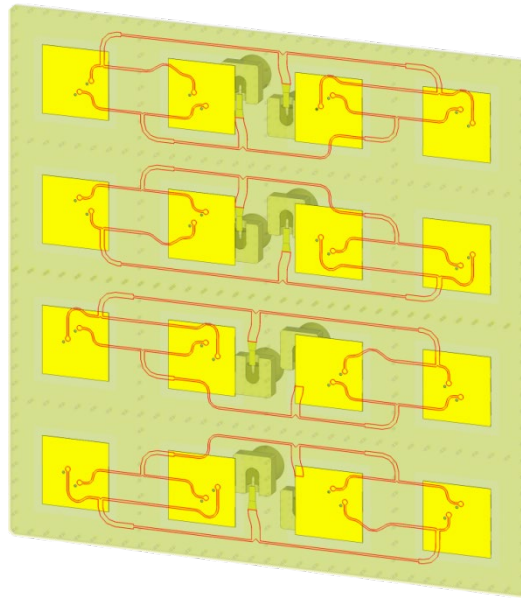


Figure 5-11 – Integrated 4x4 Imaged Sub-Array with Feeding Network for 1D Elevation Scanning

5.4 Simulation Results

Using CST MWS (FD solver) relevant polarimetric result figures have been calculated to validate the proposed antenna design with an integrated feeding network.

Note: in the following sub-sections only main results will be shown. The full result set is reported in Appendices C and D.

5.4.1 Results for the 4x4 Baseline Sub-Array

Polarimetric simulation results for the *baseline* design in are reported Figure 5-10. The performance of a non-imaged sub-array does not fulfil the weather radar requirements specified in sections 1.3 and 2.2.

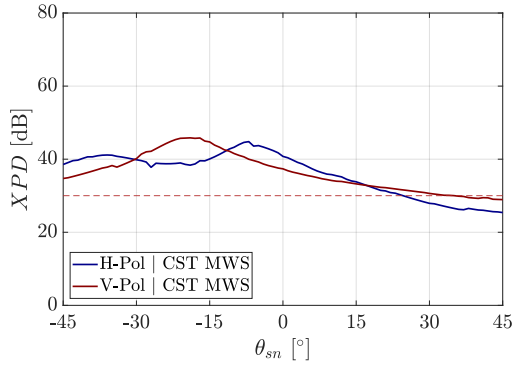
	Nominal Scanning Angle (θ_{sn}, ϕ_{sn})	XPD $@(\theta_{sr}, \phi_{sr})$	$IXPD^{6dB}$	$ICPR$	Z_{DRb}
H-Pol	$(00^\circ, \forall\phi)$	28.08 dB	27.90 dB	-25.06 dB	-0.07 dB
	$(15^\circ, 90^\circ)$	25.91 dB	25.36 dB	-24.05 dB	0.12 dB
	$(30^\circ, 90^\circ)$	23.56 dB	22.29 dB	-19.61 dB	-0.26 dB
	$(45^\circ, 90^\circ)$	21.63 dB	19.78 dB	-22.63 dB	-0.50 dB
V-Pol	$(00^\circ, \forall\phi)$	36.12 dB	34.78 dB	-24.05 dB	-0.07 dB
	$(15^\circ, 90^\circ)$	44.51 dB	39.75 dB	-23.89 dB	0.12 dB
	$(30^\circ, 90^\circ)$	43.91 dB	36.77 dB	-16.48 dB	-0.26 dB
	$(45^\circ, 90^\circ)$	37.60 dB	32.54 dB	-16.97 dB	-0.50 dB

Table 5.12 – 4x4 Baseline Sub-array with Integrated Feed-net, Post-Processed Polarimetric Scan Assessment

Moreover, major polarimetric imbalances between H and V polarizations motivated an in depth analysis of the polarimetric performance over the scan range (-45° to 45° degrees).

Cross-polarization Discrimination¹⁴

$$XPD \triangleq \frac{|E_{Cp}(\theta_{si}, \phi_{si})|^2}{|E_{Xp}(\theta_{si}, \phi_{si})|^2} > 30 \text{ dB}$$



Integrated Cross-polarization Discrimination

$$IXPD^{6dB} \triangleq \frac{\oint |E_{Cp}(\theta, \phi)| d\Omega_{6dB}}{\oint |E_{Xp}(\theta, \phi)| d\Omega_{6dB}}$$

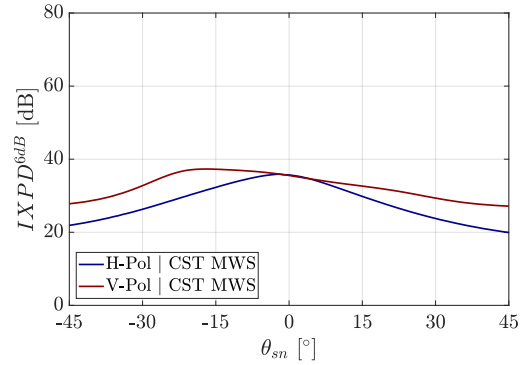


Table 5.13 – 4x4 Baseline Sub-array with Integrated Feed-net, Full-scan Polarimetric Assessment

Three undesired drawbacks of the baseline design can be deduced from Table 5.13:

- ✔ Asymmetric polarimetric performance over the scan range, especially for V-Pol in the $IXPD^{6dB}$ curve.
- ✔ Imbalanced polarimetric performance for the H and V polarizations.
- ✔ $IXPD^{6dB}$ and XPD below 30 dB for some scanning angles.

In spite of the drawbacks, the performance of the design with integrated feeding network improves with respect to the design with ideal ports. Additionally, key S-Parameters are reported for comparison with the imaged design in sub-section 5.4.2. The integrated antenna design is matched around the frequency of interest 9.41 GHz, surprisingly providing improved cross-pol isolations as a result of adding an optimized feeding network, but still, lower than the imaged sub-array.

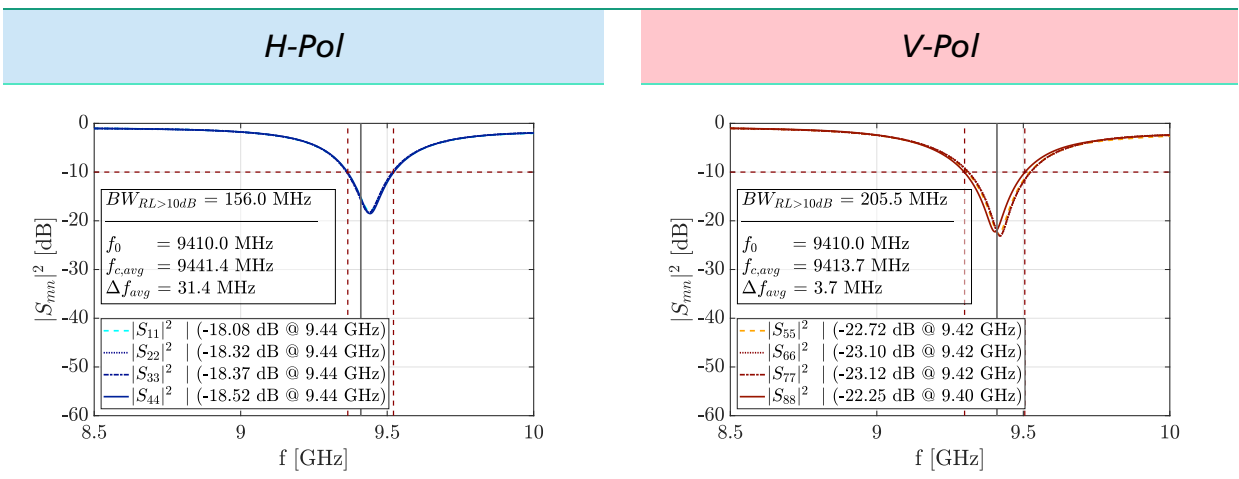


Table 5.14 – 4x4 Baseline Sub-array with Integrated Feed-net (Simulated Reflection Coefficients)

14

Real scanning angle: $(\theta_{sr}, \phi_{sr}) = (\theta, \phi) | \max \{ |E_{Cp}(\theta, \phi)|^2 \}$

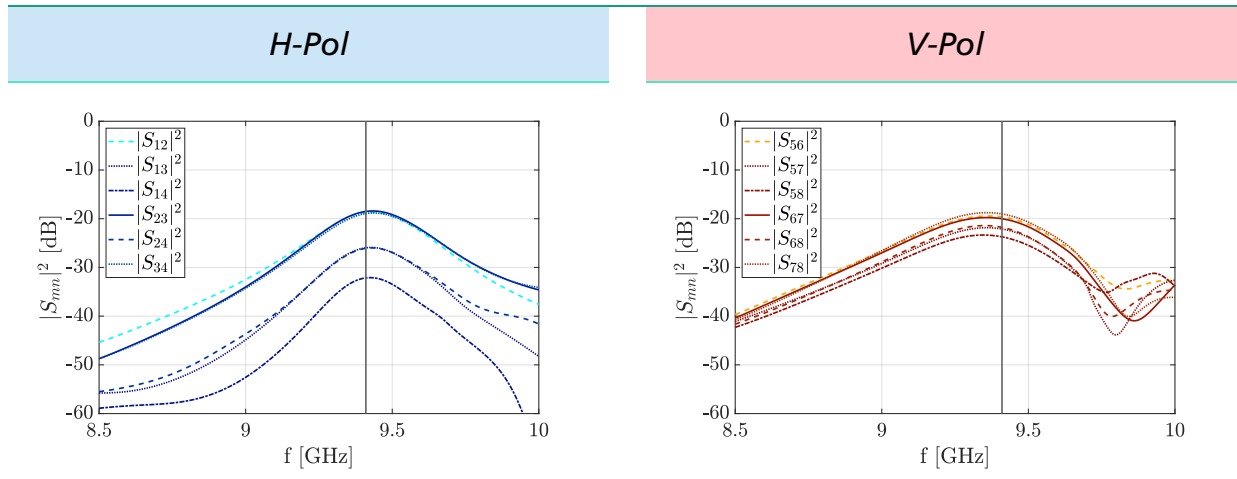


Table 5.15 – 4x4 Baseline Sub-array with Integrated Feed-net (Simulated Co-pol Port Isolations)

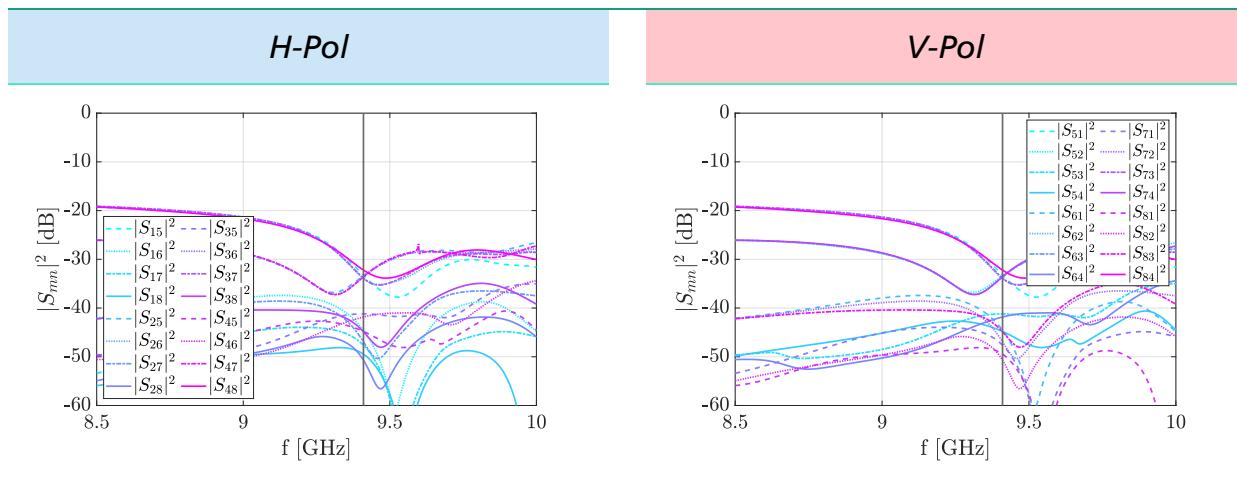


Table 5.16 – 4x4 Baseline Sub-array with Integrated Feed-net (Simulated Cross-pol Port Isolations)

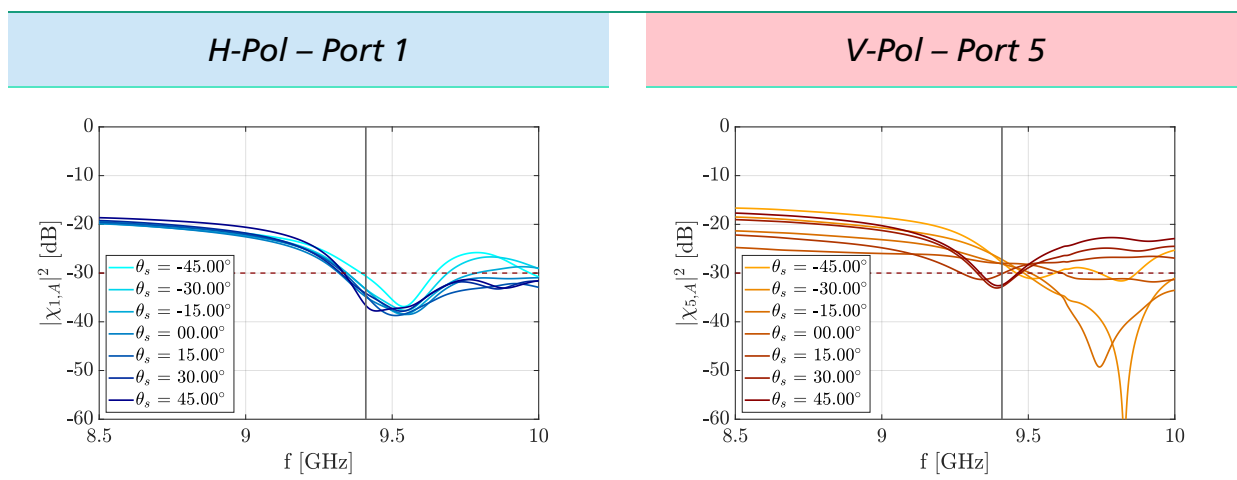


Table 5.17 – 4x4 Baseline Sub-array with Integrated Feed-net (Active Cross-polar Port Isolations)

5.4.2 Results for 4x4 Imaged Sub-Array

The main polarimetric results of the simulated imaged 4x4 sub-array are shown in Table 5.18. The full characterization of the proposed design is reported in Appendix D.

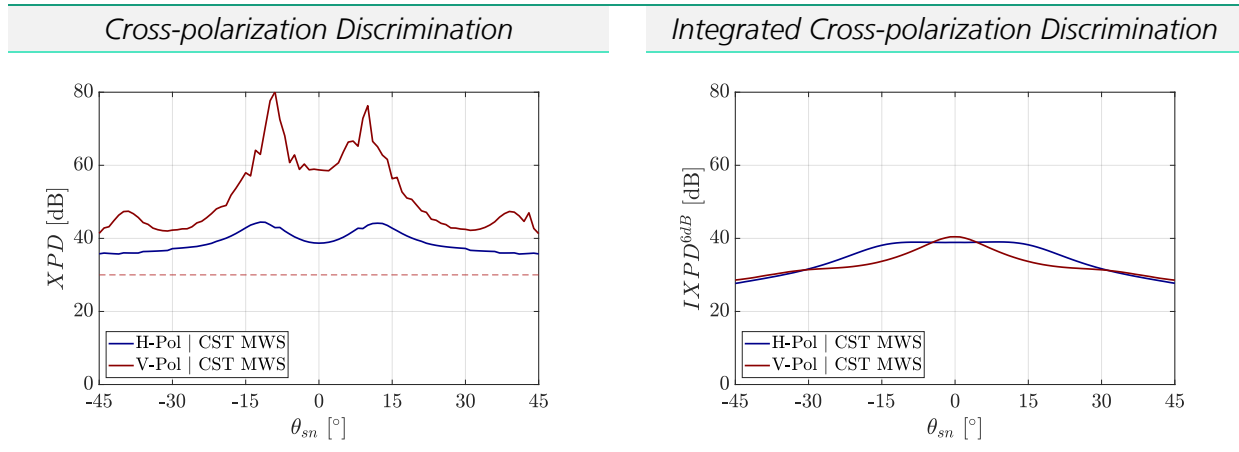


Table 5.18 – 4x4 Imaged Sub-array with Integrated Feed-net, Full-scan Polarimetric Assessment

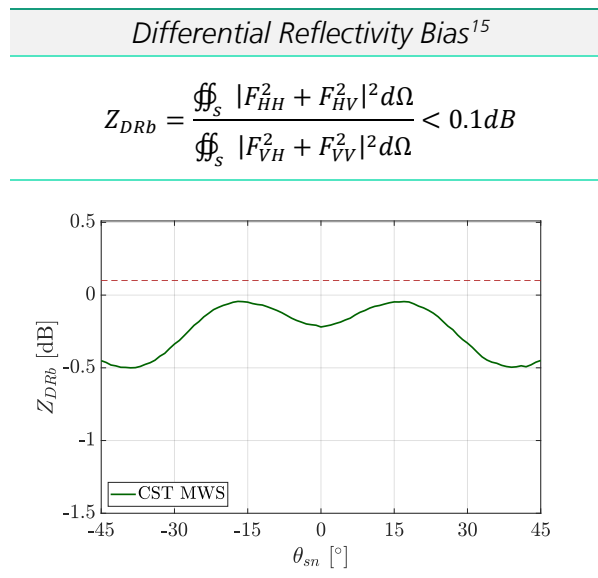


Table 5.19 – 4x4 Imaged Sub-array with Integrated Feed-net, Z_{DRb}

These polarimetric results contrast with Table 4.16 and Table 5.4, where ideal ports were used and worse polarimetric performance was observed. This fact supports the idea that better cross-polar port isolation can be achieved with an optimized feeding network. On the other hand, if comparing results from Table 5.12 with Table 5.18, polarimetric improvements with respect to the *baseline* sub-array in terms of symmetry within the scan range and balance between H and V polarizations can be clearly seen in the IXPD^{6dB}.

¹⁵ Considering a phased array that does not use T/R modules or other active elements.

The XPD and $IXPD^{6dB}$ curves also show that integrating the beam above the $-6dB$ threshold and computing the co- and cross-polar ratio provides more realistic polarimetric performance estimation than just taking a punctual point. This result suggest the need for an explicit weather radar requirement based on the $IXPD^{6dB}$ rather than the XPD at the peak of the co-polar beam. Further optimization of the unitary element can allow achieving values over 30 dB of $IXPD^{6dB}$ for the $\pm 45^\circ$ scan range as well. Such optimization has been here omitted, since patch antennas have been constrained to be squared to maximize symmetry, disregarding the asymmetrical consideration of the elevation scan (see sub-section 4.2.1).

Despite these observations, the 4×4 imaged sub-array with integrated feed-net shows great polarimetric results (Z_{DRb} well below 0.1 dB , see Table 5.19). Overall, the usage of an integrated feeding network is beneficial for the polarimetric performance of the array. This is mainly caused by an improvement of isolation between the orthogonal ports of adjacent antenna elements as already seen for the baseline design. To quantify the isolation between ports and the antenna performance, the relevant S-Parameters are shown in Table 5.22.

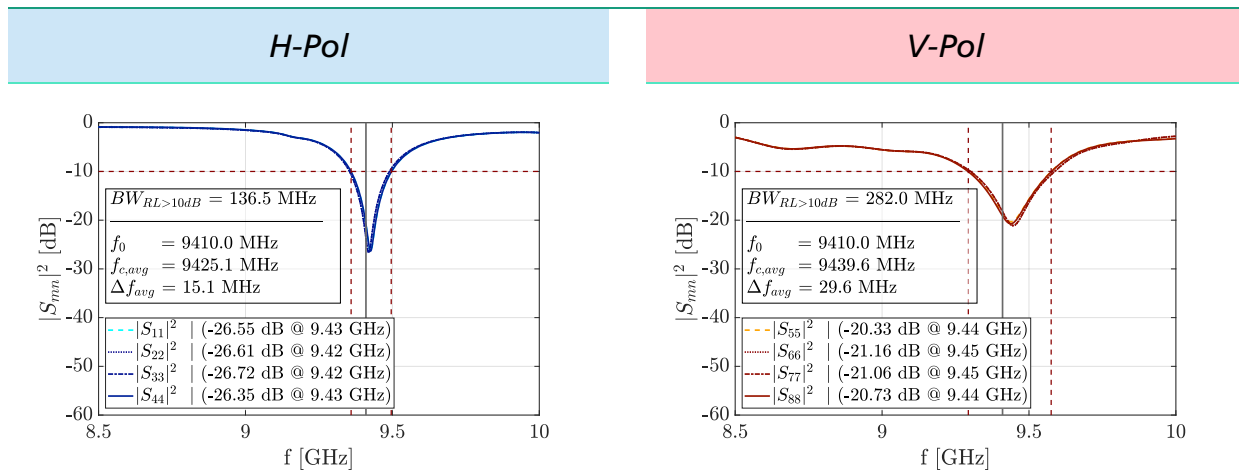


Table 5.20 – 4×4 Imaged Sub-array with Integrated Feed-net (Simulated Reflection Coefficients)

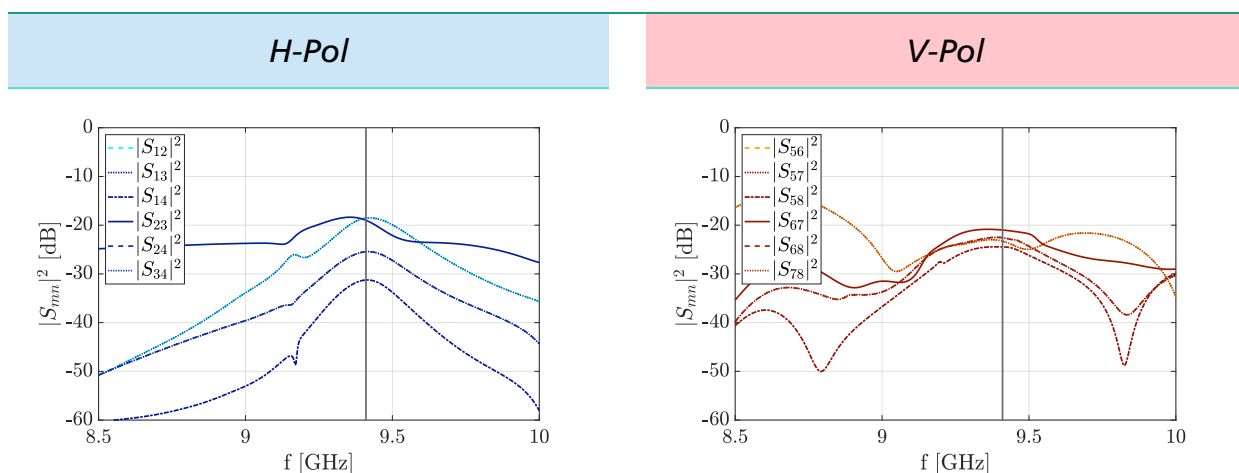


Table 5.21 – 4×4 Imaged Sub-array with Integrated Feed-net (Simulated Co-pol Port Isolations)

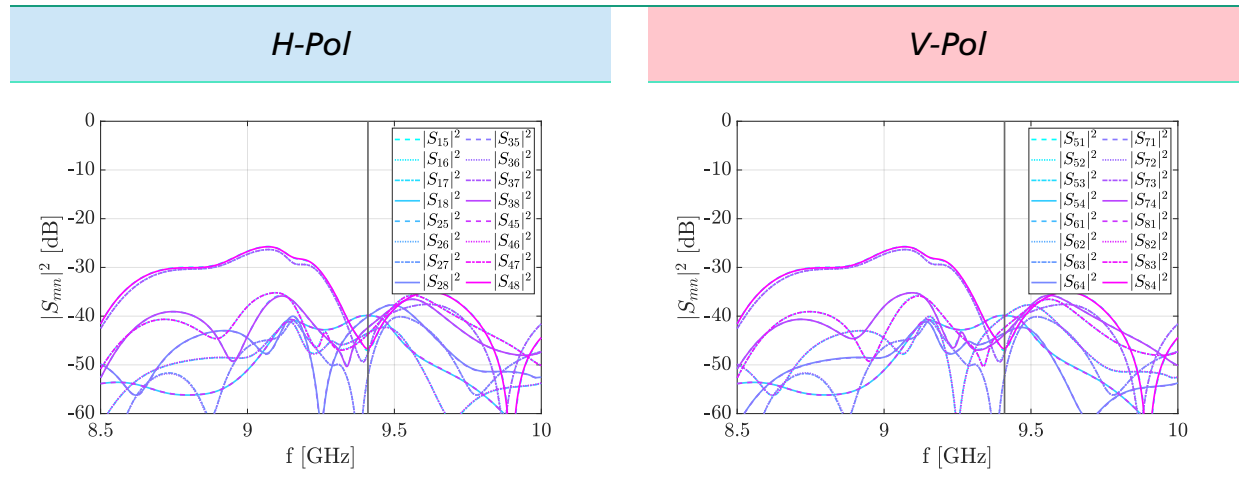


Table 5.22 – 4x4 Imaged Sub-array with Integrated Feed-net (Simulated Cross-pol Port Isolations)

The simulated S-Parameters show good antenna performance in terms of matching, bandwidth and polarimetric isolation. A few comments are listed following the results analysis:

- The *Return Losses* (RL) for all the ports at $f_0 = 9.41 \text{ GHz}$ are over 20 dB .
- Bandwidths are around 136 and 282 MHz for the H and V channels considering, the most critical port and using the $RL > 10 \text{ dB}$ condition.
- If the RL condition is relaxed to 7 dB , bandwidths increase up to 211.5 and 435 MHz for the H and V ports respectively.
- The bandwidth of the V ports is higher since less meandering has been applied. However, its matching is overall 5.10 dB worse with respect to the H-Port. This is caused by a residual optimization margin and also, because the H feed-net is longer, which implies greater losses and therefore better matching (less reflections).
- The isolation of co-polar ports is at worst 19 dB , which indicates that no undesired modes are propagating.
- The isolation of cross-polar ports (XPI) is 40 dB for the worst case and show an improvement of 15 dB compared to the worst case for the imaged sub-arrays with ideal ports.
- Based on Table 5.22 it can be seen that cross-polar port isolations are the same.

Despite the positive results of the 4x4 imaged sub-array, the static scattering parameters do not take into account the actual port performance when the ports are active. For this reason and considering the feeding scheme of the array (Table 5.10 and Table 5.11) the Active S-Parameters have also been computed. Since the radar unit is expected to operate in *Alternate Transmit Alternate Receive* (ATAR) mode, only one polarization will be transmitted and received at a time, which constraints the excitation of ports to only one polarization at a time.

Active Reflection Coefficient (ARC, Γ) and Active Isolation Coefficient (AIC, χ) at the ports **1** and **5** can be computed analytically as:

ARC, Γ	AIC, χ	
Reflection coefficient when all the co-polar elements are active.	Coupled power when all the cross-polar elements are active.	
<i>Target value: -10 dB</i>	<i>Target value: -30 dB</i>	
$\Gamma_{1A} = S_{11} + S_{12} \frac{a_2}{a_1} + S_{13} \frac{a_3}{a_1} + S_{14} \frac{a_4}{a_1}$	$\chi_{1A} = S_{15}a_5 + S_{16}a_6 + S_{17}a_7 + S_{18}a_8$	XPI- H ₁ V
$\Gamma_{5A} = S_{55} + S_{56} \frac{a_6}{a_5} + S_{57} \frac{a_7}{a_5} + S_{58} \frac{a_8}{a_5}$	$\chi_{5A} = S_{51}a_1 + S_{52}a_2 + S_{53}a_3 + S_{54}a_4$	XPI- V ₅ H

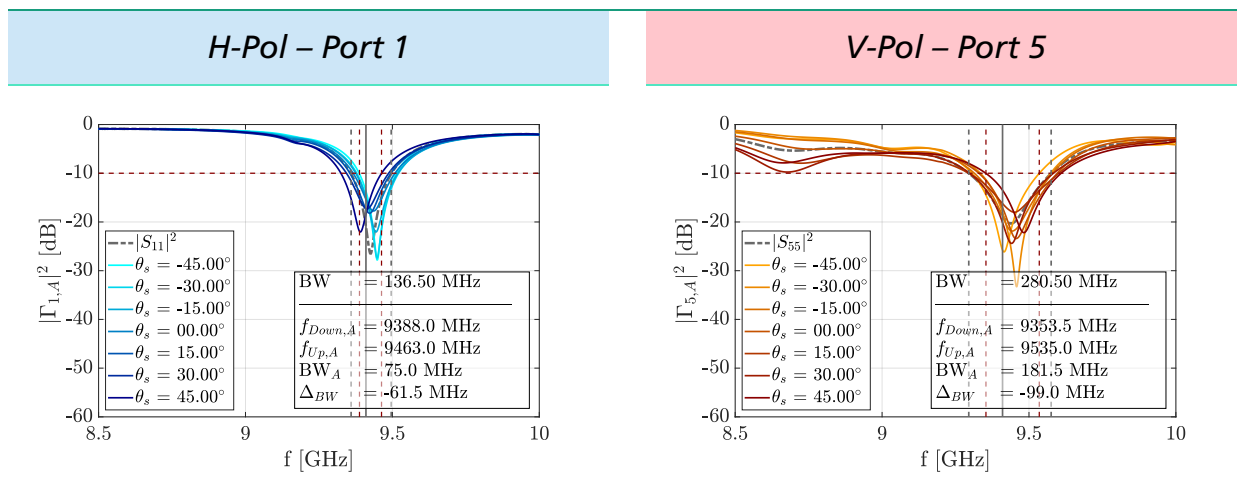
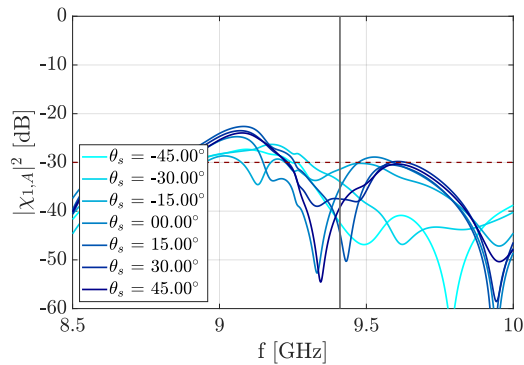
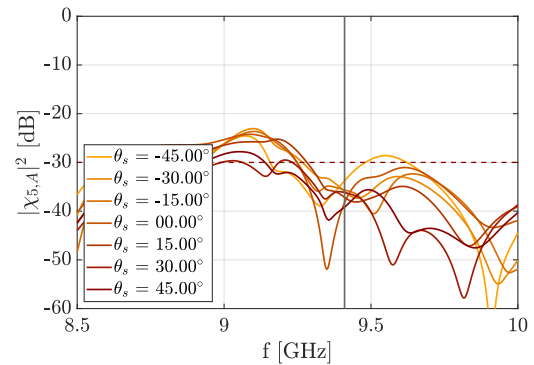


Table 5.23 – 4x4 Imaged Sub-array with Integrated Feed-net (Active Reflection Coefficients)

By considering the active performance of the array, a significant bandwidth reduction and element matching can be observed at Port – 1 (H_1) and 5 (V_1) as in Table 5.23. If all the co-polar ports are taken into account, and the maximum f_{Down} and minimum f_{Up} are used to compute the *effective active bandwidth* for $\theta_s = \pm 45$, 73.50 MHz for the H-Pol and 159 MHz for V-Pol are obtained.

If the same process is repeated using all the ports, the final *effective active bandwidth* of the sub-array is reduced to 73.50 MHz at a *central frequency* (f_c) of 9.425 GHz (more details are reported in Appendix D).

H-Pol – Port 1**V-Pol – Port 5****Table 5.24 – 4x4 Imaged Sub-array with Integrated Feed-net (Active Cross-polar Port Isolations)**

The isolation of a specific port when the orthogonal ports are active decreases by 10 dB with respect to the static case. At worst, the active isolations reach values slightly over 31 dB for the H-Pol and 34 dB for the V-Pol feeding network. The 3 dB imbalance can be seen as a result of the increased meandering of the H-Pol feed-net, which increases the coupled radiation when the V-Ports are excited. Nonetheless, the reported active isolations still signify a performance in line with the needs of provide of a PAR weather radar operating in ATAR mode.

5.4.3 Comparative Simulation

Finally, after a comparative simulation with Ansys HFSS for cross-validation has been forwarded for manufacturing to advance the validation via instrumental measurements. Table 5.25 shows identical performance of the some S-parameters for the 4x4 imaged sub-array simulated with CST MWS and Ansys HFSS.

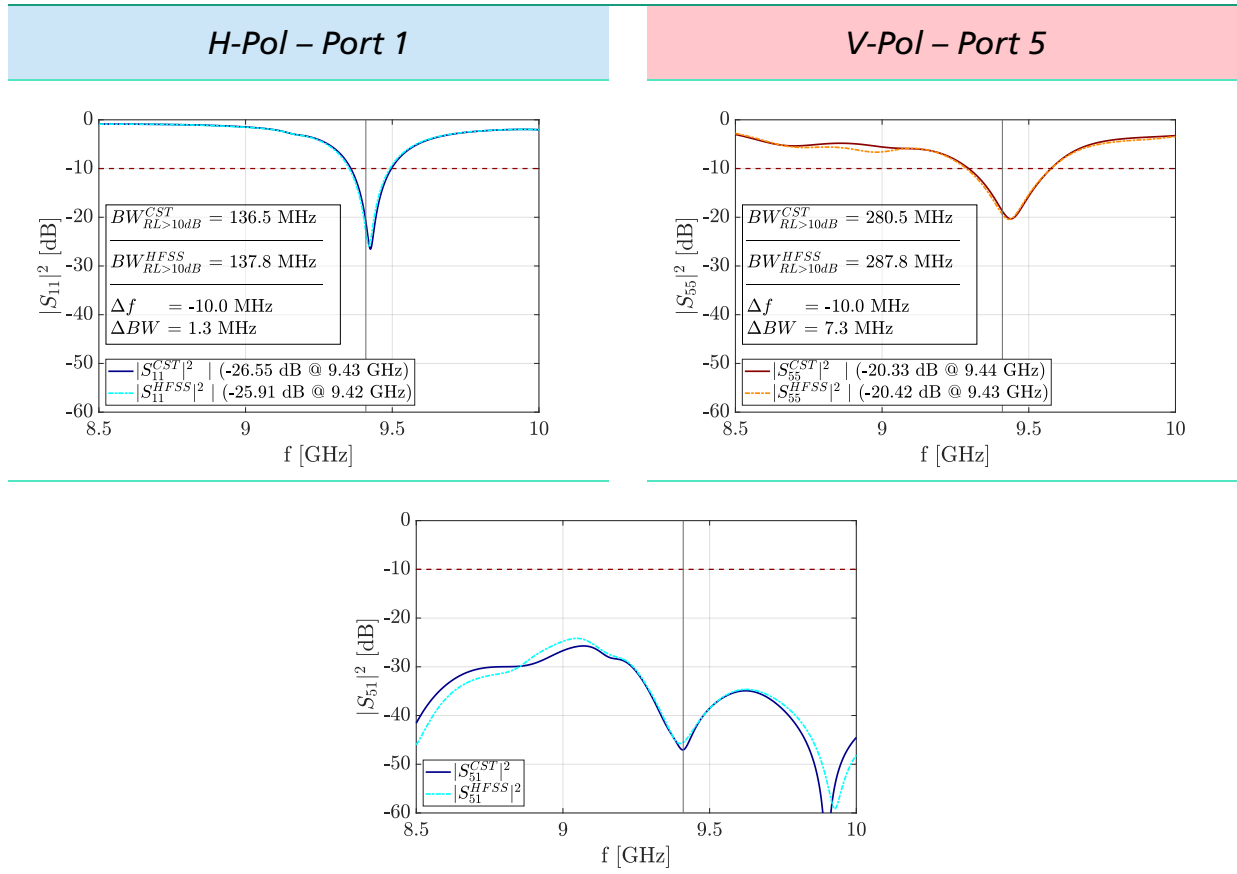


Table 5.25 – 4x4 Imaged Sub-array with Integrated Feed-net (S-Parameters Comparison)

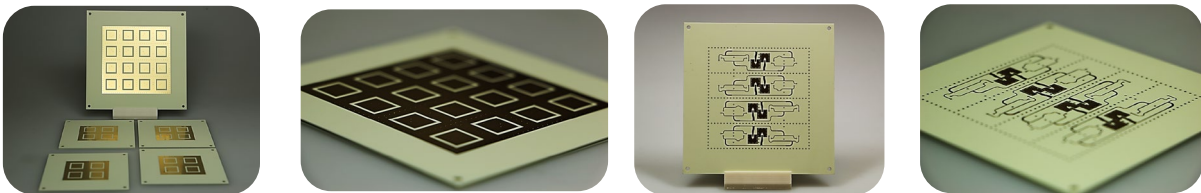


Figure 5-12 – Manufactured Sub-Arrays with Integrated Feeding Networks

5.5 Prospective Improvements

As it can be seen in Figure 5-9, due to board surface, feeding network implementation for a 8x8 sub-array can be hardly achieved. To alleviate the issue, a change of the feeding stage substrate with higher ϵ_r is preferred to achieve more compact design (due to $\lambda_{eff} \downarrow$) and minimize the radiation losses [57]. A greater feed network would increase the insertion loss (3 dB for every splitting stage) but it would also provide a bandwidth enlargement. Additionally, the usage of longer lines would increase microstripline losses ($\eta_{array} \downarrow$) but less power would be reflected to the port, improving the port matching.

To remove the effect of feed-net cross-talk, the H and V feeding networks could be placed in different layers using stripline technology (Table 5.1 a) at the expense of increased cost due to the addition of blinded or buried vias. Alternatively, a GCPW feed-net could be also used if smaller values of Z_{REF} were selected or if a different substrate was chosen so that microstrip lines and ground gaps had dimensions larger than 0.1 mm.

Following these recommendations, in this work a hybrid topology has been investigated: a *grounded microstripline feeding network* (shown in Figure 5-13). Although improvements of 1.2 dB in XPD at the co-polar peak throughout the scanning range have been observed in simulation, the usage of surrounding vias (cost \uparrow) and the increased design complexity have been the main factors to discard this proposal.

Finally, for larger sub-arrays a shielded microstripline with elevated ground (see Figure 5-14) would be worth further investigation.

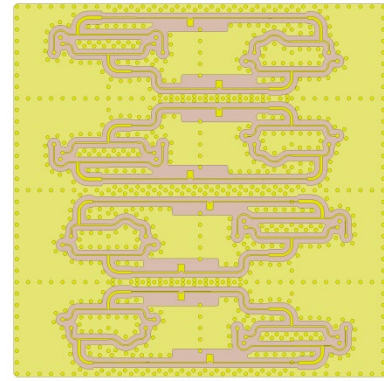


Figure 5-13 – 4x4 Imaged Sub-Array with Grounded Feeding Network

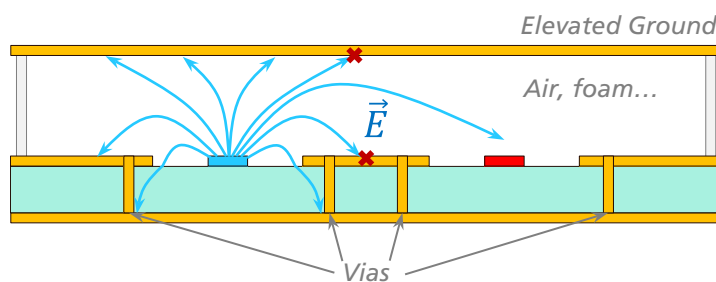


Figure 5-14 – Minimization of cross-talk through an Elevated Ground Plane and Shield

Chapter 6 - Measurements and Validation

This chapter is devoted to the instrumental validation of the 4x4 baseline and imaged sub-arrays. Upon successful simulations a manufactured prototype has been analyzed through different measurement runs, allowing to establish further comparisons between simulated and measured performance of S-parameters and polarimetric performance.

Through an initial overview of the proposed measurement methodology, a validation discussion follows, providing physical insight behind measurement disagreements with simulations. Guidelines and suggestions for design and measurements of future polarimetric antenna designs are also provided taking into account the challenges faced in the validation stage.

The proposed design in Chapter 5 has been manufactured and the PCB has been connectorized. Additionally a measurement assembly has been built to place and align the antenna *antenna under test* (AUT) with the rotation axis of the motorized measurement unit.

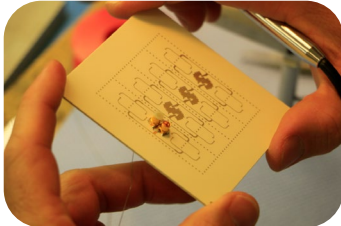
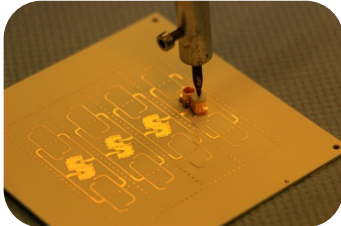
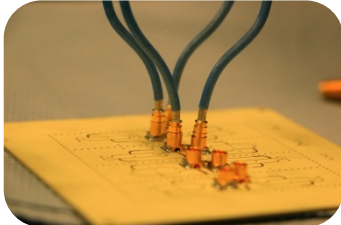
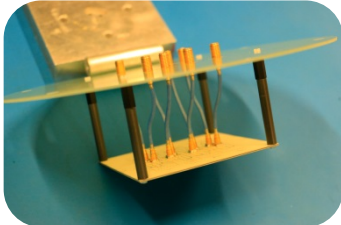
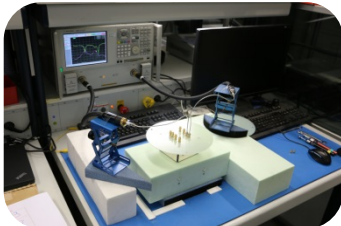

Connectorization		
Antenna Assembly		
Measurement Set-up		

Table 6.1 – Manufacturing and Measurement Highlights

6.1 Validation Methodology

The manufactured PCBs have been validated by instrumental measurement campaigns and microscope visual inspections. The subject of validation has been the concordance of simulated and measured S-Parameters performance and most importantly the low cross-polarization feature of the sub-array.

Visual inspections (see Figure 6-1) have been performed to quantify the manufacturing tolerances in etching (so-called, *under-* or *over-etching*). For this narrowband design, tolerances in the dielectric permittivity or in patch size can remarkably affect the antenna performance (central frequency and polarimetric performance).

Based on the observed tolerances, the EM antenna model can be updated and simulated again. If the simulation results match with measurements, a second design iteration can compensate for the tolerances of a specific manufacturer.

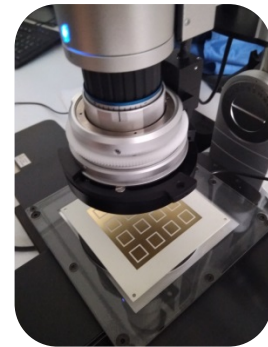


Figure 6-1 – Microscope Antenna Inspection

6.2 Set-up Description

Two measurement runs were performed to obtain the S-Parameters and the Far-Field patterns. Prior to the measurements, efforts have been devoted on developing consistent and standardized set-ups for measurements. This work mainly involved developing a mounting mechanism for the antenna and cables, as well as a *polarimetric check* of available facilities (i.e. an assessment of the measurable levels of cross-polarization in the measurement chamber). Other aspects of the two measurements runs are discussed in the following sections.

6.2.1 S-Parameters Measurements

Using a 2-port *Vector Network Analyzer* (VNA), the S-parameters of the 8-port sub-arrays have been retrieved. The initial calibration of the device has been based on an ad-hoc TRL calibration kit, to place the reference plane of the measurements right after the connector and its transition line.

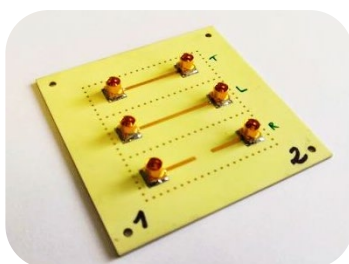


Figure 6-2 – Ad-hoc TRL calibration kit

The instrument calibration was performed through a series of three measurements of loading conditions (namely THROUGH, LINE and REFLECTION, as depicted in Figure 6-2). In this way, the calibration accounts for the transition from the connector to the microstrip line.

To standardize the measurement runs and ensure repeatability conditions at all ports, special emphasis has been placed on cable fixation as shown in Figure 6-3.

The *Antenna Under Test* (AUT) has been placed on a foam material with $\epsilon_r \cong 1$ and at a total distance from the bench greater than $3\lambda_0$. In this way, the set-up has been simplified to perform the measurement in the laboratory instead of the anechoic chamber, where other pattern measurements were on-going.

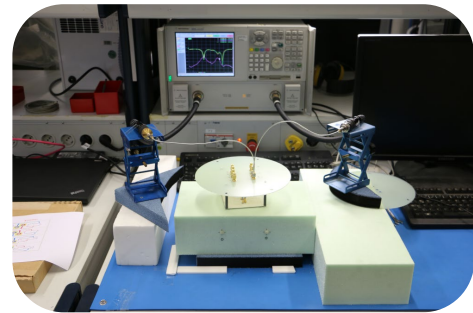
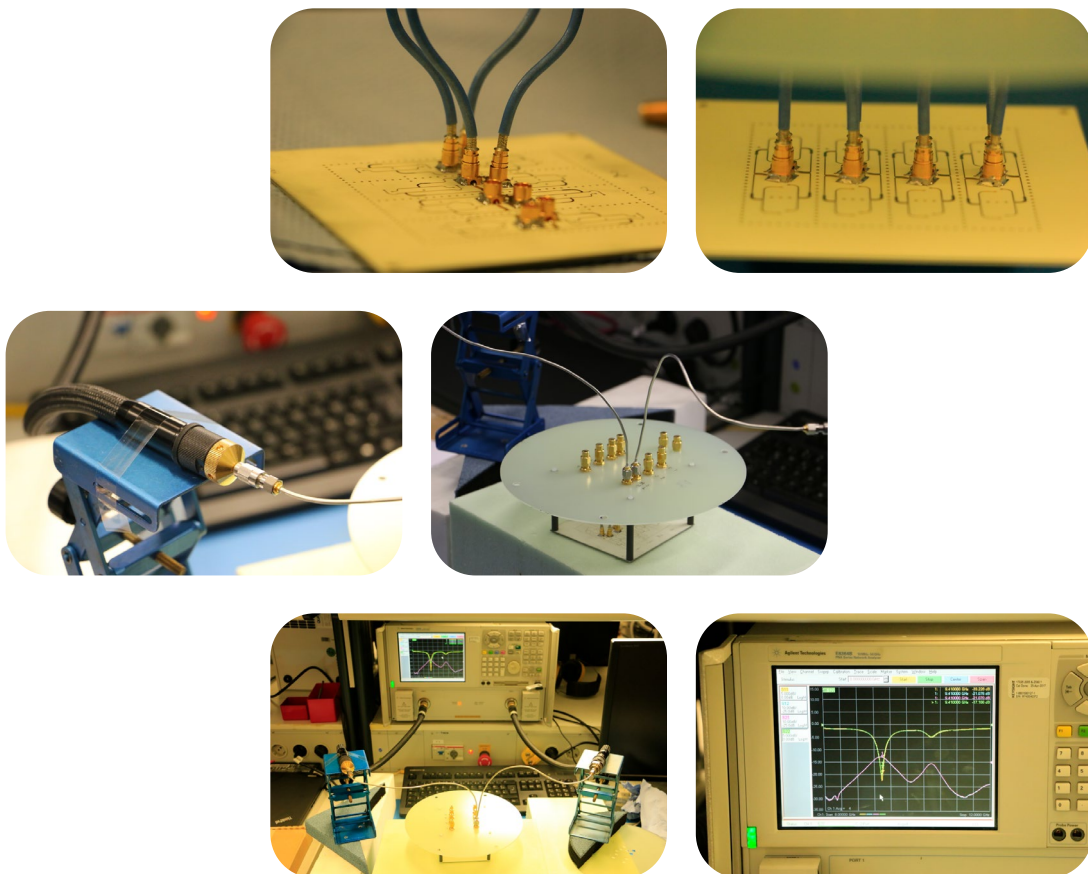


Figure 6-3 – S-Parameter Measurement Set-up

By loading the unused ports with a 50Ω loads and performing measurements in pairs, a total of 28 measurements have been performed to fill the 64 element matrix. Further post processing has been implemented to combine the measurements and obtain the *active S-parameters* (listed in Appendix E).



6.2.2 Anechoic Chamber Measurements

An *anechoic chamber* consists of a regular room whose walls, floor and ceiling are covered by *Radar Absorbing Material* (RAM). A total of three rotating axes operated by motorized units allow to measure the far-field electric field components of a given AUT. A sketch of the chamber is depicted in Figure 6-4.

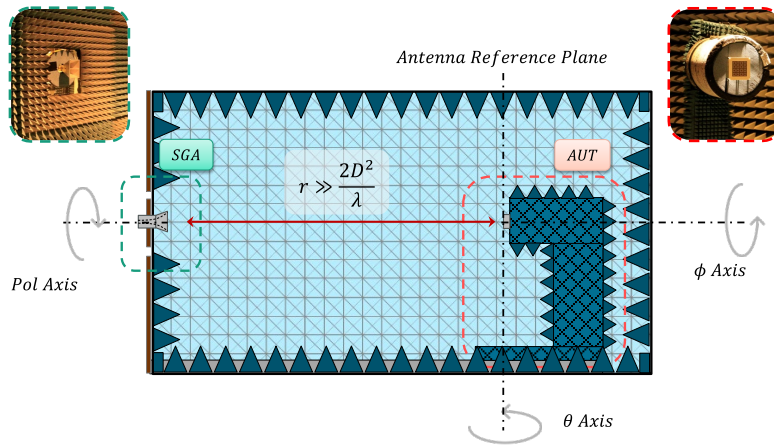


Figure 6-4 – Simplified Anechoic Chamber of AEM Department (Fraunhofer FHR)

The *Standard Gain Antenna* (SGA) and the AUT have been connected to the VNA Port 1 and Port 2 respectively. By measuring the S_{21} parameter, the SGA acts as the *transmitter* and the AUT as the *receiver* and the electric field component for a specific θ and ϕ is measured for a total of 1601 frequency points over a span from 8 to 12 GHz. Through a 90° on-axis rotation of the SGA, the E_θ and E_ϕ components are measured. An *Electronic Control Unit* (ECU) supported by remote VNA control routines allows for fully automated measurements. Raw data is then post-processed to obtain the polarimetric performance. The process is summarized in the following drawing:

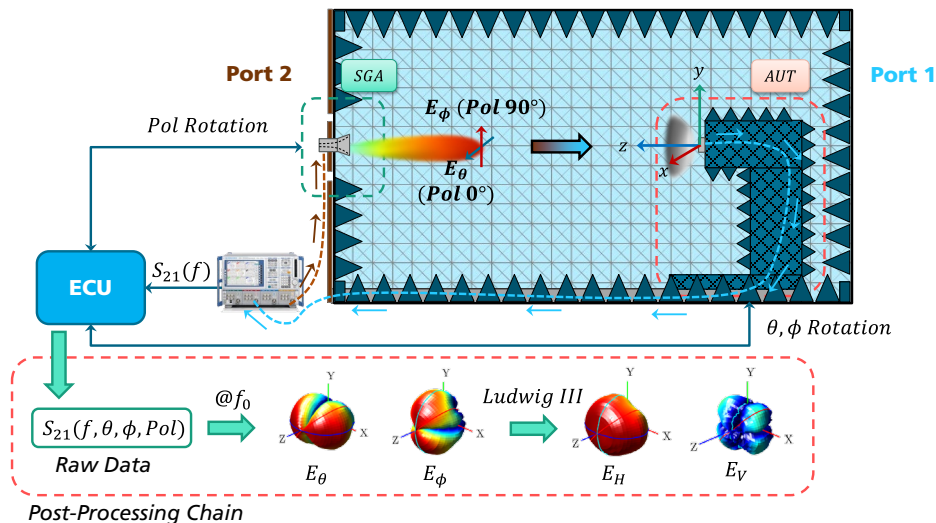

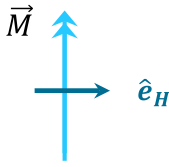


Figure 6-5 – Measurement Process for Cross-polarization Assessment

Though direct Ludwig III measurements are technically possible given the measurement set-up the Ludwig III definition of horizontal and vertical polarizations has been computationally applied as a post-processing stage. Since for this study, its definition is $\hat{e}_H = \hat{x}$ and $\hat{e}_V = \hat{y}$ at broadside, for magnetic sources such as the (magnetic) dipoles of the patch antennas, the polarization terms according to the Ludwig III definition [63] follows:

\hat{x} Magnetic Source	\hat{y} Magnetic Source
	
$\hat{e}_H = \hat{e}_{Cross} = \cos \phi \hat{\theta} - \sin \phi \hat{\phi}$	$\hat{e}_H = \hat{e}_{Co} = \cos \phi \hat{\theta} - \sin \phi \hat{\phi}$
$\hat{e}_V = \hat{e}_{Co} = \sin \phi \hat{\theta} + \cos \phi \hat{\phi}$	$\hat{e}_V = \hat{e}_{Cross} = \sin \phi \hat{\theta} + \cos \phi \hat{\phi}$

Where the \hat{e}_V is obtained by rotating \hat{e}_H by 90° about the \hat{z} axis.

Time-gating the S_{21} Transmission

In order to improve the accuracy of the measurements, the S_{21} measurement has been time-gated reducing all the environment reflections. Through a time gate, the frequency spectrum is no longer affected by ripples and more stable measurements can be obtained (see Figure 6-6).

Handled reflections are not limited to reflected signals in the anechoic chamber. Also reflections within the cables connecting the AUT to the VNA can be removed with this technique.

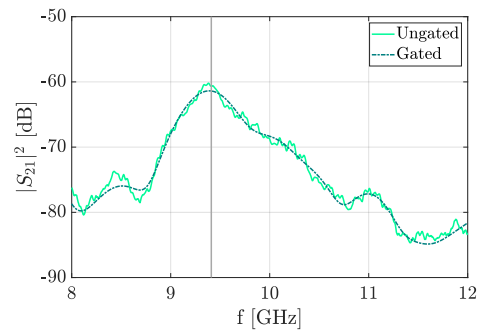


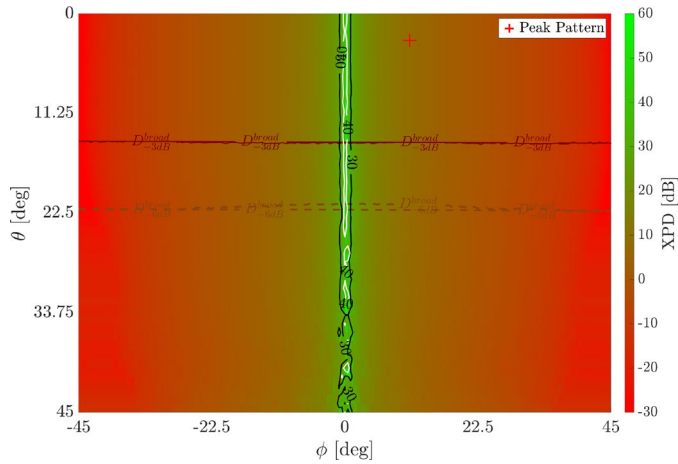
Figure 6-6 – Comparison of Original and Time-gated Measurements

Polarimetric Assessment of the SGA

While the S-parameters measurements for the 4x4 array do not involve specific complexity, the polarimetric study of the radiated fields was found to be limited by the polarimetric purity performance of the probe (a reference horn antenna). To measure very low cross-polarization values a perfect polarimetric radiator at broadside ideally should have been used. Yet, practical imperfections have to be expected.

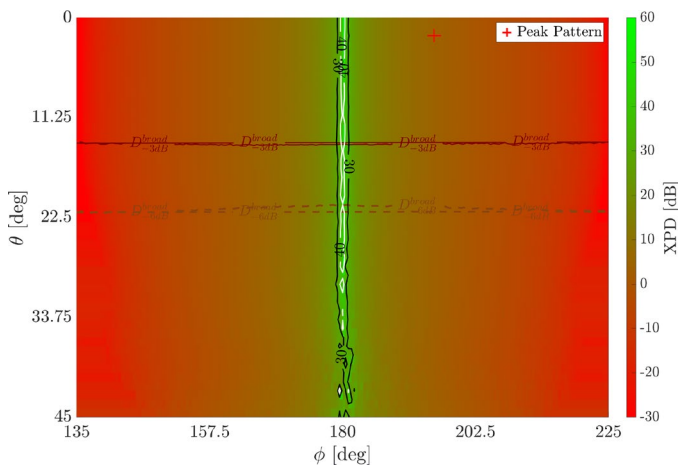
Therefore, the usage of a dipole tuned to the frequency of operation (9.41 GHz) was been initially proposed. At X-Band however, tuning the phase difference of the dipole arms and other manufacturing aspects are practically problematic. For this reason the usage of dipoles has been avoided. Instead, a *reference ridged horn* antenna has been used and the lower polarimetric

bound measured. Small geometrical imperfections at the horn aperture as well as in the internal dipole probe have been found to yield a lower limit of XPD_{meas} of 56.2 dB. Iterative measurements with three different horn antennas have been performed to assess this boundary. Measurement results in Figure 6-7 and Figure 6-8 show measurement discrepancies between two ridged horn antennas due to flipping up and down the AUT (a 180° rotation around the its longitudinal axis). In this context, selecting the best case has allowed to increase the XPD bound by 10 dB.



<i>SGA</i>	<i>BBHA 9120 C</i>
<i>AUT</i>	<i>NARDA 640</i>
$\theta \in [00^\circ, 45^\circ]$	$\Delta\theta = 1^\circ$
$\phi \in [-45^\circ, 45^\circ]$	$\Delta\phi = 1^\circ$
$XPD(0,0) = 45.64 \text{ dB}$	

Figure 6-7 – High Resolution Measurement of XPD Diagram of NARDA – V-Pol



<i>SGA</i>	<i>BBHA 9120 C</i>
<i>AUT</i>	<i>NARDA 640</i>
$\theta \in [00^\circ, 45^\circ]$	$\Delta\theta = 1^\circ$
$\phi \in [135^\circ, 225^\circ]$	$\Delta\phi = 1^\circ$
$XPD(0, 180) = 56.2 \text{ dB}$	

Figure 6-8 – High Resolution Measurement of XPD Diagram from NARDA – V-Pol (up-down flip)

The XPD upper bound set by the available reference horns is not an issue for the due measurements, since cross-polarization of a single row of imaged patches does not reach XPD values of over 50 dB. After analytically beamforming, thanks to the feed rotation technique, cross-polarized components in the principal planes are suppressed numerically and reach values up to 60 dB of XPD independently from the measurement bounds.

Although small angular adjustments of 0.1..0.5° have provided maximum XPD values up to 60 dB, the BBHA 9120 C reference gain horn has been consistently positioned to the real 0° tilt.

Antenna Positioning

In order to set the geometrical tilt to 0° degrees, a simple adjustment was performed using a *spirit level* and a *plumb line* as shown in Figure 6-9.



Figure 6-9 – Antenna Positioning using a Spirit Level (Top) and a Plumb Line (Bottom)

This measurement process has been found to yield consistent readings and acceptable accuracy in spite of the sub-optimal set-up. In order to ensure higher accuracy and measure smaller values of cross-polarized measurements further project activities should focus on optimized measurement procedures for the assessment of low cross-polarization antennas.

6.3 S-Parameters

Despite that a total of 8 antenna designs were manufactured for this work, only the **4x4 baseline** and **4x4 imaged sub-arrays** have been analyzed. For both designs full S-parameters characterization validations of the AUT in terms of matching and isolations have been performed. A small shift in the resonant frequency has been observed for the reflection coefficients ($\Delta f = 50.70 \text{ MHz}$), still preserving acceptable matching at 9.41 GHz .

Note: in the following sub-sections only selected results will be shown. The full result is reported in Appendices E and F.

6.3.1 Scattering Measurements for the 4x4 Baseline Sub-Array

Related to the simulation results in sub-section 5.4.1, selected measurements of the S-parameters for the 4x4 baseline sub-array follow.

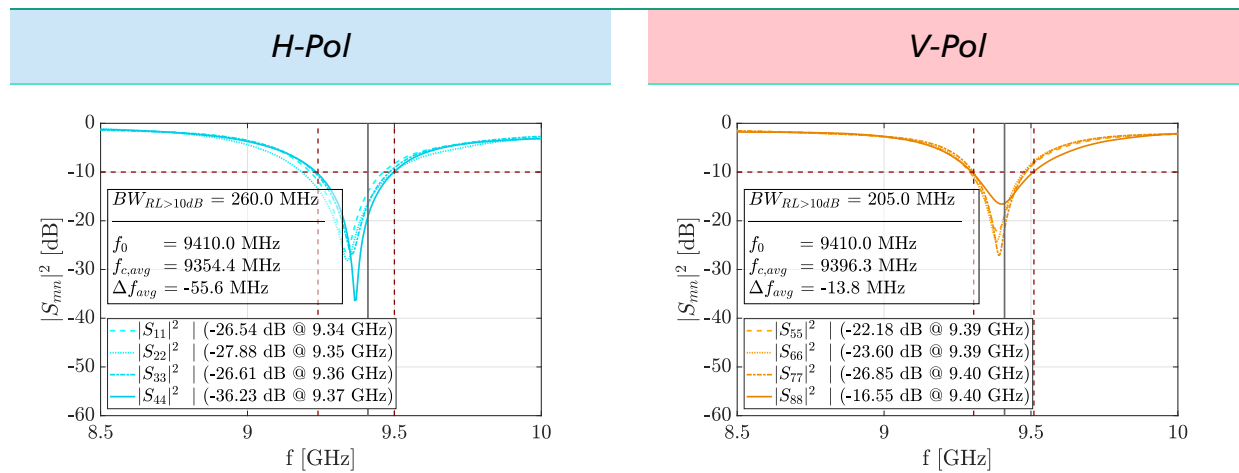


Table 6.2 – 4x4 Baseline Sub-array with Integrated Feed-net (Measured Reflection Coefficients)

Comparing measurements port 1 and port 5 with the simulated reflection coefficients, a remarkable shift in the central frequency can be easily spotted (see Table 6.3). Although the shift is around 70 MHz for H-Pol Port 1, the port is still matched. Smaller shifts are also measured for the imaged sub-array depending on manufacturing tolerances (see section 6.5).

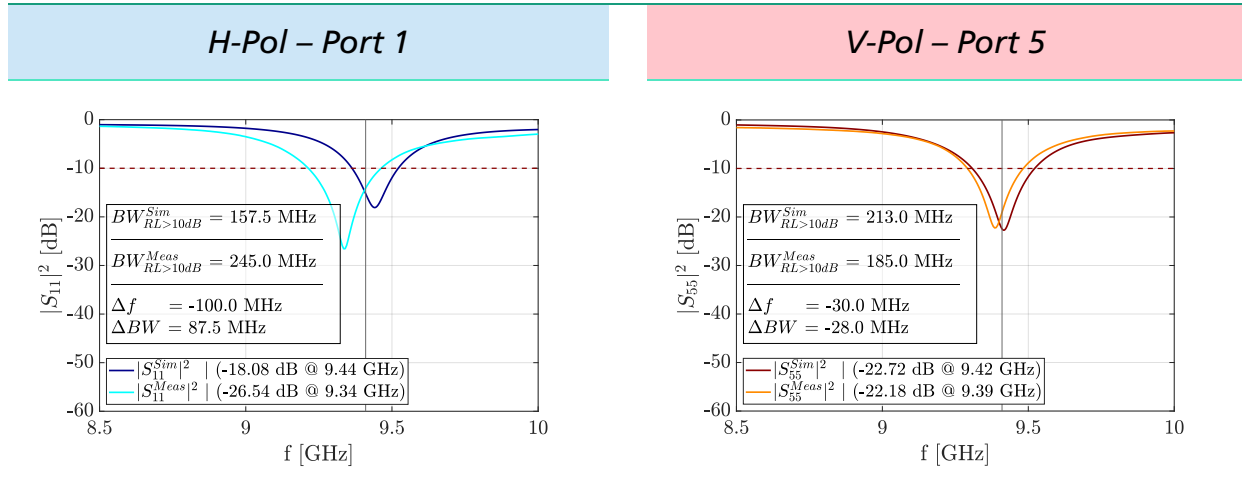


Table 6.3 – 4x4 Baseline Sub-array with Integrated Feed-net (Reflection Coefficients, Simulation vs Measurements)

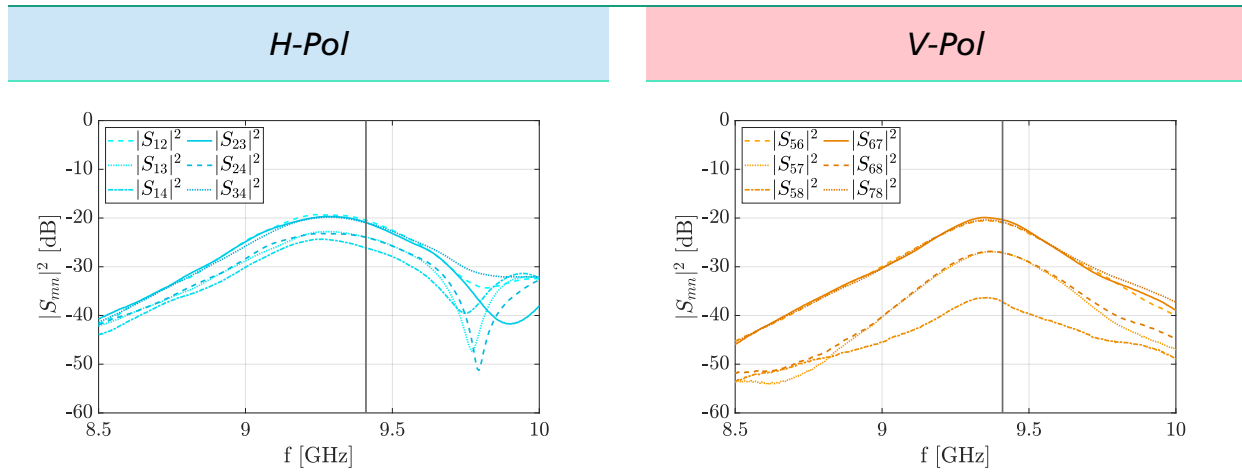


Table 6.4 – 4x4 Baseline Sub-array with Integrated Feed-net (Measured Co-polar Port Isolations)

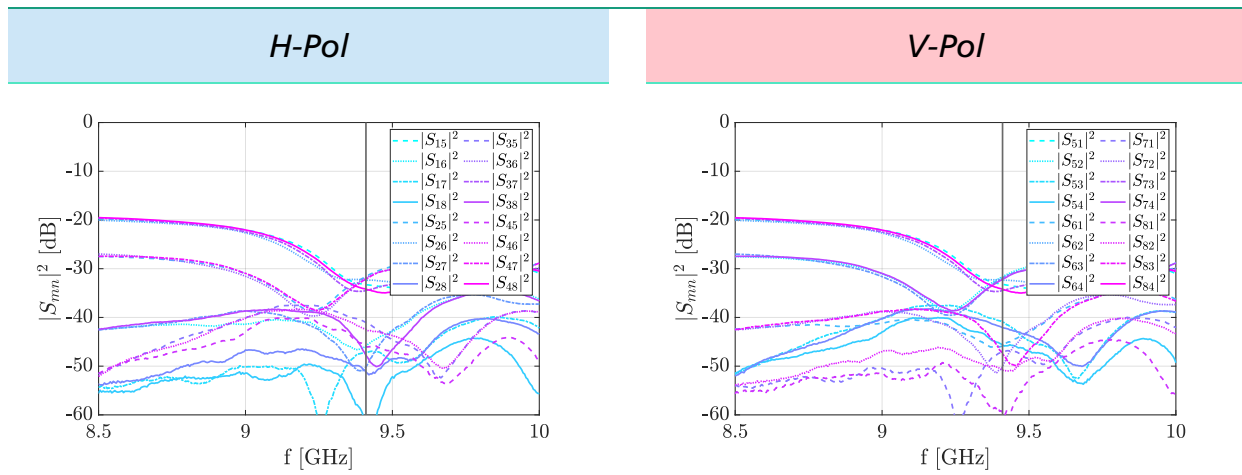


Table 6.5 – 4x4 Baseline Sub-array with Integrated Feed-net (Measured Cross-polar Port Isolations)

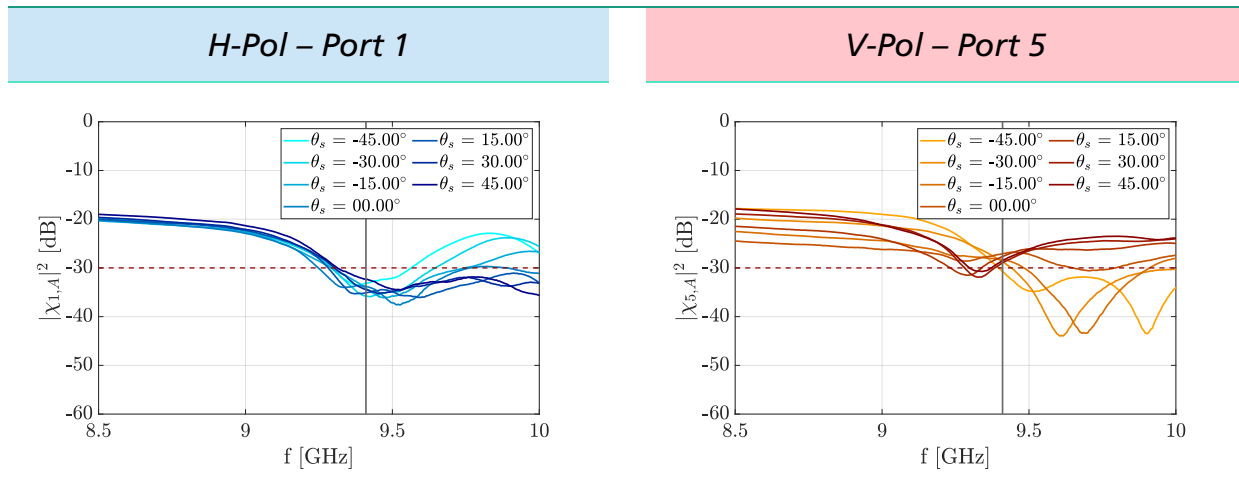


Table 6.6 – 4x4 Baseline Sub-array with Integrated Feed-net (Measured Active Cross-polar Port Isolations)

In agreement with simulations, the 4x4 baseline sub-array design has limited performance concerning the cross-polar port isolation, with detrimental impact on reaching the XPD and $IXPD^{6dB}$ requirements (however if XPI is below 30 dB, the XPD can still be greater than 30 dB, as the cross-polarization cancellation occurs on the radiated patterns).

6.3.2 Scattering Measurements for the 4x4 Imaged Sub-Array

As in the previous sub-section, the selected measured S-parameters for the 4x4 imaged sub-array follow, with specific emphasis on the active S-Parameters that allow computing the effective active bandwidth for the H and V channels.

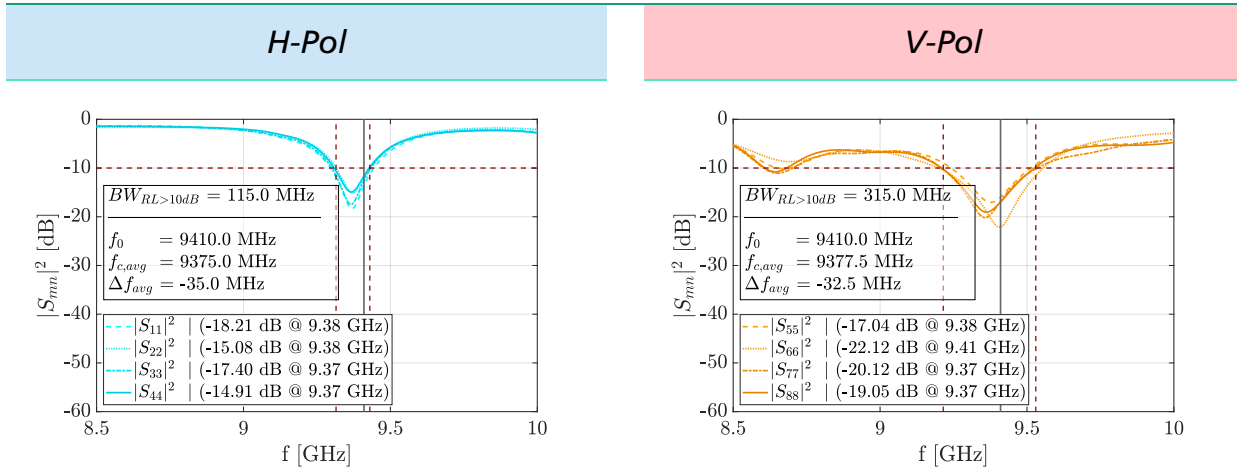


Table 6.7 – 4x4 Imaged Sub-array with Integrated Feed-net (Measured Reflection Coefficients)

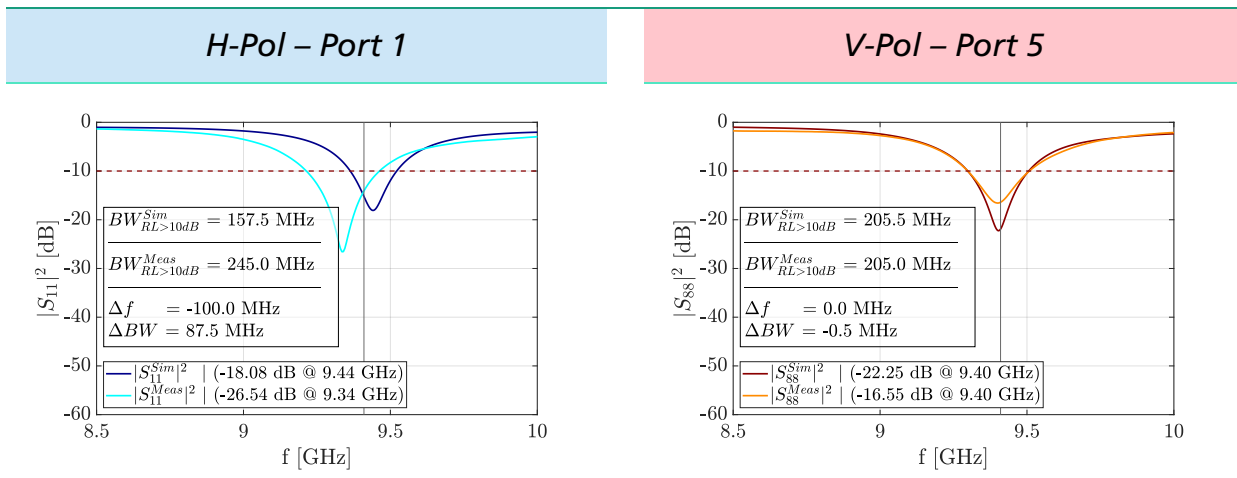
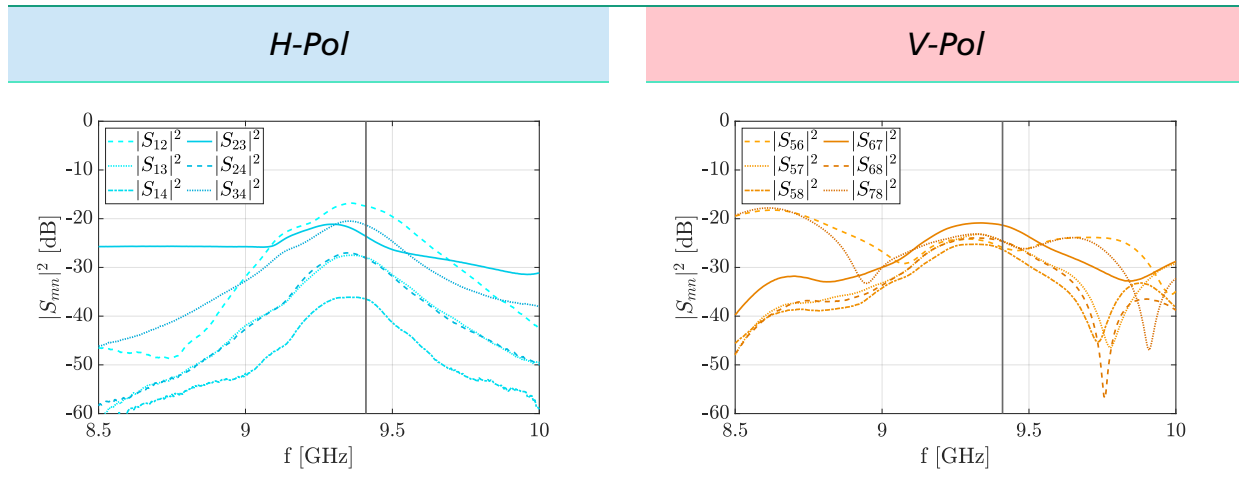
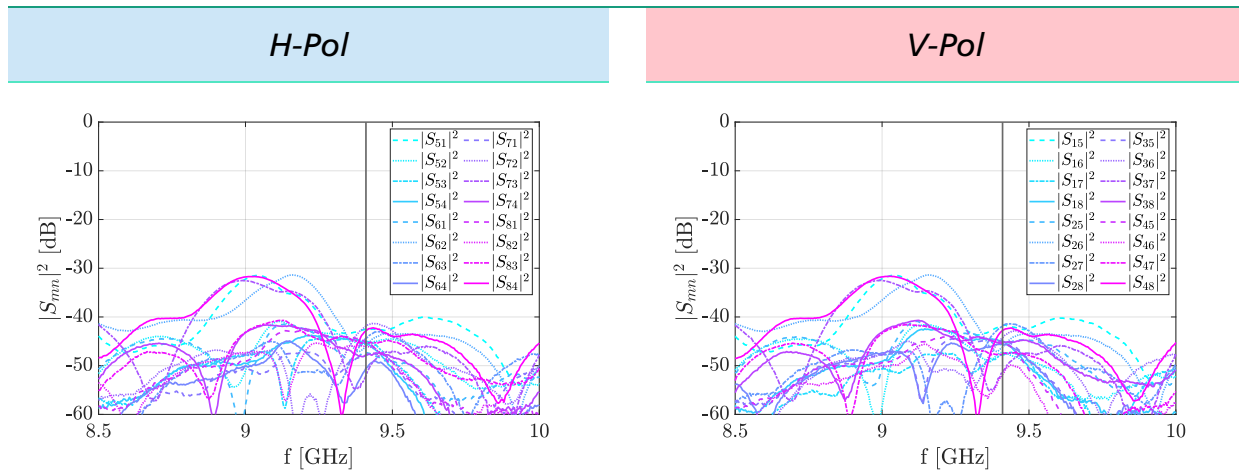


Table 6.8 – 4x4 Imaged Sub-array with Integrated Feed-net (Reflection Coefficients – Simulation vs Measurements)


Table 6.9 – 4x4 Imaged Sub-array with Integrated Feed-net (Measured Co-polar Port Isolations)

Table 6.10 – 4x4 Imaged Sub-array with Integrated Feed-net (Measured Cross-polar Port Isolations)

The main outcomes based on reported measurements follow:

- Return losses at $f_0 = 9.41 \text{ GHz}$ are over 15 dB for all the ports.
- Bandwidths are around 115 and 315 MHz for H and V channels considering the most restrictive port using the $RL > 10 \text{ dB}$ condition.
- If relaxing the condition down to 7 dB , bandwidths increase up to 200 and 510 MHz for the H and V ports respectively.
- The isolations of co-polar ports are at worst 17 dB , which indicates that no undesired modes are propagating.
- Isolations of cross-polar ports (XPI) are over 40 dB for the worst case.
- Despite the stated frequency shift, limited to static S-parameters measurements, the manufactured design is validated.

Using the same ports specification as in sub-section 5.3.2, the Active S-Parameters have been computed and the *effective active bandwidth* retrieved. For illustration, two out of eight ports are shown in Table 6.11.

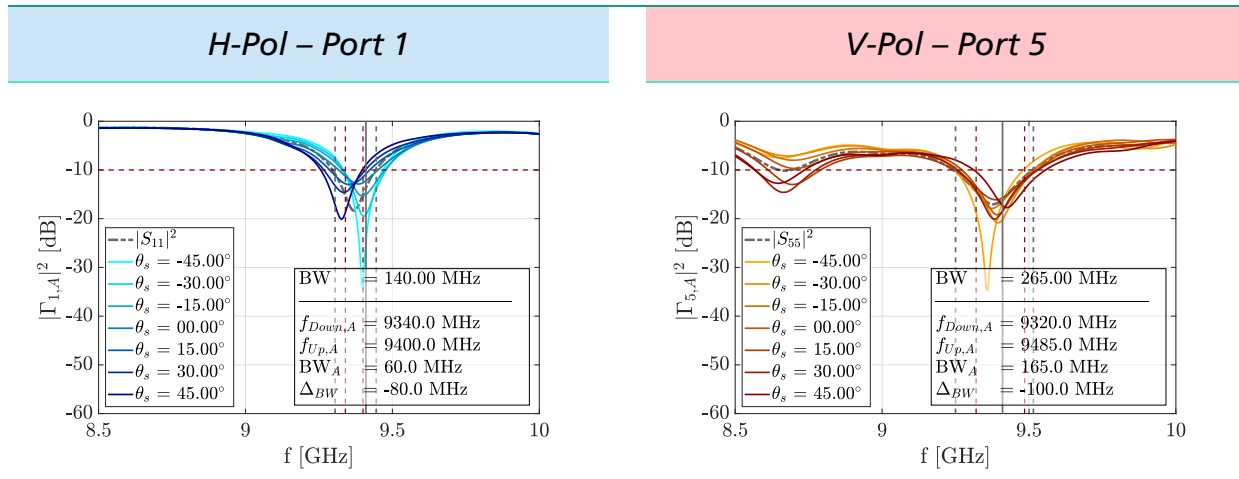


Table 6.11 – 4x4 Imaged Sub-array with Integrated Feed-net (Measured Active Reflection Coefficients)

Taking into account the co-polar ports the maximum f_{Down} and minimum f_{Up} are used to compute the *effective active bandwidth* for $\theta_s = \pm 45^\circ$, yielding *155 MHz* for the V-polarization (in simulations *159 MHz*) and no effective bandwidth for the H-polarization under the RL over 10 dB condition. This is caused by the port 2 whose ARC is over 10 dB for θ_s below -30° as shown in the following figure:

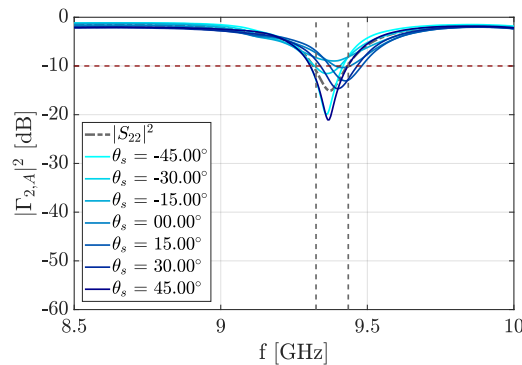


Figure 6-10 – Mismatched ARC for measured Port 2 (RL > 10 dB)

Instead, the RL can be relaxed up to 7 dB, providing 110 MHz of *effective active bandwidth* for the port 2 (see textbox from Figure 6-11)

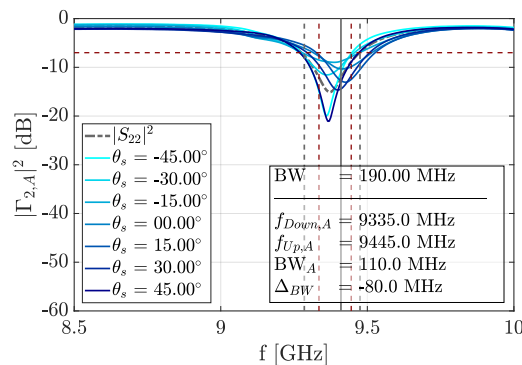


Figure 6-11 – Matched ARC for measured Port 2 (RL > 7 dB)

This individual event shows the critical performance of phased arrays under scanning conditions. For the WRAD project this also suggests the need of increased bandwidth and better matching in further antenna designs. Improved bandwidth as discussed in section 4.1 comes with a lower ϵ_r substrate for the radiation stage or by increasing the losses of the feeding network. On the other hand, better matching can be achieved by compensating the manufacturing tolerances and optimizing even more the model.

As for the present design, taking into account all the ports and the RL over 7 dB condition, the H-Pol ports limit the antenna performance, being 105 MHz the total effective bandwidth of the antenna at a f_c of 9.37 GHz (see more details in Appendix F). This represents a f_c shift of 55 MHz with respect to the 9.425 GHz of the simulation results (see sub-section 5.4.2).

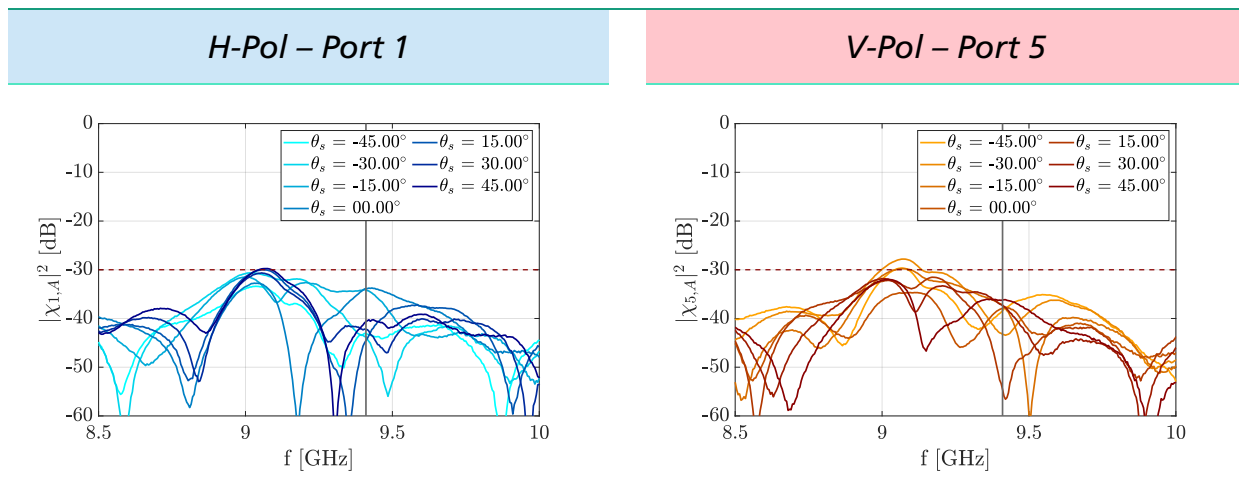


Table 6.12 – 4x4 Baseline Sub-array with Integrated Feed-net (Measured Active Cross-pol Port Isolations)

Finally, in agreement with the CST MWS simulations, the isolations of a specific port when the orthogonal ports are active decrease by above 10 dB with respect to the static case. At worst the active isolations reach values slightly over 33 dB for the H-Pol and 35 dB for the V-Pol feeding networks (in simulations, 31 dB and 34 dB respectively).

6.4 Beamforming

Being the AESA circuitry still under development, analytical beamforming has been implemented to assess the array performance. For this reason a total of 8 measurements (along a time span of about 9 hours each) have been run for both 4x4 sub-arrays. The measured angles and their resolution follow:

$\theta \in [0^\circ, 135^\circ]$	$\Delta\theta = 5^\circ$
$\phi \in [0^\circ, 360^\circ]$	$\Delta\phi = 5^\circ$

Measurements beyond 135° along the θ -axis could not be taken to characterize the entire pattern of the arrays. For this reason, and given the coarse resolution, all the metrics involving full-pattern integrations were discarded, being able to evaluate only the XPD , the $IXPD^{6dB}$ and the mono-scanning performance. An example of the performed analytical beamforming follows:

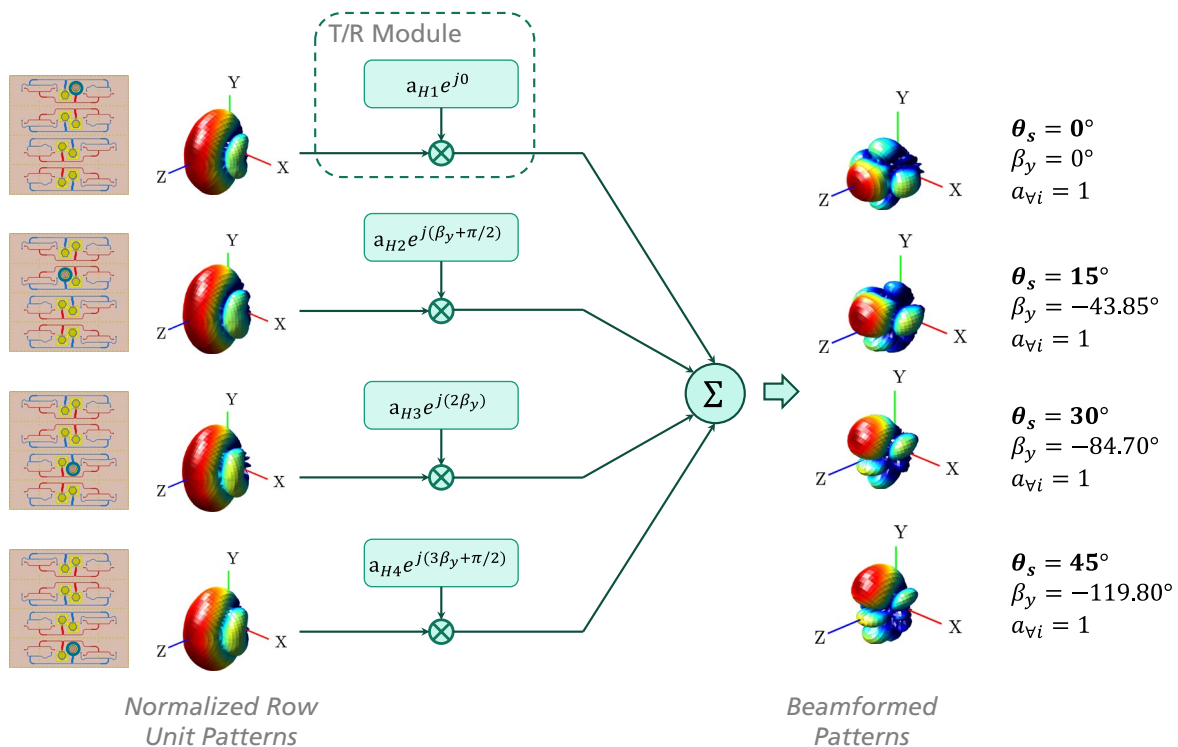


Figure 6-12 – Analytical Beamforming for 4x4 Imaged Sub-Array (H-Pol)

To validate the cross-polarization suppression achieved through feed rotation, the XPD at the copolar beam was measured for each row and then compared to the beamformed case. This was done first for the 4x4 baseline sub-array and then for the imaged case.

4x4 Baseline Sub-array

	H-Pol				V-Pol			
	Row 1	Row 2	Row 3	Row 4	Row 1	Row 2	Row 3	Row 4
XPD_{meas}	30.62 dB	28.16 dB	37.56 dB	32.88 dB	30.10 dB	28.93 dB	30.23 dB	27.85 dB

Table 6.13 – XPD Results by Rows (4x4 Baseline Sub-Array)

As shown in Table 6.13, the individual peak XPD measurements for the baseline architecture already fail to reach the 30 dB requirement. Following these results, a polarimetric assessment is also performed for the scan range of the beamformed patterns (see Table 6.14 and Table 6.15)

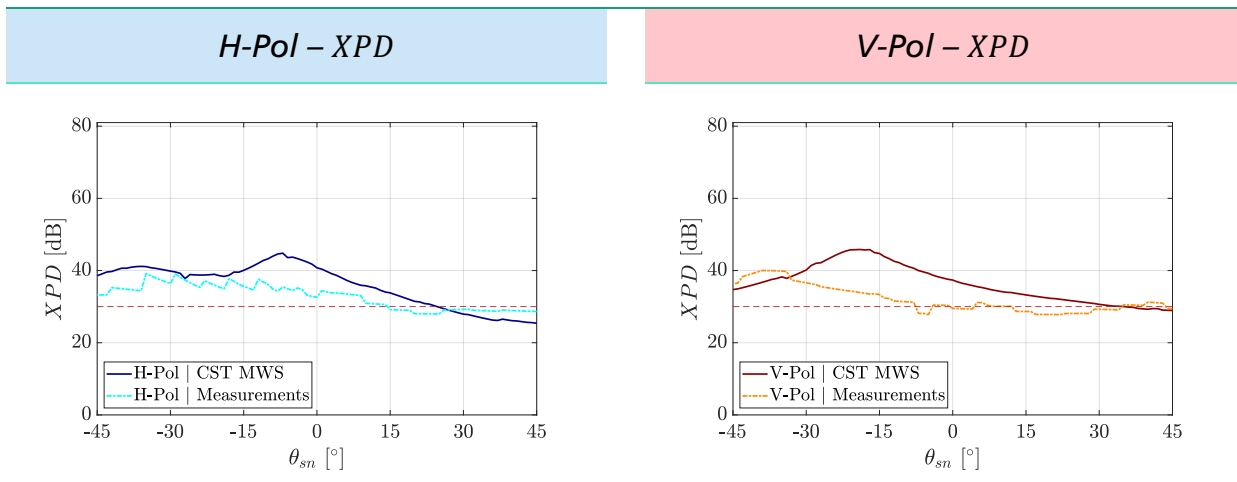


Table 6.14 – 4x4 Baseline Sub-array with Integrated Feed-net, Full-scan XPD Assessment (Simulations vs. Measurements)

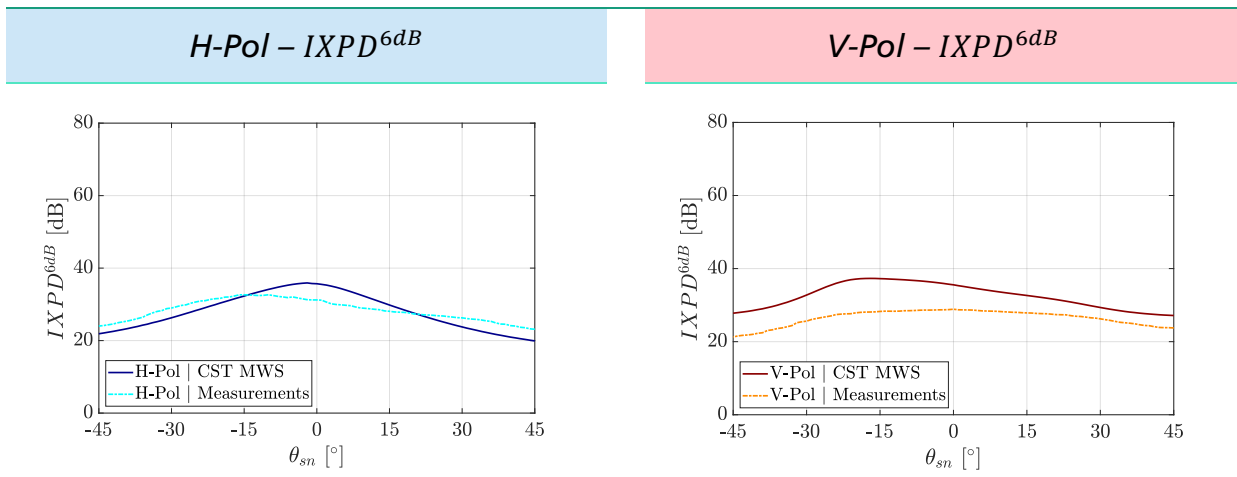


Table 6.15 – 4x4 Baseline Sub-array with Integrated Feed-net, Full-scan IXPd Assessment (Simulations vs. Measurements)

Limited to the $IXPD^{6dB}$ metric, simulated and measured curves follow a similar trend in spite of the measurement resolution. Nonetheless, the measured baseline sub-array fails does not meet the polarimetric requirements at all scanning angles and also presents major imbalances along both polarizations

4x4 Imaged Sub-array

	H-Pol				V-Pol			
	Row 1	Row 2	Row 3	Row 4	Row 1	Row 2	Row 3	Row 4
XPD_{meas}	45.50 dB	42.38 dB	40.14 dB	43.04 dB	47.89 dB	47.99 dB	47.62 dB	50.49 dB

Table 6.16 – XPD Results by Rows (4x4 Imaged Sub-Array)

In comparison with Table 6.13, the peak XPD values in Table 6.16 show that the feed rotation provides a sensible polarimetric improvement at already the row level. However, the measured XPD at the maximum of the co-polar beam for each row, does not actually provide meaningful information, as the maximum pointing direction is not well defined due to broadside nature of the pattern in elevation (see Figure 6-12). In this sense, beamformed patterns have been computed and analyzed along the 1D scan range (see Table 6.17 and Table 6.18).

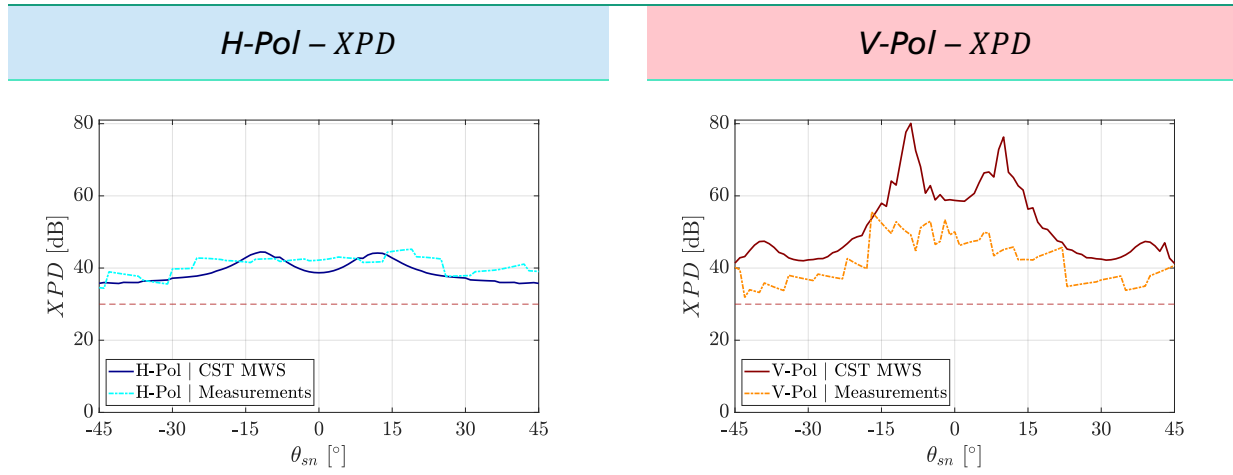


Table 6.17 – 4x4 Imaged Sub-array with Integrated Feed-net, Full-scan XPD Assessment (Simulations vs. Measurements)

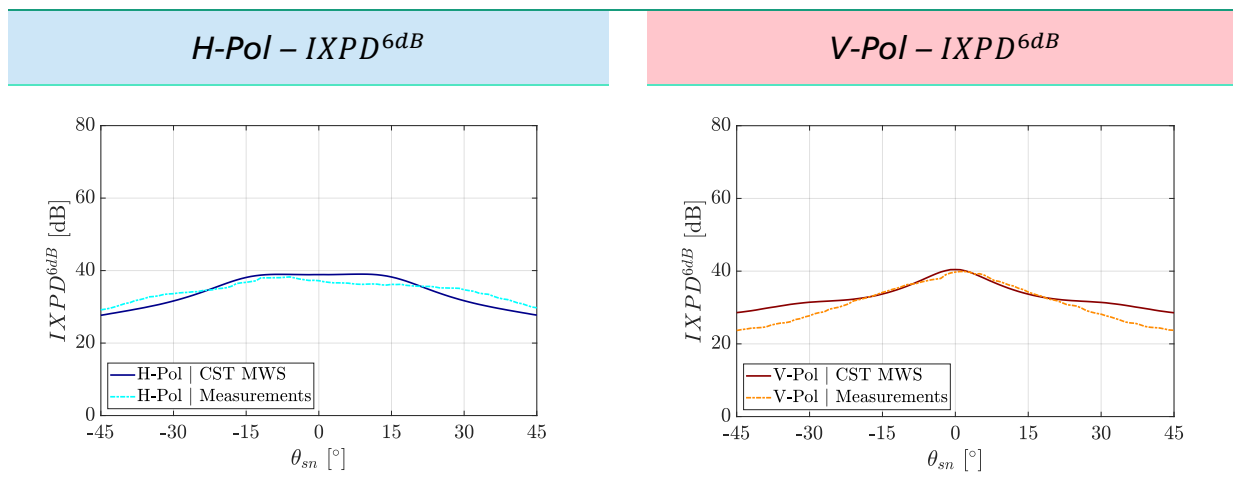


Table 6.18 – 4x4 Imaged Sub-array with Integrated Feed-net, Full-scan IXPD Assessment (Simulations vs. Measurements)

Both measured XPD and $IXPD^{6dB}$ curves show reasonable agreement with simulations. The XPD requirement is achieved throughout the entire scan range, thus validating the design and the feed rotation concept. The $IXPD^{6dB}$ metric shows improvements respect to the baseline sub-array in terms of increased polarimetric performance, scan symmetry and balance between the H- and V-polarizations. However, major disagreements with the simulation results can be noted at the edges of the scan range, where especially the V-polarization provides $IXPD^{6dB}$ values below 30 dB .

A second measurement run with finer angular resolution ($\Delta\theta \downarrow$ and $\Delta\phi \downarrow$) is suggested to increase the accuracy of the beamformed patterns and its the integrated performance metrics. The inaccuracies due to the chosen measurements resolution yield a significant impact on the Z_{DRb} metric, which, although is below the 0.1 dB threshold, does not actually agree with the simulations, but still, reveals similar trend.

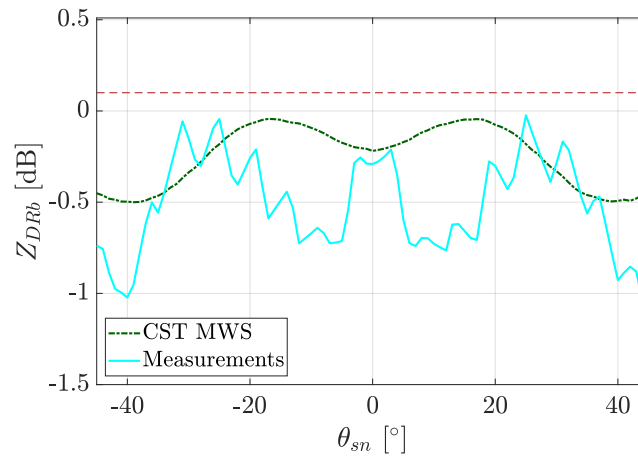


Figure 6-13 – 4x4 Imaged Sub-array with Integrated Feed-net, Full-scan Z_{DRb} Assessment (Simulations vs. Measurements)

6.5 Further Validations

Based on the scattering and pattern measurements, the polarimetric requirements stated in Chapter 1 have been fulfilled. Nonetheless, further investigations have been performed to explain the disagreements with the simulation results.

Considering for instance, in the reflection coefficients, small frequency shifts for the central frequency have been observed. This could be either caused by variations of the dielectric permittivity or due to manufacturing over- or under-etching. Some microscope inspections are shown in Figure 6-14.

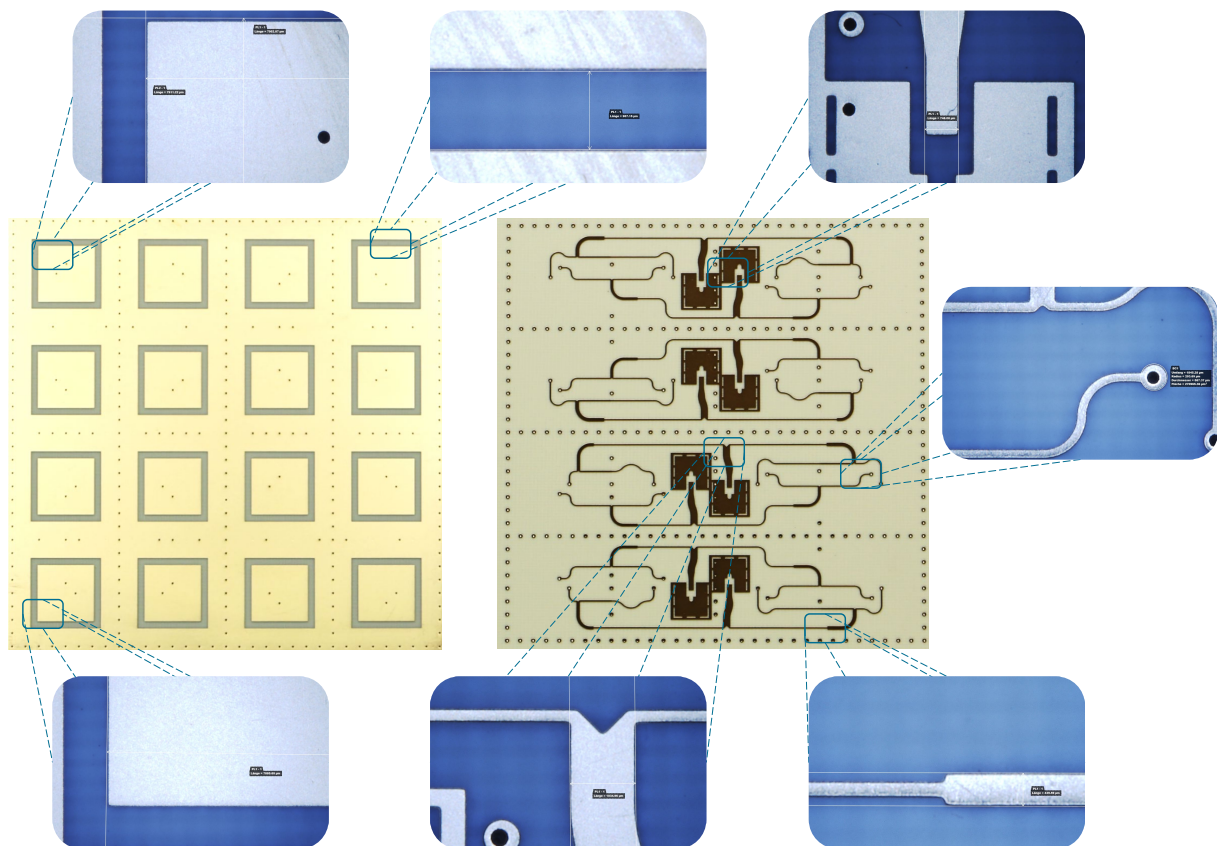


Figure 6-14 – Microscope Measurement Samples

After the measurement runs, microscope investigations have revealed an average of about $10\mu\text{m}$ over-etching variation on the printed elements. In Table 6.19 some parameters of the CAD design in CST MWS are compared to the measured ones, $10\mu\text{m}$ over-etching on average.



Table 6.19 – Microscope Validation and Over-etching

Due to manufacturing imperfections, the etched lines can be thinner or wider, and better tolerances than $\pm 10 \mu m$ imply a sensible increased cost. In this sense. To mitigate such imperfection the effect of over-etching should be included in further iterations (if and only if, the same manufacturer produces the PCB layout).

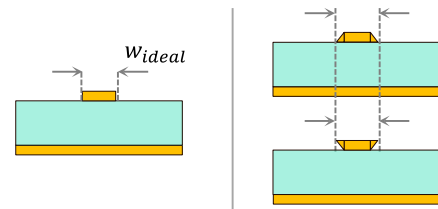


Figure 6.15 – Ideal vs Manufactured Microstripline and Etching Effects

Additional simulations to account for the measured $10 \mu m$ of over-etching shows a $20 MHz$ shift in frequency towards the measured matching point, as shown in figure Table 6.20.

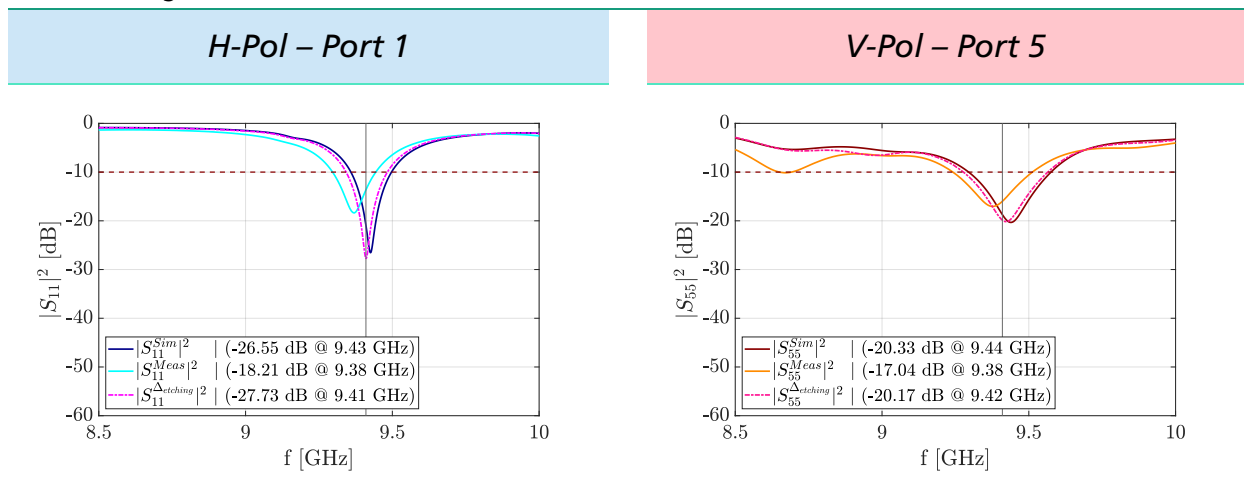
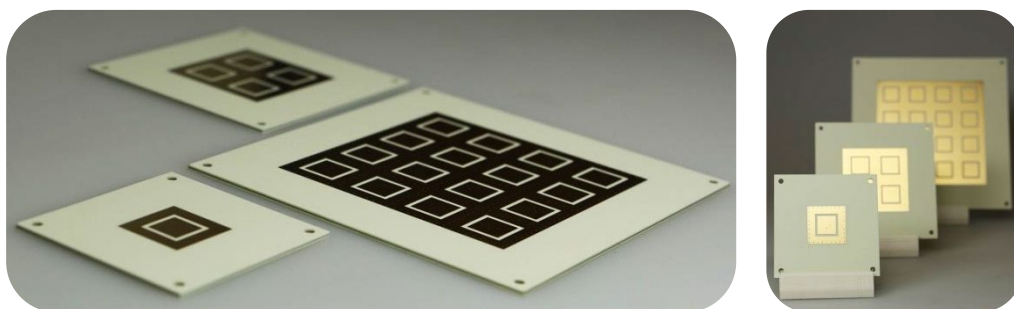


Table 6.20 – 4x4 Baseline Sub-array with Integrated Feed-net (Reflection Coefficients, Simulations vs. Measurements)

However the lack of a *ring resonator* on the manufactured calibration kit (to verify the actual permittivity of the actual substrate) has prevented to reach a finer agreement with measurements. Further analysis is left as a follow-up activity, mainly by slightly increasing the Rogers 4350B ϵ_r of the simulation model.

Chapter 7 - Conclusions and Future Work

In this Thesis, the antenna development process of a 4x4 sub-array optimized for weather radar applications has been performed. Through a comprehensive analysis targeting *low-cost* and *polarization purity* a X-band probe-fed dual-polarized microstrip patch antenna has been designed as the elementary radiator for 2x2 and 4x4 test sub-arrays. A feeding rotation has been investigated to achieve low cross-polarization and high-isolation, so to comply with the requirements of actively scanned modern weather radars aiming at a differential reflectivity accuracy below 0.1 dB.



Probe-fed dual-polarized microstrip patch antennas have been analyzed to understand the main sources of cross-polarization. Exciting patch antennas via probe-feeding has been shown to generate additional asymmetric surface currents that significantly degrade the polarimetric performance. To suppress these additional terms a feed rotation technique has been implemented and proved effective to cancel the undesired polarimetric terms within the principal planes. Additionally, further comparisons with a non-imaged sub-array has quantified the performance gain of the imaged technique, highlighting more balanced polarimetric performance over the entire scan range for both horizontal and vertical polarizations.

An optimized feeding network for each row of the sub-array has been designed to reach isolations levels up to 40 dB among cross-polarized ports. After an initial validation of the 4x4 imaged sub-array, the feed rotation technique can be applied to develop larger arrays, providing that a suitable substrate is selected to meet the board surface constraints. Furthermore, polarimetric optimizations of the unit cell might allow to counteract the imbalances observed between the H- and V-polarizations in the vertical plane.

An antenna prototype has been manufactured, measured and validated. Production tolerances have been shown to have a critical impact on the effective bandwidth. Nonetheless, instrumental measurements have confirmed fulfillment of the specified requirements, ultimately validating the imaged feeding technique as suitable to provide effective cancellation of the undesired polarization terms. Accounting for the manufacturing tolerances and optimizing the polarimetric accuracy of the measurement set-up are key aspects for further enhancements of demanding polarimetric antenna designs.

Future Work

Three main topics are suggested for further investigation, namely, *phased array conception applied to weather radar*, *advanced polarimetric AESA designs* and *optimization of polarimetric measurement set-ups*.

Phased Array Requirements for Weather Radar

Simulation results supported by instrumental verification, suggest the need for more realistic metrics for polarimetric metrics for the assessment of phased array weather radars. Assuming a non-uniform beam filling condition, an integrated cross-polarization ratio extended to the -6 dB beam threshold is proposed. Future investigations should advance the definition of polarimetric antenna requirements more closely related to operational conditions. Focusing only on the polarimetric performance at the peak of the beam is therefore discouraged.

Advanced Polarimetric AESA Designs

Advanced designs should focus on a slight bandwidth increase by selection of a thicker substrate with lower ϵ_r , or even by using a stacked patch topology. A dielectric with higher ϵ_r for the feeding stage would decrease the board surface requirements possibly allowing full integration of the front-end circuitry with the feeding network on the antenna bottom layer.

To further improve the polarimetric performance, the unitary dual-polarized patch antenna can be further optimized to compensate for its inherent asymmetries. Rectangular patch antennas are a possible solution to achieve better unitary pattern symmetry for the desired steering conditions.

Polarimetric Measurements Optimization

An initial step towards optimization of the anechoic chamber for demanding polarimetric assessments might involve the usage of optimal polarimetric sources in chamber with improved symmetry. Using an optimal dipole tuned at the specific frequency of interest is a prospective solution, though it implies major manufacturing concerns, namely fine calibration of the phase difference at the input port and symmetrization non-idealities (especially at X-band).

The time demands required for high resolution measurements¹⁶ call for the integration of in-line AESA functionalities, to take advantage of programmable steering capabilities during the measurement process.

¹⁶ Measurement of a single port with an example resolution of 5 degrees in θ and ϕ takes around 9 hours. Full measurement of an 8 port antenna requires around 8 days for completion.

Open Research Questions

The sub-array rotation mechanism can be extended to a periodic structure to mitigate the effects of cross-polarized components along specific planes while suppressing undesired sidelobes [59]. In this work, its usage has been constrained to a mono-dimensional scanning application bound to the tight polarimetric requirements for weather radar systems. While feed rotations have been applied to a single element level, the possibility to implement similar schemes at a sub-array level (see Figure 7-1) is left to further advancements.

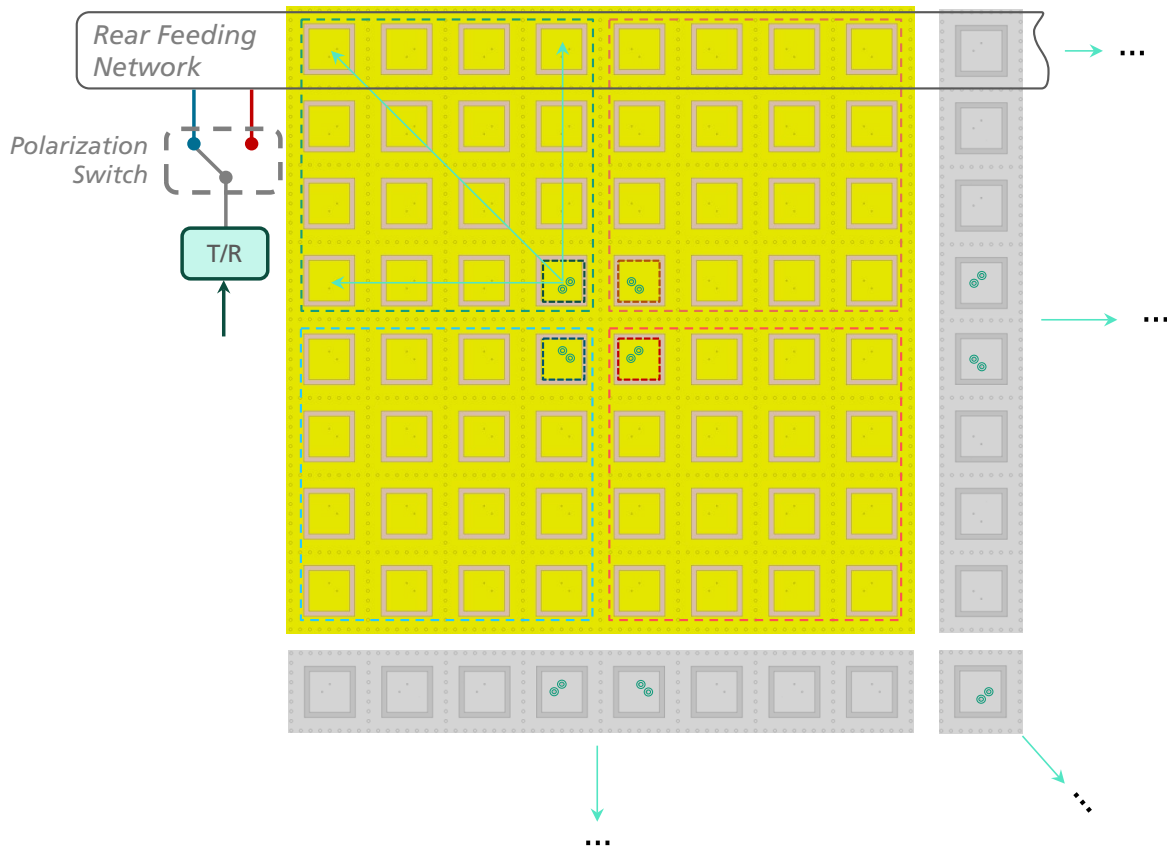


Figure 7-1 – Concept Feed Rotation applied to a 4x4 Baseline Sub-Array

On the other hand, high-end radar systems usually implement AESA architectures to provide high-gain and biaxial scanning capabilities. In that case, differential feeding approaches have already been shown to fulfill the stringent polarimetric requirements.

As AESA technology advancements keeps being supported by more mature engineering tools, larger scale of integration and manufacturing processes allowing for lower production costs, new research opportunities push forward the level of sophistication that today's antenna systems can reach. Phased array technology is made available for a broader research community, offering a wider chance to formulate new questions, attempt new answers, and accept the challenges that will ultimately benefit the Society of Tomorrow.

Bibliography

- [1] S. Turso, S. Paoletta, M. Gabella and G. Perona, "MicroRadarNet: A network of weather micro radars for the identification of local high resolution precipitation patterns. Atmospheric Research," *Atmospheric Research*, vol. 119, 2011.
- [2] G. Zhang, *Weather Radar Polarimetry*, CRC Press, 2017.
- [3] R. J. Doviak, D. S. Zrnic and D. S. Sirmans, "Doppler Weather Radar".
- [4] John Heimmer, "Multi-mission phased array radar (MPAR) national radar RD project," 2008.
- [5] C. Fulton and W. J. Chappell, "Calibration of a digital phased array for polarimetric radar," in *IEEE MTT-S International Microwave Symposium Digest*, 2010.
- [6] S. Turso, T. Bertuch, M. Jager, S. Stanko, P. Knott, S. Tromel and C. Simmer, "A low-cost mechanically-steered weather radar concept," in *2018 IEEE Radar Conference (RadarConf18)*, 2018.
- [7] S. Turso, T. Bertuch, S. Bruggenwirth, A. Danklmayer and P. Knott, "Electronically steered cognitive weather radar - A technology perspective," in *2017 IEEE Radar Conference, RadarConf 2017*, 2017.
- [8] T. Otto, "Advances in Polarimetric X-band Weather Radar," TU Delft, Delft, 2012.
- [9] D. McLaughlin and P. Drake, "Update on Low Cost X-band Phased Array Radar Technology for High Resolution Atmospheric Sensing Applications," WakeNet-Europe, Paris, 2013.
- [10] J. Figueras i Ventura, "Design of a High Resolution X-band Doppler Polarimetric Weather Radar," 2009.
- [11] A. Yarovoy and O. Krasnov, "High Resolution FMCW Polarimetric Doppler Weather Radar with Dual-Orthogonal Waveforms," *International Radar Symposium (IRS)*, Ulm (Germany), 2019.
- [12] T. D. -. MS3, "Delft Multi-Sensor Information System for Situation Awareness," [Online]. Available: <http://regenradar.tudelft.nl/index.php>. [Accessed 20 06 2019].
- [13] C. Fulton and W. Chappell, "Calibration of panelized polarimetric phased array radar antennas: A case study," in *IEEE International Symposium on Phased Array Systems and Technology*, 2010.
- [14] J. E. Stailey and K. D. Hondl, "Multifunction Phased Array Radar for Aircraft and Weather

- Surveillance," *Proceedings of the IEEE*, 2016.
- [15] C. Fulton, J. Herd, S. Karimkashi, G. Zhang and D. Zrnic, "Dual-polarization challenges in weather radar requirements for multifunction phased array radar," in *IEEE International Symposium on Phased Array Systems and Technology*, 2013.
- [16] D. S. Zrnic and R. J. Doviak, "System Requirements for Phased Array Weather Radar".
- [17] I. Gresham and D. Corman, "An AESA Revolution Utilizing the Disruptive Technology of Highly-Integrated Silicon ICs".
- [18] J. Herd, S. Duffy, D. Carlson, M. Weber, G. Brigham, C. Weigand and D. Cursio, "Low cost Multifunction Phased Array Radar concept," in *IEEE International Symposium on Phased Array Systems and Technology*, 2010.
- [19] D. Carlson, "Breaking Through the Cost Barrier for Phased Arrays," 2018.
- [20] C. Fulton and W. Chappell, "A dual-polarized patch antenna for weather radar applications," in *2011 IEEE International Conference on Microwaves, Communications, Antennas and Electronic Systems, COMCAS 2011*, 2011.
- [21] J. D. Diaz, J. L. Salazar, J. A. Ortiz, C. Fulton, N. Aboserwal, R. Kelley and R. Palmer, "A dual-polarized cross-stacked patch antenna with wide-angle and low cross-polarization for fully digital multifunction phased array radars," in *IEEE International Symposium on Phased Array Systems and Technology*, 2017.
- [22] H. Saeidi-Manesh and G. Zhang, "High-Isolation, Low Cross-Polarization, Dual-Polarization, Hybrid Feed Microstrip Patch Array Antenna for MPAR Application," *IEEE Transactions on Antennas and Propagation*, vol. 66, 2018.
- [23] G. Zhang, R. J. Doviak, D. S. Zrnić, R. Palmer, L. Lei and Y. Al-Rashid, "Polarimetric phased-array radar for weather measurement: A planar or cylindrical configuration?," *Journal of Atmospheric and Oceanic Technology*, vol. 28, no. 1, pp. 63-73, 1 2011.
- [24] A. Krishnamurthy, "ScholarWorks@UMass Amherst Design of an FPGA-based Array Formatter for Casa Phase-Tilt Radar System "Design of an FPGA-based Array Formatter for Casa Phase-Tilt Radar System", " 2011.
- [25] R. Palumbo, E. Knapp, K. Wood, D. J. McLaughlin, C. McCarroll and S. J. Frasier, "Phase-tilt weather radar: Calibration and preliminary results," in *2013 International Conference on Radar - Beyond Orthodoxy: New Paradigms in Radar, RADAR 2013*, 2013.
- [26] T. Bertuch, M. Pamies, C. Locker, P. Knott, H. Erkens, R. Wunderlich and S. Heinen, System aspects of a low-cost coherent radar system with aesa antenna for maritime applications.
- [27] R. B. Waterhouse, "Design of probe-fed stacked patches," *IEEE Transactions on Antennas and Propagation*, 1999.

- [28] G. Mayhew-Ridgers, J. W. Odendaal and J. Joubert, "Efficient full-wave modeling of patch antenna arrays with new single-layer capacitive feed probes," *IEEE Transactions on Antennas and Propagation*, vol. 53, no. 10, pp. 3219-3228, 10 2005.
- [29] H. T. Shivamurthy, "Wideband, Wide-Scan Planar Connected Slot Array Enhanced with Artificial Dielectrics," 2014.
- [30] M. Rütchlin, T. Wittig and Z. Iluz, "Phased Array Design in CST STUDIO SUITE".
- [31] B. A.K., *Phased Array Antennas - Floquet Analysis*, Wiley, 2006, pp. 62-87.
- [32] J. S. Herd, S. M. Duffy and H. Steyskal, "Design considerations and results for an overlapped subarray radar antenna," in *IEEE Aerospace Conference Proceedings*, 2005.
- [33] H.-J. S. a. M. E. Bialkowski, "A Multilayer Microstrip Patch Antenna Subarray Design Using CAD," *Microwave Journal*, 1 March 1997.
- [34] "MathWorks - Subarrays in Phased Array Antennas," [Online]. Available: https://nl.mathworks.com/help/phased/examples/subarrays-in-phased-array-antennas.html?s_eid=PEP_16543. [Accessed 20 11 2018].
- [35] K. Woelders and J. Granholm, "Cross-polarization and sidelobe suppression in dual linear polarization antenna arrays," *IEEE Transactions on Antennas and Propagation*, 1997.
- [36] O. Krasnov, "Polarimetric Radar Measurements with Non-Ideal Antenna," Delft, 2019.
- [37] D. S. Zrnica, V. M. Melnikov and R. J. Doviak, "A draft report on Issues and challenges for polarimetric measurement of weather with an agile-beam phased array radar".
- [38] D. Zrnica, R. Doviak, G. Zhang and A. Ryzhkov, "Bias in differential reflectivity due to cross coupling through the radiation patterns of polarimetric weather radars," *Journal of Atmospheric and Oceanic Technology*, vol. 27, no. 10, pp. 1624-1637, 10 2010.
- [39] A. C. Ludwig, "The definition of cross polarization," *IEEE Transactions on Antennas and Propagation*, pp. 116-119, 1973.
- [40] C. A. Balanis, *Antenna Theory*, Wiley, 2016.
- [41] K. F. Lee and J. S. Dahele, *Handbook of Microstrip Antennas*, vol. I, J. R. James and P. S. Hall, Eds., London: Peter Peregrinus, 1989, pp. 111-217 .
- [42] C. A. Balanis and J. Huang, *Modern Antenna Handbook*, Wiley, 2008, pp. 157 - 200.
- [43] C. A. Balanis, *Antenna Theory - Analysis and Design*, Wiley, 2016.
- [44] H. J. Visser, *Array and Phased Array Antenna Basics*, John Wiley & Sons, 2005.

- [45] R. P. Owens, Handbook of Microstrip Antennas, vol. II, J. James and P. S. Hall, Eds., London: Peter Peregrinus, 1989, pp. 815-869 (ch. 14).
- [46] A. Yarovoy and J. Puskely, "Lecture 5 - Patch Antennas ('Antenna Systems' course, ET4015)," Delft, 2018.
- [47] Yarovoy and A., "Lecture 5 - Patch Antenna (Antenna Systems, EE4016)," TU Delft, Delft, 2018.
- [48] R. F. Harrington, Time-Harmonic Electromagnetic Fields, Syracuse: McGraw Hill, 1961, pp. 198-263, Ch. 5 (Cylindrical Wave Functions).
- [49] M. Rütchlin, T. Wittig and Z. Iluz, "Phased antenna array design with CST STUDIO SUITE," in *2016 10th European Conference on Antennas and Propagation, EuCAP 2016*, 2016.
- [50] R. Caso, A. Serra, A. Buffi, M. Rodriguez-Pino, P. Nepa and G. Manara, "Dual-polarised slot-coupled patch antenna excited by a square ring slot," *IET Microwaves, Antennas & Propagation*, 2011.
- [51] Haider; Nadia, "Antennas for Frequency Reconfigurable Phased Arrays," 2015.
- [52] D. Vollbracht, "Understanding and optimizing microstrip patch antenna cross polarization radiation on element level for demanding phased array antennas in weather radar applications," *Advances in Radio Science*, 2015.
- [53] J. James and P. Hall, Handbook of Microstrip Antennas, vol. I, J. R. James and P. S. Hall, Eds., London: Peter Peregrinus, 1989.
- [54] J. Huang and C. A. Balanis, Modern Antenna Handbook, Wiley, 2008.
- [55] L. Shafai and A. Kishk, Handbook of Microstrip Antennas, vol. I, J. James and P. Hall, Eds., London: Peter Peregrinus, 1989, pp. 73-85.
- [56] L. G. Maloratsky, "Reviewing the Basics of Microstrip Lines," *Microwaves & RF*, pp. 79-88, 2000.
- [57] J. Rod, "Microwave Journal: Minimize Microstrip Radiation Effects," 6 June 2012. [Online]. Available: <https://www.microwavejournal.com/blogs/1-rog-blog/post/17702-minimize-microstrip-radiation-effects>. [Accessed 20 June 2019].
- [58] G. S. A. Shaker and S. Safavi-Naeini, "A technique for realizing compact arrays of microstrip antennas," in *Proceedings - 2007 IEEE Radio and Wireless Symposium, RWS, 2007*.
- [59] J. Granholm and K. Woelders, "Dual Polarization Stacked Microstrip Patch Antenna Array With Very Low Cross-Polarization," 2001.
- [60] E. J. Denlinger, "Losses of Microstrip Lines," *IEEE Transactions on Microwave Theory and Techniques*, Vols. MTT-28, no. 6, pp. 513-521, 1980.

- [61] J. H. Howe, "Stripline Circuit Design," Artech House, Inc., Norwood, MA, 1974.
- [62] B. C. Wadell, "Transmission Line Design Handbook," Artech House, Inc, Norwood, MA 02062, 1991.
- [63] N. A. Abooserwal, J. L. Salazar, J. A. Ortiz, J. D. Diaz, C. Fulton and R. D. Palmer, "Source Current Polarization Impact on the Cross-Polarization Definition of Practical Antenna Elements: Theory and Applications," *IEEE Transactions on Antennas and Propagation*, vol. 66, no. 9, pp. 4391-4406, 1 9 2018.
- [64] Y. T. Lo, D. Solomon and W. F. Richards, "Theory and Experiment on Microstrip Antennas," 1979.

APPENDIX – A

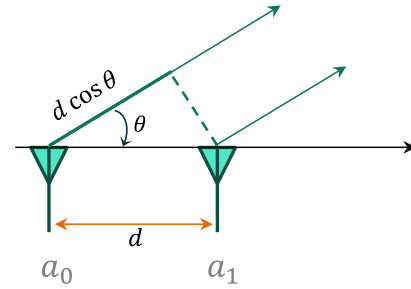
NOTES ON LINEAR PHASED ARRAYS
(A geometrical demonstration)

Notes on Phased Arrays

(A geometrical approach)

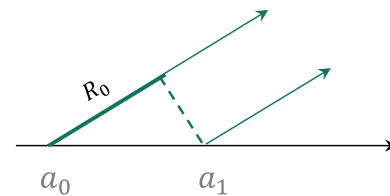
$$\vec{E}_{array} = \sum_n \vec{E}_0 a_n \frac{e^{-jk_0 R_n}}{R_n}$$

$$\vec{E}_{array} \approx \vec{E}_0 \sum_n a_n \frac{e^{-jk_0 R_n}}{R_0}$$



R_0	$R_0 - d \cos \theta$	$R_0 - 2d \cos \theta$
a_0	a_1	a_2

$$\vec{E}_{array} \approx \vec{E}_0 \left(a_0 \frac{e^{-jk_0 R_0}}{R_0} + a_1 \frac{e^{-jk_0 (R_0 - d \cos \theta)}}{R_0} + \dots \right)$$



$$\vec{E}_{array} \approx \vec{E}_0 \sum_n a_n \frac{e^{-jk_0 (R_0 - n d \cos \theta)}}{R_0} = \vec{E}_0 \frac{e^{-jk_0 R_0}}{R_0} \sum_n a_n e^{-jk_0 n d \cos \theta}$$

$$a_n = a_0 e^{j\beta} \rightarrow \vec{E}_{array} \approx \vec{E}_0 \frac{e^{-jk_0 R_0}}{R_0} a_0 \sum_n e^{-j(k_0 n d \cos \theta + \beta)}$$

$$\psi \triangleq kd \cos \theta + \beta \rightarrow \vec{E}_{array} \approx \vec{E}_0 \frac{e^{-jk_0 R_0}}{R_0} a_0 \sum_n e^{-j\psi}$$

$$\begin{aligned} \sum_{n=1}^{N-1} a^n &= \frac{a^N - 1}{a - 1} \rightarrow AF(\psi) = a_0 \sum_n e^{-j\psi} = a_0 \frac{e^{jN\psi} - 1}{e^{j\psi} - 1} = a_0 \frac{1 - e^{jN\psi}}{1 - e^{j\psi}} = \\ &= a_0 \frac{e^{\frac{jN\psi}{2}} \left(e^{-\frac{jN\psi}{2}} - e^{\frac{jN\psi}{2}} \right)}{e^{\frac{j\psi}{2}} \left(e^{-\frac{j\psi}{2}} - e^{\frac{j\psi}{2}} \right)} = a_0 e^{\frac{j(N-1)\psi}{2}} \frac{-\sin\left(\frac{N\psi}{2}\right)}{-\sin\left(\frac{\psi}{2}\right)} \end{aligned}$$

Uniform Distribution	$ AF_n(\psi) = \left \frac{\sin\left(\frac{N\psi}{2}\right)}{\sin\left(\frac{\psi}{2}\right)} \right $	$a_n = 1 (\forall n)$
		$\psi \triangleq kd \cos \theta + \beta$

At the scanning angle θ_s ... $\psi = 0 \Leftrightarrow \theta = \theta_{scan}$	$0 = kd \cos \theta_s + \beta \Rightarrow \beta = -kd \cos \theta_s$
---	--

Maximum Spacing Condition to avoid appearance of Grating Lobe (for $\theta_s < \pi/2$)

$$\psi_{min} = -2\pi \left(\frac{M-1}{M} \right) = kd \cos \theta + (-kd \cos \theta_s)$$

$$\psi_{min} \text{ i. i. f } \theta = \pi \mid \theta_s \in [0, \pi/2]$$

$$-2\pi \left(\frac{M-1}{M} \right) = -kd - kd \cos \theta_s = 2\pi \frac{d}{\lambda} (-1 - \cos \theta_s)$$

$$\frac{M-1}{M} = \frac{d}{\lambda} \Big|_{max} (1 + \cos \theta_s) \Rightarrow \frac{d}{\lambda} \Big|_{max} = \frac{\frac{M-1}{M}}{1 + \cos \theta_s}, \theta_s \in [0, \pi/2]$$

$$\frac{d}{\lambda} \Big|_{max} = \frac{\frac{M-1}{M}}{1 + |\cos \theta_s|}, \forall \theta_s$$

Maximum Spacing Condition to avoid appearance of Grating Lobe (for $\theta_s > \pi/2$)

$$\psi_{max} = 2\pi \frac{M-1}{M} \rightarrow 2\pi \frac{M-1}{M} = kd \cos \theta + (-kd \cos \theta_s)$$

$$\psi_{max} \text{ i. i. f } \theta = 0 \mid \theta_s \in [\pi/2, \pi]$$

$$-2\pi \left(\frac{M-1}{M} \right) = kd - kd \cos \theta_s = 2\pi \frac{d}{\lambda} (1 - \cos \theta_s)$$

$$\frac{M-1}{M} = \frac{d}{\lambda} \Big|_{max} (1 - \cos \theta_s) \Rightarrow \frac{d}{\lambda} \Big|_{max} = \frac{\frac{M-1}{M}}{1 - \cos \theta_s}, \theta_s \in [\pi/2, \pi]$$

APPENDIX – B

DUAL-POL PROBE-FED PATCH ANTENNA DESIGN
(Guidelines, manufacturing concerns and CEM solver choice)

Design Guidelines for a Dual-Pol Probe-Fed Patch Antenna

In this Appendix initial design guidelines are provided to support the patch design decision presented in Chapter 4. Based on the cavity model and theoretical background, simple physical explanations are provided to further justify the matching procedure and feeding probe design.

As seen in section 3.2, the fundamental mode of a rectangular patch antenna TM_{010}^z provides the best polarization purity (ideally no cross-polarization at broadside).

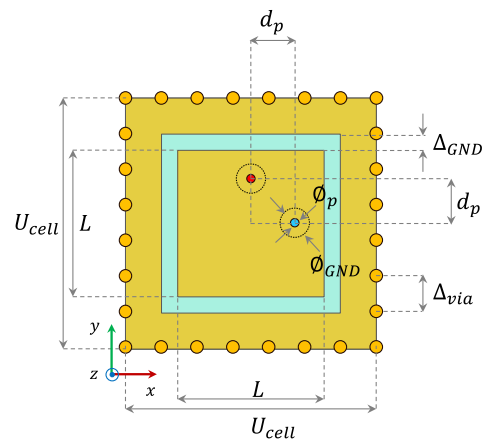


Figure B-1 – Dual-pol Probe-fed Patch Antenna

The narrowband resonant frequency (f_{010}) can be properly tuned by changing L , while for a mono-polarized patch width (w) affects the bandwidth. Since dual-polarized radiation is desired, w is constrained to be the same as L .

Guideline for L	Increase L (decrease f_{010}), decrease L (increase f_{010}).
-------------------	---

The narrowband nature of the TM modes reflects into the resonant behavior of the input impedance ($Z_{in} = R_{in} + jX_{in}$) which is to be matched to reference impedance of design (Z_{REF}) (see Figure B-2)

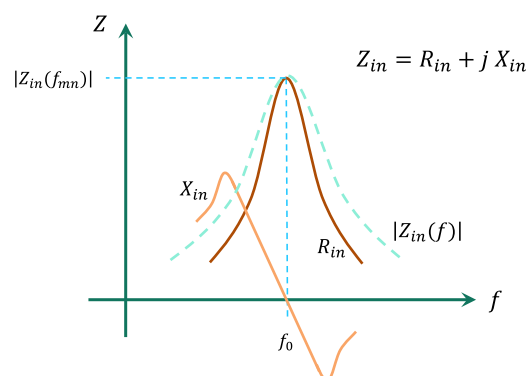


Figure B-2 - Generic Matching Condition for Patch Antennas

While L allows tuning the resonance of the input impedance ($X_{in} = 0, R_{in,max}$), the real part (R_{in}) can be tuned axially moving the probe or the inset feed towards the center of the patch ($d_p \downarrow \Rightarrow R_{in} \downarrow$) or outwards ($d_p \uparrow \Rightarrow R_{in} \uparrow$). This effect can be explained by the cavity model, where for the center of the patch the voltage distribution is minimal and thus the ratio V/I ($\approx Z_{in}$). Additionally, the R_{in} is inversely affected by the probe diameter (ϕ_p), as a greater probe will yield a lower R_{in} . This effect is a function of the probe surface as a smaller probe ($\phi_p \downarrow$) supports a smaller current flow ($I = J_s \cdot \pi D_p^2/4$) and therefore the ratio V/I increases ($R_{in} \uparrow$).

Guideline for d_p	Increase d_p (increase Z_{in}), decrease d_p (decrease Z_{in}).
---------------------	---

Guideline for ϕ_p	Increase ϕ_p (decrease Z_{in}), decrease ϕ_p (increase Z_{in}).
------------------------	---

Finally, probe requires a copper clearance in the ground plane. This hole (ϕ_{GND}) is required to avoid short-circuiting the patch antenna, but introduces a capacitive effect on the Z_{in} and a slight shift of the $Z_{in,max}$ towards lower frequencies (depicted in Figure 4.8). Although the copper clearance provides another design degree of freedom, its main disadvantage is the slight reduction on the impedance bandwidth. Overall, for smaller gaps between the probe and the ground plane the greater capacitive effects have to be expected..

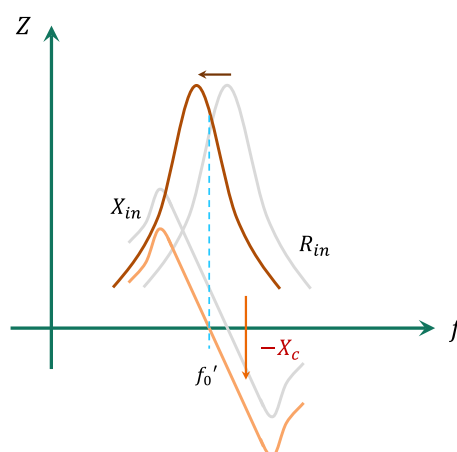


Figure B-3 - Effects of Copper Clearance on the Input Impedance

No major comments have been drafted on the substrate choices (ϵ_r, h) as a specific discussion is already provided in section 4.1. However, shot guidelines regarding its impact on BW, Z_{in} and η_{eff} follow:

Guideline for ϵ_r	Increase ϵ_r (decrease BW, η_{eff} and increase Z_{in}), decrease ϵ_r (increase BW, η_{eff} and decrease Z_{in}).
----------------------------	--

Guideline for h	Increase h (increase BW), decrease h (increase BW). η_{eff} depends on the appearance of surface waves which can be mitigated by a via fence.
-------------------	---

Additionally, a grounded via fence can be included to mitigate surface waves and suppress inter-element coupling. The shown dimensions in sub-section 4.4 are the result of an iterative optimization process where radiated cross-polarization has been found to be minimal and not affecting the matching performance.

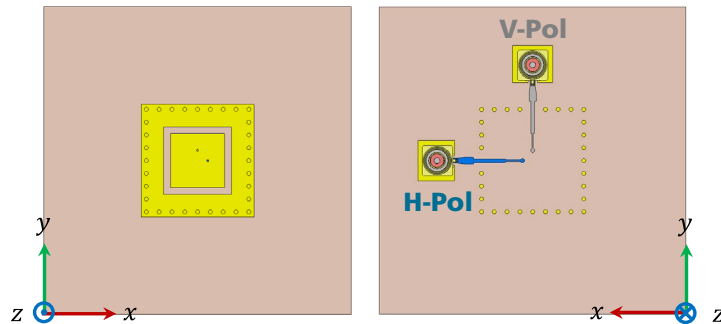


Figure B-4 – CAD Model from CST MWS Studio

Manufacturing Guidelines

The parameters ϕ_p and ϕ_{GND} can be constrained by the machinery accuracy of the PCB manufacturer. A standard value of 0.3 mm for the via drill for the hole diameter (ϕ_p) has been taken. The same value has been used for the via fence, with the additional constraint that on the external surface of the substrate copper has to be present, in case there is no copper, a clad of at least 0.6 mm can be added. Finally, the distance between the probe and the gap of the ground has to be at least 0.3 mm , constraining ϕ_{GND} to be equal or greater than 0.6 mm .

Concerning microstrip lines, widths up to 0.1 mm can be achieved by most manufacturers at low-cost with etching tolerances around $\pm 10\mu\text{m}$.

CEM Solver Choice

Based on the previous guidelines and the difficulties to proceed with an analytical design (see 3.2.2), a full-wave solver has been used to design the unit cell. Based on the in-house availability of GPUs in-house and the expected size of the antenna panel, the *Time Domain* (TD) solver from CST MWS has been initially selected.

Further comparisons with the *Frequency Domain* (FD) solvers (implemented within CST MWS and ANSYS HFSS) showed similar results in terms of the estimated S-Parameters and radiated pattern. However, a drastic disagreement of polarimetric estimations has been noted mainly caused by the solver inability to handle small cross-polarized components. For some cases, the solver disagreements has exceeded 40 dB in spite of defining local cells and mesh optimizations. For this reason, the TD solver has been discarded to prevent unrealistic cross-polarization levels.

For narrowband and low-cross polarization antenna designs, the combined usage of *Finite-Element Method* (FEM) and *Method of Moments* (MoM) is more suitable. These methods provide greater **accuracy**, stability and convergence, but are computationally demanding. On the other hand, the TD solvers (FDTD-based) are preferred for broadband applications where high accuracy is not required. The combined usage of GPUs makes TD also feasible to simulate large structures. However when retrieval of accurate cross-polarization values is desired the mesh cell size has to be small and uniform, resulting in practical difficulties for iterative designs.

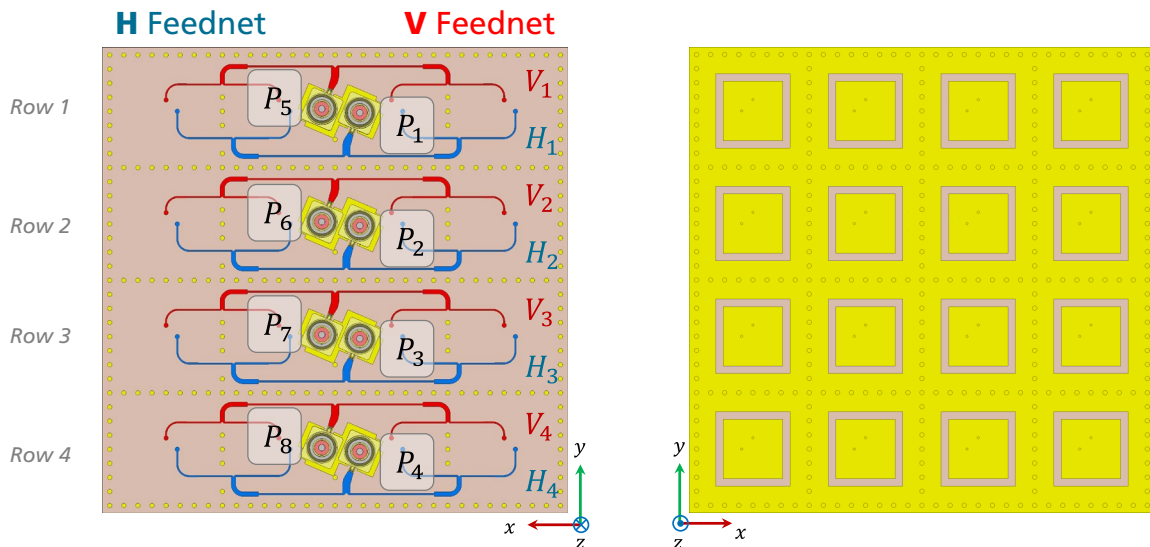
APPENDIX – C

RESULTS SIMULATION (CST MWS – FD)

Integrated 4x4 Baseline Sub-Array

Integrated 4x4 Baseline Sub-Array (CST MWS FD Simulations)

Port Specification



Port Excitations

Assuming a uniform distribution, the excitations for each port are specified in the following tables:

Port	1	2	3	4
H-Port	H_1	H_2	H_3	H_4
Phase Excitation	0°	β_y	$2\beta_y$	$3\beta_y$

Table C-1 – Specification for 4x4 Imaged Sub-Array for H-Pol

Port	5	6	7	8
V-Port	V_1	V_2	V_3	V_4
Phase Excitation	0°	β_y	$2\beta_y$	$3\beta_y$

Table C-2 – Specification for 4x4 Imaged Sub-Array for V-Pol

$$\beta_y = -\frac{2\pi}{\lambda_0} d_y \sin \theta_{max} \xrightarrow{d_y = \lambda_0/2} \beta_y = -\pi \sin \theta_{max} [rad]$$

Static S-Parameters

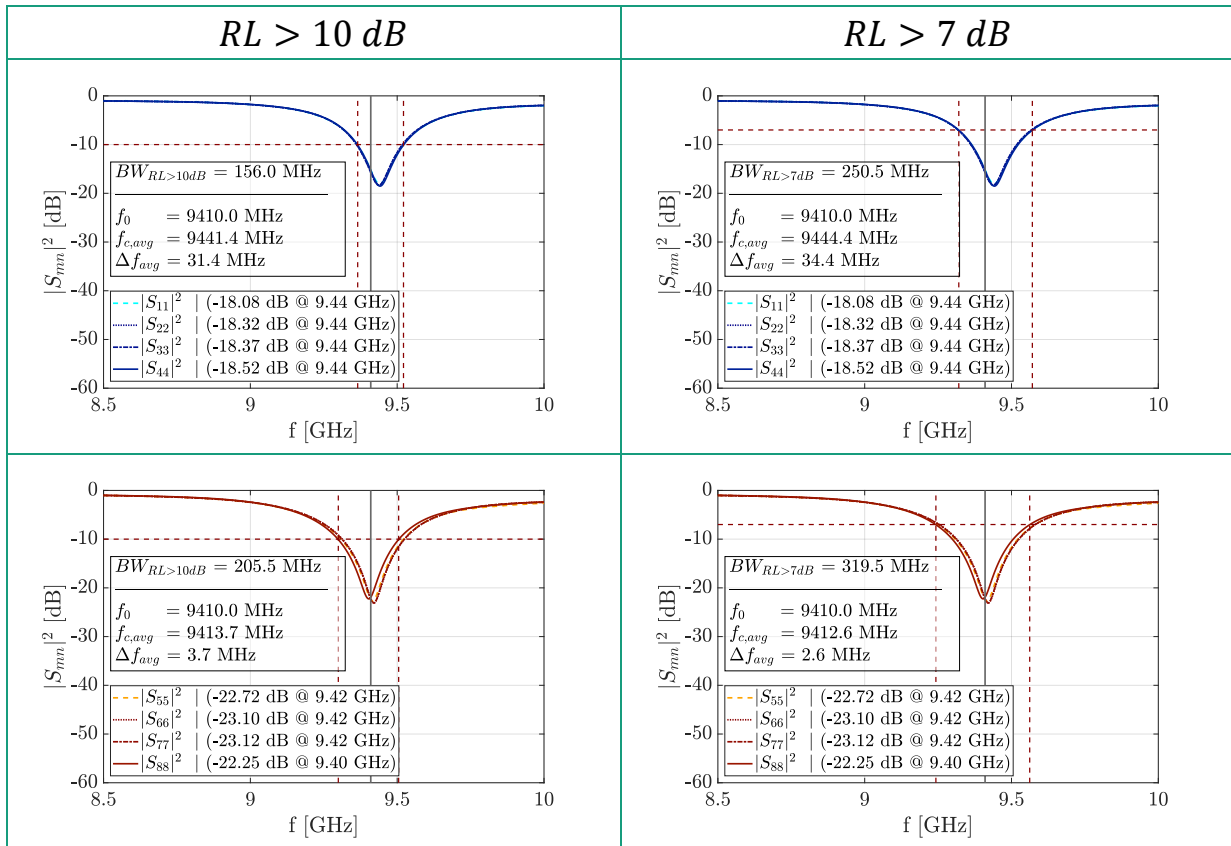


Table C-3 – Reflection Coefficients (H-Pol and V-Pol)

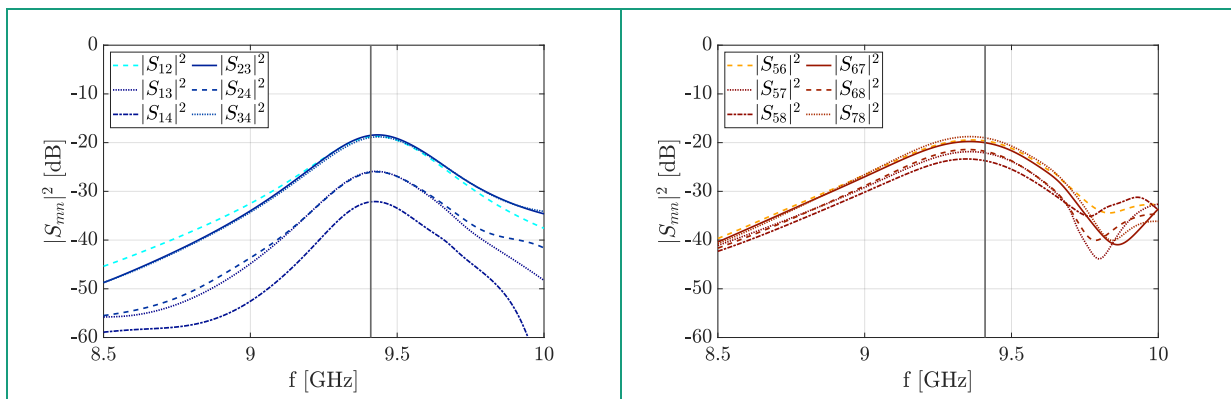


Table C-4 – Co-Polar Port Isolation (H-Pol and V-Pol)

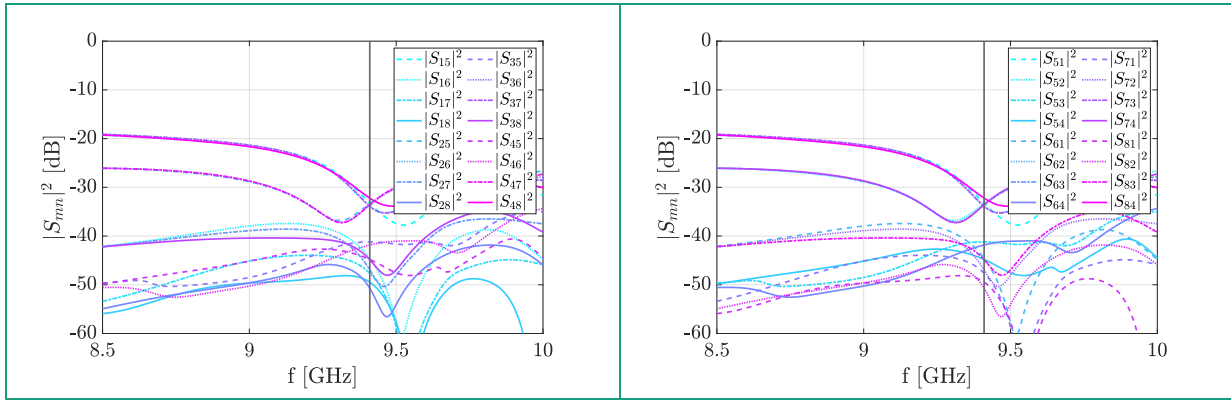


Table C-5 - Cross-Polar Port Isolation (H-Pol and V-Pol)

Active Reflection Coefficients (ARC)

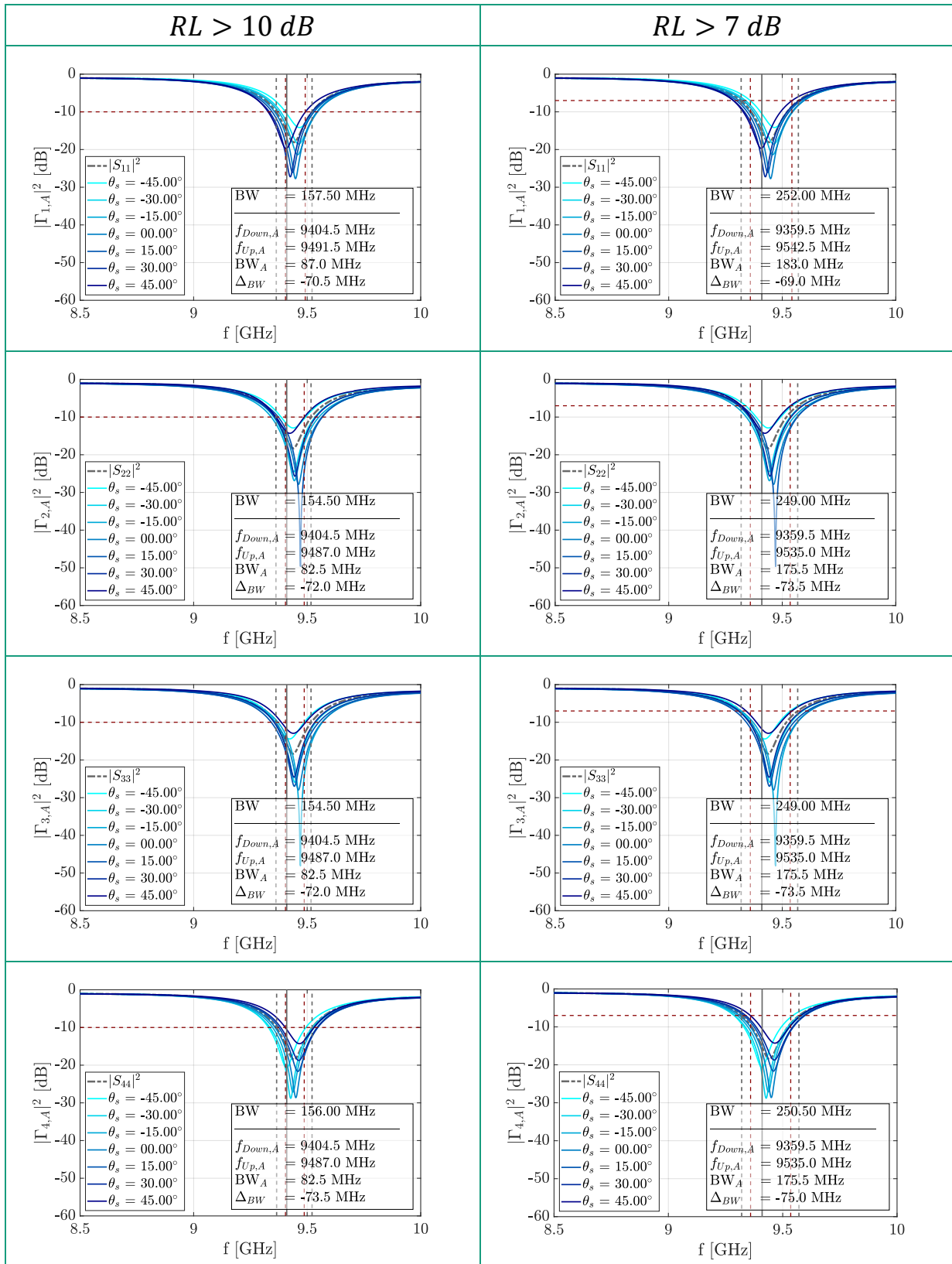


Table C-6 – Active Reflection Coefficients for H-Pol

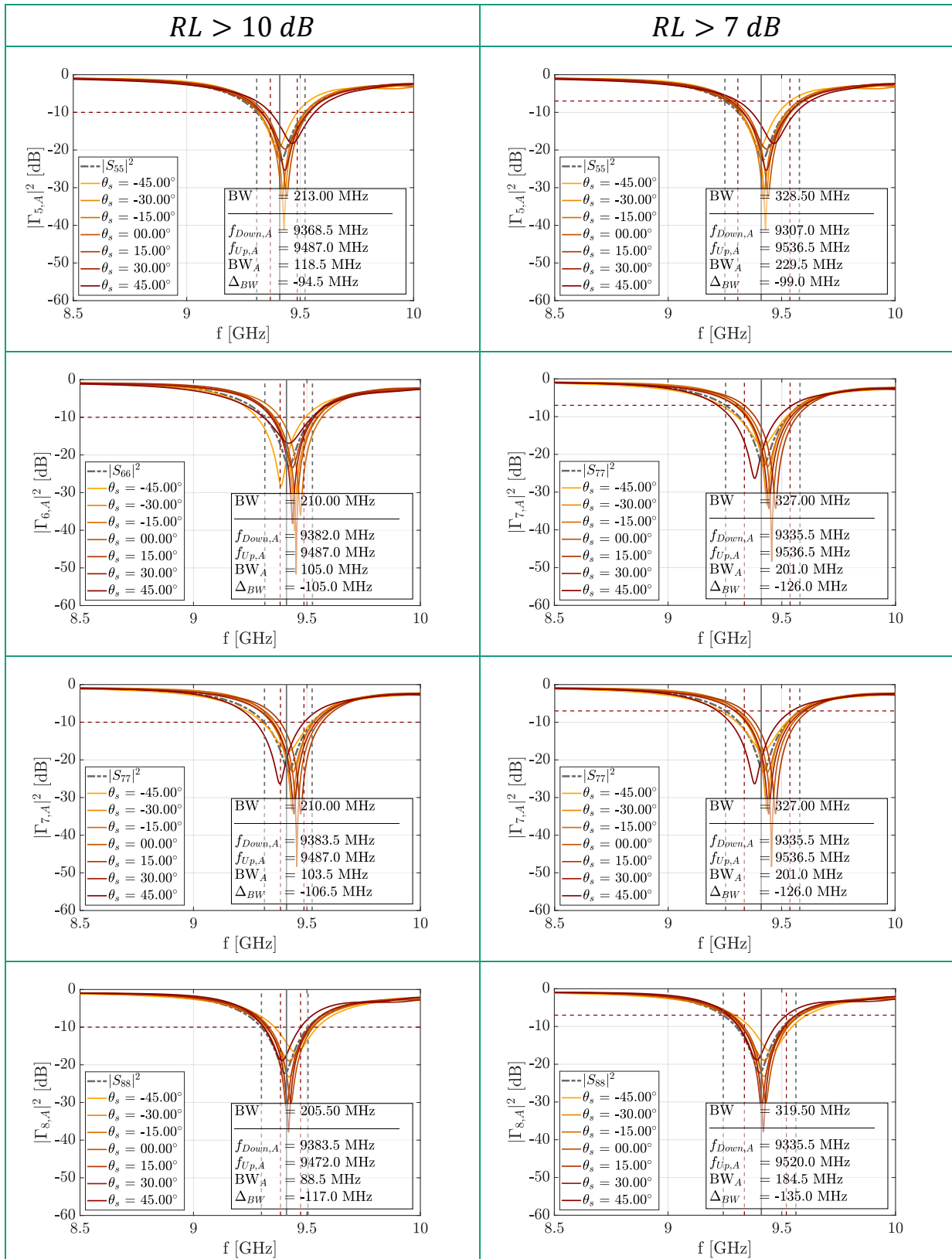
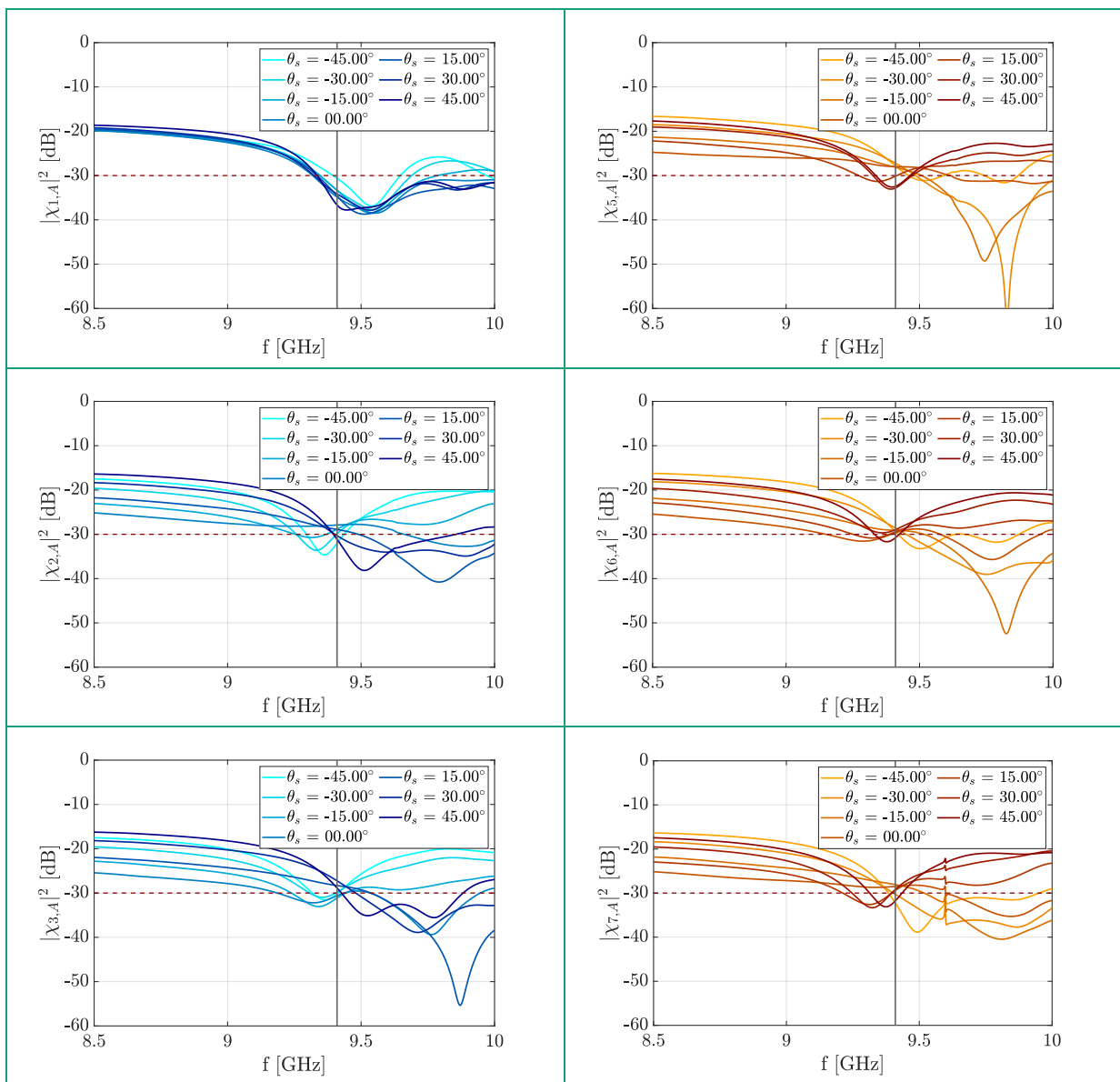


Table C-7 – Active Reflection Coefficients for V-Pol

	RL > 10 dB			RL > 7 dB		
	$f_{down,max}$	$f_{up,min}$	$BW_{eff,a}$	$f_{down,max}$	$f_{up,min}$	$BW_{eff,a}$
H-Pol	9400 MHz	9490 MHz	82.50 MHz	9360 MHz	9540 MHz	175.5 MHz
V-Pol	9380 MHz	9470 MHz	88.50 MHz	9340 MHz	9520 MHz	184.5 MHz
System	9380 MHz	9470 MHz	88.50 MHz	9340 MHz	9520 MHz	184.5 MHz

Table C-8 – Active Bandwidth

Active Isolation Coefficients (AIC)



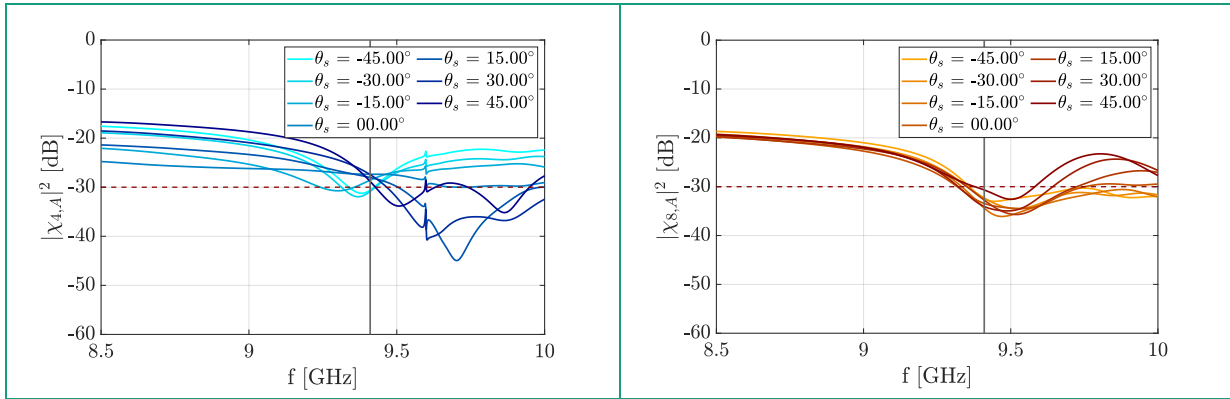


Table C-9 – Active Isolation Coefficients (H-Pol and V-Pol)

Radiation patterns and Cross-polarization Discrimination (XPD)

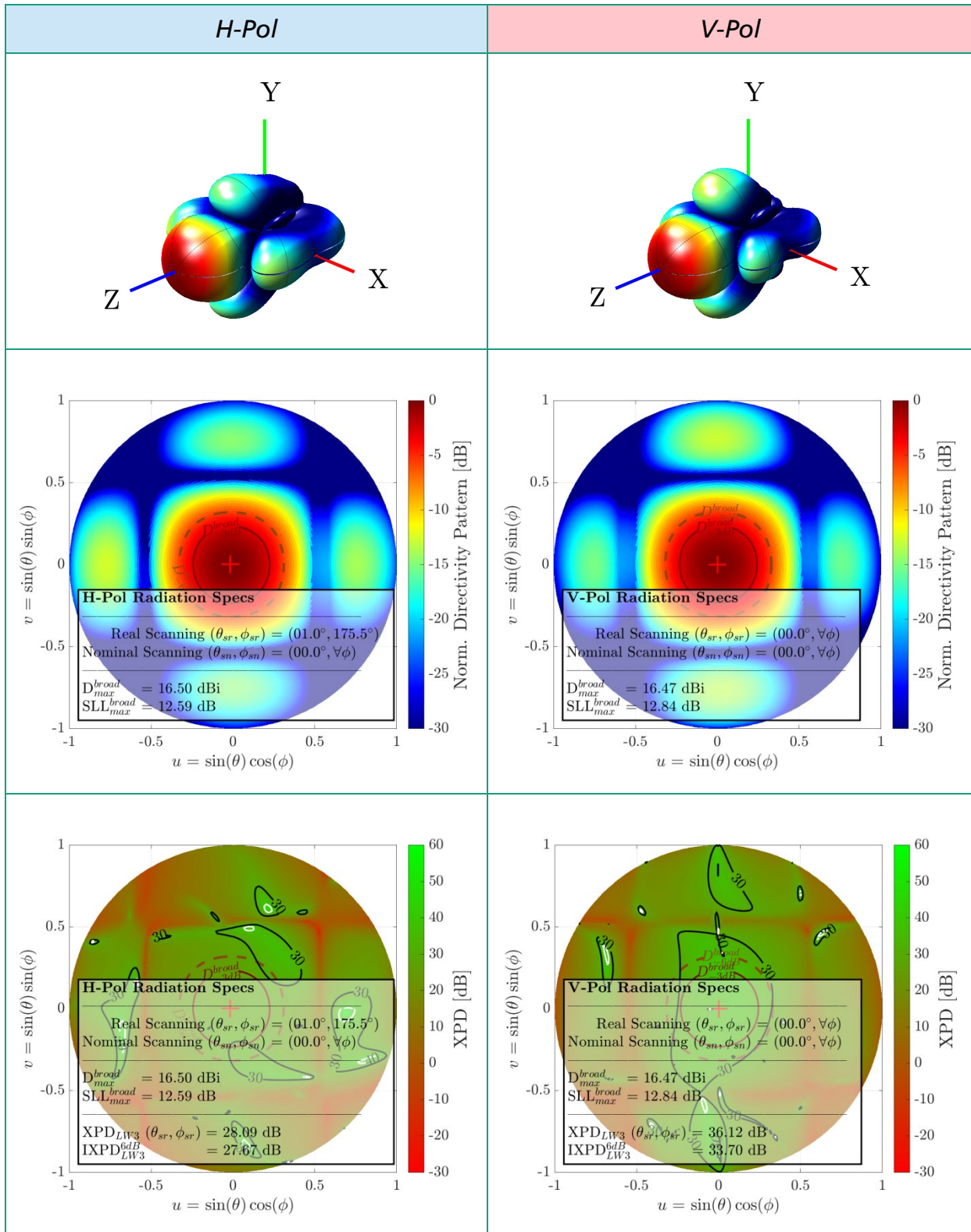


Table C-10 – Polarimetric and Radiation performance at $\theta_s = 00^\circ$ (Broadside)

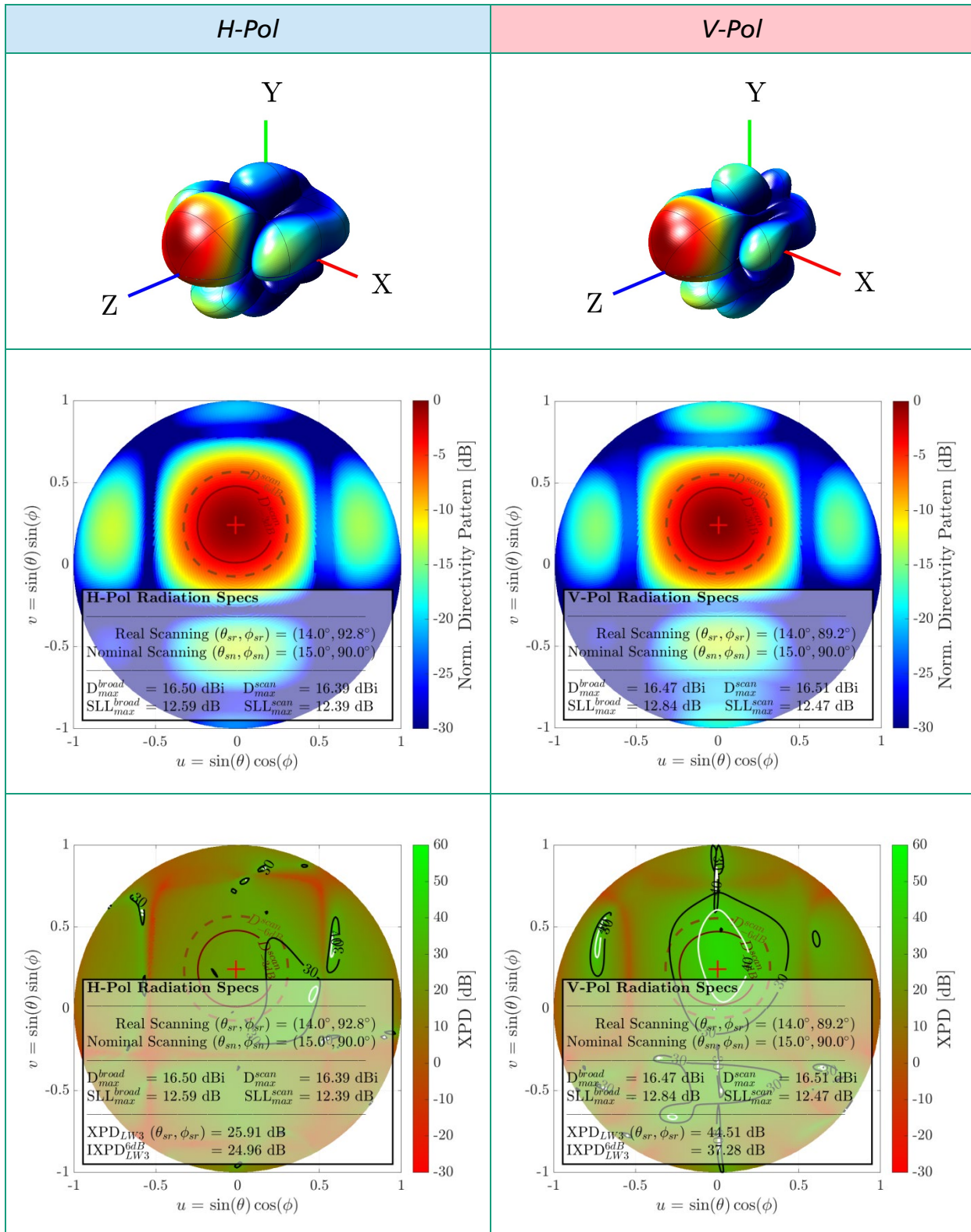


Table C-11 – Polarimetric and Radiation performance at $\theta_s = 15^\circ$

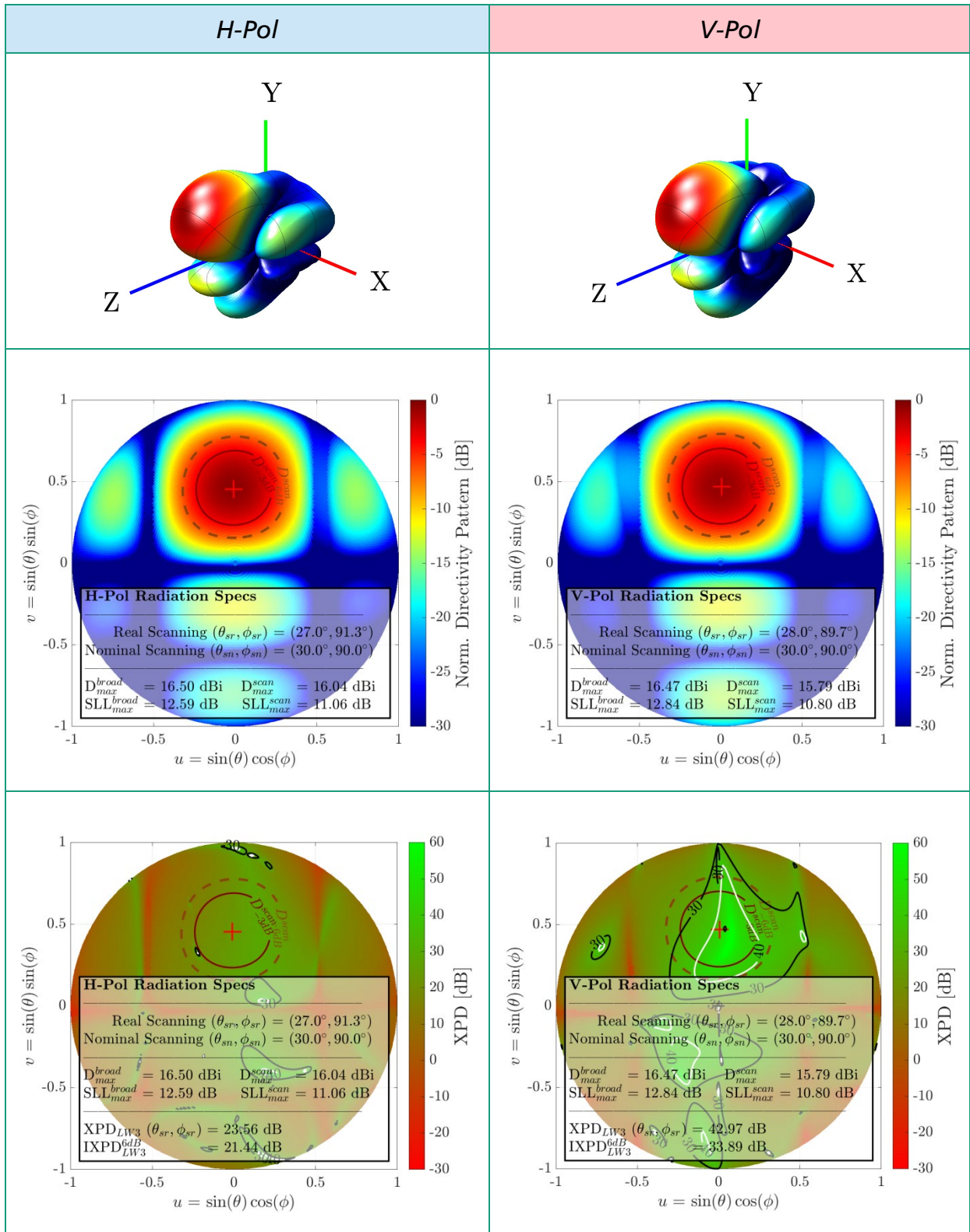


Table C-12 – Polarimetric and Radiation performance at $\theta_s = 30^\circ$

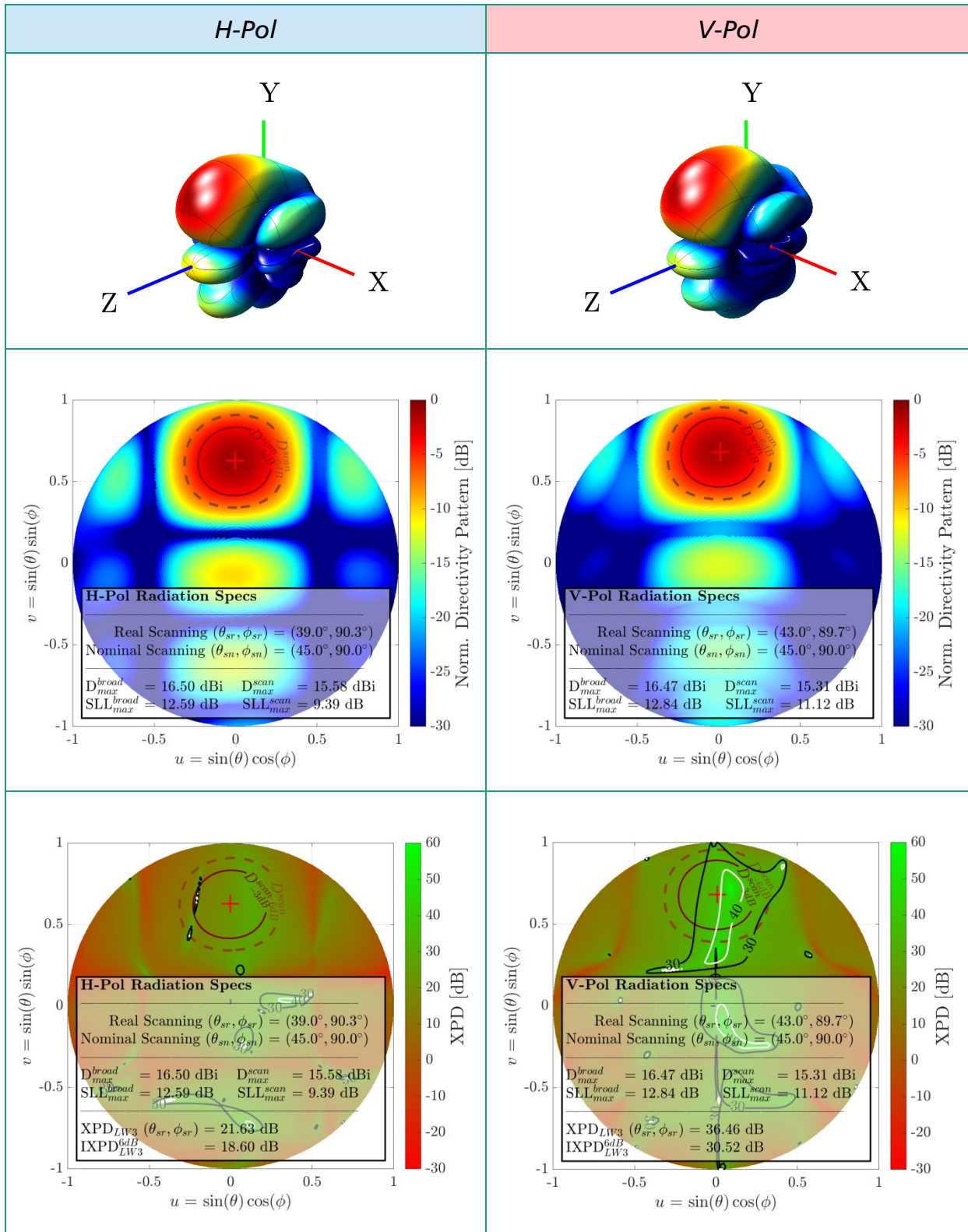


Table C-13 – Polarimetric and Radiation performance at $\theta_s = 45^\circ$

Scan Assessments

	Nominal Scanning Angle (θ_{sn}, ϕ_{sn})	Real Scanning (θ_{sr}, ϕ_{sr})	SLL_{max}	Dir	η_{rad}
H-Pol	(00°, $\forall\phi$)	(01.0°, 175.5°)	12.59 dB	16.50 dBi	76.88%
	(15°, 90°)	(14.0°, 92.8°)	12.39 dB	16.39 dBi	76.19%
	(30°, 90°)	(27.0°, 91.3°)	11.06 dB	16.04 dBi	72.43%
	(45°, 90°)	(40.7°, 90.3°)	10.23 dB	15.52 dBi	69.04%
V-Pol	(00°, $\forall\phi$)	(00.0°, $\forall\phi$)	12.84 dB	16.47 dBi	77.04%
	(15°, 90°)	(14.0°, 90.8°)	12.47 dB	16.51 dBi	76.92%
	(30°, 90°)	(28.0°, 89.7°)	10.80 dB	15.79 dBi	76.59%
	(45°, 90°)	(40.0°, 90.3°)	09.58 dB	14.82 dBi	76.79%

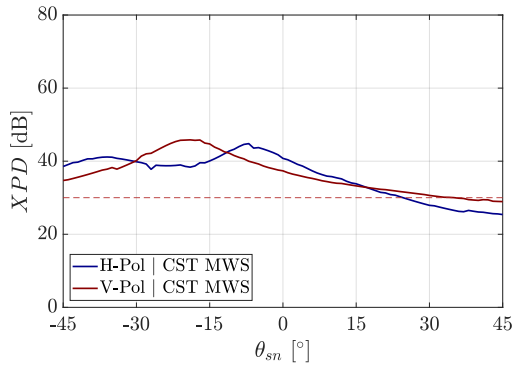
Table C-14 – Radiation Scan Assessment

	Nominal Scanning (θ_{sn}, ϕ_{sn})	XPD @(θ_{sr}, ϕ_{sr})	$IXPD^{6dB}$	$ICPR$	Z_{DRb}
H-Pol	(00°, $\forall\phi$)	28.08 dB	27.90 dB	-25.06 dB	-0.07 dB
	(15°, 90°)	25.91 dB	25.36 dB	-24.05 dB	0.12 dB
	(30°, 90°)	23.56 dB	22.29 dB	-19.61 dB	-0.26 dB
	(45°, 90°)	21.63 dB	19.78 dB	-22.63 dB	-0.50 dB
V-Pol	(00°, $\forall\phi$)	36.12 dB	34.78 dB	-24.05 dB	-0.07 dB
	(15°, 90°)	44.51 dB	39.75 dB	-23.89 dB	0.12 dB
	(30°, 90°)	43.91 dB	36.77 dB	-16.48 dB	-0.26 dB
	(45°, 90°)	37.60 dB	32.54 dB	-16.97 dB	-0.50 dB

Table C-15 – Polarimetric Scan Assessment

Cross-polarization Discrimination¹

$$XPD \triangleq \frac{|E_{Cp}(\theta_{si}, \phi_{si})|^2}{|E_{Xp}(\theta_{si}, \phi_{si})|^2} > 30 \text{ dB}$$



Integrated Cross-polarization Discrimination

$$IXPD^{6dB} \triangleq \frac{\oint |E_{Cp}(\theta, \phi)| d\Omega_{6dB}}{\oint |E_{Xp}(\theta, \phi)| d\Omega_{6dB}}$$

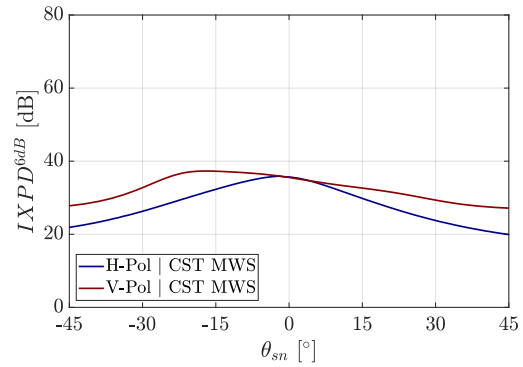


Table C-1 – 4x4 Baseline Sub-array with Integrated Feed-net, Full-scan Polarimetric Assessment

Final Note

The reports simulation results have been obtained using CST MWS 2019, Frequency Domain Solver. The simulated dataset has been extracted and processed with custom MATLAB functions.

¹

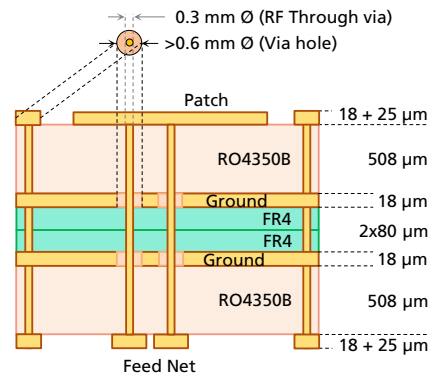
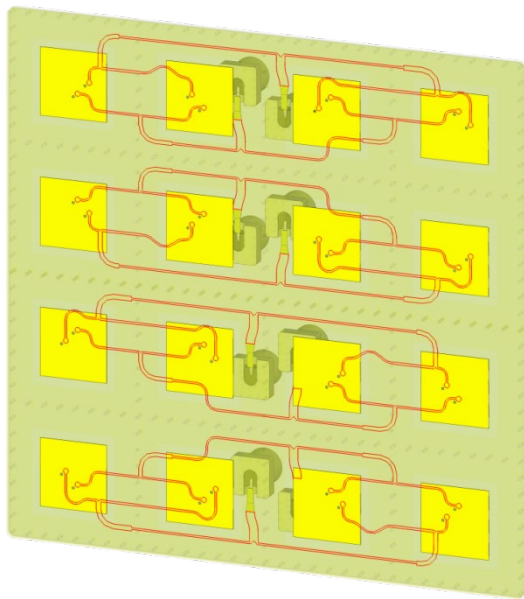
Real scanning angle: $(\theta_{sr}, \phi_{sr}) = (\theta, \phi) | \max \{ |E_{Cp}(\theta, \phi)|^2 \}$

APPENDIX – D

RESULTS SIMULATION (CST MWS – FD)

Integrated 4x4 Imaged Sub-Array

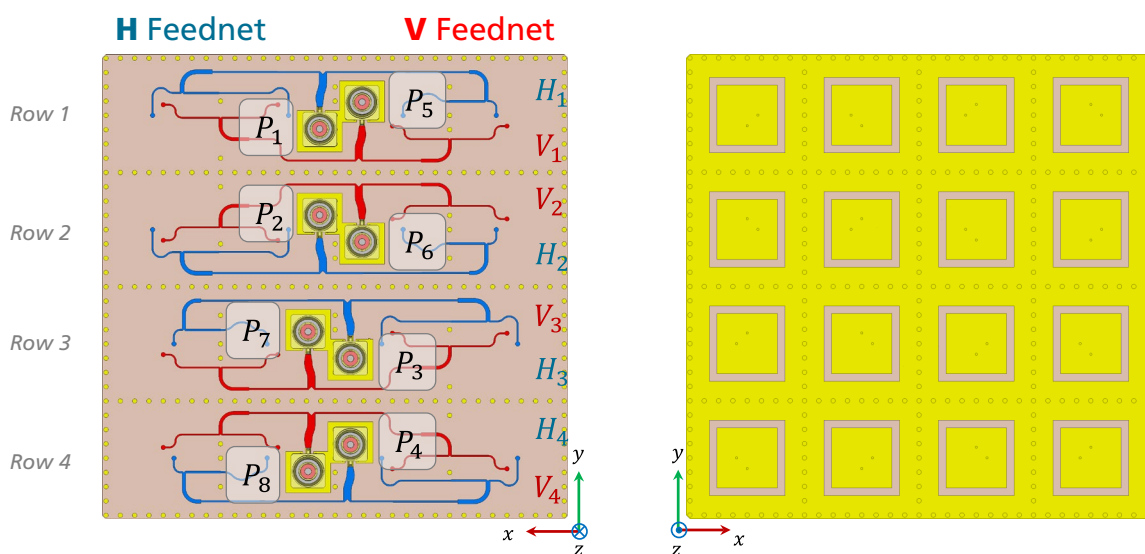
Integrated 4x4 Imaged Sub-Array (CST MWS FD Simulations)



Structure Highlights:

- **4-layer** structure.
- **Symmetric** structure to prevent delamination.
- **Low-profile**.
- Buried vias are avoided to minimize cost (**low-cost**).

Port Specification



Port Excitations

Assuming a uniform distribution, the excitations for each port are specified in the following tables:

Port	1	2	3	4
H-Port	H_1	H_2	H_3	H_4
Phase Excitation	0°	β_y	$2\beta_y + 180^\circ$	$3\beta_y + 180^\circ$

Table D-1 – Specification for 4x4 Imaged Sub-Array for H-Pol

Port	5	6	7	8
V-Port	V_1	V_2	V_3	V_4
Phase Excitation	0°	$\beta_y + 180^\circ$	$2\beta_y$	$3\beta_y + 180^\circ$

Table D-2 – Specification for 4x4 Imaged Sub-Array for V-Pol

$$\beta_y = -\frac{2\pi}{\lambda_0} d_y \sin \theta_{max} \xrightarrow{d_y = \lambda_0/2} \beta_y = -\pi \sin \theta_{max} \text{ [rad]}$$

Static S-Parameters

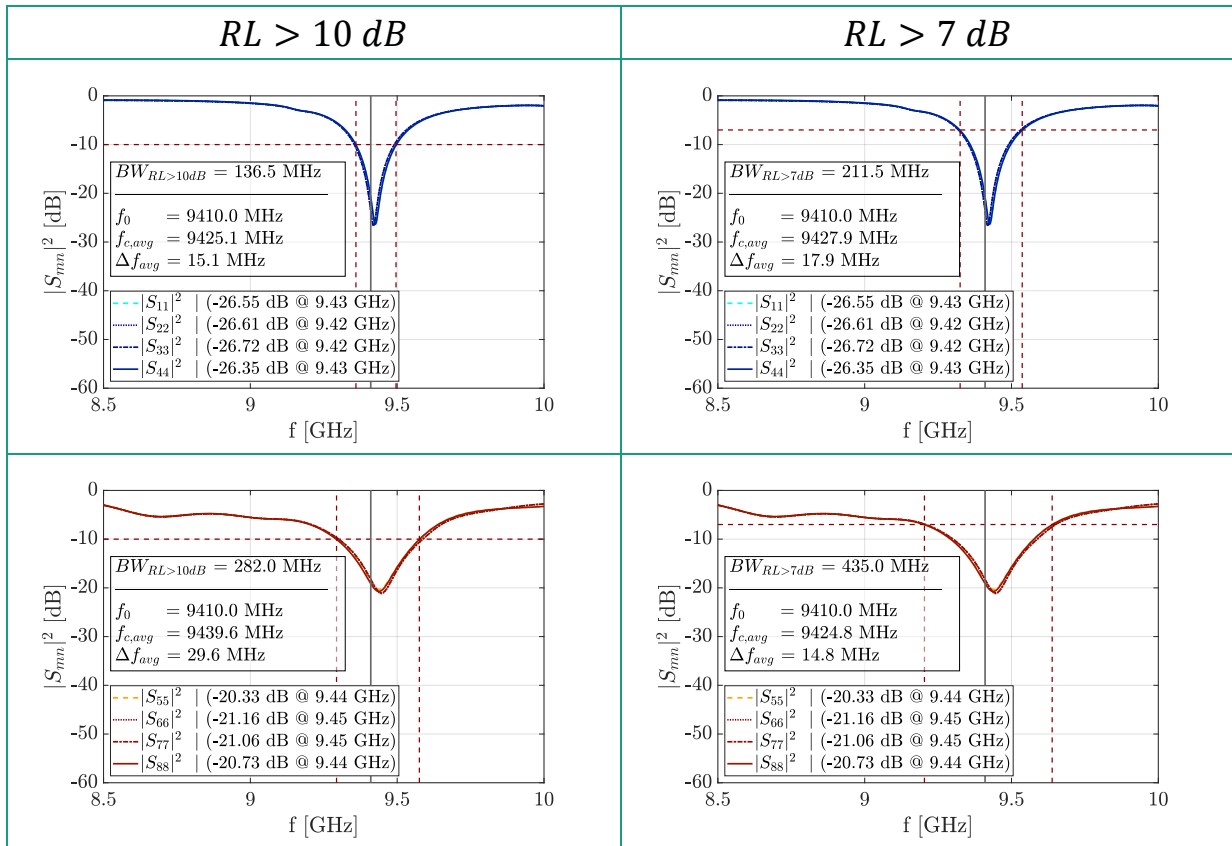


Table D-3 – Reflection Coefficients (H-Pol and V-Pol)

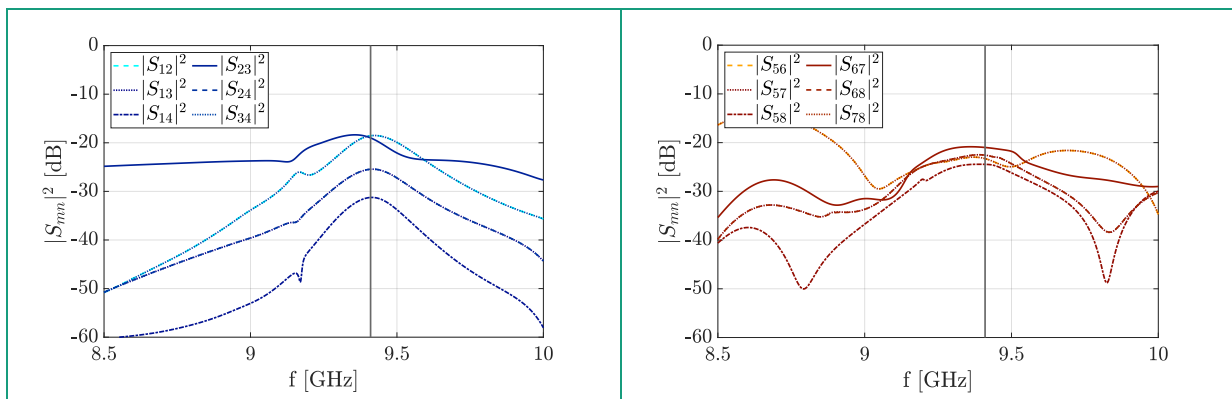


Table D-4 – Co-Polar Port Isolations (H-Pol and V-Pol)

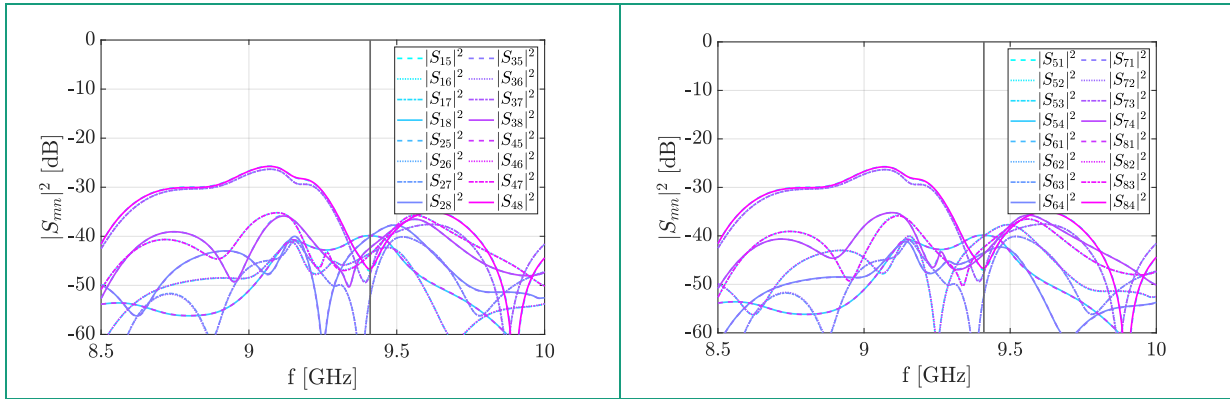


Table D-5 – Cross-Polar Port Isolations (H-Pol and V-Pol)

Active Reflection Coefficients (ARC)

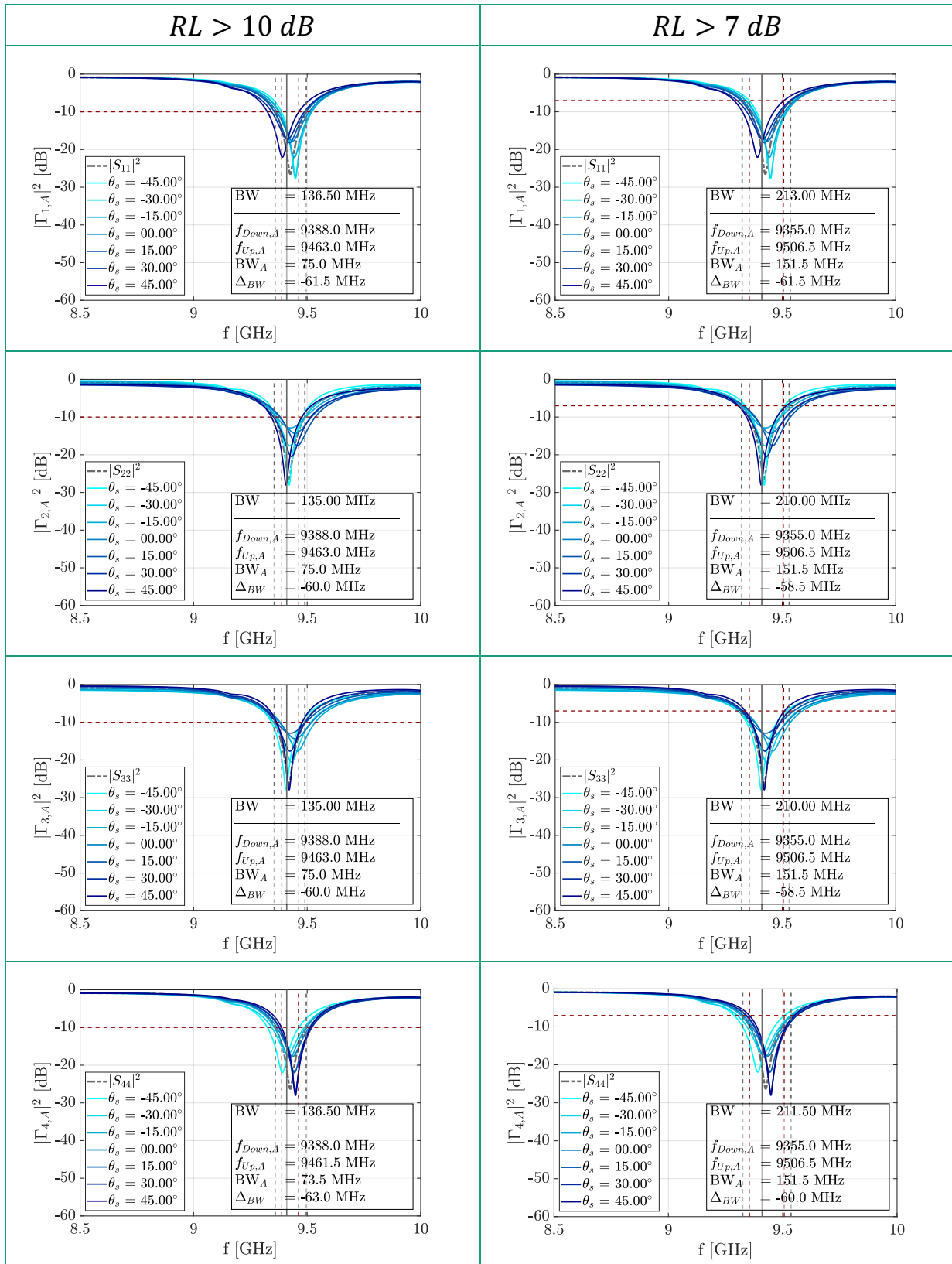


Table D-6 – Active Reflection Coefficients for H-Pol

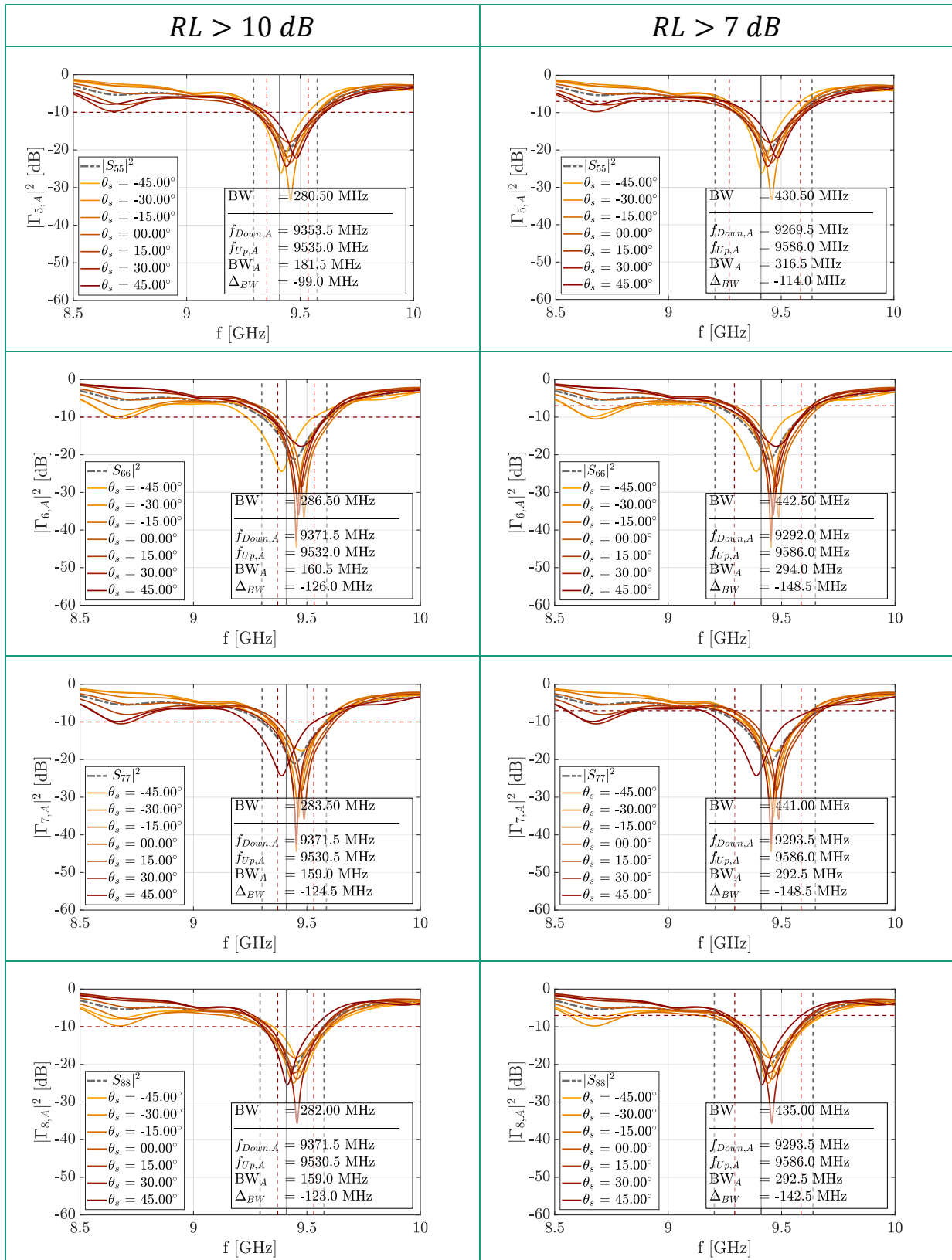
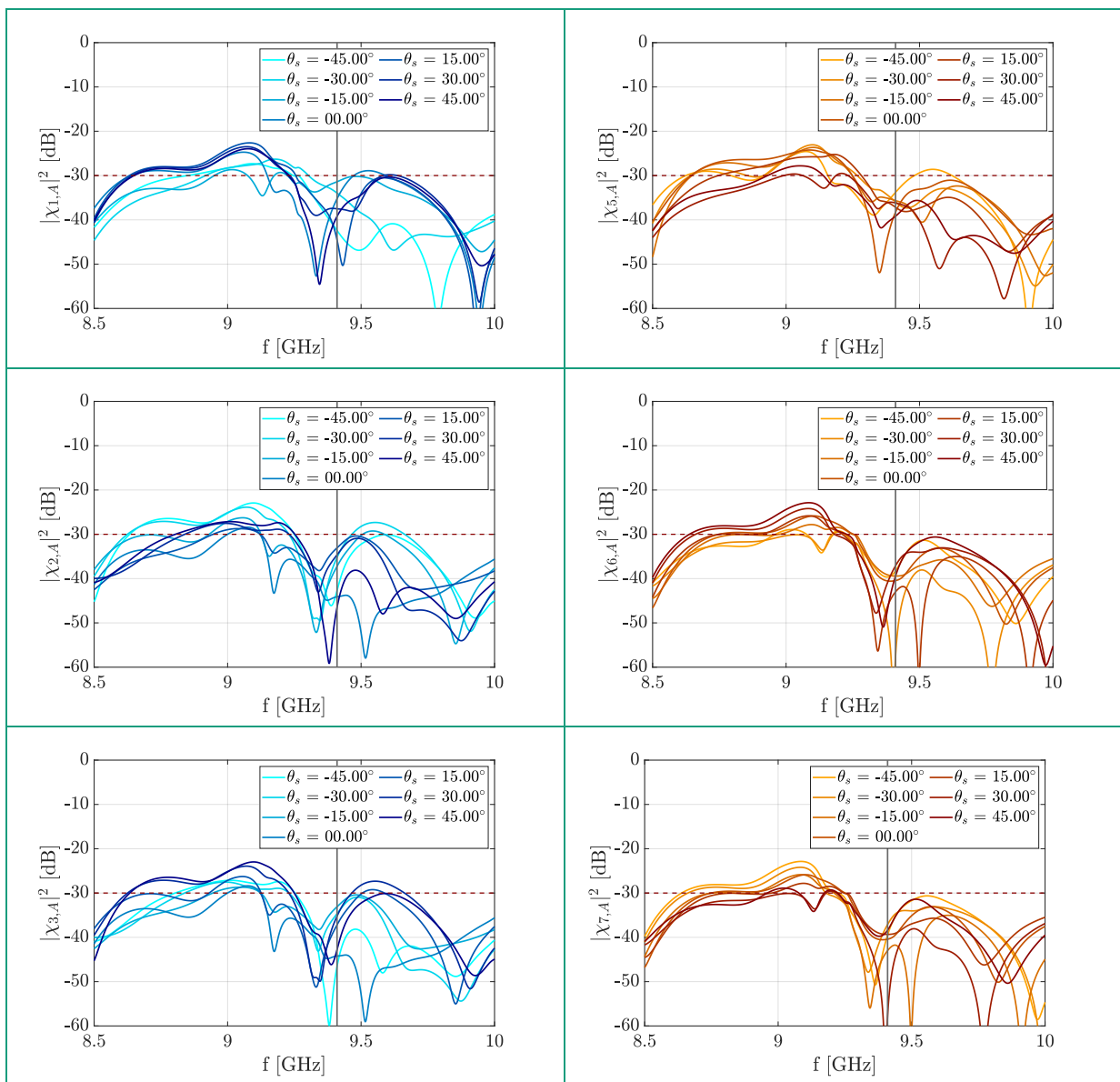


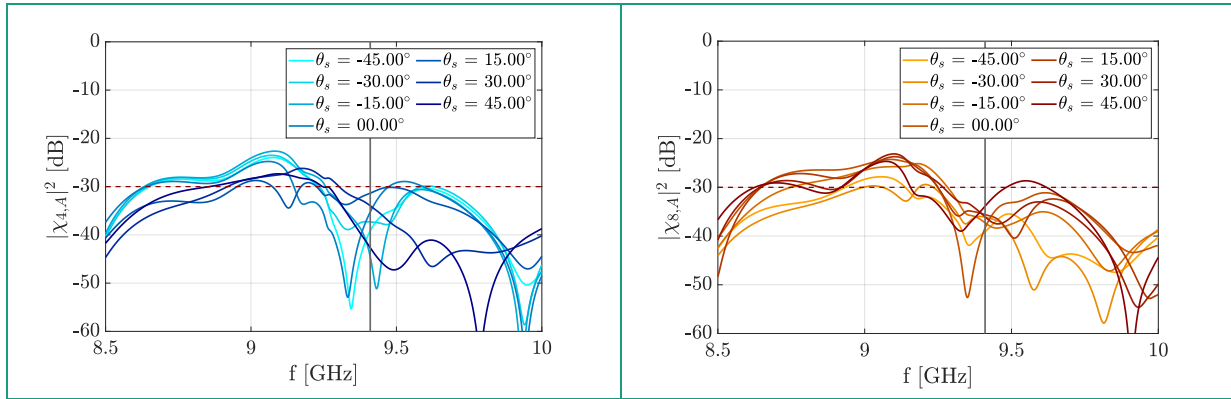
Table D-7 – Active Reflection Coefficients for V-Pol

	<i>RL > 10 dB</i>			<i>RL > 7 dB</i>		
	$f_{down,max}$	$f_{up,min}$	$BW_{eff,a}$	$f_{down,max}$	$f_{up,min}$	$BW_{eff,a}$
H-Pol	9390 MHz	9460 MHz	73.50 MHz	9360 MHz	9510 MHz	151.5 MHz
V-Pol	9370 MHz	9530 MHz	159.0 MHz	9290 MHz	9590 MHz	292.5 MHz
System	9390 MHz	9460 MHz	73.50 MHz	9360 MHz	9510 MHz	151.5 MHz

Table D-8 – Active Bandwidth

Active Isolation Coefficients (AIC)



**Table D-9 – Active Isolation Coefficients (H-Pol and V-Pol)**

Radiation patterns and Cross-polarization Discrimination (XPD)

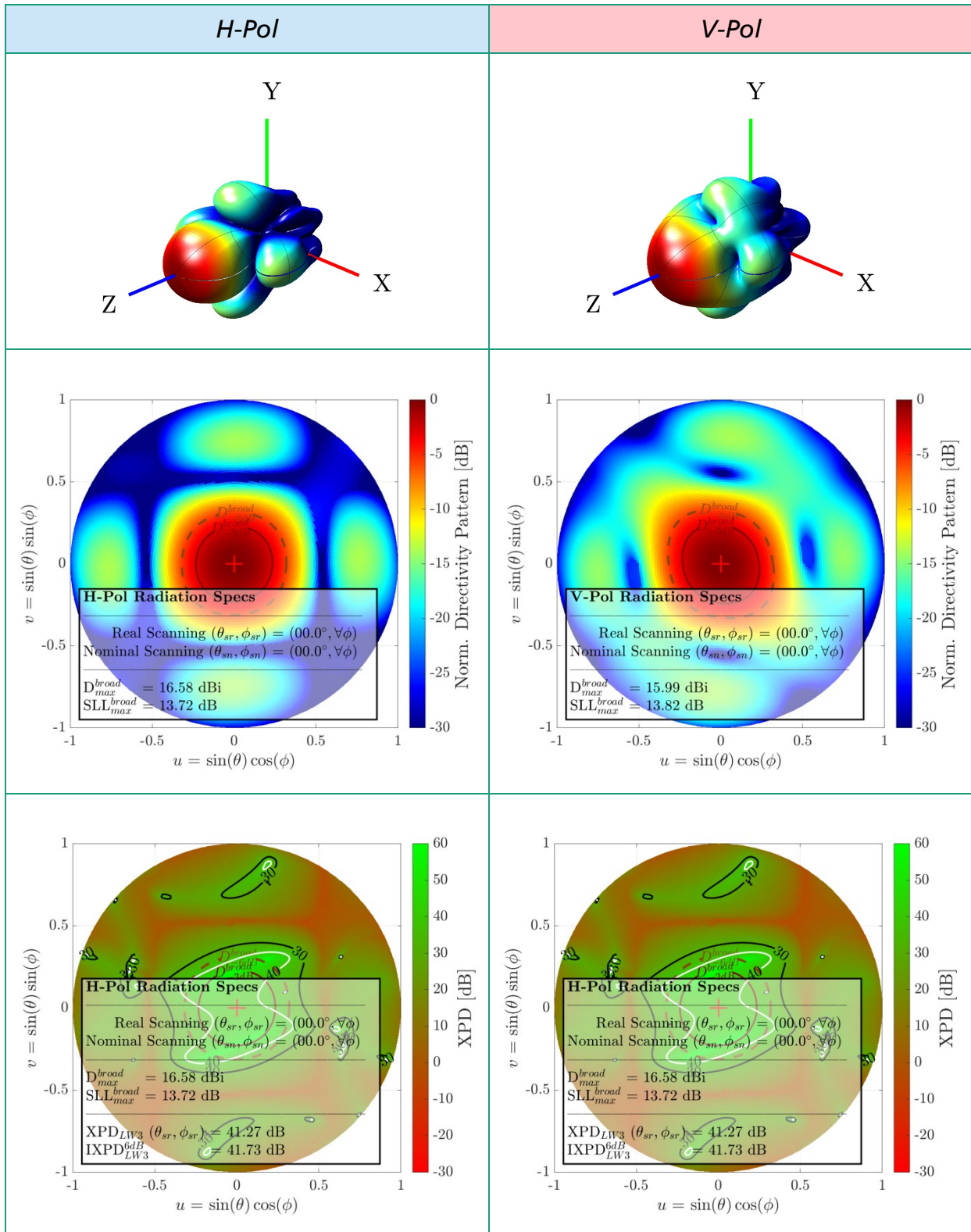


Table D-10 – Polarimetric and Radiation performance at $\theta_s = 00^\circ$ (Broadside)

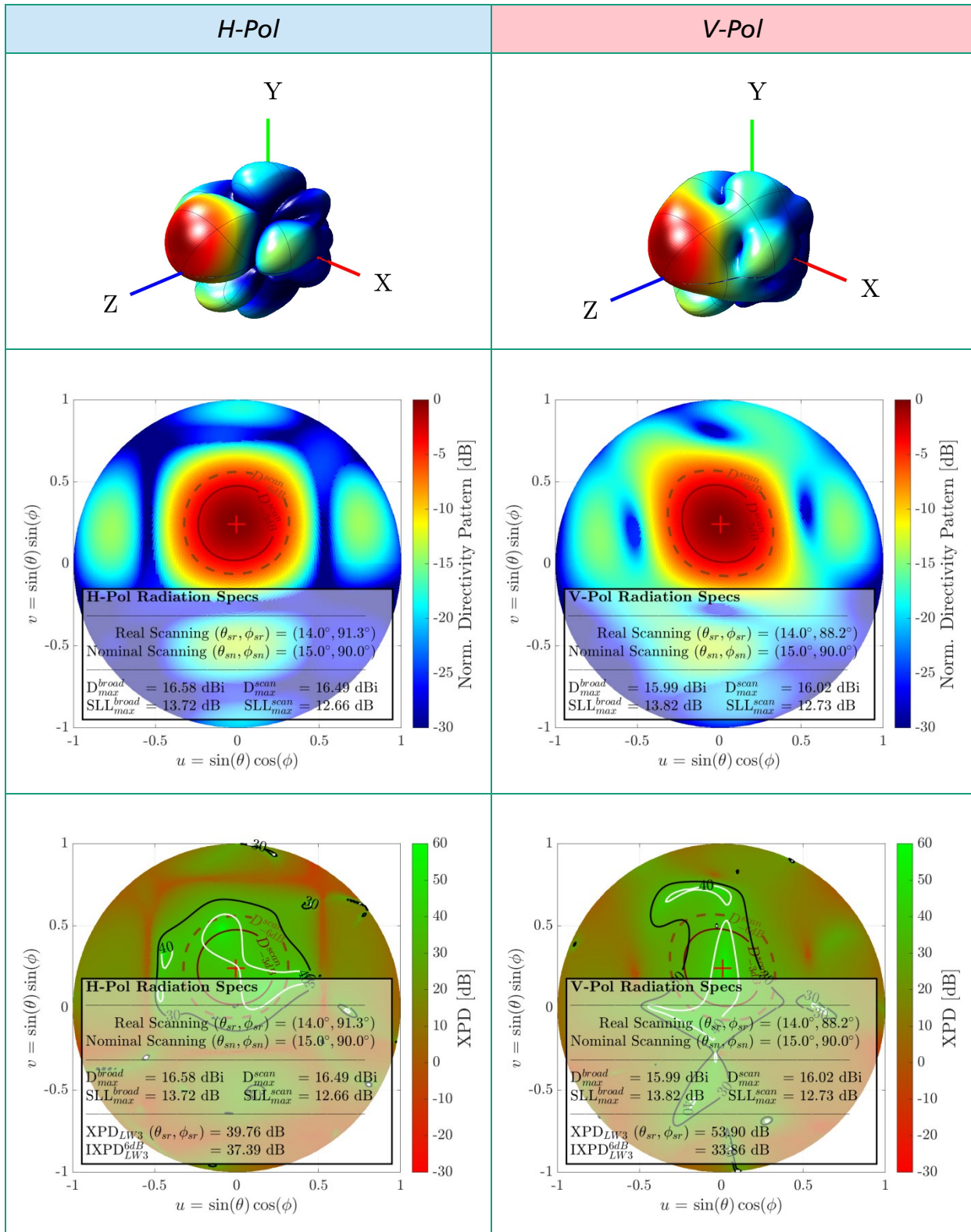


Table D-11 – Polarimetric and Radiation performance at $\theta_s = 15^\circ$

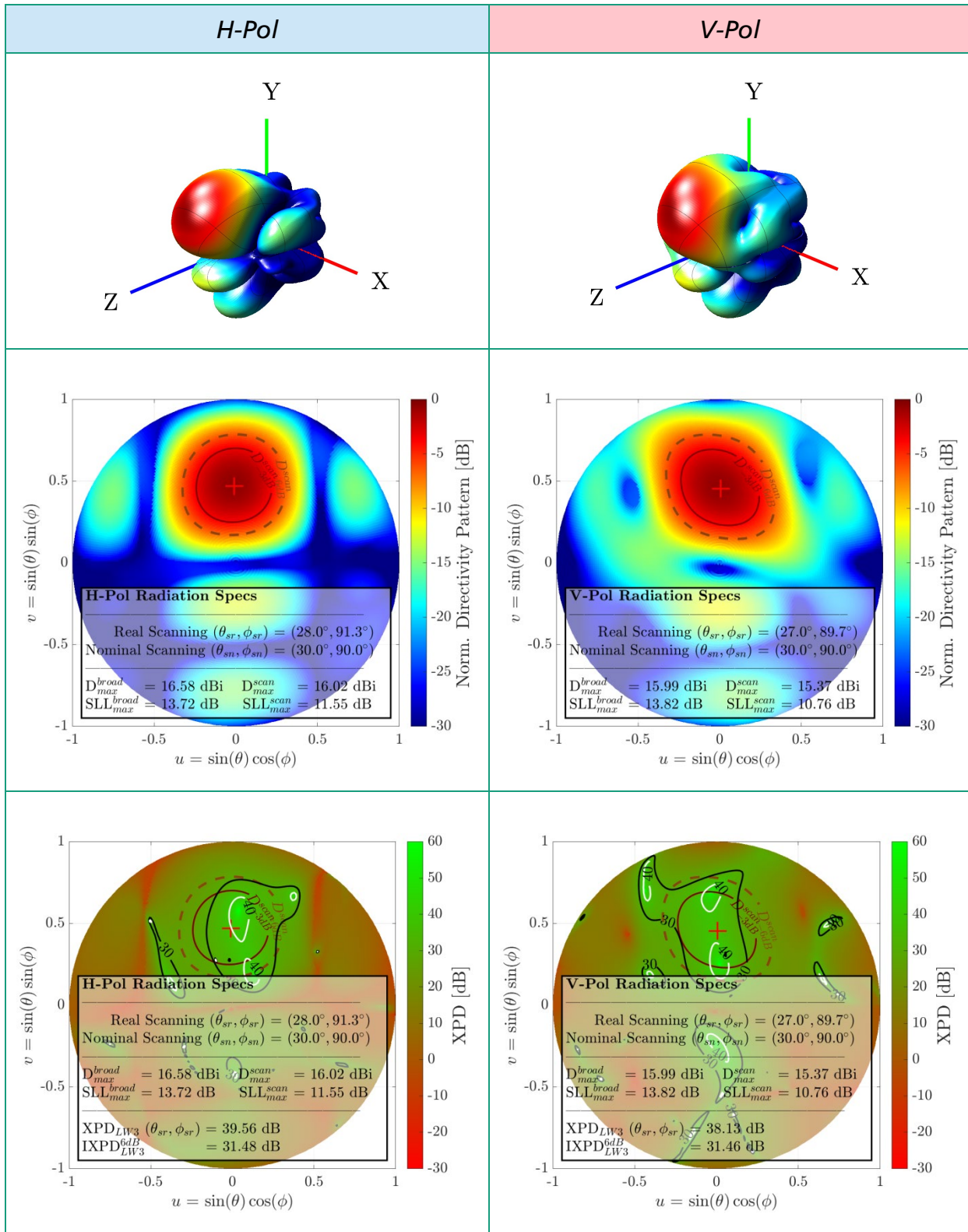


Table D-12 – Polarimetric and Radiation performance at $\theta_s = 30^\circ$

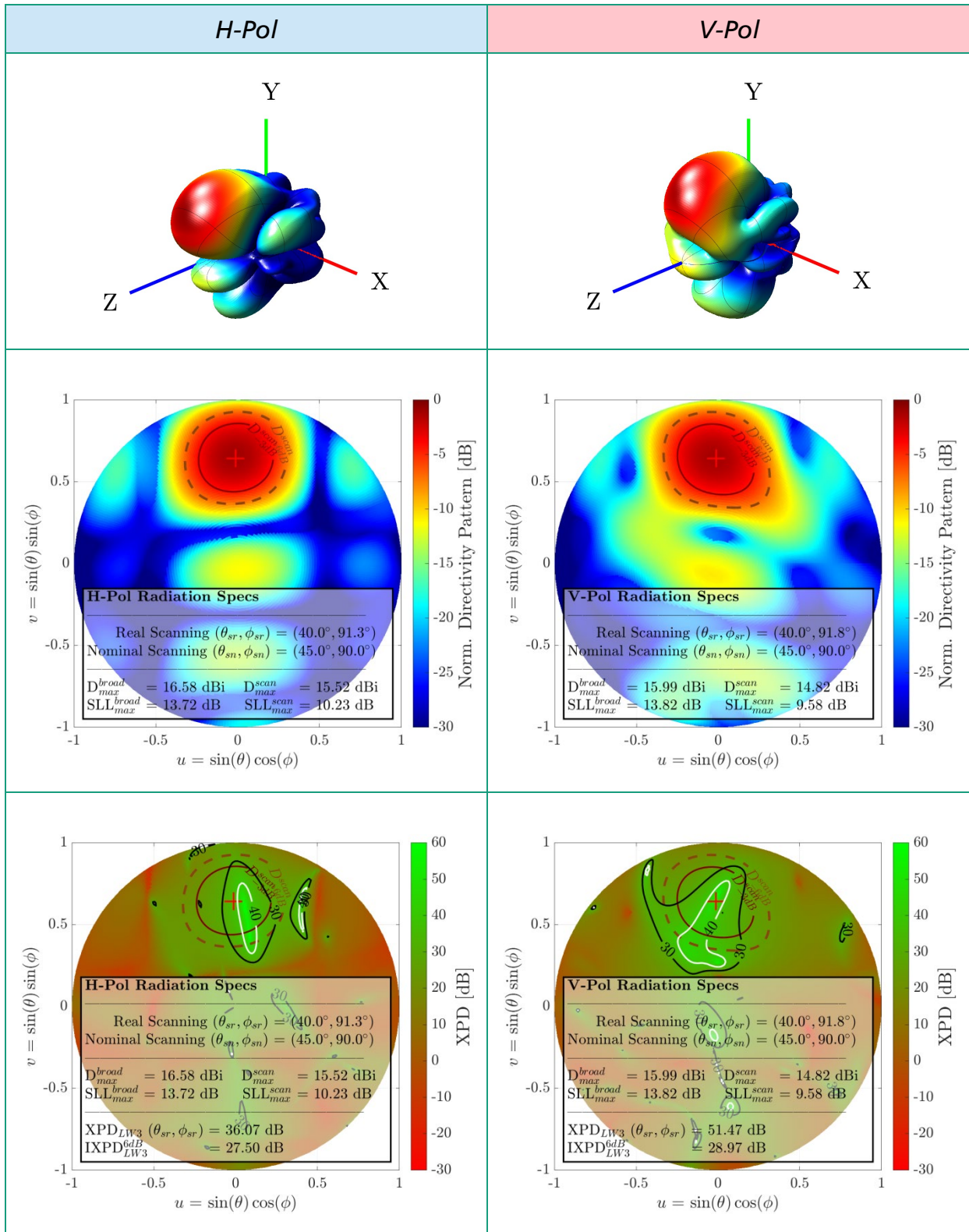


Table D-13 – Polarimetric and Radiation performance at $\theta_s = 45^\circ$

Scan Assessments

Scan Assessments

	Nominal Scanning Angle (θ_{sn}, ϕ_{sn})	Real Scanning (θ_{sr}, ϕ_{sr})	SLL_{max}	Dir	η_{rad}
H-Pol	(00°, $\forall\phi$)	(00.0°, $\forall\phi$)	13.72 dB	16.58 dBi	75.94%
	(15°, 90°)	(14.0°, 89.7°)	12.73 dB	16.49 dBi	74.86%
	(30°, 90°)	(28.0°, 90.3°)	11.55 dB	16.02 dBi	73.45%
	(45°, 90°)	(40.7°, 90.3°)	10.23 dB	15.52 dBi	66.64%
V-Pol	(00°, $\forall\phi$)	(00.0°, $\forall\phi$)	13.82 dB	15.99 dBi	75.32%
	(15°, 90°)	(14.0°, 90.8°)	12.73 dB	16.02 dBi	75.18%
	(30°, 90°)	(27.7°, 89.7°)	10.76 dB	15.37 dBi	75.04%
	(45°, 90°)	(40.0°, 90.3°)	09.58 dB	14.82 dBi	74.17%

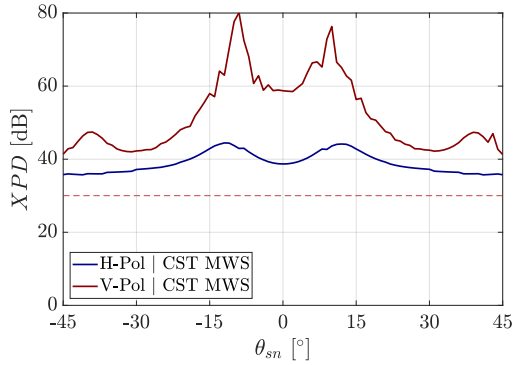
Table D-14 – Pattern Scan Assessment

	Nominal Scanning (θ_{sn}, ϕ_{sn})	XPD @(θ_{sr}, ϕ_{sr})	$IXPD^{6dB}$	$ICPR$	Z_{DRb}
H-Pol	(00°, $\forall\phi$)	41.27 dB	40.73 dB	-34.82 dB	-0.29 dB
	(15°, 90°)	39.76 dB	38.43 dB	-30.85 dB	-0.17 dB
	(30°, 90°)	39.56 dB	31.48 dB	-26.77 dB	-0.33 dB
	(45°, 90°)	36.07 dB	25.50 dB	-22.63 dB	-0.31 dB
V-Pol	(00°, $\forall\phi$)	47.42 dB	40.17 dB	-35.11 dB	-0.29 dB
	(15°, 90°)	53.90 dB	33.86 dB	-31.03 dB	-0.17 dB
	(30°, 90°)	37.89 dB	31.46 dB	-27.10 dB	-0.33 dB
	(45°, 90°)	54.93 dB	28.97 dB	-22.94 dB	-0.31 dB

Table D-15- Polarimetric Scan Assessment

Cross-polarization Discrimination¹

$$XPD \triangleq \frac{|E_{Cp}(\theta_{si}, \phi_{si})|^2}{|E_{Xp}(\theta_{si}, \phi_{si})|^2} > 30 \text{ dB}$$



Integrated Cross-polarization Discrimination

$$IXPD^{6dB} \triangleq \frac{\iint |E_{Cp}(\theta, \phi)| d\Omega_{6dB}}{\iint |E_{Xp}(\theta, \phi)| d\Omega_{6dB}}$$

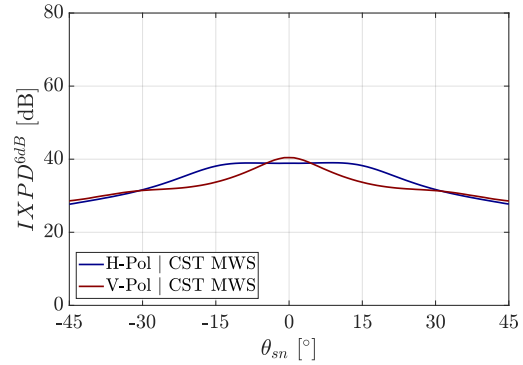


Table D-16– 4x4 Baseline Sub-array with Integrated Feed-net, Full-scan Polarimetric Assessment

Differential Reflectivity Bias²

$$Z_{DRb} = \frac{\iint_s |F_{HH}^2 + F_{HV}^2|^2 d\Omega}{\iint_s |F_{VH}^2 + F_{VV}^2|^2 d\Omega} < 0.1 \text{ dB}$$

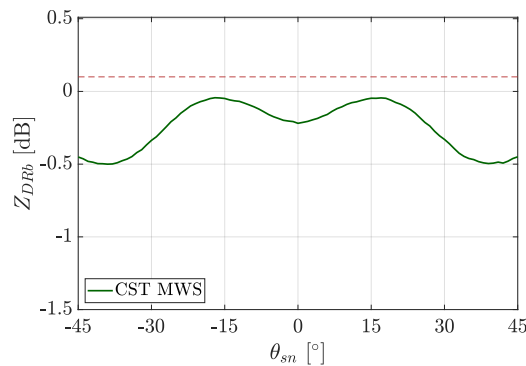


Table D-17 – 4x4 Imaged Sub-array with Integrated Feed-net, Z_{DRb}

Final Note

The reports simulation results have been obtained using CST MWS 2019, Frequency Domain Solver. The simulated dataset has been extracted and processed with custom MATLAB functions.

¹

Real scanning angle: $(\theta_{sr}, \phi_{sr}) = (\theta, \phi) | \max \{ |E_{Cp}(\theta, \phi)|^2 \}$

² Considering a phased array that does not use T/R modules or other active elements.

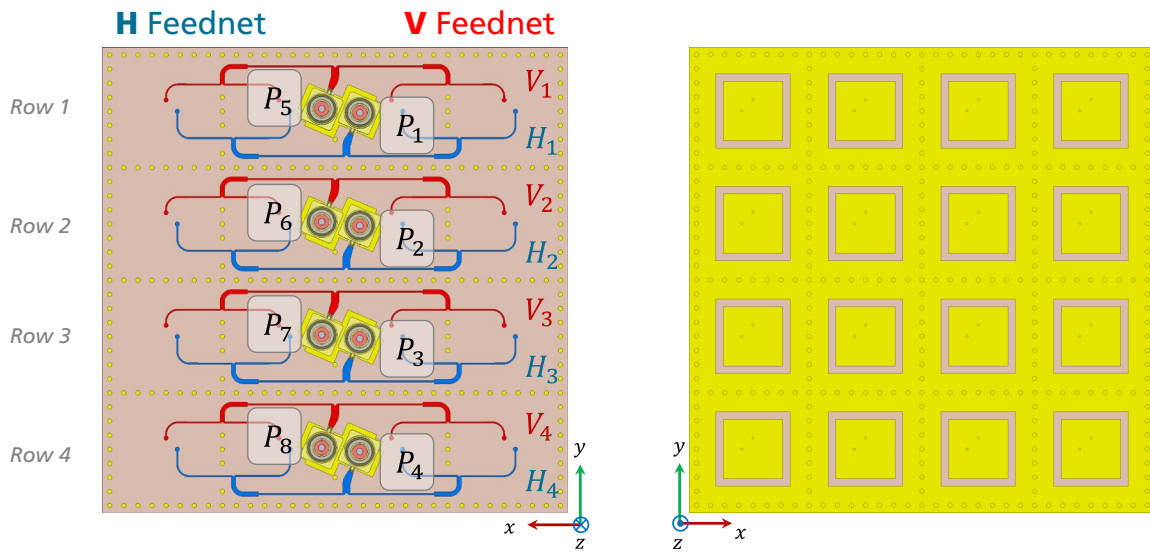
APPENDIX – E

RESULTS MEASUREMENTS

Integrated 4x4 Baseline Sub-Array

Integrated 4x4 Baseline Sub-Array (Measurements)

Port Specification



Port Excitations

Assuming a uniform distribution, the excitations for each port are specified in the following tables:

Port	1	2	3	4
H-Port	H_1	H_2	H_3	H_4
Phase Excitation	0°	β_y	$2\beta_y$	$3\beta_y$

Table E-1 - Specification for 4x4 Imaged Sub-Array for H-Pol

Port	5	6	7	8
V-Port	V_1	V_2	V_3	V_4
Phase Excitation	0°	β_y	$2\beta_y$	$3\beta_y$

Table E-2 - Specification for 4x4 Imaged Sub-Array for V-Pol

$$\beta_y = -\frac{2\pi}{\lambda_0} d_y \sin \theta_{max} \xrightarrow{d_y=\lambda_0/2} \beta_y = -\pi \sin \theta_{max} \text{ [rad]}$$

Static S-Parameters

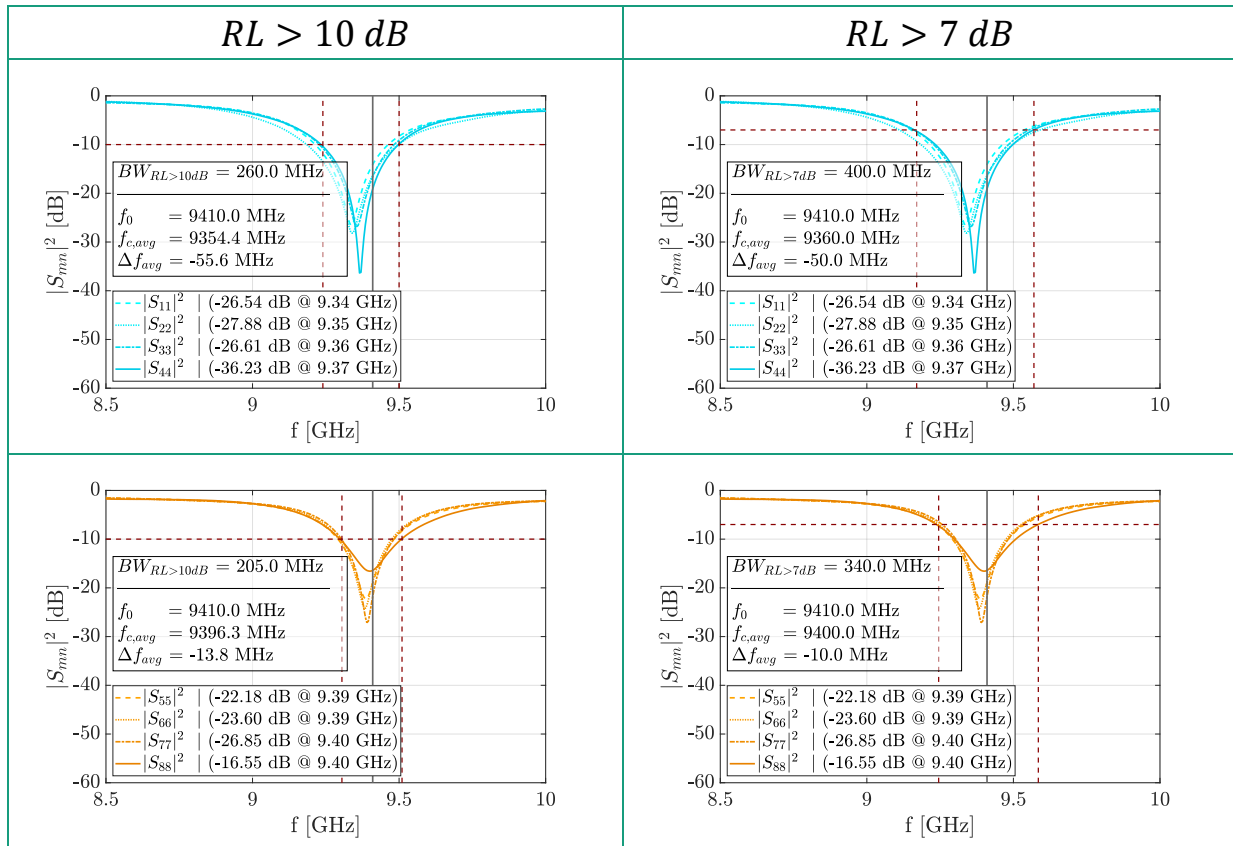


Table E-3 – Reflection Coefficients (H-Pol and V-Pol)

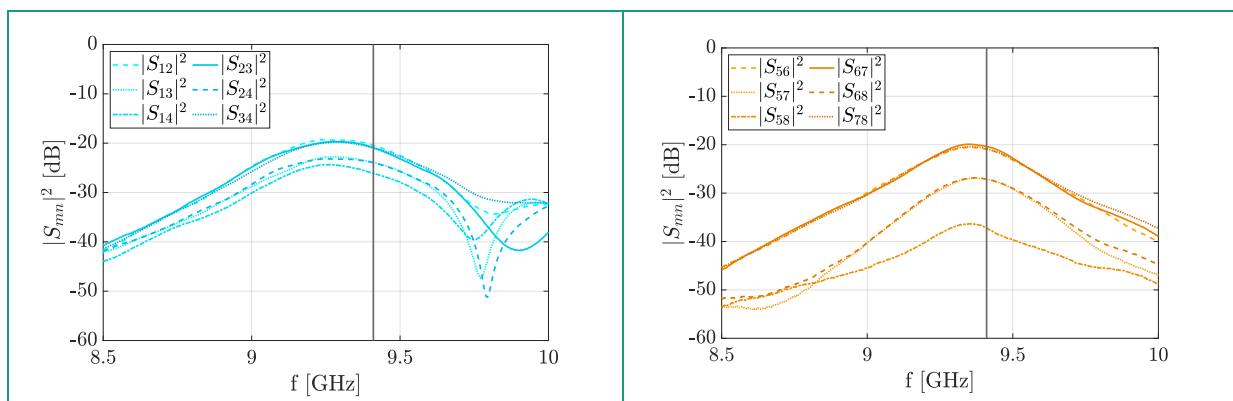


Table E-4 - Co-Polar Port Isolations (H-Pol and V-Pol)

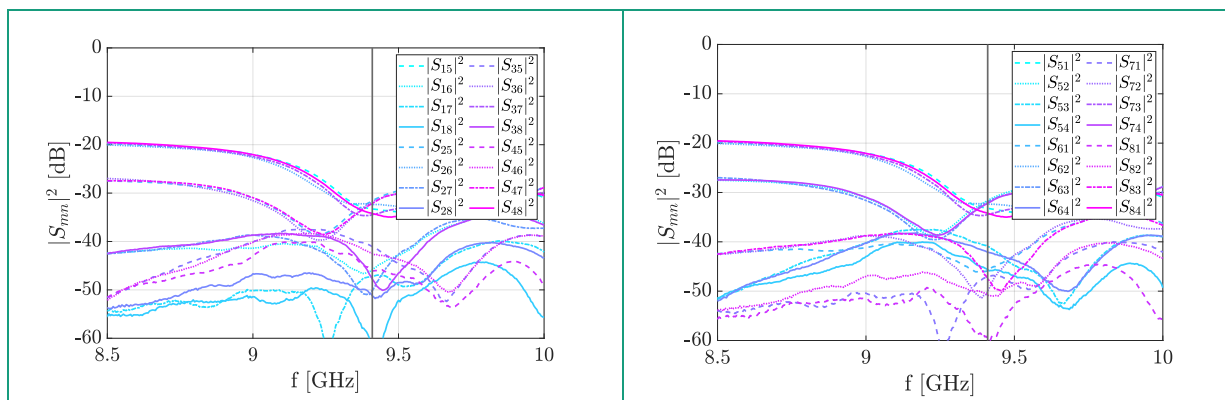


Table E-5 - Cross-Polar Port Isolations (H-Pol and V-Pol)

Active Reflection Coefficients (ARC)

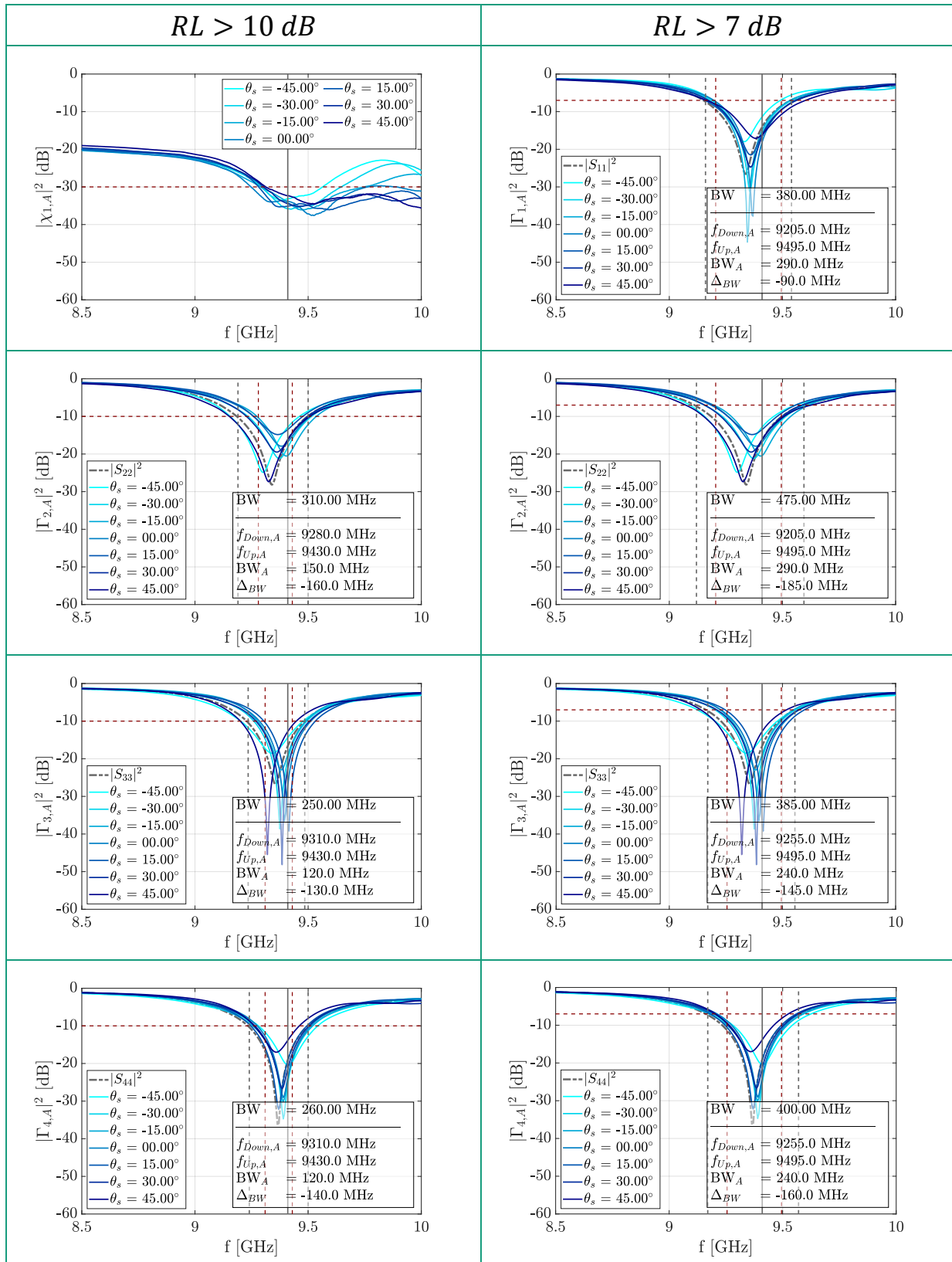


Table E-6 – Active Reflection Coefficients for H-Pol

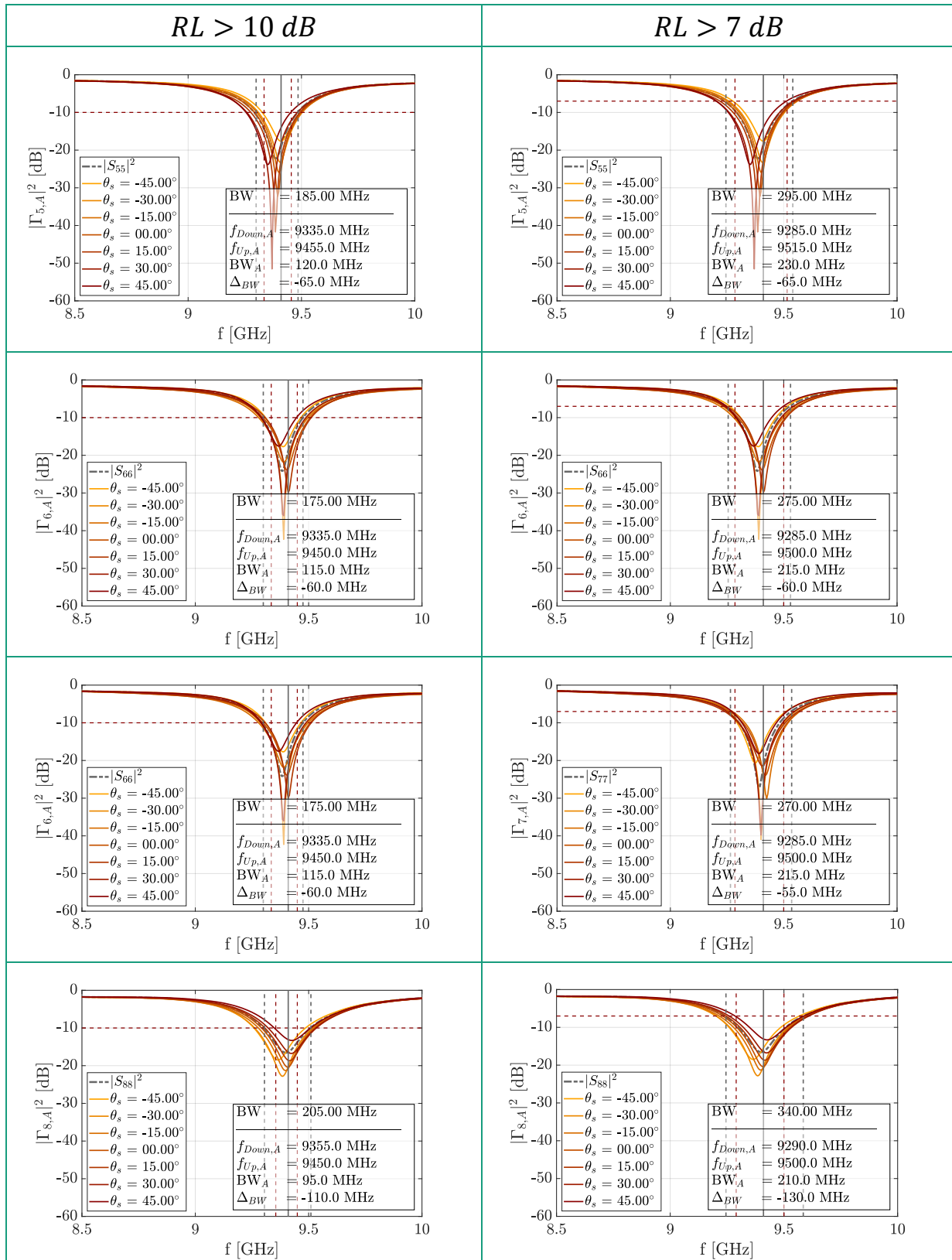
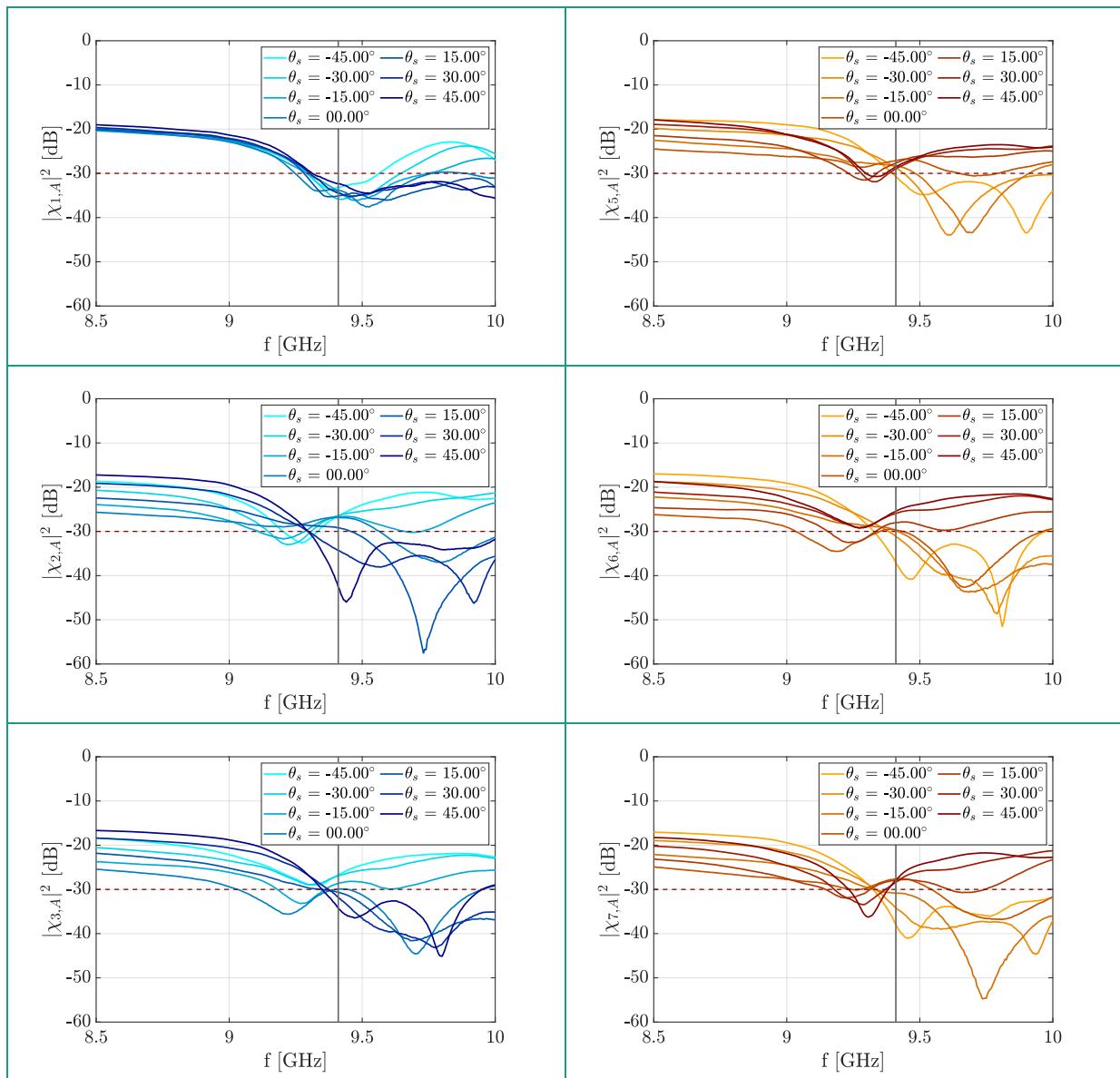


Table E-7 – Active Reflection Coefficients for V-Pol

	RL > 10 dB			RL > 7 dB		
	$f_{down,max}$	$f_{up,min}$	$BW_{eff,a}$	$f_{down,max}$	$f_{up,min}$	$BW_{eff,a}$
H-Pol	9310 MHz	9430 MHz	120.0 MHz	9260 MHz	9490 MHz	230.0 MHz
V-Pol	9360 MHz	9450 MHz	95.0 MHz	9290 MHz	9500 MHz	210.0 MHz
System	9310 MHz	9430 MHz	70.0 MHz	9290 MHz	9490 GHz	200.0 MHz

Table E-8 - Active Bandwidth

Active Isolation Coefficients (AIC)



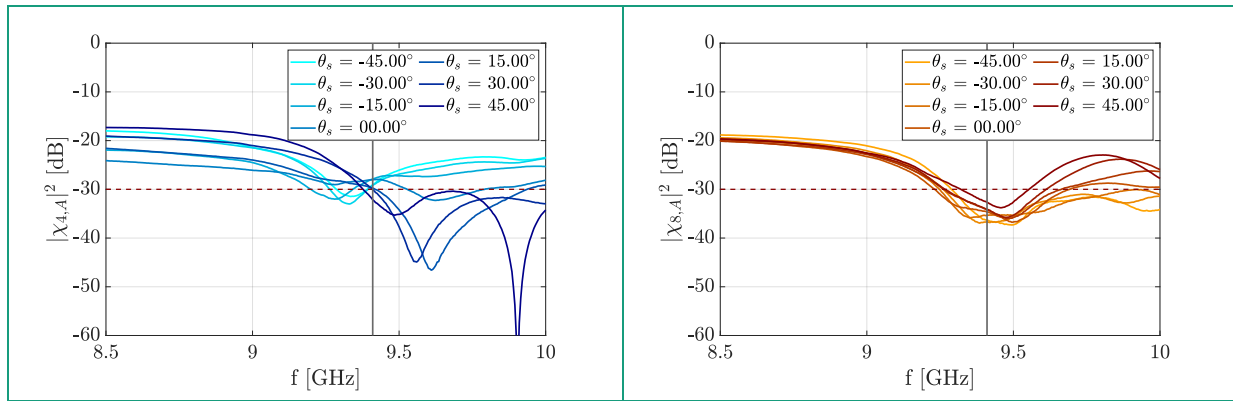


Table E-9 – Active Isolations Coefficients (H-Pol and V-Pol)

Comparison Simulations vs. Measurements

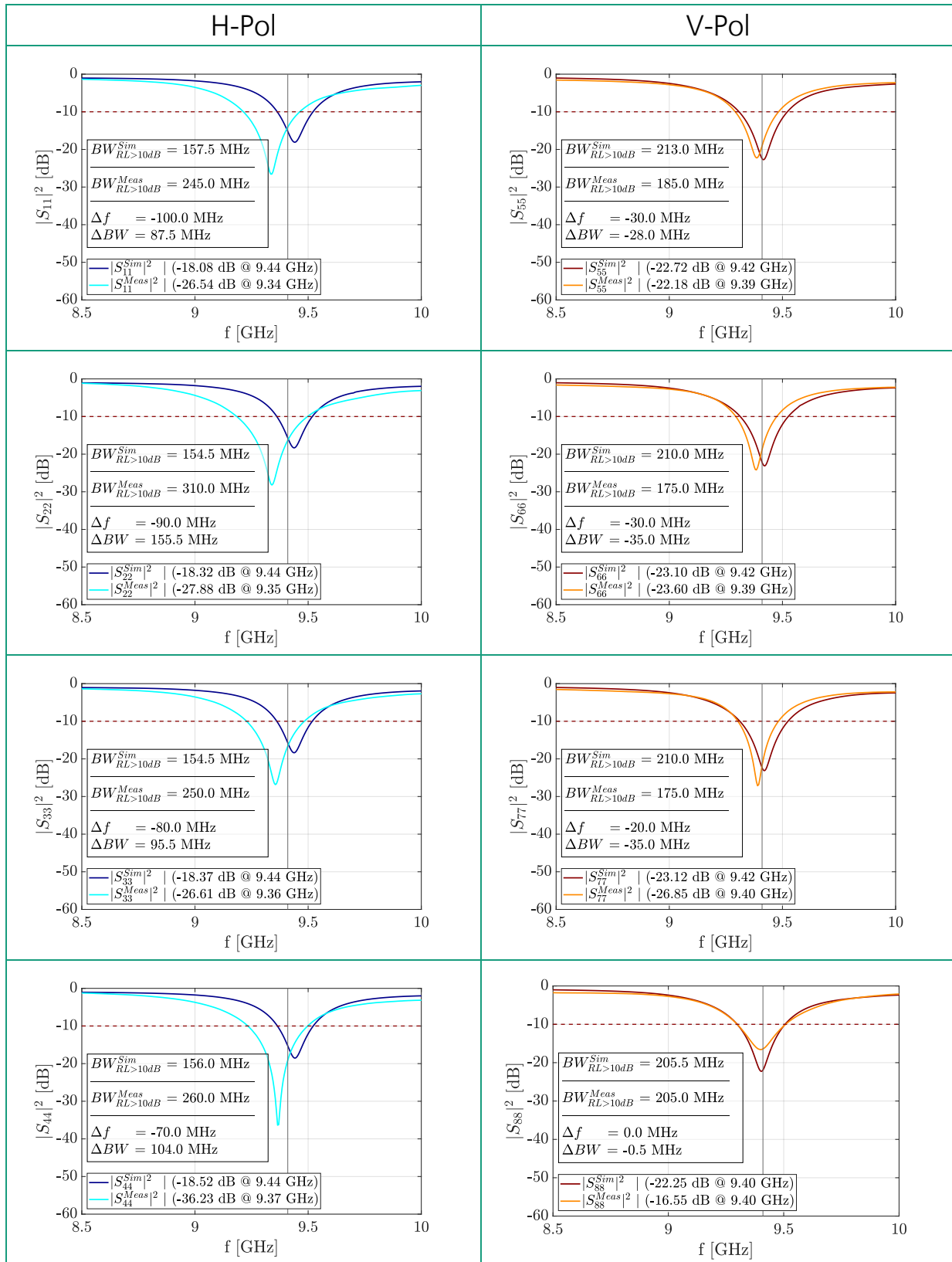


Table E-10 – Reflection Coefficients (H-Pol and V-Pol, Simulations vs. Measurements)

Radiation patterns and Cross-polarization Discrimination (XPD)

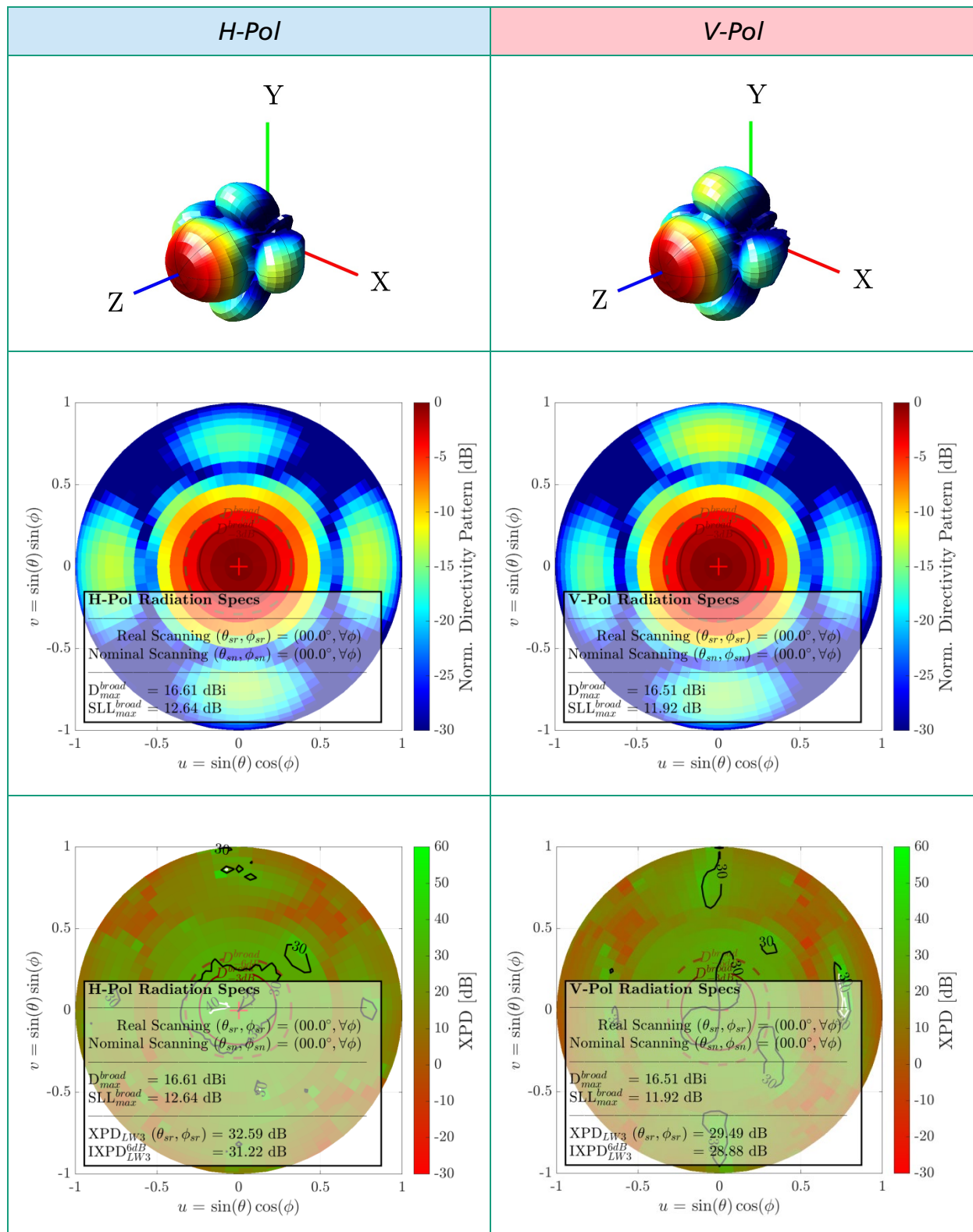


Table E-11 - Polarimetric and Radiation performance at $\theta_s = 00^\circ$ (Broadside)

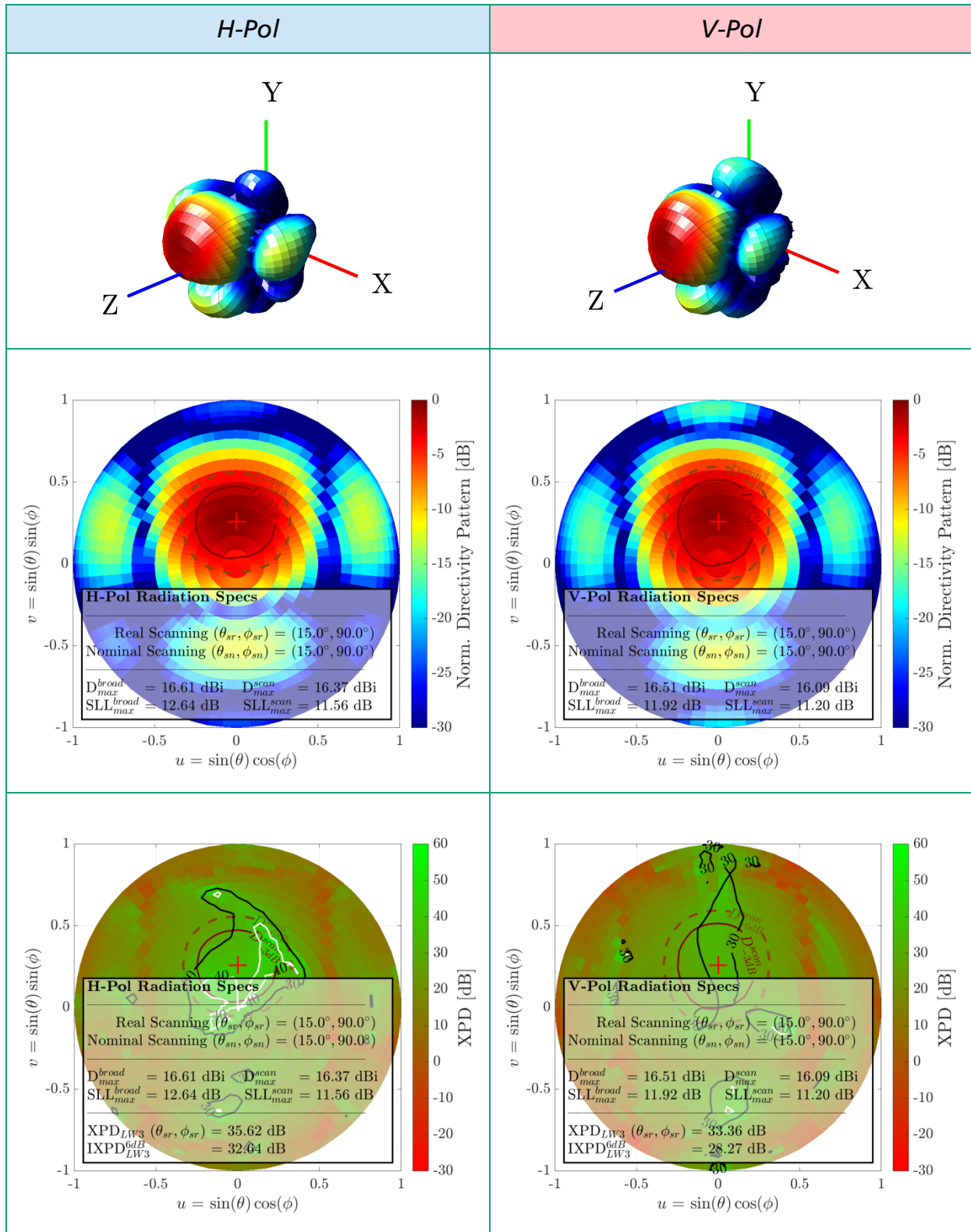


Table E-12 - Polarimetric and Radiation performance at $\theta_s = 15^\circ$

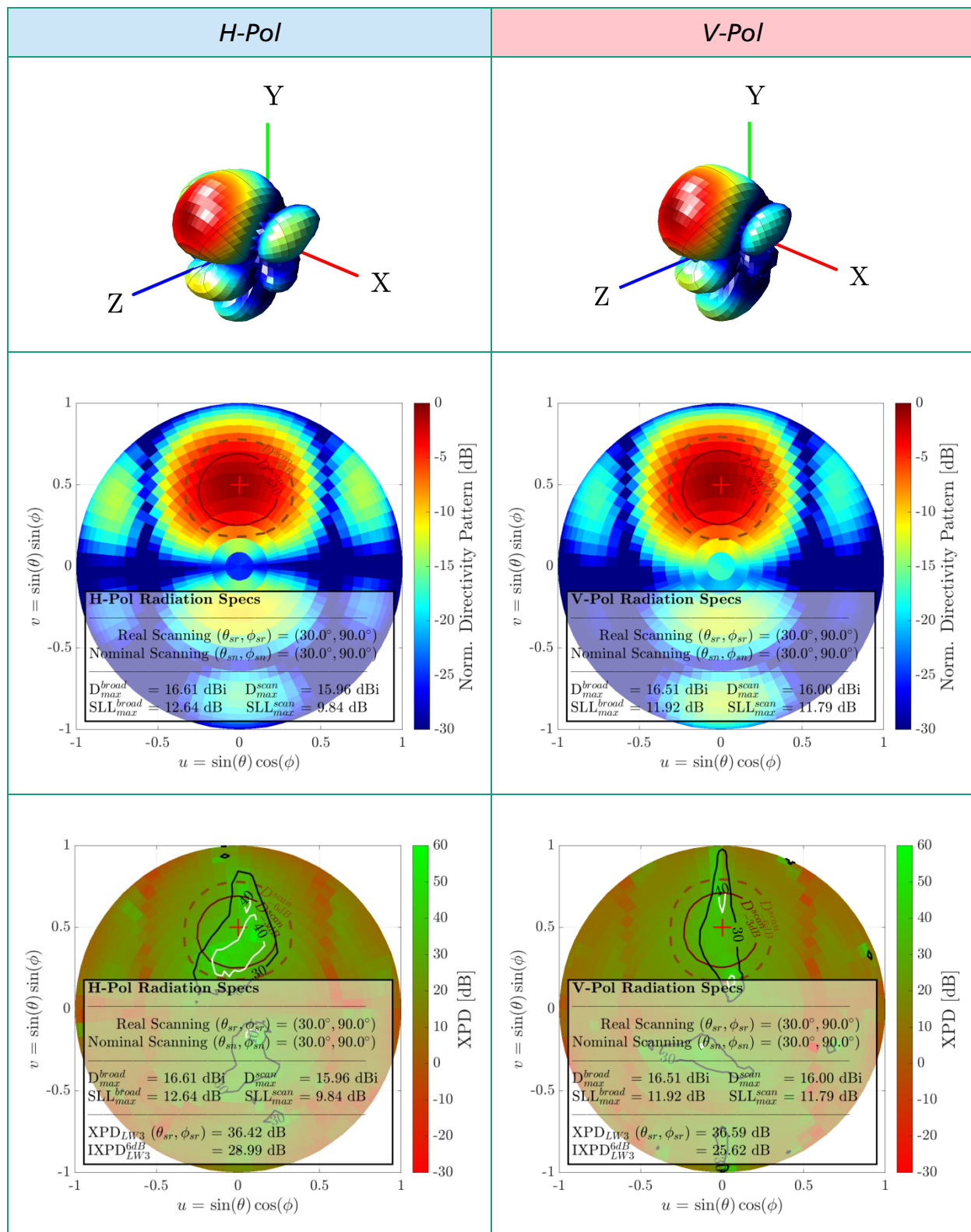


Table E-13 - Polarimetric and Radiation performance at $\theta_s = 30^\circ$

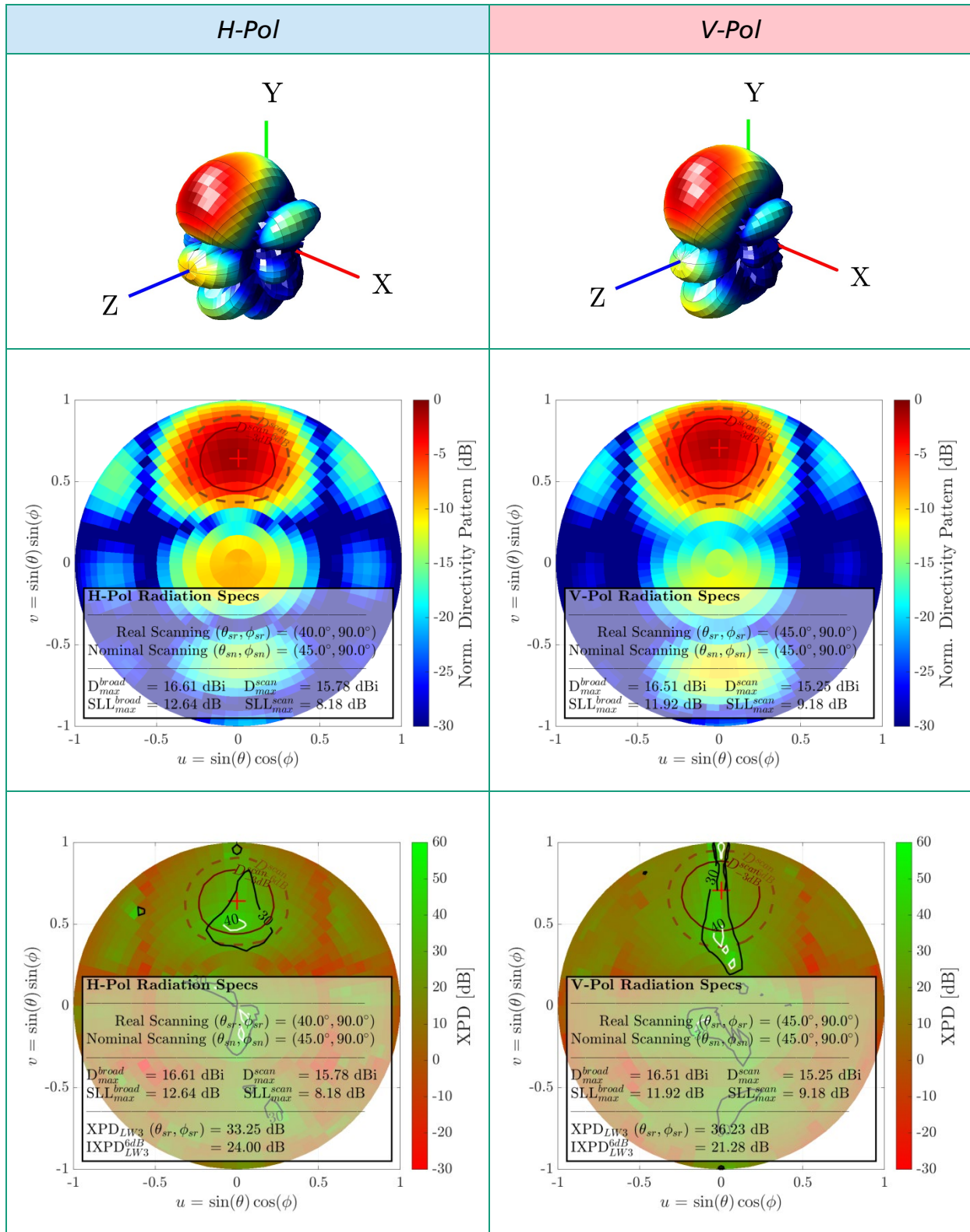
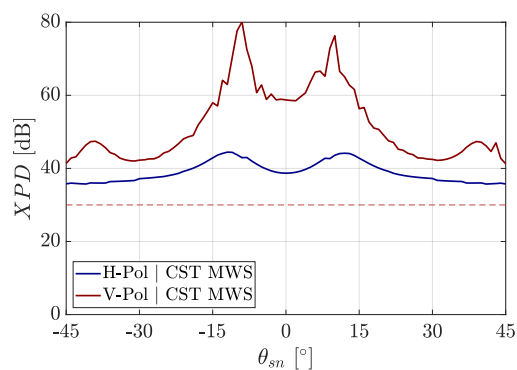


Table E-14 - Polarimetric and Radiation performance at $\theta_s = 45^\circ$

Scan Assessments

Cross-polarization Discrimination¹

$$XPD \triangleq \frac{|E_{Cp}(\theta_{si}, \phi_{si})|^2}{|E_{Xp}(\theta_{si}, \phi_{si})|^2} > 30 \text{ dB}$$



Integrated Cross-polarization Discrimination

$$IXPD^{6dB} \triangleq \frac{\oint |E_{Cp}(\theta, \phi)| d\Omega_{6dB}}{\oint |E_{Xp}(\theta, \phi)| d\Omega_{6dB}}$$

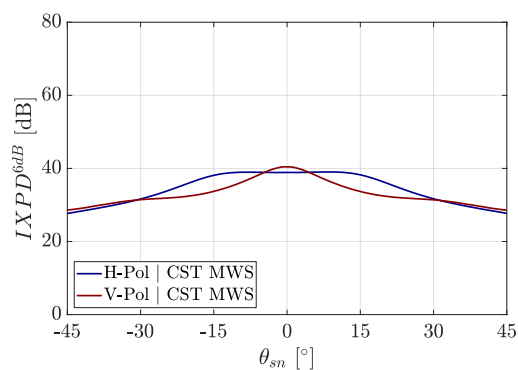


Table E-15– 4x4 Baseline Sub-array with Integrated Feed-net, Full-scan Polarimetric Assessment

Final Note

The reports measurements results have been obtained at Fraunhofer FHR facilities in Wachtberg (Germany). The measured dataset has been extracted and processed with custom MATLAB functions.

¹

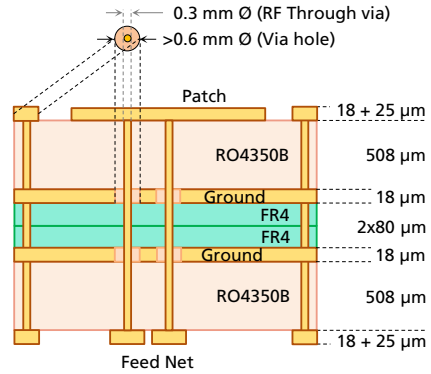
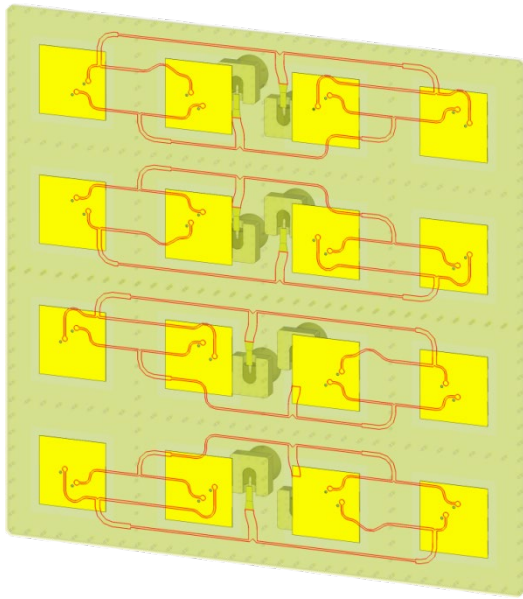
Real scanning angle: $(\theta_{sr}, \phi_{sr}) = (\theta, \phi) | \max \{ |E_{Cp}(\theta, \phi)|^2 \}$

APPENDIX – F

RESULTS MEASUREMENTS

Integrated 4x4 Imaged Sub-Array

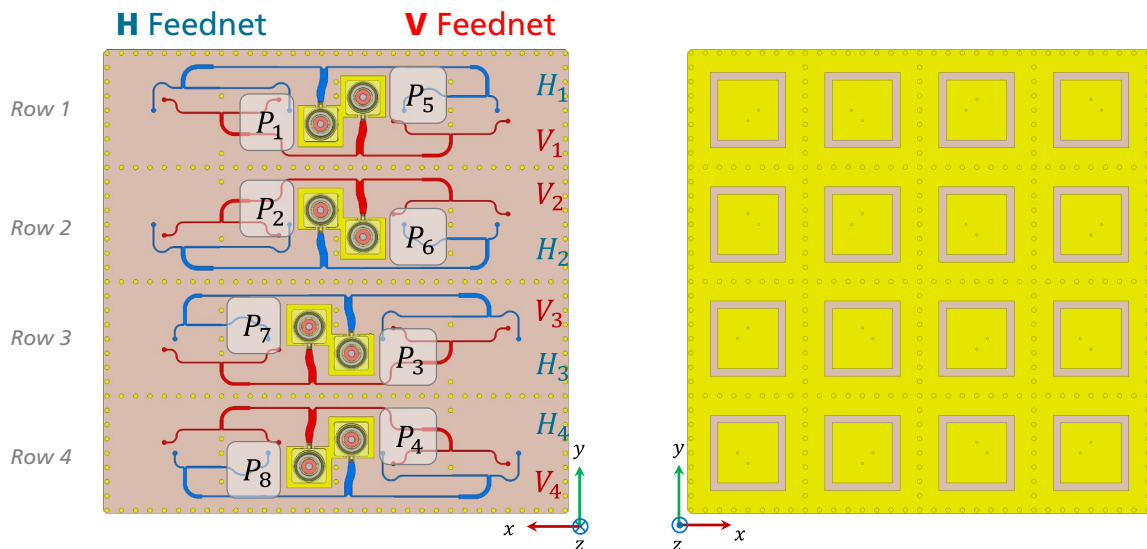
Integrated 4x4 Imaged Sub-Array (Measurements)



Structure Highlights:

- **4-layer** structure.
- **Symmetric** structure to prevent delamination.
- **Low-profile**.
- Blinded vias are avoided to minimize cost (**low-cost**).

Port Specifications



Port Excitations

Assuming a uniform distribution, the excitation for each port follows:

Port	1	2	3	4
H-Port	H_1	H_2	H_3	H_4
Phase Excitation	0°	β_y	$2\beta_y + 180^\circ$	$3\beta_y + 180^\circ$

Table F-1 - Specification for 4x4 Imaged Sub-Array for H-Pol

Port	5	6	7	8
V-Port	V_1	V_2	V_3	V_4
Phase Excitation	0°	$\beta_y + 180^\circ$	$2\beta_y$	$3\beta_y + 180^\circ$

Table F-2 - Specification for 4x4 Imaged Sub-Array for V-Pol

$$\beta_y = -\frac{2\pi}{\lambda_0} d_y \sin \theta_{max} \xrightarrow{d_y = \lambda_0/2} \beta_y = -\pi \sin \theta_{max} \text{ [rad]}$$

Static S-Parameters

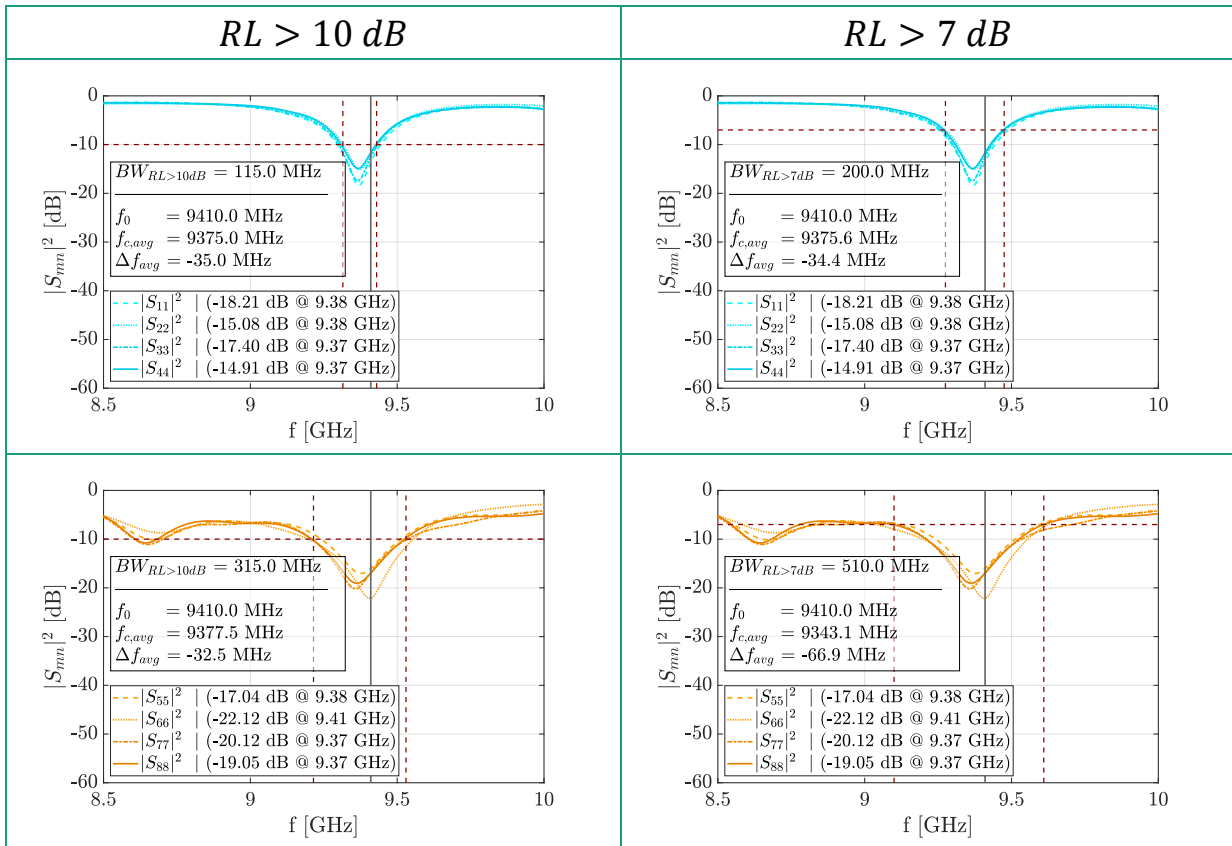


Table F-3 – Reflection Coefficients (H-Pol and V-Pol)

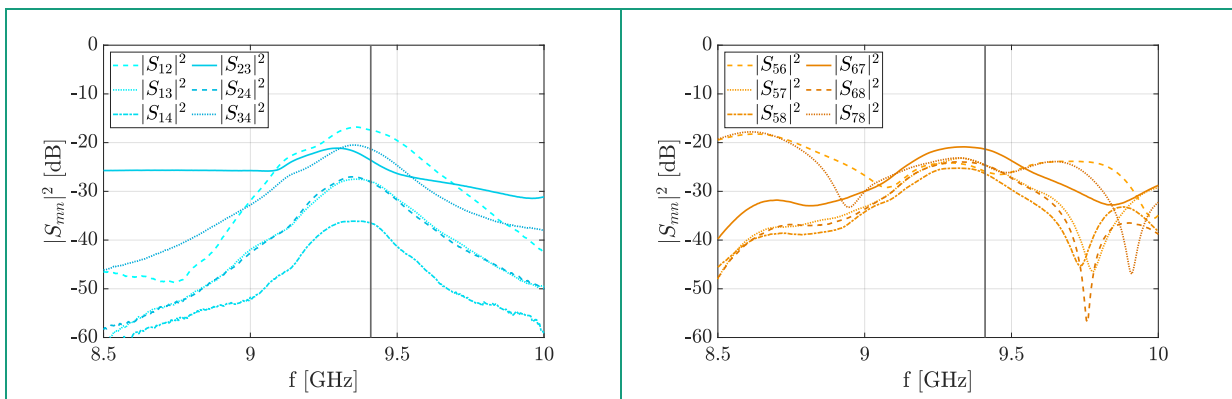


Table F-4 - Co-Polar Port Isolations (H-Pol and V-Pol)

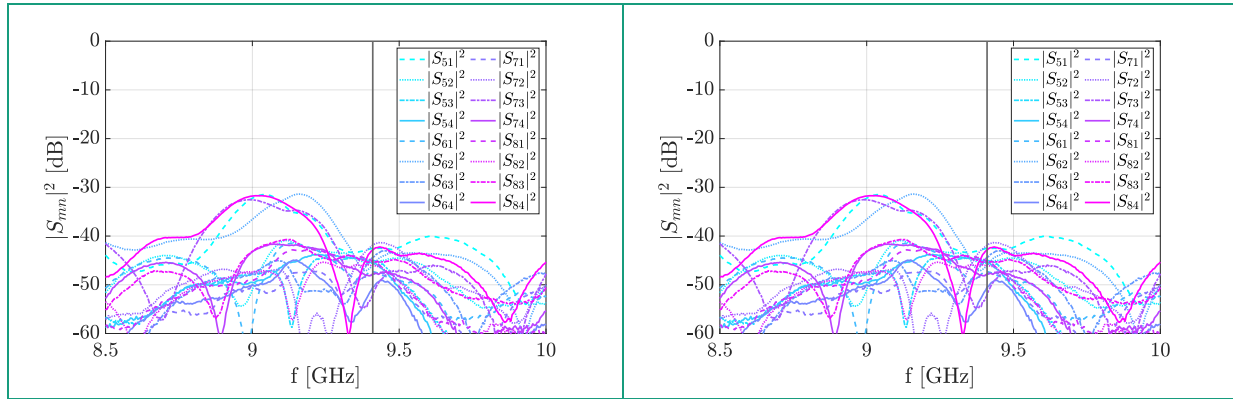


Table F-5 - Cross-Polar Port Isolations (H-Pol and V-Pol)

Active Reflection Coefficients (ARC)

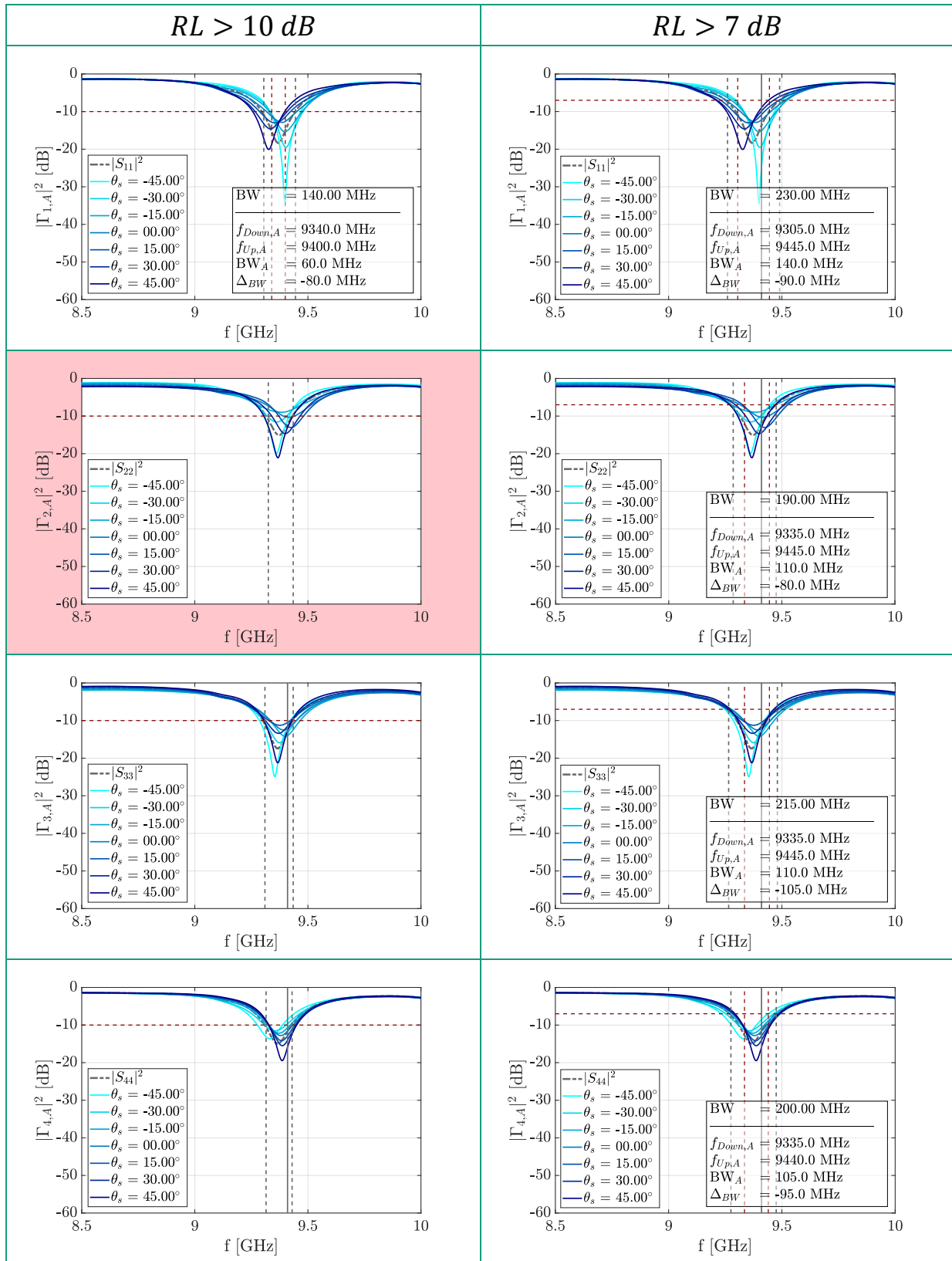


Table F-6 – Active Reflection Coefficients for H-Pol

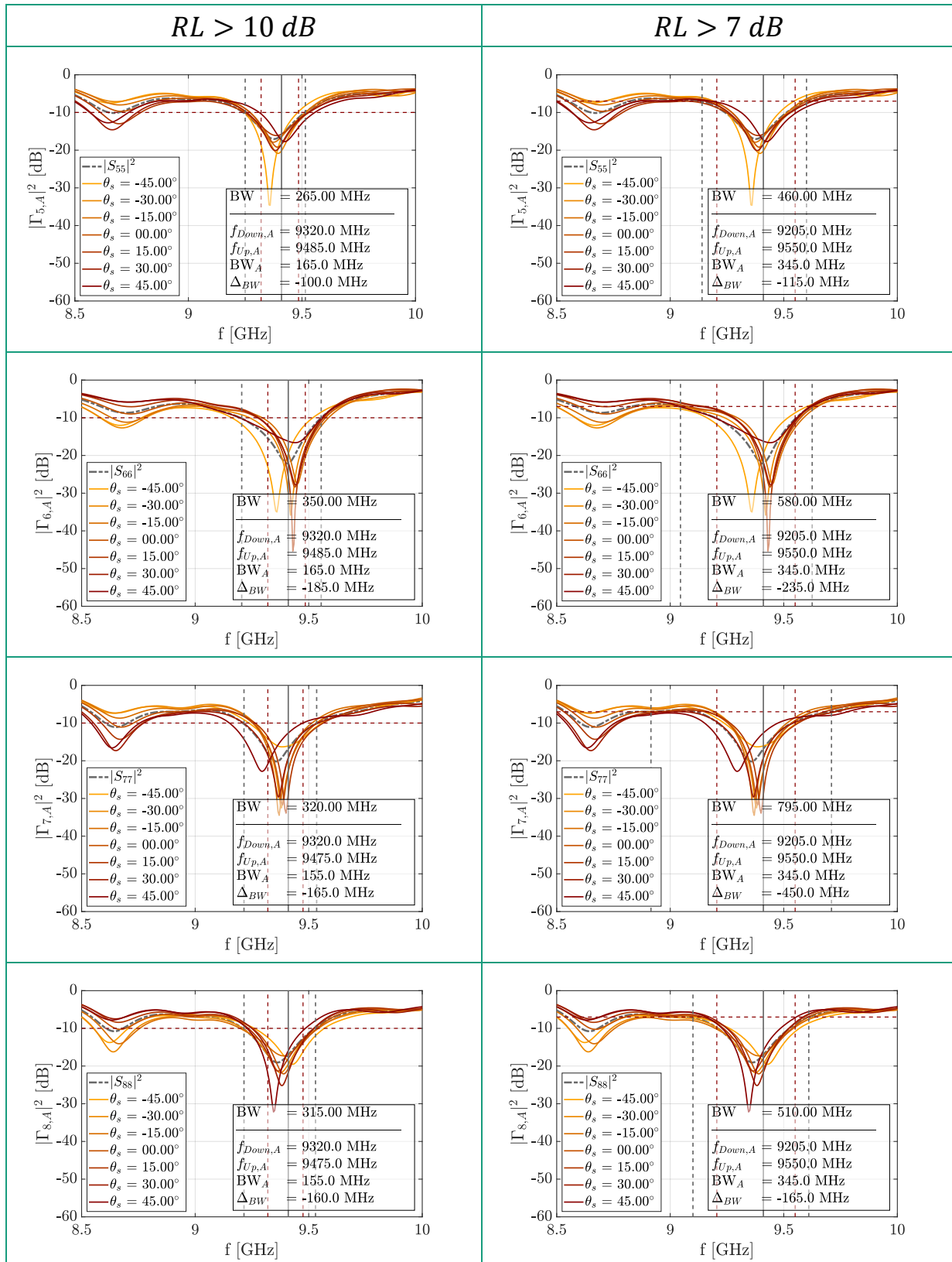


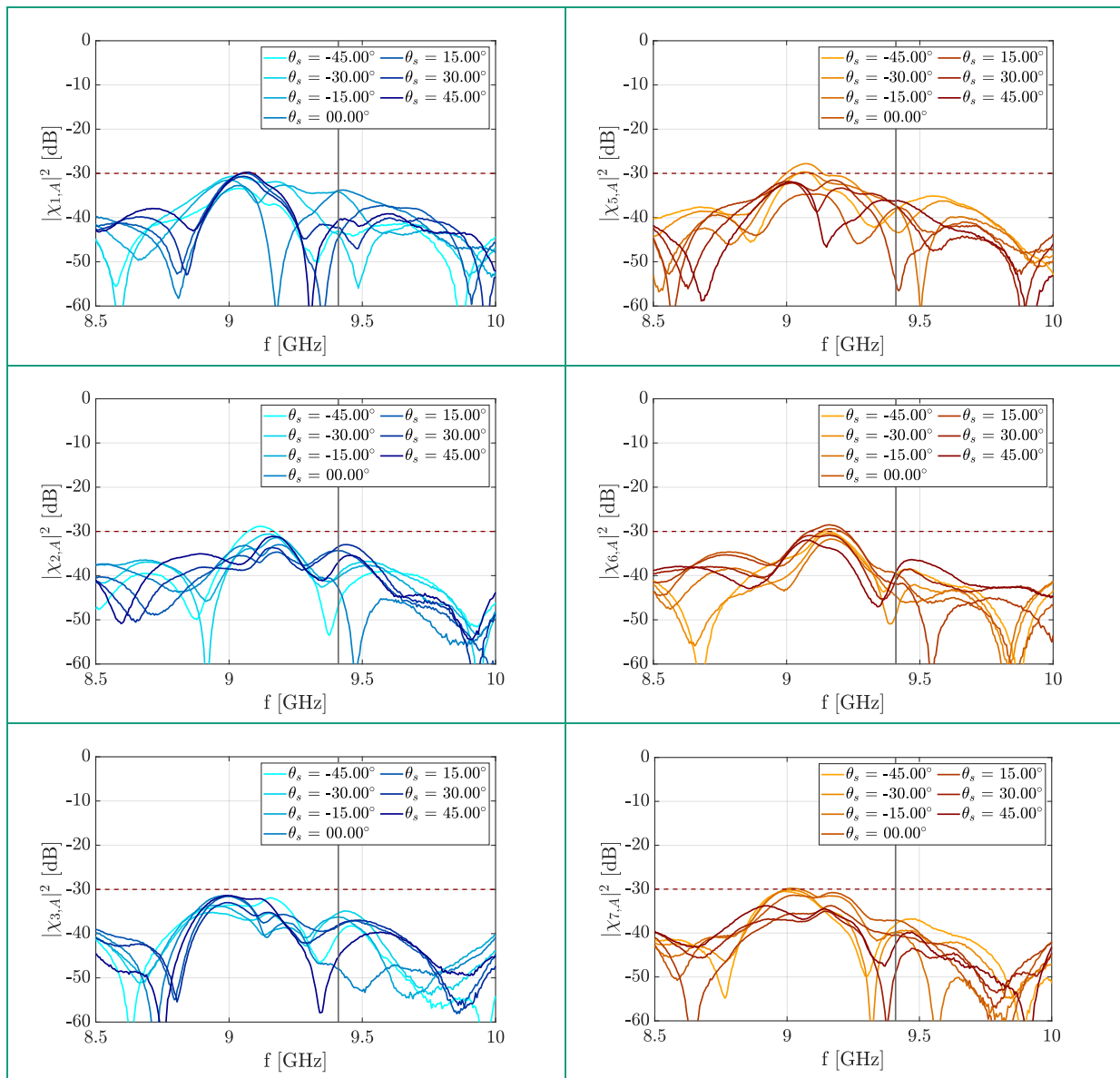
Table F-7 – Active Reflection Coefficients for V-Pol

	<i>RL > 10 dB</i>			<i>RL > 7 dB</i>		
	$f_{down,max}$	$f_{up,min}$	$BW_{eff,a}$	$f_{down,max}$	$f_{up,min}$	$BW_{eff,a}$
H-Pol	–	–	–	9340 MHz	9440 MHz	105.5 MHz
V-Pol	9320 MHz	9470 MHz	155.0 MHz	9210 MHz	9550 MHz	345.0 MHz
System	–	–	–	9340 MHz	9440 MHz	105.0 MHz

Table F-8 - Active Bandwidth

For the *RL* over 10 dB condition, the port 2 is mismatched for scanning angles below -30° .

Active Isolation Coefficients (AIC)



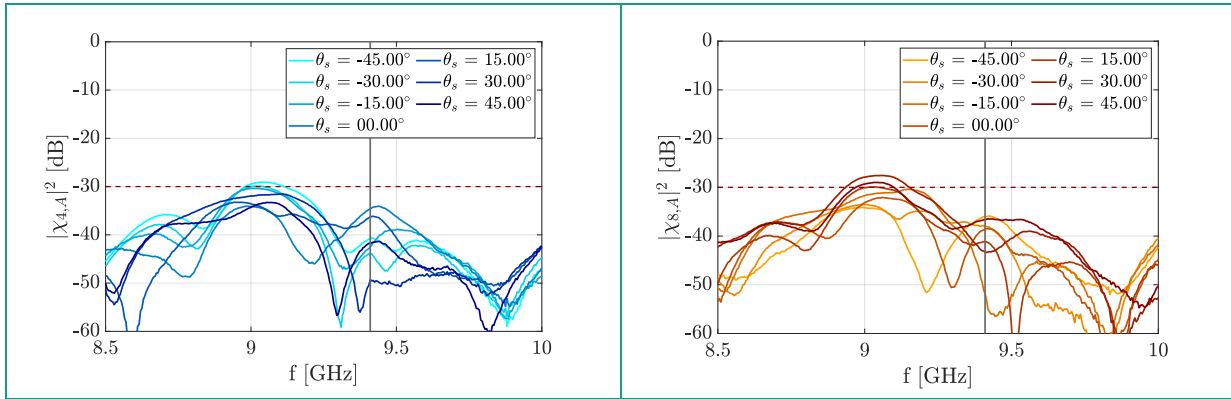


Table F-9 – Active Isolations Coefficients (H-Pol and V-Pol)

Comparison Simulations vs. Measurements

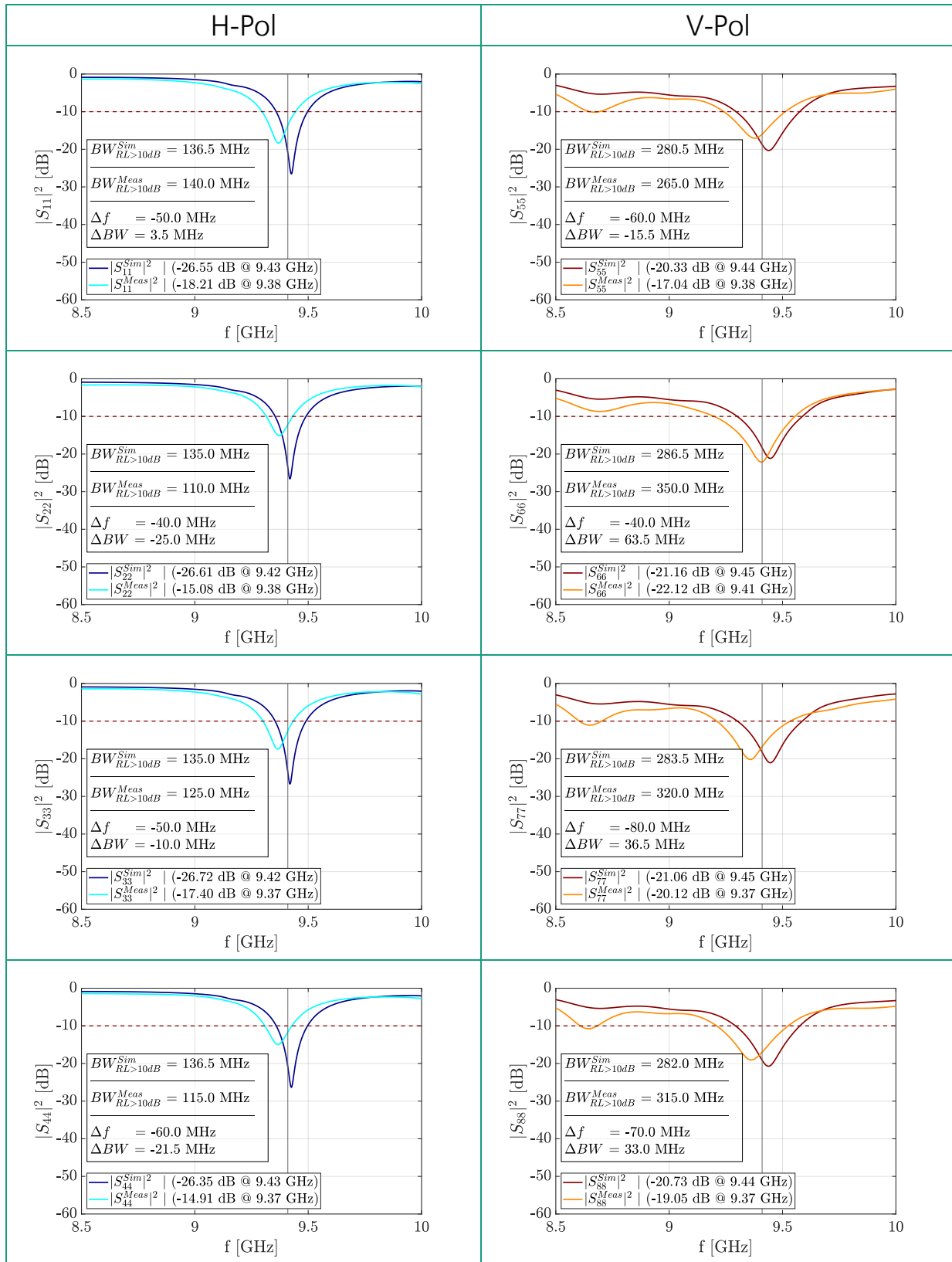


Table F-10 – Reflection Coefficients (H-Pol and V-Pol, Simulations vs. Measurements)

Radiation patterns and Cross-polarization Discrimination (XPD)

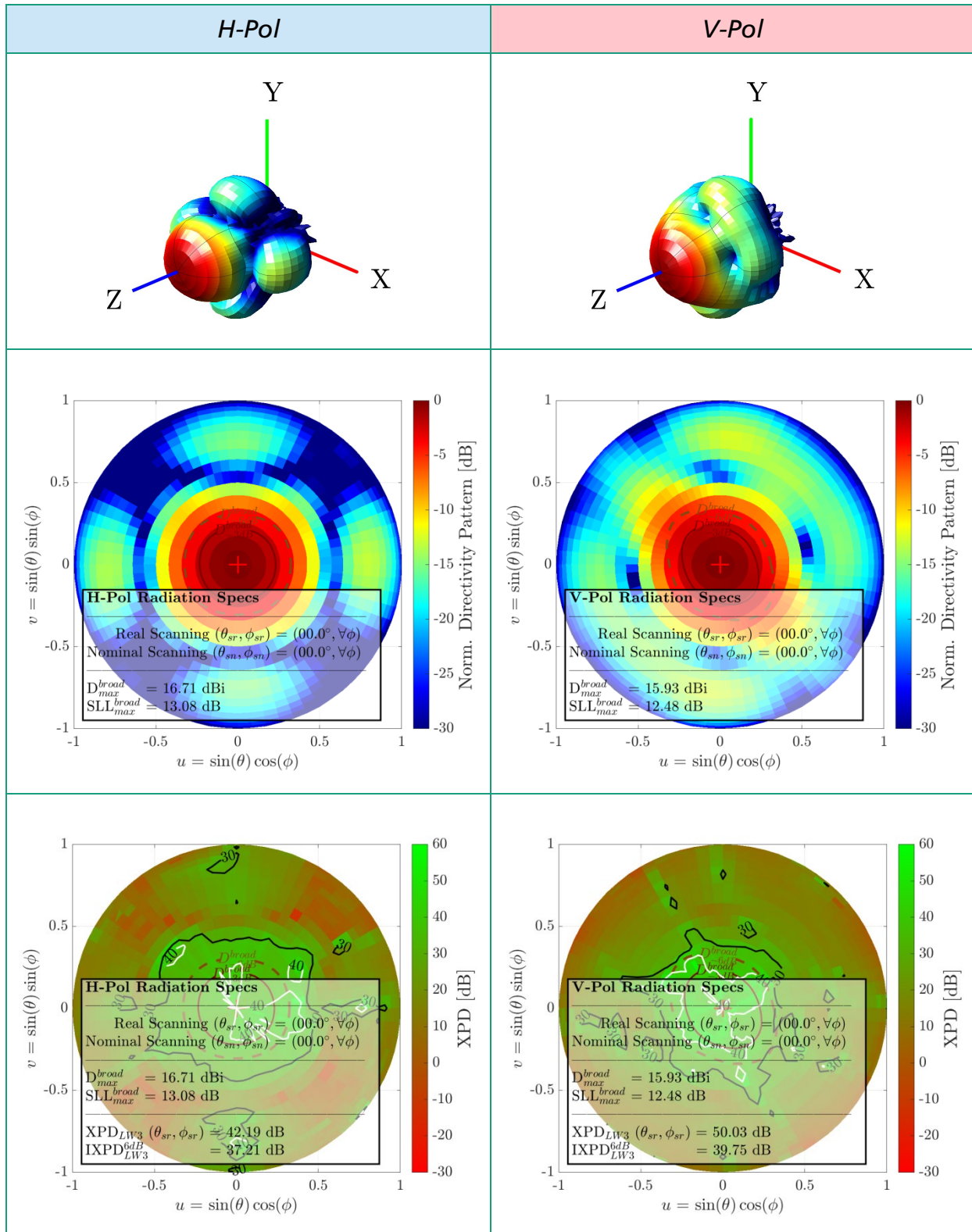


Table F-11 - Polarimetric and Radiation performance at $\theta_s = 00^\circ$ (Broadside)

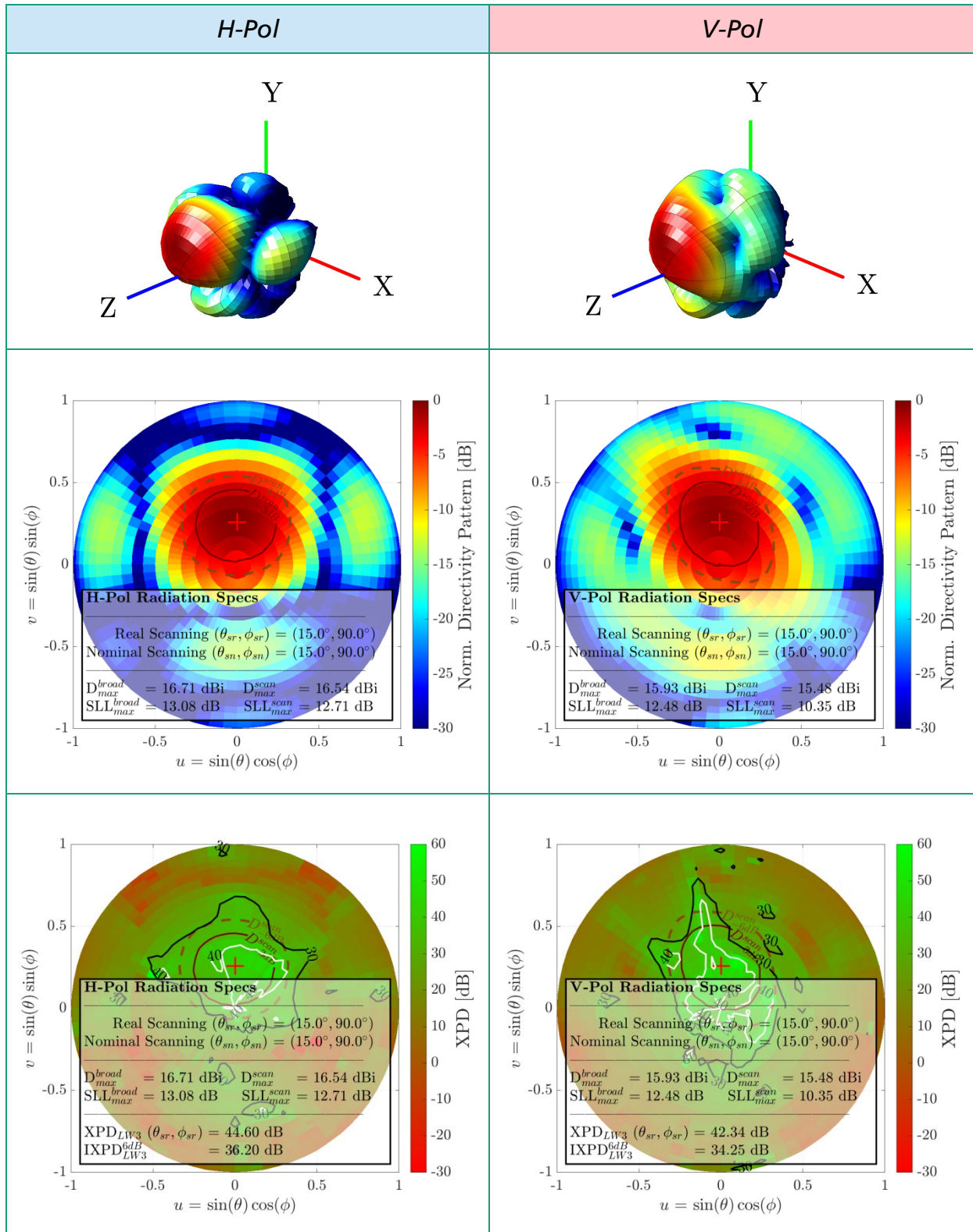


Table F-12 - Polarimetric and Radiation performance at $\theta_s = 15^\circ$

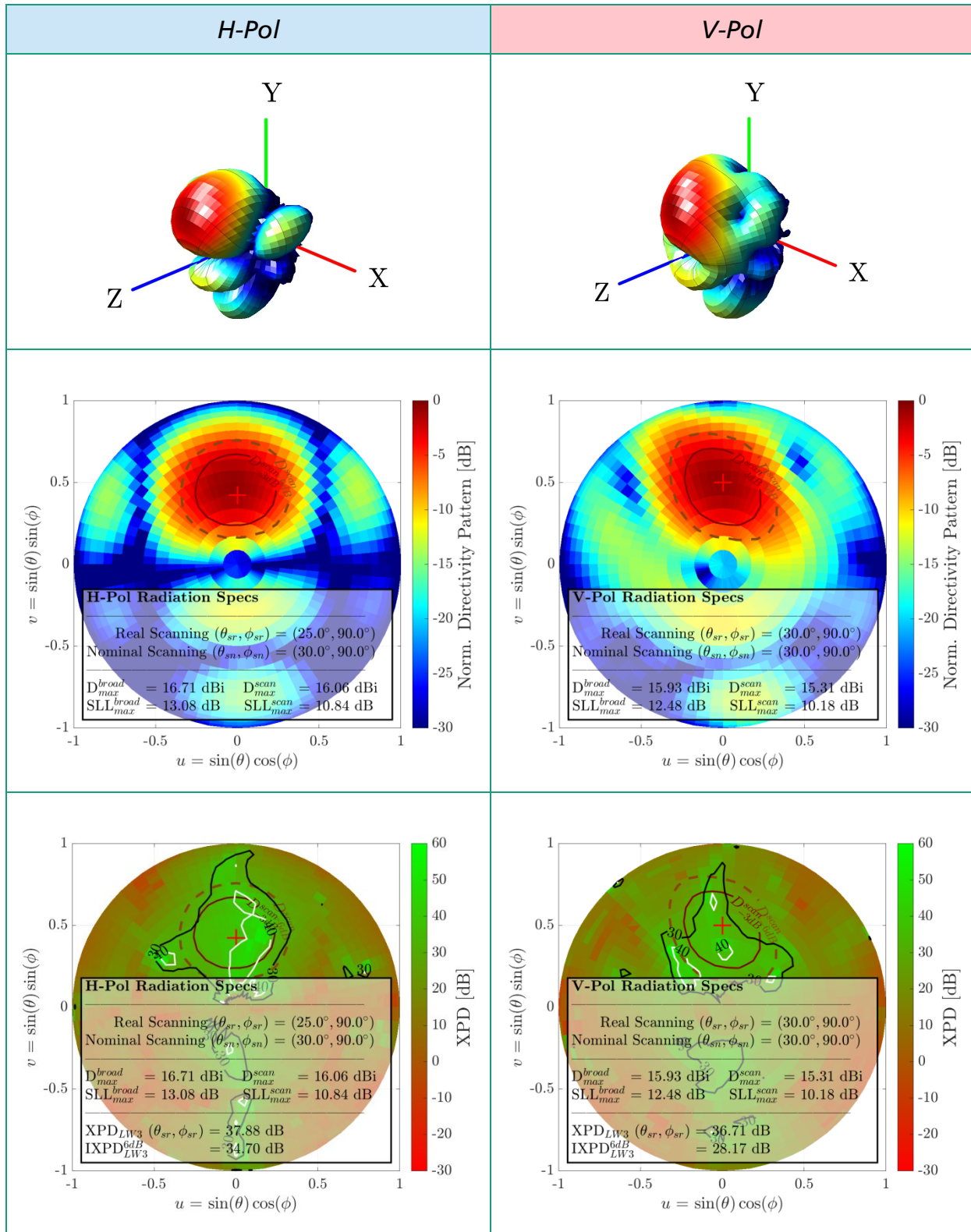


Table F-13 - Polarimetric and Radiation performance at $\theta_s = 30^\circ$

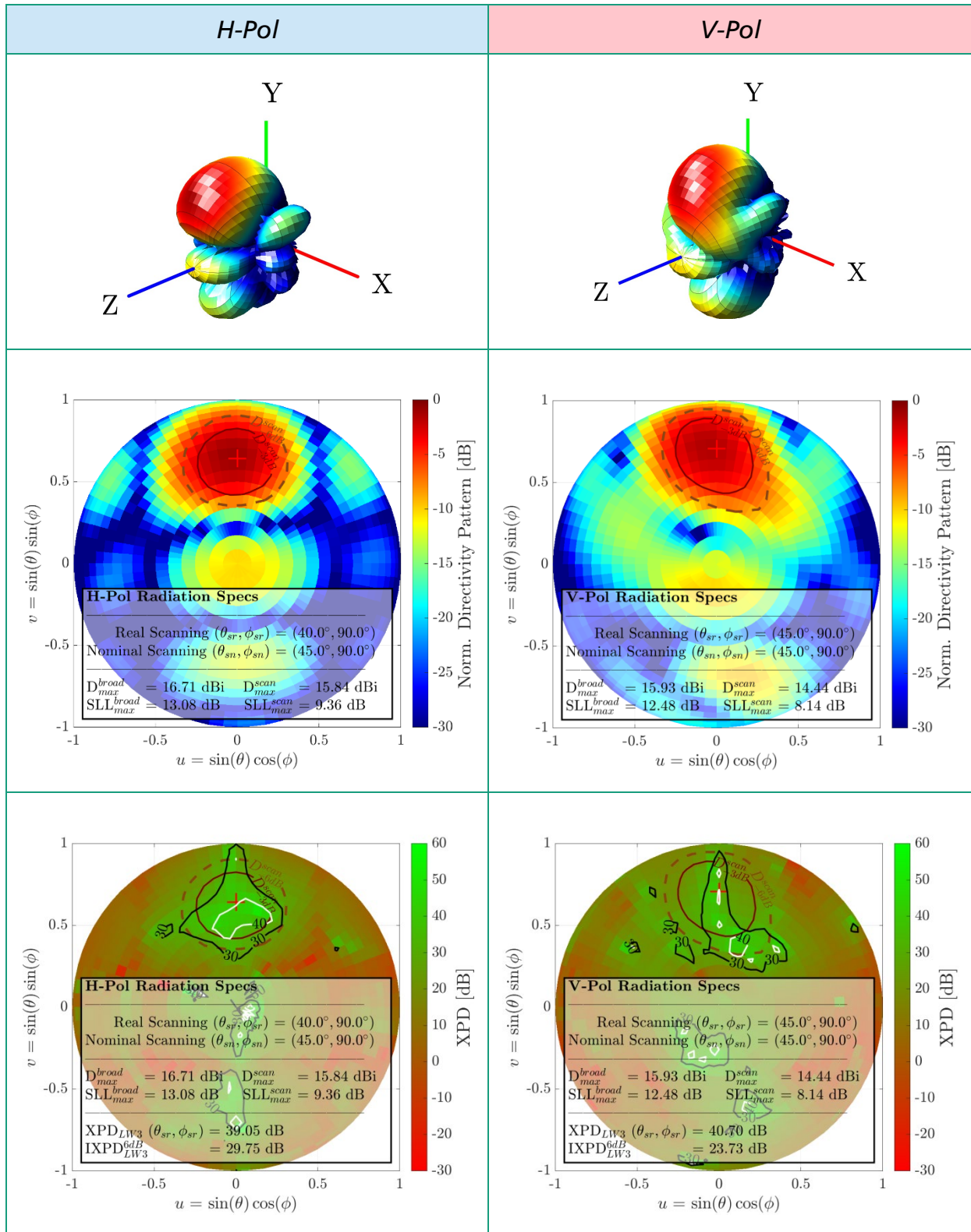


Table F-14 - Polarimetric and Radiation performance at $\theta_s = 45^\circ$

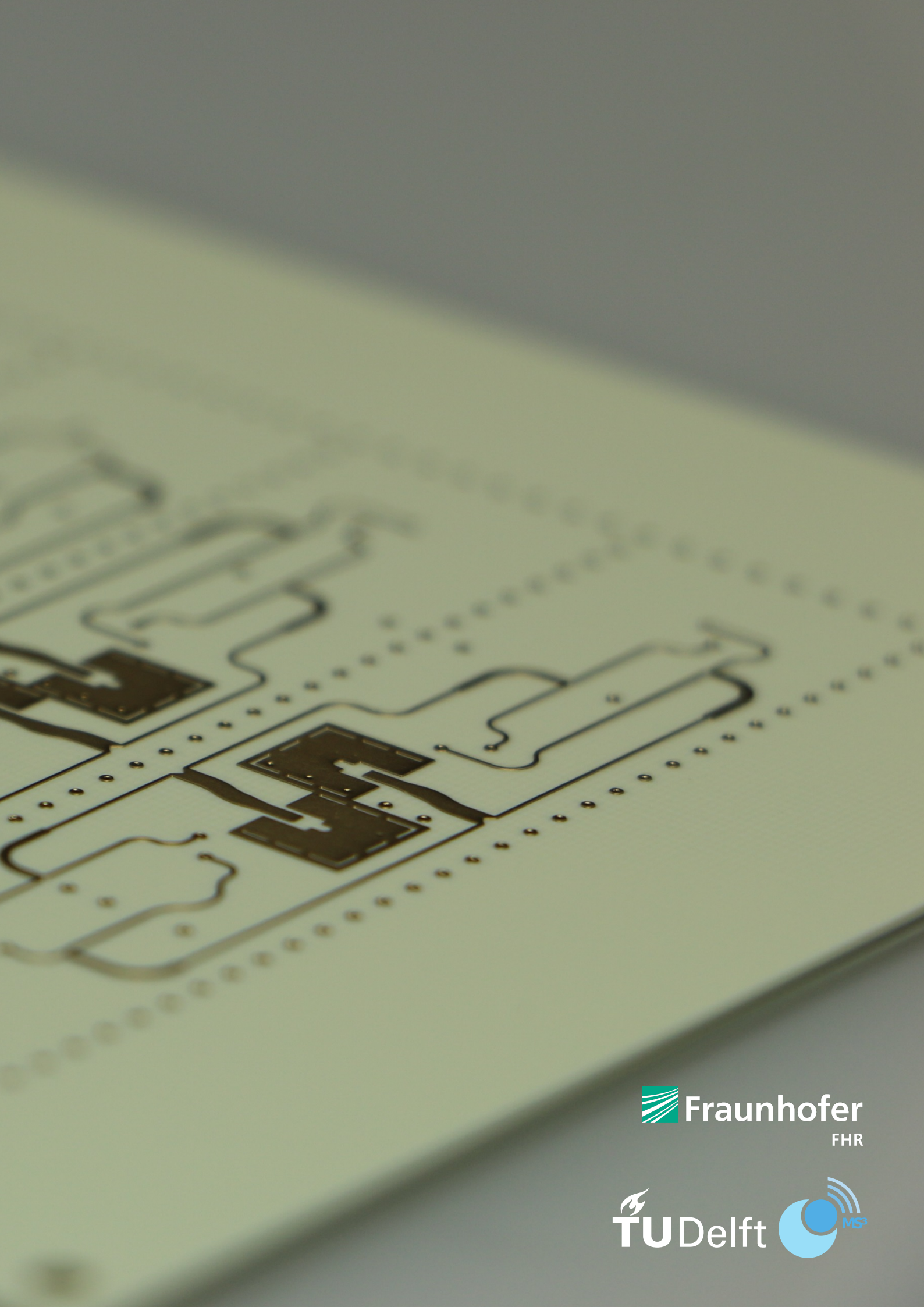
Scan Assessments

	Nominal Scanning (θ_{sn}, ϕ_{sn})	Real Scanning (θ_{sr}, ϕ_{sr})	SLL_{max}	Dir	$XPD(\theta_{sr}, \phi_{sr})$
H-Pol	(00°, $\forall\phi$)	(00.0°, $\forall\phi$)	13.08 dB	16.71 dBi	42.19 dB
	(15°, 90°)	(15.0°, 90.0°)	12.71 dB	16.54 dBi	44.60 dB
	(30°, 90°)	(28.0°, 90.3°)	10.84 dB	16.06 dBi	37.88 dB
	(45°, 90°)	(40.7°, 90.0°)	09.36 dB	15.84 dBi	39.05 dB
V-Pol	(00°, $\forall\phi$)	(00.0°, $\forall\phi$)	12.48 dB	15.93 dBi	50.03 dB
	(15°, 90°)	(15.0°, 90.0°)	10.35 dB	15.48 dBi	42.34 dB
	(30°, 90°)	(30.0°, 90.0°)	10.18 dB	15.31 dBi	36.71 dB
	(45°, 90°)	(40.0°, 90.0°)	08.14 dB	14.44 dBi	40.70 dB

Table F-15 – Radiation Scan Assessment

Final Note

The reports measurements results have been obtained at Fraunhofer FHR facilities in Wachtberg (Germany). The measured dataset has been extracted and processed with custom MATLAB functions.



 **Fraunhofer**
FHR

 **TU Delft** 